

Stony Brook University



OFFICIAL COPY

The official electronic file of this thesis or dissertation is maintained by the University Libraries on behalf of The Graduate School at Stony Brook University.

© All Rights Reserved by Author.

**Neutral Current π^0 Production Rate Measurement On-Water
Using the π^0 Detector in the Near Detector of the T2K Experiment**

A Dissertation presented

by

Karin Gilje

to

The Graduate School

in Partial Fulfillment of the

Requirements

for the Degree of

Doctor of Philosophy

in

Physics and Astronomy

Stony Brook University

August 2014

Stony Brook University

The Graduate School

Karin Gilje

We, the dissertation committee for the above candidate for the

Doctor of Philosophy degree, hereby recommend

acceptance of this dissertation

**Chang Kee Jung - Dissertation Advisor
Professor, Physics and Astronomy**

**Matt Dawber - Chairperson of Defense
Associate Professor, Physics and Astronomy**

**Patrick Meade
Assistant Professor, C.N. Yang Institute for Theoretical Physics**

**Christopher Mauger
Staff Scientist, Los Alamos National Laboratory**

This dissertation is accepted by the Graduate School

Charles Taber
Dean of the Graduate School

Abstract of the Dissertation

**Neutral Current π^0 Production Rate Measurement On-Water
Using the π^0 Detector in the Near Detector of the T2K Experiment**

by

Karin Gilje

Doctor of Philosophy

in

Physics and Astronomy

Stony Brook University

2014

The T2K Experiment is a long-baseline neutrino experiment that stretches 295 km from the east to the west coast of Japan (Tokai-Mura to Kamioka). One of the major goals of the experiment is a measurement of θ_{13} and (if θ_{13} is non-zero) potentially CP violation in the lepton sector. This is performed by searching for ν_e appearance in a ν_μ beam from the Japan Proton Accelerator Research Complex (J-PARC). The far detector, Super Kamiokande (SK), is a water Cherenkov detector. One of the dominant backgrounds for SK in the oscillation measurement is the uncertainty on the cross section of the Neutral Current Single π^0 (NC1 π^0) interaction. In order to constrain this background, the π^0 detector (P \emptyset D) was placed in the near detector complex, 280 meters from the beam origin. The P \emptyset D was constructed with a water target that can be filled and drained in order to perform a material subtraction to measure various cross sections on-water. This analysis presents the first on-water NC1 π^0 rate measurement with a neutrino beam energy less than 1 GeV. Using the NEUT Monte Carlo, a cut selection was developed in order to accentuate the difference between the signal and background shapes of the reconstructed invariant mass of the π^0 particle. The selected events and a muon decay sideband, used to constrain the shape of the background events, are then simultaneously fit in order to extract an observed number of signal events. The observed data is then compared to Monte Carlo. Using T2K Runs 1-4 (total of 6.13×10^{20} protons on target), a ratio of $0.790 \pm 0.076(\text{stat}) \pm 0.143(\text{sys})$ ($0.850 \pm 0.091(\text{stat}) \pm 0.137(\text{sys})$) is found for the P \emptyset D water-in (water-out) configuration. After calculating the subtracted number of events on-water from the water-in and water-out data, a data to NEUT Monte Carlo ratio of $0.677 \pm 0.261(\text{stat}) \pm 0.462(\text{sys})$ is found for the rate of NC1 π^0 interactions on-water.

Dedication Page

To my husband,
Joshua

Table of Contents

1	Introduction	1
1.1	Basic Particles	1
1.2	A Brief History Of Neutrinos	3
1.3	Neutrino Oscillation	13
1.4	The Neutral Current Single π^0 Interaction	17
2	T2K	19
2.1	Description of Beam Line	19
2.2	Overview of ND280 Detectors	22
2.2.1	INGRID	22
2.2.2	ND280	24
2.3	Super Kamiokande	26
3	P\emptysetD	28
3.1	Detector Construction	28
3.2	Data Acquisition	35
3.3	Software Process	37
3.4	P \emptyset D Particle Identification	40
3.4.1	Stopping Muon Sample	40
3.4.2	Creating a Map	43
3.4.3	Mapping the PID	47
3.5	Converting Deposited Charge to Energy	50
3.5.1	Creating a Photon Sample	50
3.5.2	Calculating the PEU to MeV Conversion	51
3.5.3	Checking the PEU to MeV Conversion	53
3.6	P \emptyset D Alignment	64
3.6.1	P \emptyset D Layer Resolution	64
3.6.2	Internal Alignment	65
3.6.3	Alignment to the TPC	67
3.6.4	Alignment Survey Measurements	69
4	NC1π^0 Rate Measurement	73
4.1	Reconstruction of the NC1 π^0	75
4.2	Event Selection	79
4.3	Sideband Selection	88

TABLE OF CONTENTS

4.4	Analysis	93
4.4.1	Final Sample Cross Checks	93
4.4.2	Definition of Likelihood	98
4.4.3	Fit Results	113
4.4.4	On-Water Calculation	115
4.5	T2KReWeight	116
4.5.1	Fit Results	120
4.5.2	Comparing Fit Results	126
5	Systematics	128
5.1	Energy Scale	128
5.1.1	Geometry Differences	129
5.1.2	PE Peak Uncertainty	129
5.1.3	Energy Scale	132
5.2	Detector Variations	135
5.3	Mass Uncertainty	137
5.4	Alignment	140
5.5	Fiducial Volume	140
5.5.1	Fiducial Volume Scaling	140
5.5.2	Fiducial Volume Shift	143
5.6	Flux and Event Generator Uncertainties	145
5.7	Reconstruction Uncertainties	151
5.7.1	Track PID Efficiency	151
5.7.2	Continuous Distribution Cuts	151
5.7.3	Muon Decay Systematic	157
5.8	g Factor	158
5.8.1	Statistical g Contribution	158
5.8.2	Systematic g Contribution	158
5.9	Summary of Systematic Errors	160
6	Conclusion	163
6.1	Future Improvements	164
	Appendices	167
	Appendix A Supporting Plots for Fit Result	167
A.1	Unconstrained g Fit	171

List of Figures

1.1	Standard Model view of basic particles	2
1.2	The decay of the π^0	3
1.3	Beta decay	4
1.4	Neutrino mass and the shape of the β -decay energy spectrum	5
1.5	Direct Observation of ν_τ	7
1.6	Neutrino number and the Z decay width	8
1.7	Asymmetry of atmospheric neutrinos	10
1.8	Rate of atmospheric neutrinos	11
1.9	SNO results	13
1.10	NC1 π^0 interaction	18
2.1	The J-PARC accelerator complex	20
2.2	Schematic diagrams of the beam extraction	20
2.3	Affect of the off-axis flux	21
2.4	A diagram of the ND280 Complex	23
2.5	Schematic diagram of the INGRID detector	23
2.6	Diagram of the INGRID Modules	24
2.7	Diagram of the ND280 detectors	25
2.8	A cut away view of the TPC	25
2.9	A diagram of SK	27
3.1	A schematic diagram of the P \emptyset D	29
3.2	A schematic showing a singlet and doublet hit	35
3.3	A schematic of the WLS fiber to MPPC assembly	36
3.4	A diagram of the data collection system	36
3.5	A diagram of the software process	38
3.6	A diagram of the P \emptyset D reconstruction process	39
3.7	Last P \emptyset Dule used in the stopping muon sample	41
3.8	Length of tracks in stopping muon sample	41
3.9	Vertex distribution for the water-in stopping muon sample	42
3.10	Vertex distribution for the water-out stopping muon sample	42
3.11	Angular distribution of the water-in stopping muon sample	43
3.12	Angular distribution of the water-out stopping muon sample	44
3.13	Example of the layer charge PID variable	44
3.14	Example of the layer asymmetry PID variable	45

LIST OF FIGURES

3.15	Example of the P \emptyset Dule asymmetry PID variable	46
3.16	Example of the number of empty layers PID variable	46
3.17	Example of the median PID variable	47
3.18	Comparison of deposited charge and true energy of photons with an energy less than 500 MeV.	51
3.19	Comparison of deposited charge and true energy of photons with an energy less than 1 GeV.	52
3.20	Water-in energy bin fits	54
3.21	Water-out energy bin fits	55
3.22	ECal-only energy bin fits	56
3.23	Fitting the charge to energy conversion	57
3.24	The fractional accuracy of the estimated energy	58
3.25	Estimated energy versus true energy	60
3.26	The estimated energy versus the corrected charge deposit	61
3.27	Mono-energetic test results for the water-in configuration	62
3.28	Mono-energetic test results for the water-out configuration	63
3.29	Monte Carlo predicted resolution of a singlet.	65
3.30	Monte Carlo predicted resolution of a doublet.	66
3.31	Measured resolution of a singlet.	66
3.32	Measured resolution of a doublet.	67
3.33	Internal P \emptyset D Alignment method testing.	68
3.34	Internal P \emptyset D Alignment of the in situ P \emptyset D	68
3.35	External P \emptyset D to TPC Alignment Monte Carlo test	69
3.36	External P \emptyset D to TPC Alignment in situ	70
3.37	Comparison of P \emptyset Dule Y alignment and survey	71
3.38	Comparison of P \emptyset Dule X alignment and survey	72
4.1	The NC1 π^0 vertex resolution for the water-in configuration	76
4.2	The NC1 π^0 vertex resolution for the water-out configuration	77
4.3	Angular resolution of decay photons	78
4.4	Opening angle resolution of decay photons	78
4.5	Fractional momentum resolution of the π^0	79
4.6	The N-1 plot of the fiducial cut	81
4.7	The N-1 plot of the muon decay cut	82
4.8	The N-1 plot of the shower charge cut	82
4.9	The N-1 plot of the PID weight cut	83
4.10	The N-1 plot of the π^0 direction cut	83
4.11	Diagram of overlapping 2D projections of a 3D shower	84
4.12	The N-1 plot of shower separation cut	85
4.13	Cut optimization for the water-in configuration	86
4.14	Cut optimization for the water-out configuration	87
4.15	The muon decay sideband	89
4.16	The charge in shower sideband	89
4.17	The PID weight sideband	90
4.18	The shower separation sideband	90

4.19	Comparison of background with the muon decay sideband	91
4.20	Comparison of background with the charge in shower sideband	92
4.21	Comparison of background with the PID weight sideband	92
4.22	Comparison of background with the shower separation sideband	93
4.23	The invariant mass of the selected events	94
4.24	The efficiency of the NC1 π^0 analysis as a function of the momentum of the π^0	97
4.25	The distribution of the true neutrino energy for the saved Monte Carlo events.	98
4.26	The rate of π^0 candidates observed per POT	99
4.27	The bunch timing of the observed candidates in the water-in configuration	100
4.28	The bunch timing of the observed candidates in the water-out configuration	101
4.29	The vertex distribution of selected events in the water-in configuration	102
4.30	The vertex distribution of the selected events in the water-out configuration	103
4.31	The vertex distribution of the selected events in the water-in configuration	104
4.32	The vertex distribution of the selected events in the water-out configuration	105
4.33	The reconstructed π^0 energy for the selected events.	106
4.34	The input PDFs for the P \emptyset D water-in configuration	107
4.35	The input PDFs for the P \emptyset D water-out configuration	108
4.36	The P \emptyset D water-in and water-out configuration simultaneous invariant mass fit.	112
4.37	The P \emptyset D water-in and water-out configuration simultaneous invariant mass fit with an unconstrained g factor.	114
4.38	Comparison of NEUT Monte Carlo to pre- and post-weighted BANFF values for the P \emptyset D water-in configuration	117
4.39	Comparison of NEUT Monte Carlo to pre- and post-weighted BANFF values for the P \emptyset D water-out configuration	117
4.40	Comparison of BANFF errors for the P \emptyset D water-in configuration	118
4.41	Comparison of BANFF errors for the P \emptyset D water-out configuration	118
4.42	Comparison of BANFF errors on the number of observed events for the P \emptyset D water-in configuration	119
4.43	Comparison of BANFF errors on the number of observed events for the P \emptyset D water-out configuration	119
4.44	Simultaneous invariant mass fits with BANFF PDFs for the P \emptyset D water-in configuration	121
4.45	Simultaneous invariant mass fits with BANFF PDFs for the P \emptyset D water-out configuration	122
4.46	Simultaneous invariant mass fits with BANFF PDFs for the P \emptyset D water-in configuration with an unconstrained g factor	124
4.47	Simultaneous invariant mass fits with BANFF PDFs for the P \emptyset D water-out configuration with an unconstrained g factor	125
5.1	Hit charge deposit in candidate showers	129
5.2	Number of hits in XZ and YZ projections for the P \emptyset D water-in configuration	130
5.3	Number of hits in XZ and YZ projections for the P \emptyset D water-out configuration	130
5.4	Distribution of energy scale throws	132
5.5	The distribution of weighted signal events from energy scale throws	133
5.6	Distribution of energy scale throws for an unconstrained g factor	134

LIST OF FIGURES

5.7	The distribution of weighted signal events from energy scale throws with an unconstrained g factor	134
5.8	The MIP peak after correction	136
5.9	Throws of possible mass corrections	138
5.10	Data to Monte Carlo ratio after 10,000 throws of mass corrections	138
5.11	Data to Monte Carlo ratio after 10,000 throws of mass corrections with an unconstrained g factor	139
5.12	Event rate at fiducial boundary for the P \emptyset D water-in configuration	141
5.13	Event rate at fiducial boundary for the P \emptyset D water-out configuration	142
5.14	Distance from π^0 to photon conversion. for the P \emptyset D water-in configuration .	143
5.15	Distance from π^0 to photon conversion. for the P \emptyset D water-in configuration .	144
5.16	Input BANFF correlation matrices	146
5.17	Input BANFF errors	146
5.18	The distribution of the number of signal for pre-BANFF throws	149
5.19	The distribution of the number of signal for post-BANFF throws	149
5.20	The distribution of the number of signal for pre-BANFF throws with an unconstrained g factor	150
5.21	The distribution of the number of signal for post-BANFF throws with an unconstrained g factor	150
5.22	Cumulative plots of the continuous cut values for a control sample with the P \emptyset D water-in configuration	152
5.23	Cumulative plots of the continuous cut values for a control sample with the P \emptyset D water-out configuration	153
5.24	Number of muon decay clusters reconstructed from a control sample	153
5.25	Time delay of a muon decay for a control sample in the water-in configuration	155
5.26	Time delay of a muon decay for a control sample in the water-out configuration	156
5.27	The distribution of the throws of the g factor	159
5.28	The weighted signal events due to throws of the g factor	159
A.1	The negative log likelihood curves for the energy scale parameter for both the P \emptyset D water-in and water-out configurations.	168
A.2	The negative log likelihood curves for the number of signal events in the selected region for both the P \emptyset D water-in and water-out configurations. . . .	168
A.3	The negative log likelihood curves for the number of background events in the selected region for both the P \emptyset D water-in and water-out configurations. . . .	169
A.4	The negative log likelihood curves for the number of signal events in the sideband region for both the P \emptyset D water-in and water-out configurations. . .	169
A.5	The negative log likelihood curves for the number of background events in the sideband region for both the P \emptyset D water-in and water-out configurations. . .	170
A.6	The negative log likelihood curves for the number of signal events in the sideband region for both the P \emptyset D water-in and water-out configurations. . .	170
A.7	The negative log likelihood curves for the number of background events in the sideband region for both the P \emptyset D water-in and water-out configurations. . .	171
A.8	The negative log likelihood curves for the energy scale parameter for both the P \emptyset D water-in and water-out configurations.	172

A.9	The negative log likelihood curves for the g factor parameter for both the P \emptyset D water-in and water-out configurations.	172
A.10	The negative log likelihood curves for the number of signal events in the selected region for both the P \emptyset D water-in and water-out configurations. . . .	173
A.11	The negative log likelihood curves for the number of background events in the selected region for both the P \emptyset D water-in and water-out configurations. . . .	173
A.12	The negative log likelihood curves for the number of signal events in the sideband region for both the P \emptyset D water-in and water-out configurations. . .	174
A.13	The negative log likelihood curves for the number of background events in the sideband region for both the P \emptyset D water-in and water-out configurations. . .	174
A.14	The negative log likelihood curves for the number of signal events in the sideband region for both the P \emptyset D water-in and water-out configurations. . .	175
A.15	The negative log likelihood curves for the number of background events in the sideband region for both the P \emptyset D water-in and water-out configurations. . .	175

List of Tables

1.1	Current Measurement of Mixing Matrix Elements	16
3.1	P \emptyset D Fiducial Volume Definition	30
3.2	The mass of the components of the P \emptyset D	33
3.3	The areal densities of the components of the P \emptyset D	33
3.4	The fiducial mass of the P \emptyset D	35
3.5	A raw water-in PID confusion matrix	48
3.6	A water-in PID confusion matrix	48
3.7	A raw water-out PID confusion matrix	49
3.8	A water-in PID confusion matrix	49
3.9	Summary of the charge to energy conversion	53
3.10	Summary of the mono-energetic study	61
3.11	P \emptyset D resolution	65
3.12	P \emptyset D-TPC Survey results	71
4.1	Summary of beam specifications used in the Monte Carlo generation.	74
4.2	Summary of data POT	74
4.3	Summary of NEUT Monte Carlo POT	75
4.4	The vertex position resolution of NC1 π^0 events.	75
4.5	P \emptyset D fiducial volume.	80
4.6	Summary of the background compositions of the sidebands for the P \emptyset D water-in configuration	88
4.7	Summary of the purities of the sidebands for the P \emptyset Dwater-in configuration	89
4.8	Summary of the background compositions of the sidebands for the P \emptyset D water-out configuration	91
4.9	Summary of the purities of the sidebands for the P \emptyset D water-out configuration	91
4.10	The number of events passing each cut for the P \emptyset D water-in configuration	94
4.11	The number of events passing each cut for the P \emptyset D water-out configuration	95
4.12	The breakdown of the final sample in the Monte Carlo for the P \emptyset D water-in configuration.	95
4.13	The breakdown of the final sample in the Monte Carlo for the P \emptyset D water-out configuration.	96
4.14	The breakdown of the muon decay sideband in the Monte Carlo for the P \emptyset D water-in configuration.	96

4.15	The breakdown of the muon decay sideband in the Monte Carlo for the P \emptyset D water-out configuration.	96
4.16	Summary of high invariant mass events	97
4.17	Summary of efficiency and purity	97
4.18	Summary of the simultaneous fit results	111
4.19	Summary of Monte Carlo predictions	111
4.20	Summary of the signal events observed and data to Monte Carlo ratios	111
4.21	Summary of the simultaneous fit result with unconstrained g factor	113
4.22	Summary of Monte Carlo predictions	113
4.23	Summary of the signal events observed and data to Monte Carlo ratios with an unconstrained g factor	113
4.24	Efficiencies and purities of the selection	115
4.26	Summary of fit results using pre-BANFF adjusted PDFs	120
4.27	Pre-BANFF event expectations	120
4.28	Summary of fit results using post-BANFF adjusted PDFs	120
4.29	Post-BANFF event expectations	121
4.30	Summary of fit results using pre-BANFF adjusted PDFs with an unconstrained g factor	123
4.31	Pre-BANFF event expectations with an unconstrained g factor	123
4.32	Summary of fit results using post-BANFF adjusted PDFs with an unconstrained g factor	123
4.33	Post-BANFF event expectations with an unconstrained g factor	124
4.34	Summary of the water-in and water-out configuration data to Monte Carlo ratios	126
4.35	Summary of the predictions for the number of NC1 π^0 on-water vertices.	126
4.36	Summary of the on-water NC1 π^0 event rate calculations for the P \emptyset D	126
4.37	Summary of the data to Monte Carlo ratios of the rate of NC1 π^0 interactions in the P \emptyset D	127
5.1	Summary of event loss for low charge deposit cuts for the P \emptyset D water-in configuration	131
5.2	Summary of event loss for low charge deposit cuts for the P \emptyset D water-out configuration	131
5.3	Summary of systematic error due to energy scale	132
5.4	Summary of systematic error due to energy scale with an unconstrained g factor	133
5.5	Summary of the post-correction data.	135
5.6	Event weighting correction factors based on mass	137
5.7	Summary of the throws of mass corrections	139
5.8	Summary of the throws of mass corrections with an unconstrained g factor	139
5.9	Summary of the fiducial scaling systematic errors.	140
5.10	Summary of the distance between the π^0 and the photon conversion	144
5.11	Summary of flux uncertainty	147
5.12	Summary of energy bins used for the flux uncertainty	147
5.13	Summary of cross section uncertainties	148
5.14	Summary of energy bins used for the cross section uncertainties	148

LIST OF TABLES

5.15	Summary of the widths of the pre- and post-BANFF variations	148
5.16	Summary of the widths of the pre- and post-BANFF variations with an unconstrained g factor	149
5.17	Summary of the systematic error due to continuous cuts for the P \emptyset D water-in configuration	154
5.18	Summary of the systematic error due to continuous cuts for the P \emptyset D water-out configuration	154
5.19	Summary of the purities in the control sample	155
5.20	Efficiency of finding a muon decay	155
5.21	Summary of the muon decay fit for the P \emptyset D water-in configuration	155
5.22	Summary of the muon decay fit for the P \emptyset D water-out configuration	156
5.23	Summary of error due to the error on g	158
5.24	Summary of Systematic errors.	161
5.25	Summary of constraints intended for the fit	161
5.26	Summary of systematic errors with an unconstrained g factor	162

List of Abbreviations

AGS	Alternating Gradient Synchrotron
BANFF	Beam And Neutrino Flux task Force
BNL	Brookhaven National Laboratory
CCQE	Charged Current Quasi Elastic
CECal	Central ECal, a SuperPØDule
CP	Charge Parity
CTM	Cosmic Trigger Module
CWT	Central Water Target
DONUT	Direct Observation of NU Tau
DSECal	DownStream ECal
ECal	Electromagnetic Calorimeter
FGD	Fine Grained Detector
FPN	Front-end Processing Node
FSI	Final State Interaction
INGRID	Interactive Neutrino GRID
J-PARC	Japan Proton Accelerator Research Complex
LEP	Large Electron Positron Collider
MC	Monte Carlo
MCM	Master Clock Module
MIDAS	Maximum Integrated Data Acquisition System
MIP	Minimum Ionizing Particle
MPPC	Multi-Pixel Photon Counter
MUMON	MUon MONitor
NC1 π^0	Neutral Current Single π^0
ND280	The near detector complex at 280 m from the target
ND280	The off-axis near detector at T2K
PDF	Probability Distribution Function
PE	Photo-Electron
PEU	Photo-Electron Unit, a unit of deposited charge
PID	Particle IDentification
PMT	PhotoMultiplier Tube
PØD	π^0 detector
RMM	Readout Merger Module
SCM	Slave Clock Module
SK	Super Kamiokande

LIST OF TABLES

SM	Standard Model
SMRD	Side Muon Range Detector
SSM	Standard Solar Model
T2K	A long-baseline neutrino oscillation experiment
TFB	TripT Front End Board
TPC	Time Projection Chamber
USECal	Upstream ECal, a SuperPØDule
USWT	Upstream Water Target
WLS	Wave Length Shifting (fiber)

Acknowledgements

It takes a village to raise a child, or PhD candidate. Over the last six years, many people have had a large influence on my life and on the scientific work I've done. Even before that, many people have helped me become the scientist I am today.

I would like to thank my high school physics teacher, Mr. Askey, for inspiring me to even think of physics as a possible career. I would also like to thank all the physics and math professors I've had at St. Olaf College for giving me the tools to succeed in physics and in becoming a well rounded person. In particular, I wish to acknowledge Dr. Brian Borovsky and Dr. Jason Engbrecht. Both men have encouraged me to pursue my interests. They also pushed me to apply to Stony Brook. I really appreciate the post-graduate opportunities Dr. Engbrecht has provided, allowing me to work with high school women and reinvigorating my enthusiasm for the field. Thank you to Dr. Jill Dietz, my advisor at St. Olaf, for supporting me even when I left math for physics.

At Stony Brook, I have had a wonderful support group of my peers, helping me through some difficult times. I would like to acknowledge the support and love of many people. The soccer guys have helped me stay in shape and keep my stress level down with weekly games. I have also had many running buddies throughout the years, who have provided much needed confidantes: Poppy, Shawn, Sarah T., Jeanine and Adam. I really appreciate the socialization and companionship provided by a weekly game night, even though most of the evenings ended in yelling. I especially want to thank the best friends, and bridesmaids, one could ever want, Sara Callori and Betül Pamuk who, with Vanessa Iiams, made my wedding an event to remember. A big thank you to all the cat sitters I have had over the years while I was away in Japan: Shawn, John, Joshua, Jay, Sara C., Karen, and David.

I wish to thank all the members of T2K for building and running the experiment. I would like to specifically acknowledge Helen O'Keeffe for her friendship and guidance in my analysis.

The people of the NNGroup, both past and present members, have provided me with a lot of support in my research. Thank you to Chang Kee Jung, for supporting me during my PhD. I really appreciate the legacy that Glenn Lopez left for me to work on and improve. Ian Taylor and Clark McGrew were very patient with me while I learned how to code in order to contribute to the experiment. Clark continued to be patient and supportive throughout my analysis. I would also like to thank James Imber for always listening to any new issues I found in my code and for taking care of my husband in Japan. I especially want to acknowledge the support and time that I have received from Jeanine Adam from analysis to sea otters.

Finally, I want to thank my family who have encouraged me and helped me up when I was down. My parents have put forth a phenomenal effort to make sure I was happy and

LIST OF TABLES

successful all my life. I am so grateful to all of the time and energy they have devoted to me and they have been my ‘mainstay’ and will continue to be so. I am very lucky to still have my grandmother who is always excited to hear what I have been working on even though she doesn’t know what a neutrino is. A final thank you goes to my husband, Joshua, who continues to support me and makes me believe that anything is possible.

Chapter 1

Introduction

The fundamental information needed to follow this dissertation is presented in this chapter. First, the basic building blocks of the universe are described, as well as the particles of interest for this analysis. A brief history of neutrinos and their interactions follows. In less than a century, three neutrinos have been hypothesized and discovered as well as the oscillation between the types of neutrinos. After the history section, neutrino oscillation is described in general terms. The last section in this chapter is devoted to the Neutral Current Single π^0 (NC1 π^0) interaction whose measurement is the goal of this analysis.

1.1 Basic Particles

The current view of the construction of matter, called the Standard Model (SM), holds that the universe is constructed with two types of particles, leptons and quarks, divided into three generations. In addition to these particles, there are also four gauge bosons, which are the means of communication between particles and one scalar boson that is the means of communication between particles and a Higgs field. A brief description of these particles is shown in Figure 1.1. The photon, γ , interacts with charged particles to communicate the electromagnetic forces and therefore does not interact with neutrinos or the Z or Higgs bosons. The gluon, g , is the carrier of the strong force and interacts with quarks. The Z and W^\pm bosons are the carriers of the weak force and interact with all other particles. The Z boson does not have a charge and, when used, is referred to as Neutral Current. The charged W boson is used in Charged Current events. The Z and W^\pm bosons are the only force carriers that interact with neutrinos. In other words, all neutrino interactions must be weak and are therefore rare. The last, and most recently discovered, boson is the Higgs, which is a scalar boson and provides mass for all massive particles. The word massive must be used because in Standard Model physics, neutrinos are massless. However, from various experiments, neutrinos have been found to have small non-zero masses. This breaks the Standard Model, but makes the universe far more interesting.

The quarks combine to construct the common particles of matter, such as protons and neutrons. The proton is composed of two up quarks and a down quark giving an overall charge of +1 and spin $1/2$. The neutron is composed of one up quark and two down quarks, making a neutral particle with a spin of $1/2$. These three quark particles belong to a family

1.1. BASIC PARTICLES

		Generations of Matter																
		I	II	III														
Quarks	<table border="1"> <tr> <td>1/2 2/3</td> <td>2.3 MeV</td> <td>u Up</td> </tr> <tr> <td>1/2 2/3</td> <td>1.275 GeV</td> <td>c Charm</td> </tr> <tr> <td>1/2 2/3</td> <td>173.1 GeV</td> <td>t Top</td> </tr> </table>	1/2 2/3	2.3 MeV	u Up	1/2 2/3	1.275 GeV	c Charm	1/2 2/3	173.1 GeV	t Top	<table border="1"> <tr> <td>1 0</td> <td>0 eV</td> <td>γ Photon</td> </tr> <tr> <td>0 0</td> <td>125.9 GeV</td> <td>H^0 Higgs Boson</td> </tr> </table>	1 0	0 eV	γ Photon	0 0	125.9 GeV	H^0 Higgs Boson	Scalar Bosons
	1/2 2/3	2.3 MeV	u Up															
	1/2 2/3	1.275 GeV	c Charm															
1/2 2/3	173.1 GeV	t Top																
1 0	0 eV	γ Photon																
0 0	125.9 GeV	H^0 Higgs Boson																
<table border="1"> <tr> <td>1/2 -1/3</td> <td>4.8 MeV</td> <td>d Down</td> </tr> <tr> <td>1/2 -1/3</td> <td>95 MeV</td> <td>s Strange</td> </tr> <tr> <td>1/2 -1/3</td> <td>4.18 GeV</td> <td>b Bottom</td> </tr> </table>	1/2 -1/3	4.8 MeV	d Down	1/2 -1/3	95 MeV	s Strange	1/2 -1/3	4.18 GeV	b Bottom	<table border="1"> <tr> <td>1 0</td> <td>0 eV</td> <td>g Gluon</td> </tr> </table>	1 0	0 eV	g Gluon	Gauge Bosons				
1/2 -1/3	4.8 MeV	d Down																
1/2 -1/3	95 MeV	s Strange																
1/2 -1/3	4.18 GeV	b Bottom																
1 0	0 eV	g Gluon																
Leptons	<table border="1"> <tr> <td>1/2 -1</td> <td>0.511 MeV</td> <td>e Electron</td> </tr> <tr> <td>1/2 -1</td> <td>105.7 MeV</td> <td>μ Muon</td> </tr> <tr> <td>1/2 -1</td> <td>1.777 GeV</td> <td>τ Tauon</td> </tr> </table>	1/2 -1	0.511 MeV	e Electron	1/2 -1	105.7 MeV	μ Muon	1/2 -1	1.777 GeV	τ Tauon	<table border="1"> <tr> <td>1 0</td> <td>91.2 GeV</td> <td>Z Z Boson</td> </tr> <tr> <td>1 ± 1</td> <td>80.4 GeV</td> <td>W^\pm W Boson</td> </tr> </table>	1 0	91.2 GeV	Z Z Boson	1 ± 1	80.4 GeV	W^\pm W Boson	
	1/2 -1	0.511 MeV	e Electron															
	1/2 -1	105.7 MeV	μ Muon															
1/2 -1	1.777 GeV	τ Tauon																
1 0	91.2 GeV	Z Z Boson																
1 ± 1	80.4 GeV	W^\pm W Boson																
<table border="1"> <tr> <td>1/2 0</td> <td><2 eV</td> <td>ν_e Electron Neutrino</td> </tr> <tr> <td>1/2 0</td> <td><0.19 MeV</td> <td>ν_μ Muon Neutrino</td> </tr> <tr> <td>1/2 0</td> <td><18.2 MeV</td> <td>ν_τ Tau Neutrino</td> </tr> </table>	1/2 0	<2 eV	ν_e Electron Neutrino	1/2 0	<0.19 MeV	ν_μ Muon Neutrino	1/2 0	<18.2 MeV	ν_τ Tau Neutrino									
1/2 0	<2 eV	ν_e Electron Neutrino																
1/2 0	<0.19 MeV	ν_μ Muon Neutrino																
1/2 0	<18.2 MeV	ν_τ Tau Neutrino																
Legend																		
<table border="1"> <tr> <td>Spin</td> <td>Mass</td> </tr> <tr> <td>Charge</td> <td></td> </tr> <tr> <td>Symbol</td> <td></td> </tr> <tr> <td>Particle Name</td> <td></td> </tr> </table>					Spin	Mass	Charge		Symbol		Particle Name							
Spin	Mass																	
Charge																		
Symbol																		
Particle Name																		

Figure 1.1: The basic particles in the standard model. The descriptions contain the particle name, symbol, mass, spin and charge. The blue boxes describe the quarks, where the green ones describe the leptons. The purple boxes describe the force carriers that are used to communicate between the particles. Values taken from the PDG [1].

32 called baryons. Another particle of interest for this work is called the π^0 meson, which will
 33 commonly be called the π^0 . This particle is in the meson family because it is constructed by
 34 two quarks. The π^0 has a slightly more complicated construction because it is a superposition
 35 of two states. The quark composition is

$$\pi^0 = \frac{u\bar{u} - d\bar{d}}{\sqrt{2}}. \quad (1.1)$$

36 As the π^0 is a composition of quarks and their antiparticles, it lives for a very short time
 37 before annihilation. The mean lifetime is measured to be $(8.52 \pm 0.18) \times 10^{-17}$ seconds [1].
 38 The π^0 decays to two photons $(98.823 \pm 0.034)\%$ of the time [1]. Figure 1.2 shows the lowest
 39 order Feynman diagrams of the decay of the π^0 particle. The mass of the π^0 particle has
 40 been measured to be 134.9766 ± 0.0006 MeV/ c^2 [1]. This will be used in the work presented
 41 to be a central value of the reconstructed invariant mass peak.

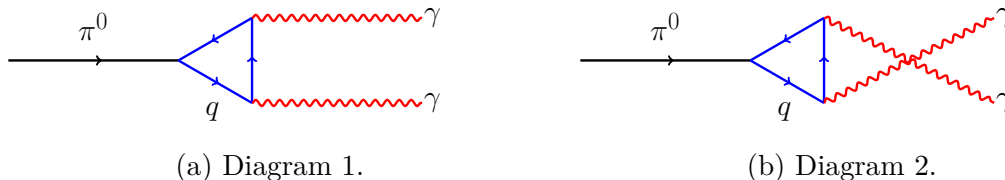


Figure 1.2: Shown are the highest order decays of the π^0 particle. Since the π^0 decays through a chiral anomaly, the decay must be described by a triangle diagram. The black line indicates the original bound state of the π^0 particle. The blue lines represent the quark that annihilates with its antiparticle. The quarks are either up or down quarks. The red lines represent the photons that come out of the decay. Diagram 1 and Diagram 2 are mathematically different, but experimentally indistinguishable. In both diagrams, time propagates to the right.

42 1.2 A Brief History Of Neutrinos

43 The creation of the field of particle physics is a relatively recent development. In fact,
 44 the idea of a neutrino is less than a century old. Part of the lag behind other areas of
 45 physics was the ability to resolve the small scales necessary to investigate the structures
 46 of the universe. In 1897, J.J. Thompson discovered the electron [2]. It was the first truly
 47 fundamental particle examined in physics. This led to the idea that atoms were not the
 48 elemental building blocks in matter, which in turn led to a deeper investigation of the fine
 49 structure of the universe.

50 The discovery of the electron also led scientists to understand more about the β -decay of
 51 an atom. A β -decay occurs when a neutron in the nucleus turns into a proton and an electron
 52 is emitted. The proton can turn into a neutron and emit a positron as well. Several studies
 53 were conducted on the spectrum emitted from an atom during β -decay. The nucleus, before
 54 and after the decay, has a specific mass. The mass difference was expected to contribute to
 55 the mass of the electron and its kinetic energy, leading to an expected discrete kinetic energy
 56 spectrum of the electron. James Chadwick, in 1914, proved beyond any doubt that the
 57 spectrum was a continuous function, which violates the conservation of energy and rocked
 58 the physics world to its core [2].

59 It wasn't until 1930 that a possible explanation was put forward. To the "Radioactive
 60 Ladies and Gentlemen," Wolfgang Pauli presented "a desperate remedy" to reconcile the
 61 continuous β -decay spectrum with the expected discrete distribution. Pauli suggested the
 62 existence of "electrically neutral particles ... which have spin $1/2$ and obey the exclusion
 63 principle." He continued to list some properties of this new particle, eventually named *neu-*
 64 *trino* by Enrico Fermi, and summarized that it would account for any of the missing energy
 65 in the reaction. Additionally, Pauli expressed regret for theorizing a particle that would be
 66 incredibly difficult to detect and it would prove to remain elusive throughout the next several
 67 decades [3].

68 Using the idea of a neutrino and considering the continuous spectrum of the β -decay,
 69 Enrico Fermi published his theory of β decay in 1934. Fermi's theory, which includes the
 70 concept of neutrinos and particle creation and annihilation, has proven robust over time, see
 71 Figure 1.3. He treats the emission of an electron from the nucleus as though it were a photon

1.2. A BRIEF HISTORY OF NEUTRINOS

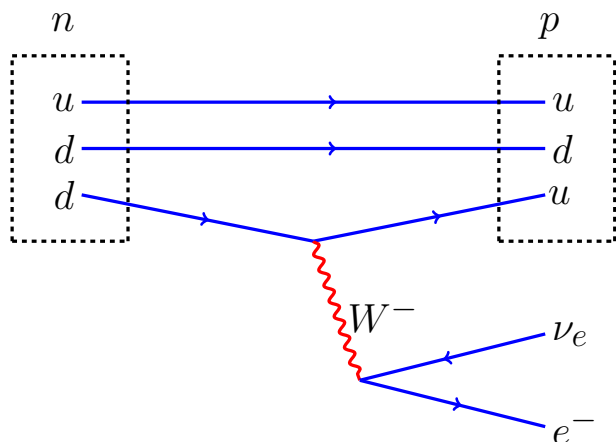


Figure 1.3: This diagram shows a neutron in a nucleus transforming into a proton through β -decay. The nucleus emits a W^- boson, red line, that decays into an electron antineutrino (or a backwards-going electron neutrino) and an electron. The W^- boson was introduced later as a force carrier in this interaction. It was not a part of Fermi’s original theory. Time propagates to the right.

72 escaping the nucleus due to de-excitation. He additionally prepared for the reverse process
 73 (electron or positron capture) considering that it “must be associated with the annihilation
 74 of an electron and a neutrino.” In addition, he made the first prediction of the so-called
 75 forbidden β -decays where the decay is highly disfavored due to a vanishing term in the
 76 transition operator. Fermi even made the first approximation of a very small neutrino mass,
 77 denoted by μ , by predicting the maximum energy of the continuous emission spectrum. He
 78 noted that the existence of a massive neutrino would affect the spectrum shape. Given
 79 Figure 1.4 he “conclude[d] that the rest mass of the neutrino is either zero, or . . . very small
 80 in comparison to the mass of the electron.” He compared the contemporary experiments
 81 to his theoretical predictions and asserted that the “greatest similarity . . . is given by the
 82 theoretical curve for $\mu = 0$ ” [4].

83 In 1952, the first indirect evidence of a neutrino was found. George Rodeback and James
 84 Allen conducted an electron capture experiment. This experiment studied the transformation
 85 of Argon-37 ($^{18}\text{A}^{37}$) to Chlorine-37 ($^{17}\text{Cl}^{37}$). This interaction is described as

$$^{18}\text{A}^{37} + e_{K,L} \rightarrow ^{17}\text{Cl}^{37} + \nu + Q, \quad (1.2)$$

86 where $e_{K,L}$ describes the orbital the electron was taken from, K , and captured to, L , ν is
 87 a neutrino and Q is the disintegration energy. The electron is pulled from an orbital shell
 88 to combine with a proton, which results in a neutron. An Auger electron is emitted often
 89 during this process. An Auger electron is a low energy electron that is ejected from an
 90 outer shell when an excited atom returns to the ground state. Essentially, the energy of the
 91 de-excitation of the atom is directed to an outer shell electron rather than a photon. This
 92 experiment measured the difference in time between the Auger electron and the recoil of
 93 the nucleus. They were then able to measure the initial kinetic energy of the atom based
 94 on the ejected Auger electron and use the recoil information in order to then look for any

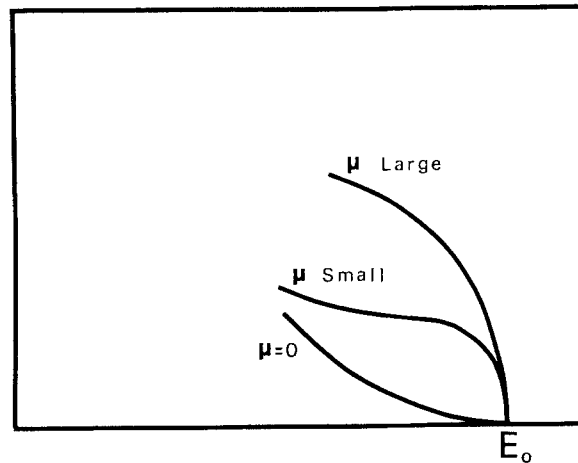


Figure 1.4: The expected shape of the continuous β -decay spectrum predicted by Fermi in 1934. The maximum possible electron kinetic energy is denoted by E_0 . Here, the effect of a neutrino mass on the shape is shown for zero, small, and large masses [4].

95 missing energy that could be attributed to a neutrino. The results were consistent with the
 96 hypothesis of single neutrino emission from the nucleus [5].

97 Finally, a neutrino had been observed. Additional studies were made to try to understand
 98 the properties of the neutrino. Was there only one? How many were there? Did an anti-
 99 neutrino exist? In 1957, Maurice Goldhaber conducted an experiment to measure the helicity
 100 of neutrinos. The experiment used Europium-152m (${}^{63}\text{Eu}^{152m}$), a meta-stable element which
 101 undergoes β capture with a half life of 9.3 hours. The process relied on the conservation
 102 of angular momentum and on the short life time of the excited state of the decay product
 103 of ${}^{63}\text{Eu}^{152m}$. Consider a parent particle, A , with spin zero and a decay product, B , with
 104 spin zero that has an excited state, B^* , with a spin of one. The direction of the spin of the
 105 neutrino can be deduced from this information by examining the polarization of the outgoing
 106 photon. The excited state, B^* , has three possible spin projections (+1, 0, -1) which imply
 107 the projection of the spin of the neutrino. The photon carries the spin away from B^* as it
 108 enters its ground state, B . For example, assuming the electron has a spin projection of $+1/2$
 109 and the excited state of the nucleus has a spin projection of +1,

$$\begin{aligned} A(J = 0) + e^-(J = +1/2) &\rightarrow B^*(J = +1) + \nu_e(J = -1/2) \\ &\rightarrow B(J = 0) + \gamma(J = +1) + \nu_e(J = -1/2). \end{aligned} \quad (1.3)$$

110 If the neutrino is assumed to be emitted in the +Z direction and the photon is then emitted in
 111 the opposite direction, both the neutrino and photon will have a negative helicity. Likewise,
 112 the inverse of Equation 1.3 shows that when the photon has positive helicity, the neutrino
 113 will as well. Samarium-152 (${}^{62}\text{Sm}^{152}$) is the decay product of ${}^{63}\text{Eu}^{152m}$ and has a mean half-
 114 life of $3 \pm 1 \times 10^{-14}$ seconds. The short lifetime of the excited state of ${}^{62}\text{Sm}^{152}$ is necessary
 115 to prevent the dissipation of the momentum into the recoil of the nucleus. In other words,
 116 Goldhaber and his team want to insure that the majority of the momentum leaves with

1.2. A BRIEF HISTORY OF NEUTRINOS

117 the photon. They discovered that the light emitted from the decay was mostly circularly
118 polarized, giving the light ray an effective negative helicity. Thus, they concluded that the
119 neutrino was left-handed. They also suggested that a similar study could be performed on
120 a nucleus that β -decays to study the helicity of the anti-neutrino [6].

121 The first direct detection of the neutrino was published in 1959. F. Reines and C.
122 Cowan Jr. spearheaded an experiment at the Savannah River Plant that not only verified
123 the existence of the free antineutrino, $\bar{\nu}$, but also provided an initial measurement of the
124 neutrino cross section. They placed a 1400 liter liquid scintillator detector in a number
125 of places, with a variety of shielding, around the plant. The scintillator was doped with
126 a cadmium compound which captured free neutrons which resulted in a photon signature.
127 They searched for the interaction

$$\bar{\nu} + p^+ \rightarrow \beta^+ + n^0 \quad (1.4)$$

128 where an antineutrino would interact with a proton, p^+ , to turn it into a neutron, n^0 , and
129 release a positron. The antineutrinos were provided by the nearby reactor. The positron
130 annihilates very quickly and the resulting light is captured. After some time, the cadmium
131 doped scintillator absorbs the free neutron and emits light. By studying these delayed
132 coincidences, they measured a cross section of $(11 \pm 2.6) \times 10^{-44} \text{cm}^2/\bar{\nu}$ [7].

133 At the Brookhaven National Laboratory (BNL) Alternating Gradient Synchrotron (AGS),
134 G. Danby et al. constructed an experiment with two main goals. The first goal was to see if
135 the neutrino in an event with a muon was the same type of neutrino as one with an electron
136 ($\nu_\mu = \nu_e$). The second goal was to calculate the respective cross sections on nucleons to
137 compare with the theoretical calculations of Lee and Yang. At the time of the experiment,
138 physicists had started to accept the idea of different types of neutrinos. The team bombarded
139 a Beryllium target with protons to create charged pions that would then decay to neutrinos
140 and muons. In this neutrino beam, they placed a shielded spark chamber and began to
141 count the created muons and electrons. If the flavor was not conserved, they would expect
142 to see the same number of muons and electrons from the neutrino interactions. However,
143 they found 34 muons and only 6 electrons. They concluded that having at least two flavors
144 was “the most probable explanation” [8].

145 A third lepton, the tau lepton (τ), was discovered in 1975. Given this discovery, was
146 likely that this new lepton also corresponded to a new neutrino. It took 26 years before
147 the first direct evidence was found in 2000. The DONUT (Direct Observation of NU Tau)
148 experiment looked directly for charged current ν_τ interactions with only one outgoing lepton,
149 a tau lepton. They bombarded a tungsten target with protons to generate their neutrinos
150 from charmed meson decays. They expected 5 \pm 1% of the neutrinos to be ν_τ . The neutrinos
151 were detected with an emulsion target that contained layers of steel and plastic. After a six
152 month exposure, the DONUT group was able to tag four events as ν_τ with a background of
153 0.34 events. Figure 1.5 shows an event display of one such event typified by the evidence of
154 a kinked track [9].

155 With each neutrino flavor discovery, an effort was made to calculate how many more
156 flavors existed. At the Large Electron Positron Collider (LEP), several experiments made
157 an effort to unfold the number of flavors of the neutrino. They investigated this question by
158 examining the width of the Z boson resonance, a weak force carrier. The total decay width

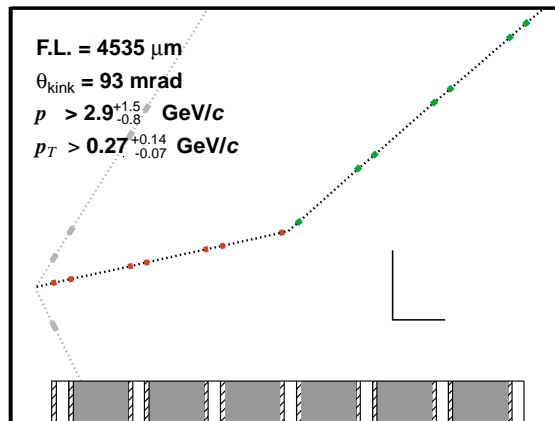


Figure 1.5: The diagram at the bottom shows the construction of the emulsion detector which has layers of steel (shaded), the emulsion sheets (hashed) and plastic (clear). The perpendicular lines provide a position scale of 1.0 by 1.0 mm. The ν_τ is incident from the left hand side. The red line represents the τ particle and the green line is an electron after the τ decay [9].

159 of the Z is split into multiple pieces. At this point, three leptons had been discovered: the
 160 electron (e), the muon (μ), and the tau lepton (τ). Each of those has a contribution to the
 161 Z decay width, denoted, for example, by Γ_e for electrons. For this experiment, the leptonic
 162 decay widths are assumed to be the same, called Γ_ℓ . However, there is a known difference due
 163 to the large mass of the tau lepton (a -0.23% difference, δ_τ). Additionally, there is a hadronic
 164 contribution that is denoted Γ_{had} which is the sum of the quark contributions. Finally there
 165 is an invisible width that is from the decays to neutrinos and therefore is not seen. This can
 166 be defined as the sum over all neutrino flavor width contributions, $\Gamma_{\text{inv}} = N_\nu \Gamma_\nu$, where N_ν
 167 is the number of neutrino flavors. In summary,

$$\Gamma_Z \approx 3\Gamma_\ell + \Gamma_{\text{had}} + \Gamma_{\text{inv}}. \quad (1.5)$$

168 Furthermore, they determined that the “hadronic pole cross-section” can be defined as

$$\sigma_{\text{had}}^0 = \frac{12\pi}{m_Z^2} \frac{\Gamma_e \Gamma_{\text{had}}}{\Gamma_Z^2}. \quad (1.6)$$

169 Using this information, the LEP experiments were able to consider the ratio of the invisible
 170 width to the leptonic width, expressed as

$$R_{\text{inv}}^0 = \frac{\Gamma_{\text{inv}}}{\Gamma_\ell} = N_\nu \left(\frac{\Gamma_{\text{inv}}}{\Gamma_\ell} \right)_{\text{SM}} = \left(\frac{12\pi R_\ell^0}{\sigma_{\text{had}}^0 m_Z^2} \right)^{1/2} - R_\ell^0 - (3 + \delta_\tau) \quad (1.7)$$

171 where $R_\ell^0 = \Gamma_{\text{had}}/\Gamma_\ell$ and $(\Gamma_{\text{inv}}/\Gamma_\ell)_{\text{SM}}$ refers to the standard model prediction. The LEP
 172 groups then measured the absolute hadronic cross section around the mass of the Z boson,
 173 seen in Figure 1.6. They found $N_\nu = 2.9840 \pm 0.0082$ to be the fitted number of neutrinos.

1.2. A BRIEF HISTORY OF NEUTRINOS

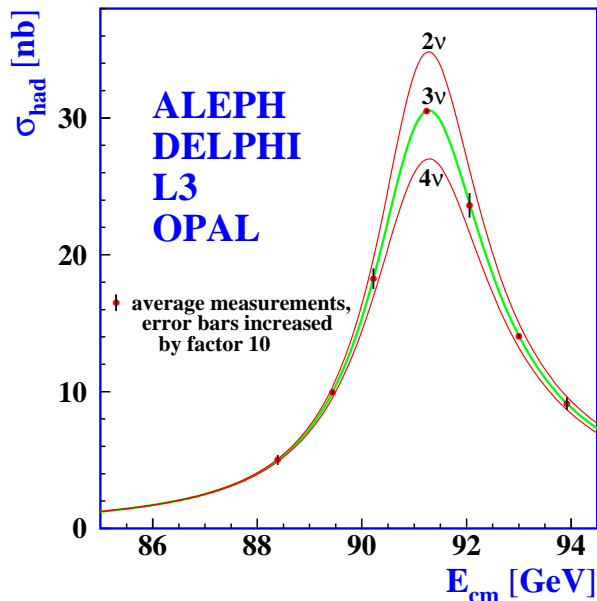


Figure 1.6: The y-axis is the measured hadronic cross section in nanobarns. The x-axis is the energy of the center of mass around the Z boson mass, 91.2 GeV. The red and green curves represent the theoretical prediction for integer number of neutrino flavors. The data points are the combined measurement from the four LEP detectors [10].

174 This coincides well with the idea of three generations of matter and the knowledge that three
 175 charged leptons had been discovered [10].

176 Around the same time as the Cowen-Reines experiment, Ray Davis began an experi-
 177 ment at BNL to see if there was a difference between neutrinos and antineutrinos in their
 178 interactions with a nucleus. Using a large tank of carbon tetrachloride, he attempted to use
 179 anti-neutrinos in an interaction that was known for neutrinos. Specifically, he compared the
 180 neutrino induces β -decay of Chlorine to Argon,



181 versus



182 This experiment placed detectors in a variety of locations. Davis was able to set upper limits
 183 on this interactions and on the solar neutrino flux. However, this experiment's lasting effect
 184 seems to be reflected as a proof of concept for the future ground breaking experiment at the
 185 Homestake mine [11].

186 Nearly a decade after the original experiment, Davis constructed a few small 500 liter
 187 tanks to test the ability to measure the solar neutrino flux. He planned to use the inverse β -
 188 decay reaction shown in Equation 1.8. He filled the tanks with a cleaning solution containing
 189 Cl^{37} . Then after a period of time elapsed, he purged and counted the Ar^{37} created. For this
 190 initial measurement Davis worked in conjunction with John Bahcall to study the internal

191 structure of the sun. From the rate of events observed by Davis, Bahcall concluded that the
 192 “central temperature of the sun is less than 20 million degrees.” Bahcall points out that this
 193 measurement is the only way to glimpse the sun’s interior mechanisms since photon cross
 194 sections are so large and their mean free path is “less than 10^{-10} of the radius of the star”
 195 and are therefore inaccessible [12][13].

196 An upgrade to the experiment yielded very curious results. In 1968, Davis and Bahcall
 197 published the first of a series of papers attempting to rectify the discrepancies between theory
 198 and experiment. Davis’s experimental setup included a 390,000 liter tank placed into the
 199 Homestake mine. His new setup was 400 times the size of the previous one and was placed
 200 underground to reduce the cosmic ray background. Davis found a neutrino capture rate of
 201 $\sum \phi \sigma \leq 0.3 \times 10^{-35} s^{-1} / \text{Cl}^{37}$ compared to the predicted background of $(2.0 \pm 1.2) \times 10^{-35} s^{-1} / \text{Cl}^{37}$
 202 [14][15]. There was an immediate flurry of papers discussing solar models to try to understand
 203 this discrepancy. This problem wasn’t solved until much later with the suggestion of neutrino
 204 oscillation.

205 There were many theories created to explain the solar neutrino problem, but other ev-
 206 idence continued to disprove these theories. In February 1987, there was a supernova that
 207 was detected by both the Kamiokande II and the IMB (Irvine-Michigan-Brookhaven) wa-
 208 ter Cherenkov experiments as an increase in the number of neutrino interactions. In fact,
 209 Kamiokande II recorded the neutrino event burst approximately 18 hours before the “first
 210 optical sighting.” One of the first important claims based on the supernova data was that
 211 the lifetimes of ν_e and $\bar{\nu}_e$ were too long to use “neutrino decay as an explanation of the
 212 solar-neutrino puzzle” [16]. Again, several theories had to return to the drawing board.

213 Then, in 1998, Super-Kamiokande, SK, released results of a curious observation which
 214 revolutionized neutrino physics. SK made a study of the number of neutrinos coming from
 215 the atmosphere. These neutrinos are naturally occurring from cosmic rays scattering in the
 216 upper atmosphere. Since neutrinos easily travel through matter, one would expect the same
 217 ν_μ to ν_e ratio from any direction. The SK collaboration examined neutrinos that travelled 15
 218 km (downward) and those that travelled 13,000 km (upward) through the charged current
 219 interactions in the detector. These interactions are typically expressed as

$$\nu + N \rightarrow \ell + X \quad (1.10)$$

220 where N is the initial nucleus and X is the final state nucleus. They found that in the whole
 221 detector the ratio of data to Monte Carlo (MC) is

$$R = \frac{(\nu_\mu/\nu_e)_{\text{data}}}{(\nu_\mu/\nu_e)_{\text{MC}}} = \begin{cases} 0.63 \pm 0.03(\text{stat}) \pm 0.05(\text{sys}), & \text{if } E_\nu \text{ is sub-GeV} \\ 0.65 \pm 0.05(\text{stat}) \pm 0.08(\text{sys}), & \text{if } E_\nu \text{ is multi-GeV} \end{cases} \quad (1.11)$$

222 Somehow, muon neutrinos were being lost. They also studied the asymmetry between the
 223 upward going events (U) and the downward going events (D), defined as

$$A = \frac{U - D}{U + D}, \quad (1.12)$$

1.2. A BRIEF HISTORY OF NEUTRINOS

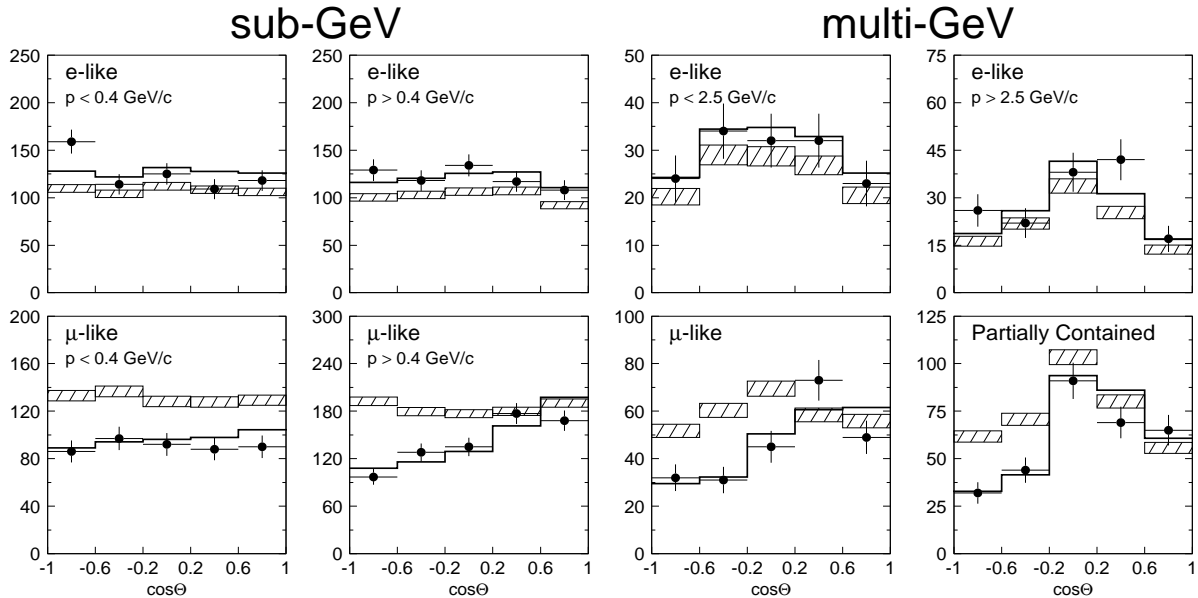


Figure 1.7: This series of plots show the interaction rate dependence on the angle and energy. The top row describes the e -like sample while the bottom row describes the μ -like sample. The x-axis is the zenith angle with $\cos \theta = 1$ coming from above and $\cos \theta = -1$ coming from below. The y-axis is the rate of events. The hashed box is the non-oscillation prediction of the rate and the line is the prediction given a best fit for ν_μ to ν_τ oscillations [17].

224 and found that although the ν_e flux was roughly constant, there were serious discrepancies
 225 in the ν_μ flux, see Figure 1.7. It should be noted that SK cannot resolve the interaction

$$\nu_\tau + N \rightarrow \tau + X \quad (1.13)$$

226 because the lifetime of the tau lepton is very short and the decay products can be easily
 227 confused with other signal. So the conclusion was that these muon neutrinos may have
 228 oscillated to ν_τ or a hypothesized sterile neutrino ν_X . Since the ν_e flux is unchanged, they
 229 concluded that the oscillation between ν_μ and ν_e is disfavored. The two flavor oscillation
 230 model, described in Section 1.3, was applied to fit the ν_μ spectrum of the length over the neu-
 231 trino energy L/E_ν , to make the first measurement of the atmospheric oscillation parameters,
 232 shown in Figure 1.8. Since this deficit is many sigma off of the null oscillation hypothesis,
 233 this is evidence of neutrino oscillation [17]. Additionally, the shape of the deficit can be used
 234 to calculate a mathematical description of the oscillation, explained further in Section 1.3.

235 In the early 2000s that the Sudbury Neutrino Observatory (SNO) definitively proved that
 236 solar neutrinos oscillate. The detector consists of a giant tank of heavy water which allows
 237 it to study much lower energy interactions, specifically neutral current (NC) and elastic
 238 scattering (ES). Heavy water typically has targets of deuterium, d , rather than a proton or
 239 a neutron. SNO examined three interactions modes:

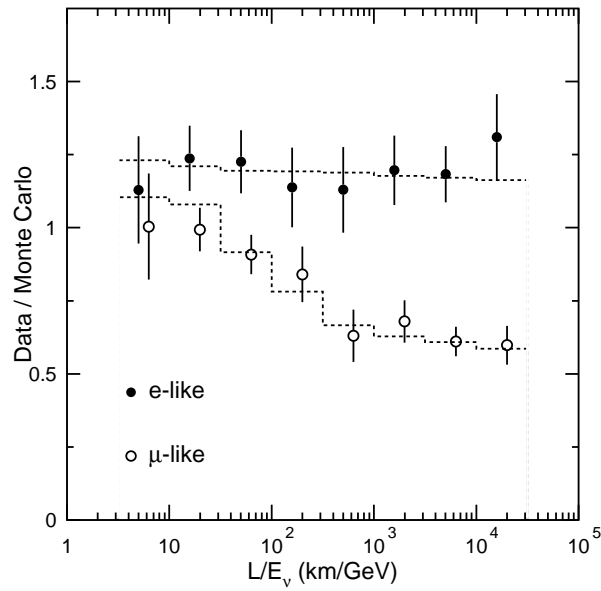


Figure 1.8: The x-axis is the length over neutrino energy metric. The y-axis is the ratio of the measured rate of events to the predicted non-oscillated rate. The filled circles represent the events that are considered to be from ν_e interactions and the empty circles represent the ν_μ interactions. The dashed lines represent a set of suggested oscillation parameters considering a two flavor oscillation between ν_μ and ν_e [17].

1.2. A BRIEF HISTORY OF NEUTRINOS

$$\begin{aligned}
 &\text{CC: } \nu_e + d \rightarrow p + p + e^-, \\
 &\text{NC: } \nu_\ell + d \rightarrow p + n + \nu_\ell, \\
 &\text{and ES: } \nu_\ell + e^- \rightarrow \nu_\ell + e^-.
 \end{aligned}
 \tag{1.14}$$

240 The CC interaction is only sensitive to ν_e , similar to the experiments performed by Davis.
 241 The SNO experiment found a ν_e flux of

$$\phi_{\text{CC}\nu_e} = 1.76_{-0.05}^{+0.06}(\text{stat}) \pm 0.09(\text{sys}) \times 10^6 \text{cm}^{-2}\text{s}^{-1}.
 \tag{1.15}$$

242 The elastic scattering mode is less sensitive to ν_μ and ν_τ since it is a scatter of an electron.
 243 The measured flux is

$$\phi_{\text{ES}} = 2.39_{-0.23}^{+0.24}(\text{stat}) \pm 0.12(\text{sys}) \times 10^6 \text{cm}^{-2}\text{s}^{-1}.
 \tag{1.16}$$

244 The NC mode is equally sensitive to all three neutrino types with an overall measured flux
 245 of

$$\phi_{\text{NC}} = 5.09_{-0.43}^{+0.44}(\text{stat})_{-0.43}^{+0.46}(\text{sys}) \times 10^6 \text{cm}^{-2}\text{s}^{-1}.
 \tag{1.17}$$

246 Finally the solar neutrino problem was resolved. The different flux calculations (ϕ_{NC} , $\phi_{\text{CC}\nu_e}$,
 247 and ϕ_{ES}) should be the same if the solar neutrinos don't oscillate. In fact the standard
 248 solar model predicts a flux of $\phi_{\text{SSM}} = 5.05_{-0.81}^{+1.01} \times 10^6 \text{cm}^{-2}\text{s}^{-1}$ which agrees quite well with
 249 ϕ_{NC} . The results from SNO were also important to unfold the parameters that describe solar
 250 neutrino oscillation. SNO split the measured solar flux into an electron flavor part and a
 251 muon/tauon flavor part, measured to be

$$\begin{aligned}
 \phi_e &= 1.76 \pm 0.05(\text{stat}) \pm 0.09(\text{sys}) \\
 \phi_{\mu\tau} &= 3.41 \pm 0.45(\text{stat})_{-0.45}^{+0.48}(\text{sys}).
 \end{aligned}
 \tag{1.18}$$

252 This measurement is shown as a global fit of the three interaction rates in Figure 1.9. These
 253 results indicated a second mass splitting, one that is at least an order of magnitude smaller
 254 than that found for atmospheric neutrinos, indicating an additional layer of complexity to
 255 the structure of the neutrinos [18][19].

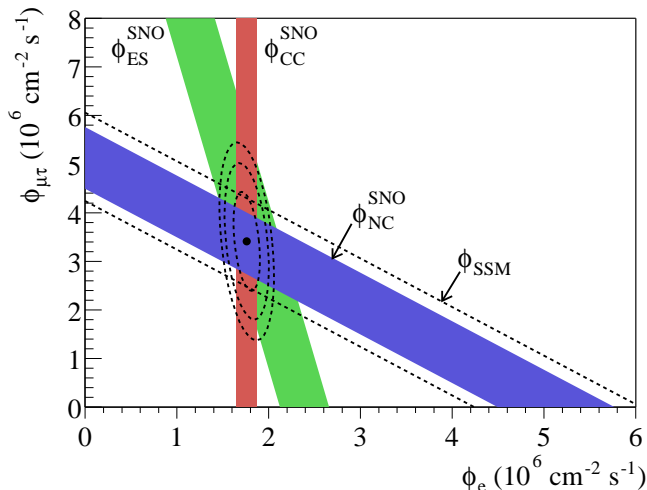


Figure 1.9: This figure displays how the three measurements (ES, CC, and NC) can be used to calculate the ν_e flux and the ν_μ and ν_τ combined flux. The x-axis represents the ν_e flux and the y-axis shows the ν_μ and ν_τ combined flux. The dashed lines show the flux prediction of the standard solar model. The dashed ellipses represent the errors on the global fit (black dot) of the three measurements [19].

1.3 Neutrino Oscillation

The oscillation between the flavors of e , μ and τ type neutrinos leads to a small neutrino mass because the mass eigenstates are superpositions of the flavor eigenstates, in other words, not one-to-one. As a neutrino travels, it falls into a mass state. The neutrino can only be observed by looking at the weak interactions that are associated with a flavor state. The mass eigenstate of a neutrino that is traveling through a vacuum can be represented by a standing wave,

$$|\nu_i(t)\rangle = e^{-i(E_i t - \vec{p}_i \cdot \vec{x})} |\nu_i(0)\rangle, \quad (1.19)$$

where E_i , \vec{p}_i , and m_i refer to the energy, momentum and mass of the i th type of neutrino and \vec{x} refers to the length traveled and t refers to the time elapsed. The i types of neutrino refer to the mass eigenstates, of which there are assumed to be three (ν_1 , ν_2 , and ν_3), although theories exist that predict far more. Any possible additional mass eigenstates are discounted for this explanation because their theorized cross sections are considered to be negligibly small. The relationship between the energy, momentum and mass of any particle is

$$E_i = \sqrt{p_i^2 + m_i^2} = p_i \sqrt{1 + \frac{m_i^2}{p_i^2}}. \quad (1.20)$$

Using a Maclaurin series, this relationship can be rearranged. Since $p_i^2 \gg m_i^2$, the series is

1.3. NEUTRINO OSCILLATION

270 truncated to first order,

$$E_i \approx p_i \left(1 + \frac{1}{2} \frac{m_i^2}{p_i^2}\right) = p_i + \frac{m_i^2}{2p_i} \quad (1.21)$$

271 The momentum, p_i , can be set to the total energy E since the mass of the neutrino is
272 negligibly small. This gives

$$E_i \approx E + \frac{m_i^2}{2E}. \quad (1.22)$$

273 Returning to Equation 1.19, E_i can be replaced with Equation 1.22 and p_i with E . In
274 addition, x refers to the oscillation length, or the baseline, L . The neutrino is assumed to
275 be traveling at approximately the speed of light, so $t = L/c$ or $t = L$ in natural units. The
276 neutrino wave equation can be rewritten as

$$\begin{aligned} |\nu_i(t)\rangle &= e^{-i(E_i t - \vec{p}_i \cdot \vec{x})} |\nu_i(0)\rangle \\ &= e^{-i\left(\left(E + \frac{m_i^2}{2E}\right)L - EL\right)} |\nu_i(0)\rangle \\ &= e^{-i\frac{m_i^2 L}{2E}} |\nu_i(0)\rangle. \end{aligned} \quad (1.23)$$

277 The relationship between the flavor eigenstates, α , and the mass eigenstates, i , are de-
278 scribed by a unitary matrix, U ,

$$\begin{aligned} |\nu_\alpha\rangle &= \sum_i U_{\alpha i}^* |\nu_i\rangle \\ &\text{and} \\ |\nu_i\rangle &= \sum_\alpha U_{\alpha i} |\nu_\alpha\rangle, \end{aligned} \quad (1.24)$$

279 where $U_{\alpha i}^*$ is the α element of the i th column of the Hermitian conjugate, U^\dagger , of U . A
280 matrix is unitary when $UU^\dagger = U^\dagger U = \mathbf{1}$, the identity matrix. The Hermitian conjugate
281 is the complex conjugate transpose of a matrix. Convention dictates that U describes the
282 transformation of the flavor states into the mass states in order to make incorporating the
283 neutrino masses into the Yukawa coupling easier. Switching the convention has no effect on
284 the final probabilities of oscillation. The probability (P) of oscillating from one flavor, α , to
285 another, β , over a given distance, L , or time, t , is calculated by

$$P_{\alpha \rightarrow \beta} = |\langle \nu_\beta | \nu_\alpha(t) \rangle|^2. \quad (1.25)$$

286 The probability in Equation 1.25 can be rewritten using bra and ket operator identities and
287 the wave equation in Equation 1.19 to be

$$P_{\alpha \rightarrow \beta} = \left| \sum_i U_{\alpha i}^* U_{\beta i} e^{-i\frac{m_i^2 L}{2E}} \right|^2. \quad (1.26)$$

288 This probability equation holds for any number of flavor states and mass eigenstates. Given
 289 the properties of complex numbers, the probability can be cast into a general form depending
 290 on the real and imaginary parts of the elements of the U . Setting $\Delta m_{ij}^2 = m_i^2 - m_j^2$, the
 291 general form of the probability is

$$\begin{aligned}
 P_{\alpha \rightarrow \beta} = & \delta_{\alpha\beta} - 4 \sum_i^{n-1} \sum_{j=i+1}^n \operatorname{Re}(U_{\alpha i}^* U_{\beta i} U_{\alpha j} U_{\beta j}^*) \sin^2 \frac{\Delta m_{ij}^2 L}{4E} \\
 & + 2 \sum_i^{n-1} \sum_{j=i+1}^n \operatorname{Im}(U_{\alpha i}^* U_{\beta i} U_{\alpha j} U_{\beta j}^*) \sin \frac{\Delta m_{ij}^2 L}{2E}
 \end{aligned} \tag{1.27}$$

292 Given a two neutrino oscillation mixing case, let the mixing be defined in the unitary
 293 matrix U where the flavor states ν_α and ν_β are related to the mass eigenstates ν_1 and ν_2 .
 294 One choice for this unitary matrix is to use a mixing angle, θ ,

$$U = \begin{bmatrix} \cos \theta & \sin \theta \\ -\sin \theta & \cos \theta \end{bmatrix}. \tag{1.28}$$

295 Assume two neutrino flavors (α and β) and two neutrino masses (1 and 2). The probability
 296 of oscillation from the α flavor to the β flavor is

$$P_{\alpha \rightarrow \beta} = \sin^2(2\theta) \sin^2\left(\frac{\Delta m_{12}^2 L}{4E}\right). \tag{1.29}$$

297 It is possible for a neutrino to remain the same flavor or oscillate back to the original flavor.
 298 This is essentially the inverse probability of Equation 1.29 that can be written as

$$P_{\alpha \rightarrow \alpha} = 1 - \sin^2(2\theta) \sin^2\left(\frac{\Delta m_{12}^2 L}{4E}\right) \tag{1.30}$$

299 Although this two flavor model appeared to work for a few years, there are two distinct
 300 mass splittings, one from SK in 1998 and one from SNO in 2002 [17][19]. This meant that the
 301 neutrino oscillation should be a three flavor model, which adds another layer of complexity.
 302 The two flavor model mixing matrix is relatively easy to understand, but the three flavor
 303 mixing matrix requires a bit more unfolding. The three flavor mixing matrix depends on
 304 four (or maybe six) angles. The first three are the mixing angles between the mass states,
 305 θ_{12} , θ_{13} , and θ_{23} . There is a Charge Parity (CP) violating phase as well, called δ_{CP} . The
 306 mixing matrix becomes

$$U = \begin{bmatrix} c_{12}c_{13} & s_{12}c_{13} & s_{13}e^{-i\delta} \\ -s_{12}c_{23} - c_{12}s_{23}s_{13}e^{i\delta} & c_{12}c_{23} - s_{12}s_{23}s_{13}e^{i\delta} & s_{23}c_{13} \\ s_{12}s_{23} - c_{12}c_{23}s_{13}e^{i\delta} & -c_{12}s_{23} - s_{12}c_{23}s_{13}e^{i\delta} & c_{23}c_{13} \end{bmatrix}, \tag{1.31}$$

307 where $c_{ij} = \cos \theta_{ij}$ and $s_{ij} = \sin \theta_{ij}$ [1]. The last two angles of interest are called the Majorana
 308 angles and only contribute if neutrinos are Majorana particles. A Majorana particle is a
 309 particle that is also its own antiparticle. At this point, it is unknown if the neutrino is
 310 Majorana. However, if the neutrino is Majorana, for three mass eigenstates, two additional
 311 CP violating phases, α_{21} and α_{31} , are added to Equation 1.31. If there exist more than three

1.3. NEUTRINO OSCILLATION

Table 1.1: The current measurements of the mixing angles and mass splittings used in the three flavor mixing matrix. The left column expresses the name of the value calculated, the right lists the value. There are three mixing angles and two mass splittings [1].

$\sin^2 2\theta_{12}$	0.857 ± 0.024
Δm_{21}^2	$(7.50 \pm 0.20) \times 10^{-5} \text{eV}^2$
$\sin^2 2\theta_{23}$	> 0.95
Δm_{32}^2	$0.00232_{-0.00008}^{+0.00012} \text{eV}^2$
$\sin^2 2\theta_{13}$	0.095 ± 0.010

mass eigenstates, say n , there will be $n - 1$ Majorana phases. Specifically, U is multiplied by an additional matrix

$$\begin{bmatrix} 1 & 0 & 0 \\ 0 & e^{i\frac{\alpha_{21}}{2}} & 0 \\ 0 & 0 & e^{i\frac{\alpha_{31}}{2}} \end{bmatrix}. \quad (1.32)$$

However, this becomes a simple phase shift and does not effect the probability of oscillation calculation.

The physics community has contributed a significant amount of resources and effort into measuring the components of the three flavor mixing matrix. Table 1.1 lists the current estimates of the important values, although some pieces are still missing. The CP Violating phase, δ_{CP} is not listed on the table. Until recently, it was unknown if the parameter could even be measured. However, given the large non-zero value for θ_{13} , it is possible that a precision measurement can and will be made in the next ten years. The sign of Δm_{32}^2 is unknown. The mass eigenstate, ν_3 , is either the largest or smallest neutrino mass. If ν_3 is the heaviest, the neutrino eigenstates are in what is called the normal hierarchy. If instead ν_3 is the lightest, the eigenstates are in an inverted hierarchy. Lastly, the octant for θ_{23} is not known. Most of the time, maximal mixing is assumed, $\theta_{23} = 45^\circ$, but it is probable that the true value is either greater or less than 45° .

Of interest is the oscillation from a ν_μ to a ν_e because it provides a window into both θ_{13} and δ_{CP} . The formula, truncated to leading order, for the probability of the oscillation is

$$\begin{aligned} P(\nu_\mu \rightarrow \nu_e) \sim & \sin^2 \theta_{23} \sin^2 2\theta_{13} \sin^2 \frac{\Delta m_{31}^2 L}{4E} \\ & - \frac{\sin 2\theta_{12} \sin 2\theta_{23}}{2 \sin \theta_{13}} \sin \frac{\Delta m_{21}^2 L}{4E} \sin^2 2\theta_{13} \sin^2 \frac{\Delta m_{31}^2 L}{4E} \sin \delta_{\text{CP}} \\ & + (\text{CP even term, matter effect term, solar term})[20]. \end{aligned} \quad (1.33)$$

The matter effect refers to a term that is a perturbation on the neutrino oscillation, which was modeled as being in a vacuum. The solar term is a term that has a primary dependence on θ_{12} . As is shown in Equation 1.33, the ability to measure δ_{CP} relies on having a non-zero θ_{13} . Precision measurements have been done at reactor experiments that study the

333 disappearance of electron antineutrinos. The probability for electron antineutrino survival
334 is

$$P(\bar{\nu}_e \rightarrow \bar{\nu}_e) \sim 1 - \sin^2 2\theta_{13} \sin^2 \frac{\Delta m_{31}^2 L}{4E_\nu} - \cos^4 \theta_{13} \sin^2 2\theta_{12} \sin^2 \frac{\Delta m_{21}^2 L}{4E_\nu} [21]. \quad (1.34)$$

335 These reactor measurements do not depend on δ_{CP} and the values of θ_{13} can be used from
336 these experiments to constrain the possible values of δ_{CP} .

337 1.4 The Neutral Current Single π^0 Interaction

338 The T2K Experiment, explained in further chapters, seeks to make a ν_e appearance
339 measurement from a ν_μ beam. The second largest background of the charged current quasi-
340 elastic (CCQE) interactions that are used to measure the appearance is due to neutral
341 current events, specifically the neutral current single π^0 (NC1 π^0) interaction. The most
342 recently published result shows that 1.0 events out of the predicted 4.3 background events
343 are from neutral current processes. One of the biggest problems with the NC1 π^0 background
344 is that the cross section, and its associated errors, are not well known. There has been one
345 previous on-water measurement done by the K2K Collaboration. K2K, the predecessor of
346 T2K, was a long baseline experiment that ran from KEK, a research lab in Tsukuba, Japan,
347 to SK. They presented the ratio of the NC1 π^0 cross section to the charged current ν_μ cross
348 section which is

$$\frac{\sigma_{\text{NC1}\pi^0}}{\sigma_{\text{CC}\nu_\mu}} = 0.064 \pm 0.001(\text{stat}) \pm 0.007(\text{sys}). \quad (1.35)$$

349 This measurement was done in a wide band neutrino beam, so the incoming neutrinos had a
350 wide range of energies. The model used to make the Monte Carlo predicted this ratio at 0.065,
351 showing excellent agreement. This work presents a rate measurement in a narrow-peaked off-
352 axis neutrino energy beam, which will be explained further in later chapters. Additionally,
353 the K2K measurement utilized a higher energy (1 - 1.5 GeV) neutrino spectrum than that
354 used for this measurement [22].

355 In experimentation, it is very difficult to separate the different modes of NC1 π^0 interac-
356 tions. Only the final state particles are measured. The requirements placed on the analysis
357 are: no outgoing leptons, one π^0 particle, no other mesons, and any number of baryons
358 (specifically if the nucleon has some recoil). These requirements all refer to particles exiting
359 the entire nucleus, not just the initial interaction since it is possible to have a cascade of
360 interactions inside the nucleus before the output particles can be seen by a detector. As
361 such, the measurement is a combination of several interaction modes. One such mode is
362 delta resonance, shown in Figure 1.10. In this interaction, a neutrino interacts with a nu-
363 cleon through a Z boson. The nucleon is then in an excited state, called either Δ^+ or Δ^0
364 depending on if the nucleon is a proton or a neutron. However, examining the final state
365 interaction (FSI) also allows for coherent π^0 creation and other nuclear effects.

1.4. THE NEUTRAL CURRENT SINGLE π^0 INTERACTION

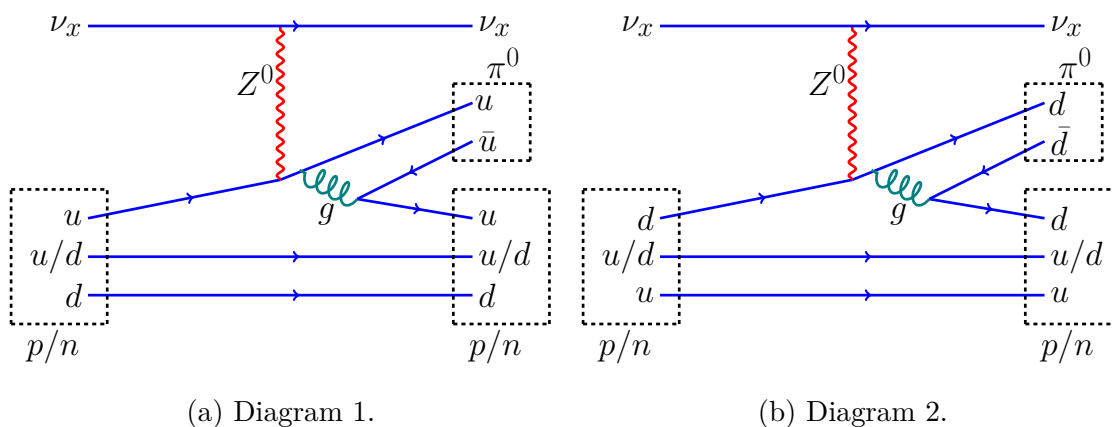


Figure 1.10: NC1 π^0 production through a delta resonance. A neutrino of any flavor interacts with a nucleon through a Z boson. The excited nucleus then radiates energy in the form of a gluon which creates a quark-antiquark pair. Diagram 1 shows the result of an $u\bar{u}$ quark pair created by the gluon. Diagram 2 displays a $d\bar{d}$ quark pair.

Chapter 2

T2K

T2K is a long-baseline neutrino experiment. A ν_μ beam is created at the Japan Proton Accelerator Research Complex (J-PARC) and is directed 2.5° off-axis towards the far detector, Super-Kamiokande (SK). Additionally, there are two near detectors, an on-axis detector, the interactive neutrino GRID (INGRID), and an off-axis detector (ND280) that are used to constrain the beam flux and make cross section measurements to constrain the errors on measurements made at SK.

T2K has several physics goals, ranging from understanding neutrino oscillations to measuring neutrino interactions on various targets. The two main oscillation analyses are the electron neutrino appearance and muon neutrino disappearance. Electron neutrino appearance at SK allows a measurement of the mixing angle θ_{13} and the CP violating phase factor, δ_{CP} , see Equation 1.33. The muon neutrino disappearance looks towards a precision measurement of θ_{23} . In order to better understand both measurements, several cross section measurements were undertaken to further ascertain the effect of the backgrounds. The $NC1\pi^0$ interaction rate measurement is one such cross section.

2.1 Description of Beam Line

The J-PARC beam line was constructed between 2004 and 2009. As a relatively new facility, it has been constantly upgraded every year to improve the proton beam power. Figure 2.1 shows the design of the J-PARC laboratory. A linear accelerator (LINAC) accelerates hydrogen atoms up to 400 MeV. The electrons are stripped from the atoms and the remaining protons are first injected into a rapid cycling synchrotron (RCS). There the protons are accelerated up to 3 GeV and finally injected into the 30 GeV Main Ring (MR). After accelerating, the protons are directed towards a graphite target in a fast extraction. These protons are monitored by an optical transition radiation (OTR) monitor. There are eight successive beam bunches filled that make up a $5\mu\text{s}$ spill.

The proton bunches are directed onto a graphite target that is 91.4 cm long (or 1.9 interaction lengths). When the protons hit the graphite hadronic showers occur. The majority of these showers result in pions, π^+ , and Kaons, K^+ . The π^+ decay to create muon neutrinos $98.98770 \pm 0.00004\%$ of the time [1]. There is a small ν_e contamination that comes from the decay of the resulting muons and from a subdominant Kaon decay. In the end, 93.6% of the

2.1. DESCRIPTION OF BEAM LINE

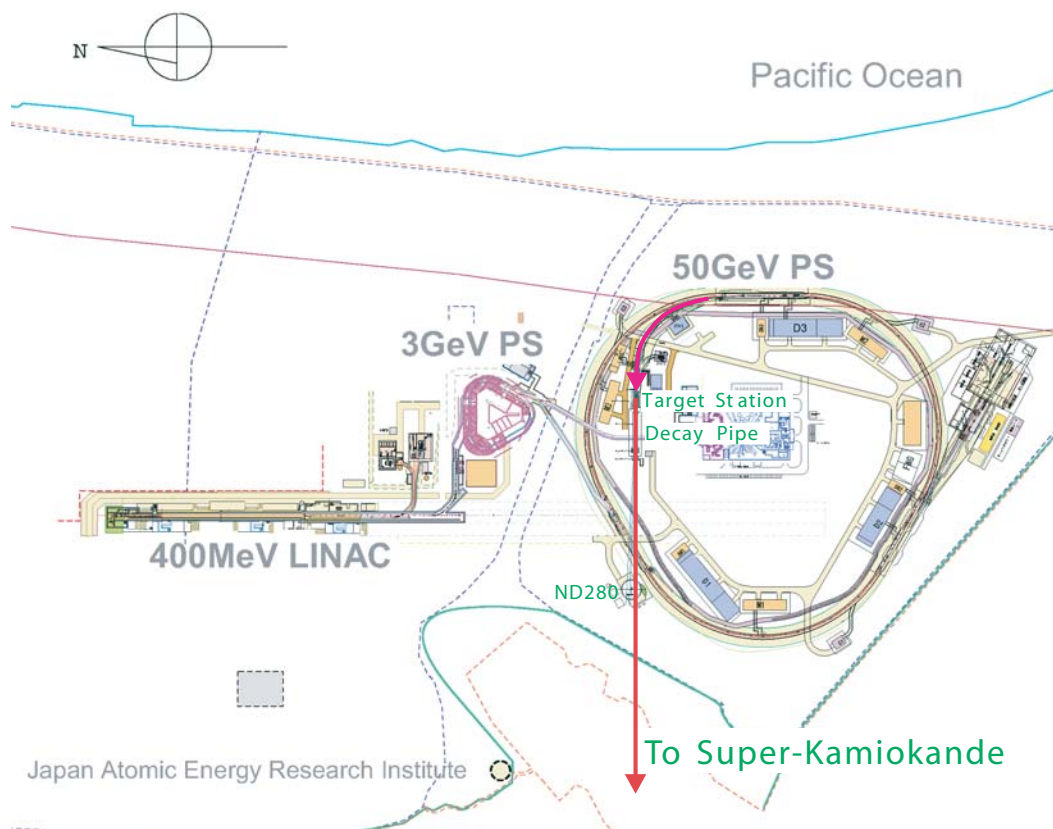


Figure 2.1: A schematic diagram of the J-PARC accelerator complex. This figure details the original design energies from the proposal of the experiment [23].

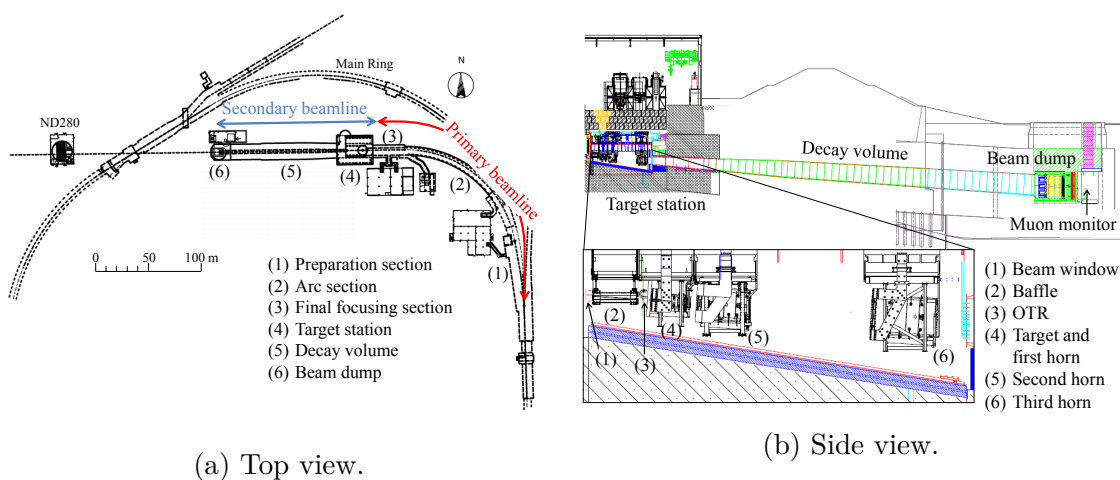


Figure 2.2: Schematic diagrams of the top and side views of the beam extraction and target station [24].

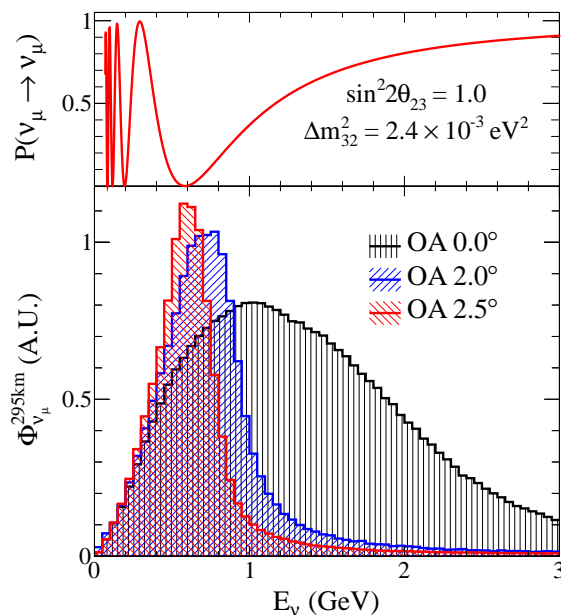


Figure 2.3: The affect of an off-axis angle on the shape of the neutrino flux. The top plot shows the muon neutrino survival probability expected at SK ($L = 295\text{km}$). The bottom plot y-axis is in arbitrary units of flux. The amplitude of the flux shape is not to scale [24].

397 neutrino flux comes from muon neutrinos, 5.4% from the muon antineutrinos and less than
 398 one percent from the electron neutrinos and antineutrinos [24].

399 The first of three neutrino horns surrounds the graphite target. These horns use a
 400 toroidal magnetic field to focus the outgoing charged particles and therefore reveal their
 401 decay neutrinos. They operate at 250 kA which creates a 1.7 T field. The horns also have
 402 the ability to run at a reversed polarity which will instead focus negatively charge particles
 403 and as a result focus an intense antineutrino beam. After the third neutrino horn, there
 404 is a large decay volume that allows the pions and kaons to decay into lighter products and
 405 neutrinos. At the end of the volume there is a beam dump designed to stop the heavier
 406 particles. A muon monitor (MUMON) is also placed at the end of the beam dump to
 407 monitor the overall flux and position of the beam. The MUMON found that the beam
 408 remained stable in the X and Y coordinates within 1 mrad (design stability) [24].

409 The beam is designed to be 2.5° off-axis at the near detector ND280 and at the far detec-
 410 tor, SK. In Figure 2.3, the muon neutrino disappearance probability is seen at a minimum
 411 (with the default assumptions of $\sin^2 2\theta_{23} = 1.0$, $L = 295 \text{ km}$ and $\Delta m_{32}^2 = 2.4 \times 10^{-3} \text{ eV}^2$)
 412 near a neutrino energy of 600 MeV. The off-axis angle was chosen to be 2.5° because the
 413 neutrino flux is sharply peaked near 600 MeV. There is a balancing act between gaining a
 414 sharper peak and losing flux the larger the off-axis angle is. The amplitudes of the flux is
 415 arbitrary in the figure, in fact the amplitude decreases quite dramatically as the beam moves
 416 away.

417 The π^+ , the most common result of the protons interacting with the graphite target,
 418 decays into a muon and a muon neutrino. The four momenta, $p_\pi = p_\mu + p_\nu$, can be rearranged

2.2. OVERVIEW OF ND280 DETECTORS

419 to

$$E_\nu = \frac{m_\pi^2 - m_\mu^2}{2(E_\pi - |\vec{p}_\pi| \cos \theta_\nu)}, \quad (2.1)$$

420 where θ_ν is the angle between the incoming π^+ and the outgoing ν_μ . If the angle, θ_ν was zero,
421 then there would be no upper bound on E_ν and one would end up with a very wide band
422 neutrino beam. The beam would only be limited by the energies of the pions produced.
423 If, however, an off-axis angle was introduced, then there would be an inflection point in
424 the equation. The maximum possible neutrino energy would depend on the minimum of
425 $E_\pi - |\vec{p}_\pi| \cos \theta_\nu$. This leads to

$$E_\nu^{\max} = \frac{m_\pi^2 - m_\mu^2}{2E_\pi^{\text{m}} \sin^2 \theta_\nu}, \quad (2.2)$$

426 where E_π^{m} refers to the inflection point. When the pion energy is above the inflection point,
427 the function slowly changes, allowing for a wide range of pion energies creating a very small
428 range of neutrino energy. By building a detector off-axis of a neutrino beam, it can receive
429 a narrow beam of energy which reduces the uncertainties of the energy of the incoming
430 neutrinos.

431 2.2 Overview of ND280 Detectors

432 There are two detectors in the near detector hall that was constructed 280 m from the
433 graphite target. The first detector is an on-axis detector called INGRID (Interactive Neutrino
434 GRID). The primary purpose of this detector is to monitor the beam stability and flux. The
435 second detector is an off-axis detector that is installed inside the UA1 magnet (from the
436 UA1 experiment at CERN). The primary purpose of this detector is to monitor the off-axis
437 flux and to measure cross sections in the ν_μ beam that will be used to constrain the analysis
438 results at SK. Figure 2.4 shows both near detectors in situ, with the UA1 magnet open. The
439 beam is directed toward the central modules of INGRID on the lower levels.

440 2.2.1 INGRID

441 INGRID is designed to monitor the beam center within 0.4 mrad. Figure 2.5 shows
442 the detector from the view of an incoming neutrino. The x and y position of the beam is
443 measured to within 10 cm. Additionally there are two detectors that are not positioned into
444 the cross that are used to measure the axial symmetry of the beam. Figure 2.6 shows an
445 exploded view of the typical INGRID module. Layers of scintillator bars are sandwiched
446 between a high-Z material, iron. To give an idea of the size of the individual modules, the
447 iron plates measure 124 cm by 124 cm. The high-Z material provides a very dense target for
448 the neutrinos and increases the rate of observed events. The scintillator bars contain wave
449 length shifting (WLS) fibers that collect the light that occurs from a particle passing through
450 the detector and directs towards a Hamamatsu Multi-Pixel Photon Counter (MPPC). Lastly,
451 there is a proton module that resides between the vertical and horizontal modules at the

2.2. OVERVIEW OF ND280 DETECTORS

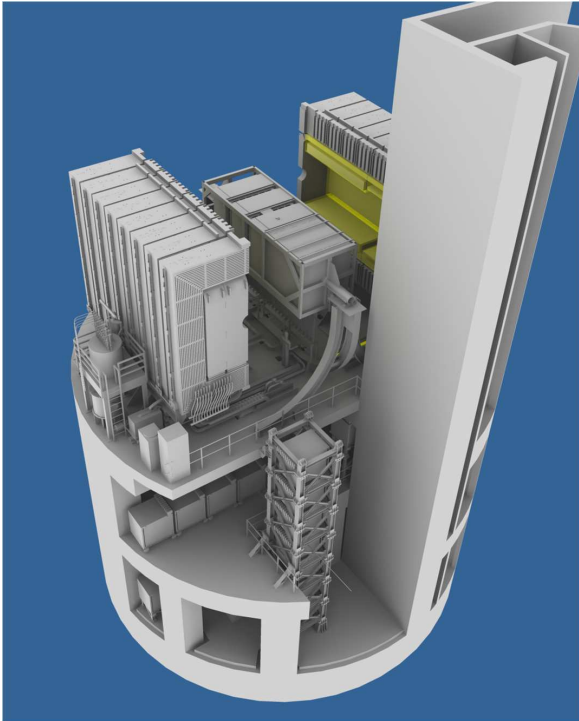


Figure 2.4: A diagram of the near detector hall with the outer walls removed. The whole set of detectors resides just beneath the surface of the earth. The top level depicts the ND280 off-axis detector with the UA1 magnet in the open position. The second level shows the horizontal axis of the INGRID detector crossed by a series of vertical modules in front. The beam is aimed toward the central modules of INGRID [25].

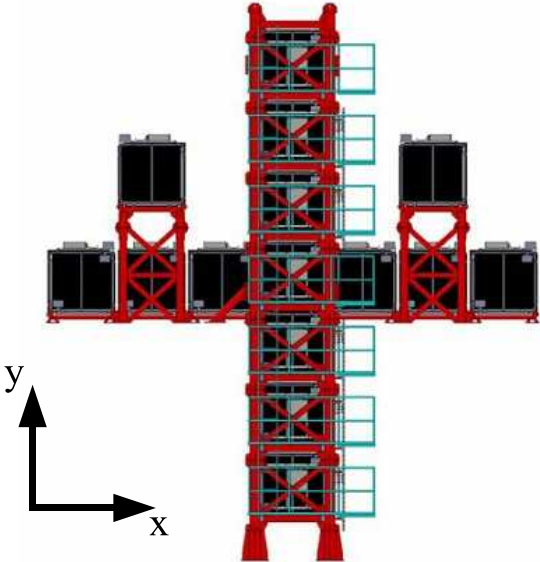


Figure 2.5: A diagram of INGRID oriented so the beam is into the page at the intersection of the vertical and horizontal modules [25].

2.2. OVERVIEW OF ND280 DETECTORS

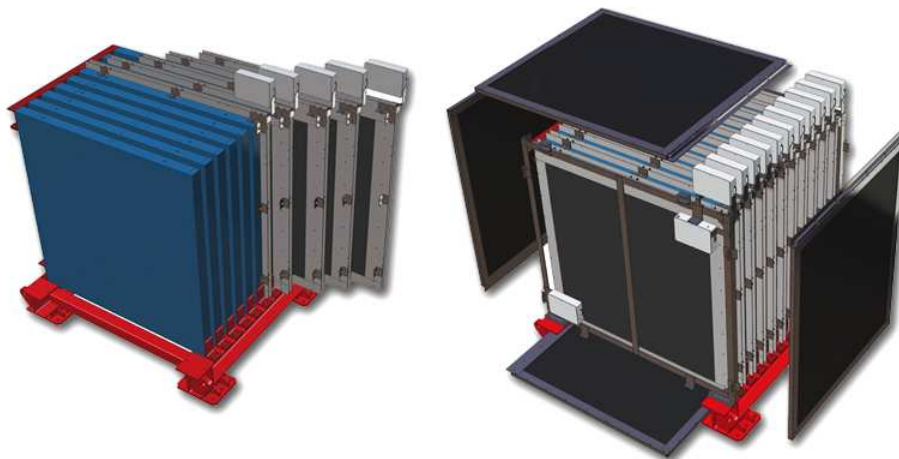


Figure 2.6: A diagram of an INGRID module in an exploded view. The left diagrams shows the layers of scintillator interleaved with iron sheets. The right diagram shows the additional veto layers that surround the module [25].

452 cross. This module is a finer grained scintillator module with no high-z material to measure
453 the quasi-elastic current in the beam [25].

454 2.2.2 ND280

455 Figure 2.7 shows the off-axis near detector, ND280. Surrounding the entire detector is
456 the UA1 magnet yoke from the UA1/NOMAD experiment at CERN. The magnet is run at
457 0.2 T. Physics data is taken with the magnet in the closed position and on. Occasionally
458 the magnet is turned off in order to take cosmic data for alignment. When necessary, the
459 magnet is opened to provide access to the different subdetectors for upgrades and repairs
460 [25].

461 Scintillator modules have been inserted into the air gaps between the flux return yokes.
462 They comprise the Side Muon Range Detector or SMRD. The SMRD triggers on cosmic rays
463 that can enter the detector and aid in providing a veto when a beam analysis is undertaken.
464 Additionally, they can measure high angle muons and their momentum as they exit the
465 detector [25].

466 Inside the magnet, there is a π^0 detector (P \emptyset D), three time projection chambers (TPCs),
467 two fine grained detectors (FGDs) and a selection of electromagnetic calorimeters (ECals).
468 The P \emptyset D will be explained in more detail in the next chapter as it is the primary detector
469 for this analysis.

470 Figure 2.8 shows a diagram of the general construction of the TPC. A TPC contains of a
471 volume of an argon-based drift gas. An electric field is applied to the gas volume so that when
472 a charged particle passes through the gas and ionizes, emitting electrons which will drift away
473 from the cathode onto a readout plane. The readout planes are called micromegas planes
474 and have a 7 mm by 9.8 mm anode segmentation. This micropattern anode combines for a
475 total of 9 m² active readout surface between the three volumes. This is the first application

2.2. OVERVIEW OF ND280 DETECTORS

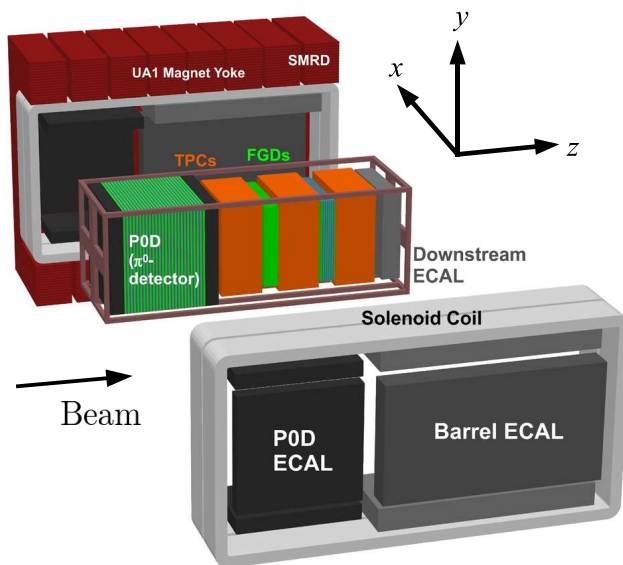


Figure 2.7: An exploded view of the ND280 off-axis subdetectors [25].

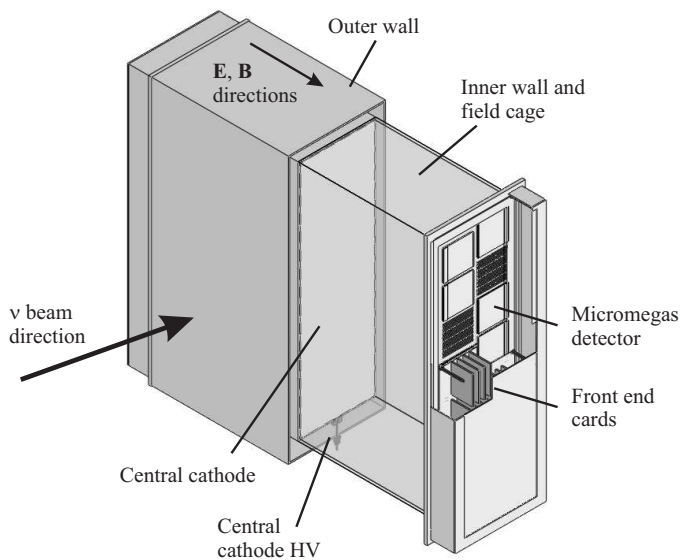


Figure 2.8: An cut away view of the TPC [25].

2.3. SUPER KAMIOKANDE

of this design. The TPC has a high precision three dimensional reconstruction and is used to measure the momenta and charge of the particles recorded in the detector. The TPC can also distinguish between different charged particles by examining the ionization deposit [25].

There are two FGDs sandwiched between the three TPCs. The FGDs have extruded scintillator bars that measure 9.61 mm by 9.61 mm by 1864.3 mm. Inside the bars are WLS fibers that direct the scintillation light to an MPPC readout. The detector layers are constructed to have a alternating layers of bars in the x direction and a layer of bars in the y direction (beam direction is z). The first FGD has 30 scintillator layers as a fully active target volume. The second FGD has a total of 14 layers that are separated into 7 xy modules. Between the xy modules are layers of water that are 2.5 cm thick. The FGD group implemented these water layers to provide a water target for neutrinos [25].

The final collection of detectors are the ECals. The ECals are also scintillator detectors, but the scintillator is layered with lead, a high Z material. The extruded scintillator bars that form the layers have a cross section of 4 cm by 1 cm, four times larger than the FGD. The ECals are arranged to encompass nearly the entire inner magnet detectors, with the exception of the upstream end of the PØD. There are three different types of ECals based on their positions in the magnet. After the last TPC, there is a downstream ECal (DSECal). This ECal has 34 layers that amount to 10.6 radiation lengths. The TPC and FGD region along with the DSECal are surrounded on the x and y sides by a Barrel ECal. The Barrel ECals have 31 layers or 9.7 radiation lengths. They can be used as a veto for incoming cosmic rays into the TPC and FGD. The PØD is surrounded by another set of ECals, called the PØD ECal. These modules are slightly smaller and contain merely six active layers with a thicker lead layer for a radiation length of 3.6 [25].

2.3 Super Kamiokande

Super-Kamikande (SK) is a large water Cherenkov detector located 295 km away from J-PARC near the Japan Sea. A version of the detector has been in operation since the early 1980s, with an update to Super-Kamiokande in 1996, and has devoted a portion of its livetime to the T2K experiment as its far detector. It is placed in a former mine, 1000m underground, in order to use the earth as shielding from cosmic rays. SK is a large cylinder that has a diameter of 39m and and height of 41m. There is an inner detector that has 11,129 50cm diameter Photomultiplier Tubes (PMTs). The outer detector has 1,885 20cm diameter PMTs, which are used as a veto to ensure that interactions start in the inner detector. The inner and outer detectors are separated by light tight shielding [25].

Cherenkov light occurs when a particle travels faster than the speed of light through a medium. The minimum limit of the particle's speed to create Cherenkov light is $v = c/n$ where c is the speed of light and n is the index of refraction. As a particle travels, a cone of Cherenkov light is created. High momentum electrons undergo bremsstrahlung emission and the resulting photons then pair produce to create a collection of high momentum electrons that travel in generally the same direction. This collection of particles creates a fuzzy ring signature that is the result of many rings overlapping. As a muon travels through the detector, it does not break and radiate other particles, so a very sharp ring is created. For the ν_e appearance measurement, a selection of one e -like ring is performed. It is possible for

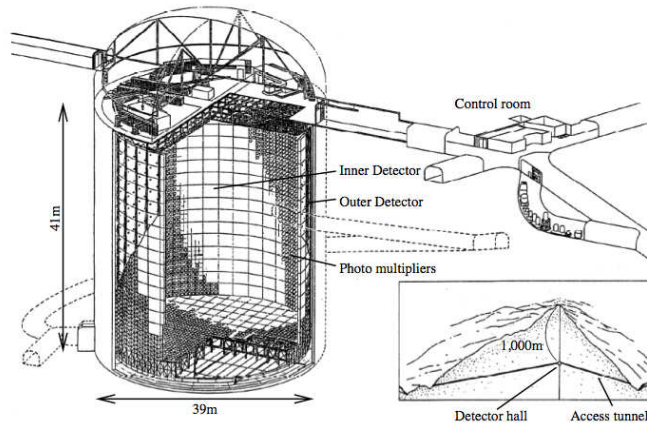


Figure 2.9: A cut away diagram of SK in the Mozumi mine at Kamioka, Japan [25].

518 a π^0 to appear as an e -like ring in SK, which is how the $\text{NC}1\pi^0$ interaction sneaks into the
 519 background. There are two ways the π^0 particle can decay to form a single observable ring.
 520 The first is a symmetric decay where the π^0 decays perpendicular to the direction of motion.
 521 If the particle is boosted enough, the angle between the decay photons will be small in the
 522 lab frame. This small angle can cause the resulting indistinct ring shapes, corresponding to
 523 each photon, to overlap and appear as a single fuzzy e -like ring. The second decay is an
 524 asymmetric decay. If the π^0 decays with one photon continuing in the direction of motion,
 525 and the other traveling opposite of the direction of motion, the photon traveling backwards
 526 may not have enough energy in the lab frame to create a cone of Cherenkov light and be
 527 above the detector's energy threshold. Only the photon, now indistinguishable from the
 528 electron, travelling in the forward direction will be recorded in this case. As such, knowledge
 529 of the $\text{NC}1\pi^0$ cross section is important in order to reduce the error on the background
 530 prediction.

Chapter 3

PØD

The PØD detector is the primary detector used in this analysis. As such, this chapter will present a more detailed description of the materials and construction of the PØD. Along with the construction, an explanation of the data acquisition process will be provided. Following that, a detailed description of the PØD software process, with a focus placed on the reconstruction PID algorithms, is given. Lastly a study of the internal alignment of the PØD and the PØD to TPC external alignment will be shown.

3.1 Detector Construction

Figure 3.1 shows the construction of the PØD detector. The detector consists of four modules called SuperPØDules, two ECals and two water targets. The upstream ECal is referred to as a USECal and the downstream ECal is called the central ECal (CECal) since a DSECal exists as a separate detector. Likewise there is an upstream water target (USWT) and central water target (CWT). The active target for all SuperPØDules is broken down into smaller pieces called PØDules. The PØDules consist of two scintillator layers, one layer for the x direction and one for the y. There are 126 X bars and 134 Y triangular bars in each PØDule. In the ECals, the PØDules are separated by lead plates. In the Water Targets, the PØDules are separated by a layer of brass as well as a layer of water. This water can be drained and refilled to give analyzers access to a mass subtraction to find on-water cross sections.

To have a rigorous definition of the fiducial mass, the fiducial volume needed to be established. The detector was optimized for the fiducial volume to be within 25cm from the edge of the active area for electron or photon based analyses. In practice this definition was inaccurate because it was relative to the ideal volume defined by particular PØDules. The position of the PØDules change when alignment parameters are applied, altering the fiducial volume. Keeping this in mind, the fiducial volume within the water targets was fixed with an X length of 1600 mm, a Y length of 1740 mm, and a Z length of 1705 mm centered around the active center of the PØD, see Table 3.1. The edges of the volume are approximately 25 cm from the edge of the active X and Y area and the Z boundary goes from halfway through the first PØDule in the USWT to halfway through the last PØDule in the CWT.

With the fiducial volume defined, a program to calculate the Monte Carlo geometry fidu-

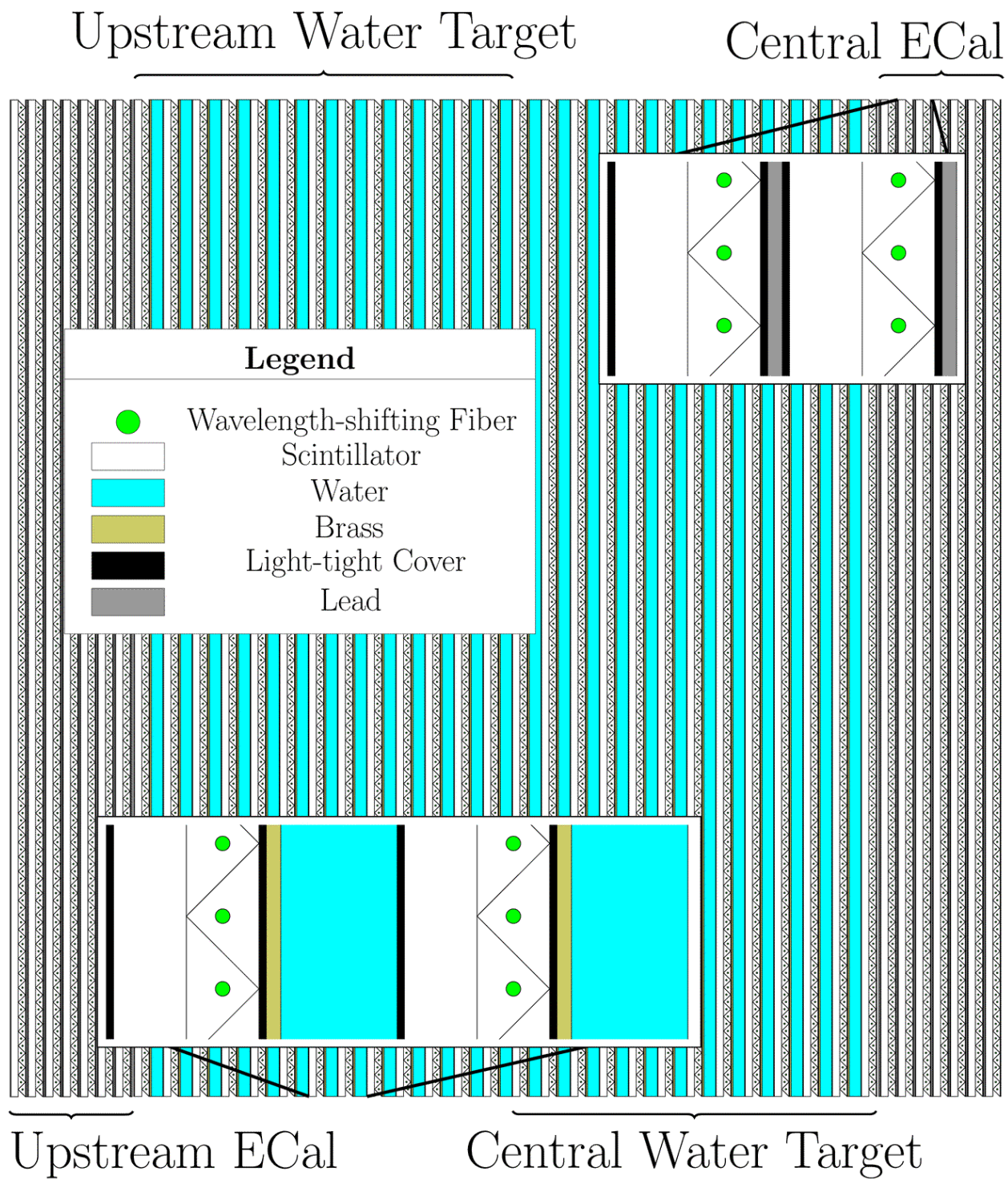


Figure 3.1: A schematic diagram of the P0D [26].

3.1. DETECTOR CONSTRUCTION

Table 3.1: Definition of the PØD fiducial volume. The second column shows the center position for all three dimensions in global coordinates. The third column shows the half-widths of the box. The last two columns give the minimum and maximum positions in the Monte Carlo geometry.

Coordinate	Center (mm)	Half-Width (mm)	Minimum (mm)	Maximum (mm)
X	-36	800	-836	764
Y	-1	870	-871	869
Z	-2116	852.5	-2969	-1264

562 cial mass was constructed. Given a particular volume in the PØD, a Monte Carlo integration
 563 to determine the average density and the statistical error of that density was done. In order
 564 to get a mass, the volume was multiplied by the average density. The summary of Monte
 565 Carlo fiducial masses follows in Table 3.2. The calculation of the mass is based off of mea-
 566 surements that were taken by various people during construction. There are four pieces in
 567 the water target area: brass, PØDule, upstream target cover, and water.

568 **Brass Radiator Mass**

569 The brass radiator mass was determined using the measured thickness and the standard
 570 density. At Stony Brook University in August 2011, the thickness of the remnant pieces of
 571 brass were measured to be 1.28 ± 0.03 mm. The thickness variation measured falls within
 572 the manufacturer specification. The brass has not been assayed to determine the density of
 573 the brass used, so the standard value for brass was taken, 8.50 ± 0.15 g/cm³. Given this
 574 information, the calculated mass for a single brass radiator layer is 30.29 ± 0.89 kg for the
 575 fiducial volume defined in Table 3.1.

576 **PØDule Mass**

577 The PØDule mass is calculated from the components: two light tight covers, two scin-
 578 tillator planes, 260 wave-length shifting (WLS) fibers and three layers of epoxy. The two
 579 light tight covers (also called skins) are made from extruded polystyrene. The thickness was
 580 measured at Stony Brook University by Clark McGrew, 1.375 ± 0.125 mm, and the density
 581 was found from a range of acceptable values online, 1.05 ± 0.02 g/cm³. The scintillator planes
 582 in the PØDule consist of one X layer and one Y layer. During construction, each plank was
 583 weighed and measured. From this information, the mass was scaled to the fiducial volume
 584 and the X layer was calculated to be 47.94 ± 0.06 kg and the Y layer was 48.06 ± 0.05 kg. In
 585 addition to the quoted plank mass uncertainties, there is an additional 0.17% systematic due
 586 to the calibration of the scales used to weigh the planks. This systematic is correlated across
 587 all planks and adds an additional 4.1 kg uncertainty to the total PØD fiducial mass. The
 588 three layers of epoxy fill the area between the skins and scintillator. During construction
 589 batches of either 1.8 kg or 2.0 kg of epoxy were mixed for use in each of the three layers, giv-

ing us an upper limit on the epoxy in the PØD. The amount of epoxy mixed for each PØDule was carefully recorded during construction. The design thickness was used to estimate the thickness of each layer of epoxy, 0.25 ± 0.0375 mm, with a 15% error. The design thickness corresponds to a total epoxy layer mass of 1.6 kg, which is reasonable given the amount mixed. This decision was made in order to reduce the dependence on a limited number of PØDule thickness measurements. The density is given as 1.36 ± 0.2 g/cm³, based on the invoice that came with the ordered epoxy. The mass of a single layer of epoxy inside the fiducial volume is calculated to be 0.95 ± 0.20 kg. There are 126 X fibers and 134 Y fibers in a PØDule. The number of fibers in the fiducial area are approximately 89 for the X fibers and 110 for the Y fibers. The design specification for the fibers gives a diameter of 0.6 ± 0.1 mm and a density of 1.05 ± 0.01 g/cm³. The fibers cross the fiducial volume completely, giving us a 0.10 ± 0.02 kg per PØDule or 2.5 ± 0.6 kg for the entire fiducial volume. Assuming correlated (density correlations only) errors for each of the components, the total mass of a single PØDule is 106.98 ± 0.96 kg (106.98 ± 0.73 kg).

604 **Water Target Cover**

There is one upstream target cover. This cover is located at the downstream edge of the USWT. It exists to provide support for the last set of water bags in the USWT. The cover is made from extruded HDPE with a density of 0.94 ± 0.01 g/cm³. The thickness, 0.25 ± 0.02 inch, was reported by the company that provided the material. The mass of the target cover contributes 16.62 ± 1.34 kg to the total fiducial mass.

610 **Water Target Mass**

Inside the water targets, there is a small contribution of mass from dead (non-water) material. Additionally, there is the fiducial mass due to the water itself. Kevin Connolly, a T2K collaborator, calculated the water fiducial mass to be 1902 ± 16 kg. A layer mass was extracted from this measurement by a simple division.

For Run 1, the dead material consists of a central support, two water bags, two pressure sensor assemblies, two level sensor assemblies, and four fill/drain pipes. For Run 2, the dead material consists of a central support, two water bags, four sensor assemblies, and four fill/drain pipes. Only the sensor assemblies differ between the two runs.

The central strut, made from HDPE, has a 28.0 ± 0.2 mm by 18 ± 0.5 mm cross section where the uncertainty is determined by the machining tolerance. Since the strut was manufactured on a computer controlled mill, the masses are assumed to be correlated between layers. It contributes 0.824 ± 0.025 kg per water dead material layer.

The fill/drain pipes are made from PVC (1/2 inch CTS CPVC 4120 pipe). This pipe, according to standard specification, has an inner diameter of 0.469 ± 0.001 in and an outer diameter of 0.625 ± 0.003 in. However, spot check measurements of spare pipes indicate a slightly wider range in the diameters. Due to the uncertainty of the material, the cross section is assumed to be 86 ± 17 mm², the spec value, with an error that covers the measured values. Assuming a typical density of PVC (1.38 ± 0.0276 g/cm³), the mass of a single pipe is 0.21 ± 0.04 kg.

The bag material is HDPE (density of 0.94 ± 0.01 g/cm³) and the thickness, given by

3.1. DETECTOR CONSTRUCTION

631 design spec, is 6.0 ± 0.6 mil. In addition to the fiducial area (in X and Y, 1600 mm by 1740
632 mm) of the bags, an added correction for bag overlap in the middle of the water target was
633 made. There was a measured 200 ± 20 mm overlap. The bags added a mass of 0.90 ± 0.09
634 kg per layer.

635 In the sensor assemblies for Run 1 and Run 2, 1/2 inch Schedule 40 PVC was used.
636 Although the pipes remained the same, the sensors changed from Run 1 to Run 2. During
637 Run 1, the sensor was positioned outside of the fiducial volume. Each layer has two bags,
638 and each bag has a primary sensor pipe and a secondary sensor pipe made from this material.
639 Given that the pipes have an inner diameter of 0.607 ± 0.001 in and an outer diameter of
640 0.840 ± 0.001 in. Again, the pipes were measured to a different cross section so a value of
641 171 ± 30 mm² was used which corresponds to the specification for the pipe with an error
642 that covers the measured value. The mass of a single pipe inside the fiducial volume is
643 0.410 ± 0.072 kg. The primary sensor pipe also has a readout cable running through it. The
644 cable is approximated to have similar dimensions as the Run 2 readout cable, but with added
645 uncertainty. Thus, the cable is assigned a linear density of 0.7 ± 0.3 oz/ft. Therefore, the
646 mass of one cable is 0.11 ± 0.05 kg.

647 For the Run 2 sensor assemblies, the sensor (Global Water WL400) was attached to the
648 bottom of a length of PVC. The total length of the PVC pipe plus the sensor was recorded
649 for each pipe installed by Rob Johnson. There are two lengths in each bag for a high sensor
650 and a low sensor. The average of the recorded measurements is used for the length and the
651 standard deviation is used as the length error. The long pipe assembly is 210.4 ± 0.4 cm
652 long and the short pipe assembly is 209.6 ± 0.2 cm long. The specifications for the Global
653 Water WL400 sensor indicate that the sensor is 5.5 ± 0.1 inches long with an error assigned
654 to the last significant figure. The sensor plus the housing weighs 12 ± 1.8 oz where there is
655 a 15% error assigned to the mass due to the uncertainty on the distribution of mass within
656 the sensor. The fiducial volume definition and the length of the sensor pipe assembly (which
657 is measured from the top of the header) is used to calculate how much of the sensor is in
658 the fiducial volume. For the long sensor assembly, $43.5 \pm 3.7\%$ of the sensor is in the fiducial
659 volume or 0.15 ± 0.03 kg. For the short sensor assembly, $49.2 \pm 0.3\%$ of the sensor is in the
660 fiducial volume or 0.17 ± 0.03 kg. The length of the sensor pipe (1/2 inch Schedule 40 PVC)
661 and the readout cable for the long assembly is 1678 ± 5 mm (the length of the assembly minus
662 the lengths of the sensor and the distance from the top of the pipe to the top of the fiducial
663 volume). For the short assembly, the length is 1670 ± 4 mm. In the specification of the cable,
664 the linear density is 0.7 ± 0.1 oz/ft where the error is assigned to the last significant figure.
665 For the long assembly, the mass of the pipe is 0.40 ± 0.07 kg and of the cable is 0.11 ± 0.02 kg.
666 For the short assembly, the mass of the pipe is 0.39 ± 0.07 kg and of the cable is 0.11 ± 0.02
667 kg.

668 For Run 1, using correlated (density correlated) errors, the mass per layer of the dead
669 material is 4.42 ± 0.36 kg (4.42 ± 0.11 kg). For Run 2, using correlated (density correlated)
670 errors, the mass per layer of the dead material is 5.20 ± 0.29 kg (5.20 ± 0.07 kg).

671 For the water out measurement, represented in Table 3.2, there should be no water in
672 the fiducial volume, only the dead material will contribute. The water sensor pipes are not
673 modeled in the Monte Carlo geometry.

Table 3.2: The mass (m) of the components of the P \emptyset D from the as-built (AB) measurements for Run 1 and Run 2 and the Monte Carlo geometries, Production 1 (P1) through Production 5 (P5). All errors are assumed to be fully correlated.

	AB (Run 1) (kg)	AB (Run 2) (kg)	P1 (kg)	P2 (kg)	P4 (kg)	P5 (kg)
Brass	30.29 ± 0.89	30.29 ± 0.89	36.9	36.9	36.9	30.2
P \emptyset Dule	106.98 ± 0.96	106.98 ± 0.96	108.1	109.9	109.9	107.0
WT Cover	16.62 ± 1.34	16.62 ± 1.34	16.6	16.6	16.6	16.6
Water	76.08 ± 0.64	76.08 ± 0.64	77.1	77.1	77.1	77.1
Dead Material	4.42 ± 0.36	5.20 ± 0.29	0.8	0.8	0.8	0.8
Lead Layer	131.24 ± 2.86	131.24 ± 2.86	131.4	131.4	131.4	131.4

Table 3.3: The areal densities (ρ_A) of the components of the P \emptyset D from the as-built (AB) measurements and the Monte Carlo geometries, Production 1 (P1) through Production 5 (P5). All errors are assumed to be fully correlated.

	AB (Run 1) (g/cm ²)	AB (Run 2) (g/cm ²)	P1 (g/cm ²)	P2 (g/cm ²)	P4 (g/cm ²)	P5 (g/cm ²)
Brass	1.088 ± 0.032	1.088 ± 0.032	1.33	1.33	1.33	1.09
P \emptyset Dule	3.843 ± 0.034	3.843 ± 0.034	3.88	3.95	3.95	3.84
WT Cover	0.597 ± 0.048	0.597 ± 0.048	0.60	0.60	0.60	0.60
Water	2.733 ± 0.023	2.733 ± 0.023	2.77	2.77	2.77	2.77
Dead Material	0.159 ± 0.013	0.187 ± 0.010	0.03	0.03	0.03	0.03
Lead Layer	4.714 ± 0.103	4.714 ± 0.103	4.72	4.72	4.72	4.72

674 ECal Radiator Mass

675 The ECals are not considered part of the fiducial volume defined above. However, for com-
676 pleteness, the mass information for the ECals is provided. The lead radiators are placed
677 between the P \emptyset Dules of the Upstream and Central ECals. The lead radiators are composed
678 of tiled lead pieces sandwiched by two layers of steel. Clark McGrew recorded the individual
679 lead piece's weights and dimensions as they were inserted into the sandwich. The lead thick-
680 ness was measured to be 3.45 ± 0.05 mm, which is the average and RMS of the measurements.
681 The lead was weighed using the same scales as were used to measure the planks. Due to
682 the use of this scale, there is an additional 0.17% systematic error on the total lead mass.
683 The same epoxy and method of mixing used to construct the P \emptyset Dules was used for the two
684 layers of epoxy within the sandwich. The steel used 26 gauge 304 stainless steel. The design
685 spec gives a thickness of 0.45 ± 0.05 mm and a density of 8.03 ± 0.24 g/cm³. A single lead
686 sandwich mass in the same fiducial XY area defined in Table 3.1 is 131.24 ± 2.86 kg with
687 fully correlated errors (131.24 ± 2.36 kg with density correlated errors).

3.1. DETECTOR CONSTRUCTION

PØD Mass Summary

Table 3.2 shows the masses of each component going into the fiducial mass calculation. The masses of the PØDules, brass, and lead layers are for single layers. There are 40 PØDules, 25 layers of brass, 25 layers of water, 25 layers of dead material (in the water target volume) and 14 layers of lead in the entire PØD. The Upstream WT cover is listed with its entire contribution to the mass of the PØD. The lead layer is outside of the water fiducial region, so the mass is for a region with the same X and Y dimensions. The table lists the as-built calculations for Run 1 and Run 2 of the mass as well as the mass for each major production of ND280 Monte Carlo. Combining the component masses with correlated errors gives a fiducial mass for the PØD of 3559 ± 34 kg for Run 1 without water and 3578 ± 34 kg for Run 2 water-out running. The Run 1 water-in fiducial mass is 5461 ± 38 kg. For Run 2 water-in running, the fiducial mass is 5480 ± 37 kg. Also provided are the areal densities for the components in Table 3.3. These densities are valid for the X coordinate range from -1041 mm to 969 mm and the Y coordinate range from -1023 mm to 930 mm in the global coordinates of the geometry. However, allowances on the applicable area should be made for alignment uncertainties and reconstruction resolution.

The as-built calculation has an additional systematic error that has been approximated to 2 kg. This systematic error comes from the slight angular rotation around the Y axis that is present in the Monte Carlo geometry that was not accounted for in the as-built calculations. The fiducial volume cut in the Z-direction falls between the X and Y layers of scintillator in a PØDule. This boundary was selected due to the behavior of the reconstruction, but can lead to an asymmetric migration of materials across the boundary (in particular the titanium oxide coating on the scintillator). However, a two kilogram uncertainty easily accounts for this migration.

Two methods of combining the uncertainties are considered. In the first, the density of similar components are assumed to be correlated while the volumes remain uncorrelated. For example, the brass radiators could have different thickness, but because they were made from one batch, the density across all radiators will be the same. In addition to the correlated densities, the correlated systematic error of the scales for weighing the planks (0.17% or 4.1 kg) is added. The resulting estimate of the dry (wet) fiducial PØD mass is 3558.86 ± 18.80 (5460.86 ± 24.69 kg) for Run 1 and 3578.30 ± 18.67 kg (5480.39 ± 24.58 kg) for Run 2 and above. The second method considers the masses for each type of material as correlated (e.g. the masses of all PØDules are correlated). The accuracy of the scales used to weigh the planks is handled separately (0.17% or 4.1 kg). This gives an estimate of a dry (wet) fiducial PØD mass of 3558.86 ± 34.23 kg (5460.86 ± 37.78 kg) for Run 1 and 3578.30 ± 33.80 kg (5480.30 ± 37.40 kg). These two error estimates bracket the true systematic error value. The final uncertainty assumes that the component masses are correlated and is presented in Table 3.4.

Table 3.4 contains the mass of the as-built calculations for Run 1 and Run 2+ as well as the mass for the simulated detector in each of the listed software productions. The differences between different versions of the Monte Carlo are due to a continual, more comprehensive understanding of the mass. The ratio of the as-built mass to the Monte Carlo mass is then used as a correction on the number of Monte Carlo events generated.

Table 3.4: The mass of the fiducial volume of the PØD for the as-built (AB) information and in the Monte Carlo geometries from Production 1 (P1) to Production 5 (P5). All component errors are correlated in the as-built information. The errors on the Monte Carlo masses are purely statistical.

	Water-In (kg)	Water-Out (kg)
AB (Run 1)	5460.86 ± 37.78	3558.86 ± 34.23
AB (Run 2)	5480.30 ± 37.40	3578.30 ± 33.80
P1	5590.09 ± 2.44	3663.67 ± 2.25
P2	5635.00 ± 2.46	3711.11 ± 2.26
P4	5634.21 ± 0.54	3707.32 ± 0.54
P5	5393.22 ± 0.56	3469.14 ± 0.55

3.2 Data Acquisition

The scintillator bars emit light as a charged particle or high energy photon passes through it. Typically either one or two bars are hit due to the geometry of the bars. If one bar is hit, it is called a singlet. A doublet occurs when two bars are hit. Figure 3.2 shows how the particle would traverse a layer to cause singlets and doublets. In the center of the bar, there is a hole that has a WLS fiber running the length of the bar. This fiber collects the scintillation light and directs it onto the MPPC.

Figure 3.3 depicts the connection between the WLS fiber and the MPPC assembly. The fiber is directed by a Ferrule which holds the fiber end in place near the MPPC. The MPPC is a solid-state photosensor with 667 50-micron pixels. The face of the MPPC is 1.3 mm by 1.3 mm [26]. There are 10,400 bars in the PØD. The electronic output is sent through the signal wires out of the external shell to the TriptT Front End Boards (TFBs).

Figure 3.4 shows the overall scheme of collecting and recording data. After a signal is sent to the TFB, it is temporarily saved to a TriptT computer chip in twenty-three cycles. If an external trigger is not sent, the information is dumped and the next batch of data is temporarily stored. There are two possible external triggers, a GPS trigger and a cosmic ray trigger. The GPS trigger is sent to both the near and far detectors by the beam group to indicate the arrival of the neutrino beam. At the near detector the trigger is received by the Master Clock Module (MCM) which in turn triggers the Slave Clock Modules (SCM). Each detector has a SCM that communicates to the Readout Merger Modules (RMMs) which in turn communicate with the TFBs. In the case of the PØD, there are 6 RMMs and each RMM

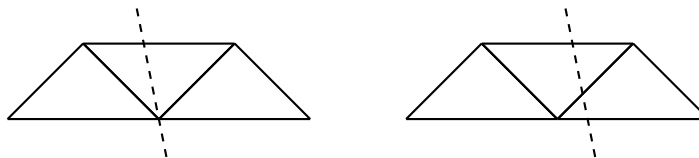


Figure 3.2: A schematic showing a singlet (left) and doublet (right) hit.

3.2. DATA ACQUISITION

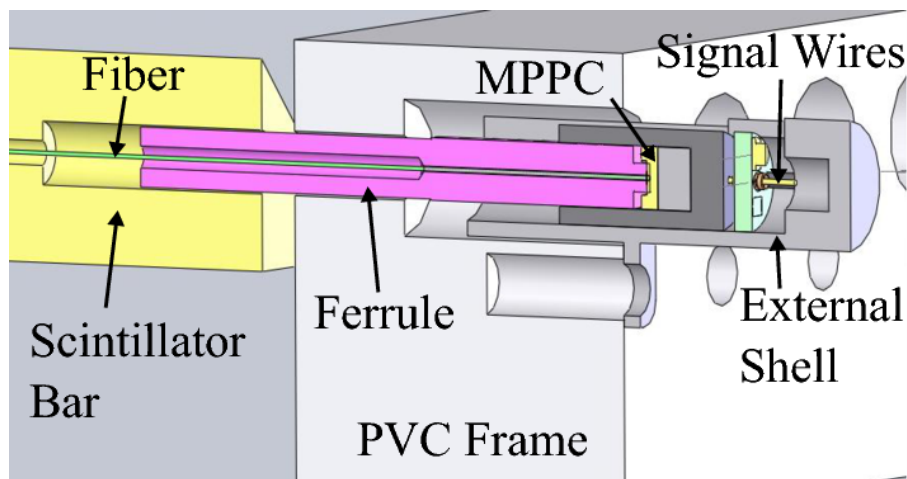


Figure 3.3: A schematic of the WLS fiber to MPPC assembly [26].

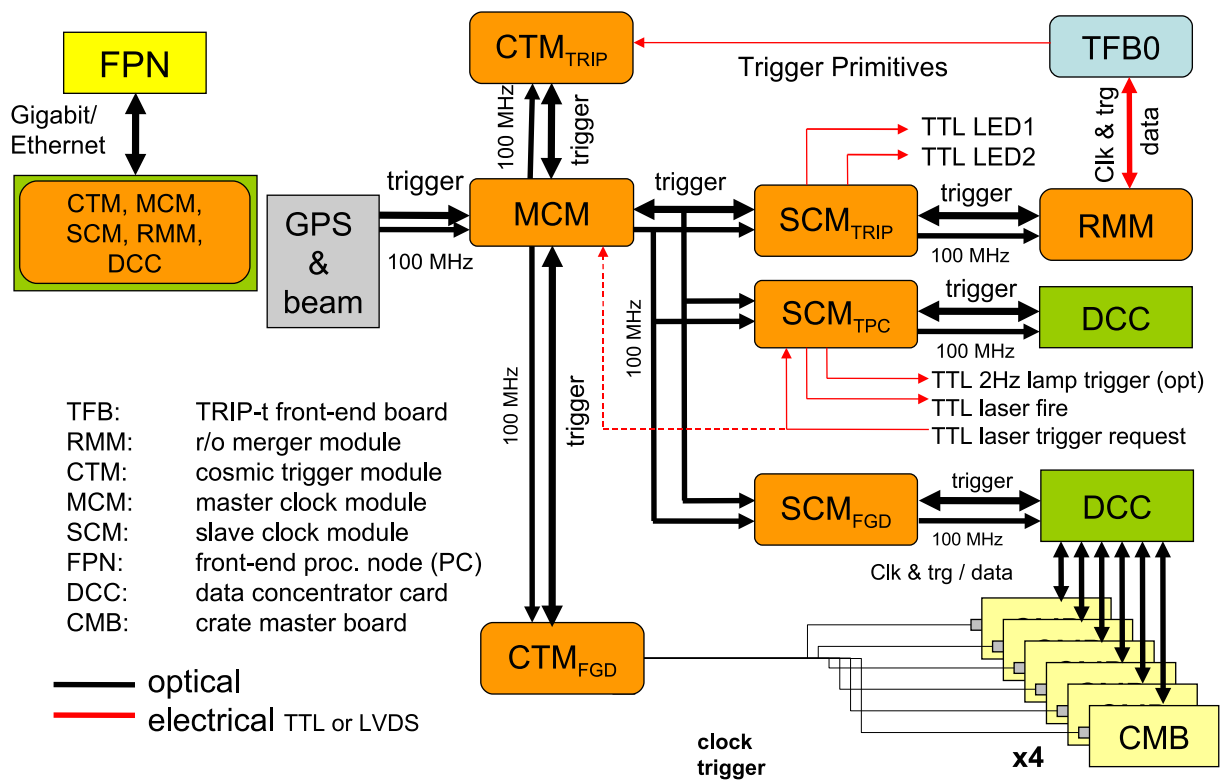


Figure 3.4: A diagram of the data collection system used at the near detector [25].

752 connects to 29 TFBs. The memory of the TFBs is refreshed to prepare for beam arrival.
 753 The beam is sent in eight bunches to the TFBs which are calibrated to have the beam arrival
 754 coincide with the fourth time cycle of the TripT chip. The other possible trigger is a cosmic
 755 ray trigger. This uses a Cosmic Trigger Module (CTM) to collect trigger primitives from
 756 the various TFBs (for the case of the P \emptyset D). The trigger primitives contain information on
 757 the twenty three buffered cycles. If at the end of the TripT chip's cycle, there appears to be
 758 a high number of hits, the CTM assumes a cosmic ray has passed through the detector and
 759 sends a request to the MCM to save the data. The MCM, CTM, SCM and RMM signals
 760 are then passed through a front end processing node (FPN) that saves the data to external
 761 computers. The structure for DAQ communication with the TPC and FGD differ from that
 762 used in the P \emptyset D and will not be detailed here.

763 During data taking, cosmic ray running is the default. There are two forms of cosmics,
 764 FGD and TripT. In TripT cosmics (which accept triggers from the P \emptyset D) any TripT detector
 765 can trigger a collection. The TripT detectors are the SMRD, the DSECal, the P \emptyset DECal,
 766 the Barrel ECal and the P \emptyset D. Additionally, there are short calibration runs that can be set
 767 up through the DAQ machines. However, any beam trigger supersedes all other triggers to
 768 ensure that the beam data is recorded.

769 3.3 Software Process

770 The overall software procedure is described in Figure 3.5. There are several steps be-
 771 tween Monte Carlo generation and data collection to get to a useful analysis output. The
 772 Monte Carlo story begins with the neutrino interaction generators. T2K primarily relies on
 773 two generators: GENIE and NEUT. Essentially, they output a list of interactions with the
 774 energies and positions of all the particles. This interaction list is passed to nd280mc which
 775 places the interactions in the geometrical volume and propagates the particles. The next
 776 step is elecSim, which controls the simulation of the electronic noise that is added to the
 777 Monte Carlo files as a digitized output. The input data is originally in a maximum integrated
 778 data acquisition system (MIDAS) file. The program oaUnpack, extracts the raw data and
 779 turns it into digitized hits. This digitized output for both data and Monte Carlo is passed
 780 to oaCalib which controls the calibration of all subdetectors. In particular, the photoelectric
 781 (PE) peaks and Minimum Ionizing Particle (MIP) peaks are calibrated to specific values
 782 in the P \emptyset D. This normalizes all MPPC responses. Additionally, any alignment parameters
 783 are also applied. The output hits of the calibration are then passed to the reconstruction,
 784 oaRecon. The reconstruction files are very large due to the amount of information that is
 785 contained in them, so a simplified file is created using oaAnalysis. This simplified file can be
 786 accessed using the ROOT program. Most analyses are then run through ROOT macros.

787 Any P \emptyset D analysis relies heavily on the output of the P \emptyset D reconstruction. The overview
 788 of the reconstruction is shown in Figure 3.6. The input into the reconstruction is the output
 789 of the calibration where the data is arranged into hits. These hits represent a single MPPC
 790 being fired and the goal of the reconstruction is to map out tracks and showers and calculate
 791 the energy and identify particles. The first step in this process is to separate out the 23
 792 cycles of the TripT chip. Each cycle gets reconstructed independently. After separation, the
 793 cycles undergo a noise cleaning. The X-Z and Y-Z hits are considered separately and have

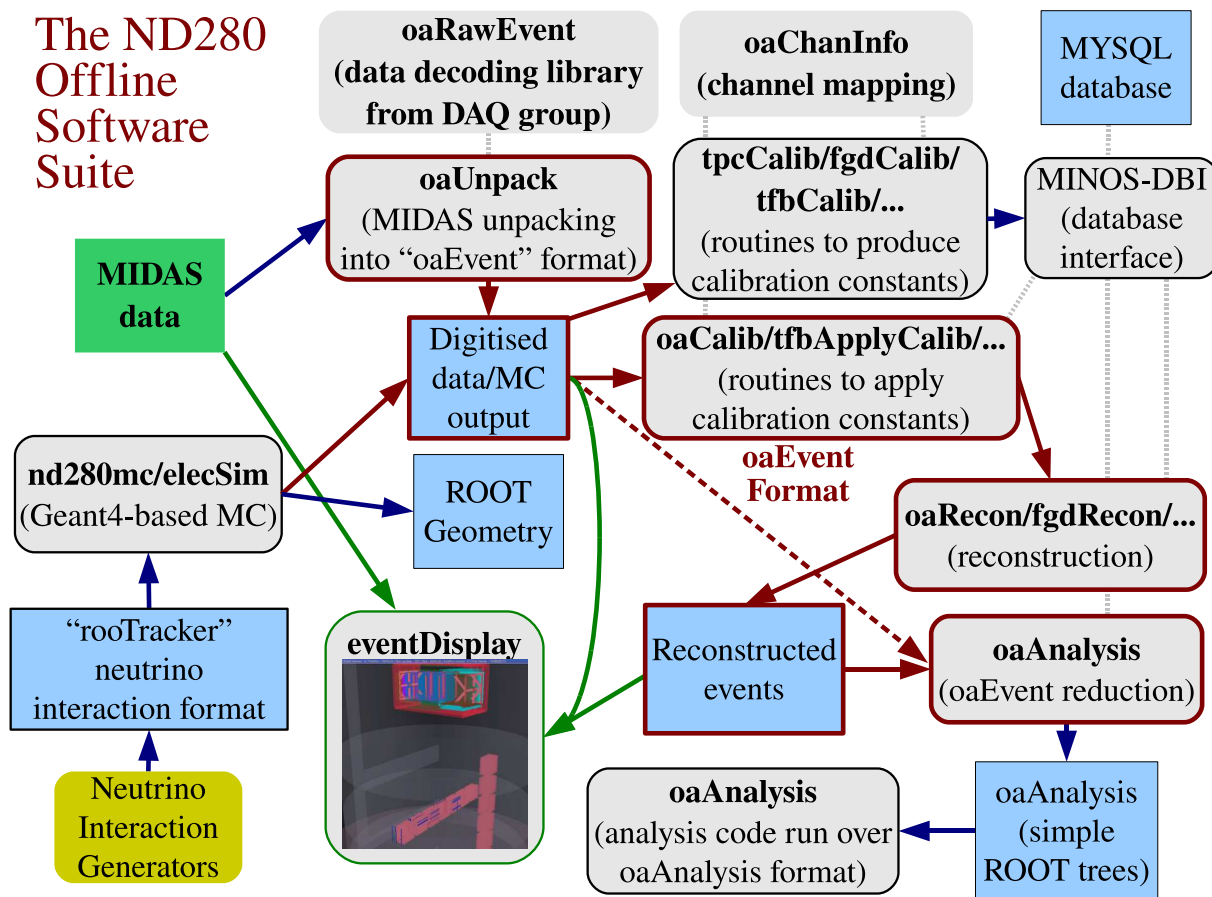
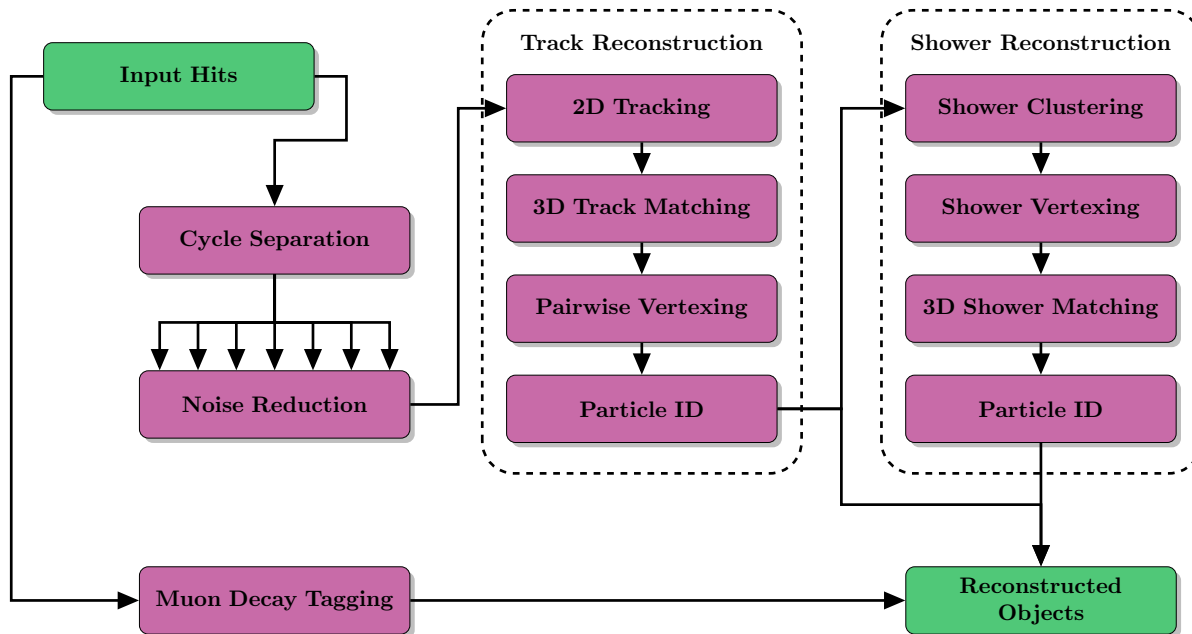


Figure 3.5: A diagram of the general software process [25].

Figure 3.6: A diagram of the P \emptyset D reconstruction process.

794 to pass a few requirements.

- 795 • The maximum time difference between compared hits is 30 ns.
- 796 • A hit above 15 PEU must have a neighbor within 20 cm.
- 797 • A hit above 7 PEU must have a neighbor within 10 cm.
- 798 • Any hit is saved if it has a neighbor within 3.5cm (adjacent bar).
- 799 • All hits need to be in a 50ns span of time, centered around the median time of the hits.

800 Additionally, since some MPPCs record hits too frequently, there are around 50 hot
 801 channels that are removed from the reconstruction since they can cause events to be mis-
 802 reconstructed. The next step in the process is track reconstruction, which is broken down
 803 further into smaller steps. First, two dimensional tracks are reconstructed, using a Hough
 804 transform to create track seeds. These tracks are then matched between the X-Z and Y-
 805 Z planes, allowing tracks to overlap in one dimension if necessary. In the end, all tracks
 806 should be matched. With the matched tracks, two options for the three dimensional fit are
 807 possible. The parametric fit is reserved for relatively short tracks. The Kalman fit is used
 808 for longer tracks and these will be run through a particle identification (PID) process. The
 809 three dimensional tracks are used to find a single pairwise vertex. The PID process, further
 810 explained in the next section, tags three types of particles based on the Kalman tracks.
 811 These are the EM particles (kEM), muons (kLightTrack), and protons (kHeavyTrack). All
 812 parametric tracks are labelled kOther and, along with the EM particles, are sent to the
 813 shower reconstruction. The protons and muons are sent directly to the output.

3.4. PØD PARTICLE IDENTIFICATION

814 The next step for EM-like and short tracks is shower reconstruction. First the hits from
815 the kEM and kOther tracks are clustered, and reconstructed into 2D showers. Then a single
816 vertex is found using the showers and tracks. Finally, the 2D showers are combined into 3D
817 ones. The showers have three to five clusters inside them, which are ellipsoid constructs that
818 describe a portion of the hits in the shower. Additionally, the charges of the showers are
819 shared between overlapping showers to separate the energy of each shower. Finally a PID
820 operation, recently added, is performed. This PID has two choices, kEM or kOther. Any
821 four or five cluster shower is automatically labelled kEM since the parent track of the shower
822 was likely a Kalman fit and has a strong preference for that identification. A log likelihood
823 analysis using PDFs is done for all three clustered showers based on the development and
824 relationship of the clusters of the shower. The results of this PID is then passed to the
825 output.

826 Lastly, external to the cycle reconstruction, there is a muon decay tagger. This tagger
827 looks for the Michel electrons that result from a muon decay. It looks across multiple cycles
828 so it must be done independent of the rest of the reconstruction. The tagger looks for clusters
829 of overlapping time-delayed hits. It is possible for one muon decay to result in many clusters,
830 as it is mostly used for rejection of events.

831 3.4 PØD Particle Identification

832 After reconstructing a three dimensional track, pØdRecon offers four possibilities of iden-
833 tification. All 3D tracks are processed with either a parametric fit or a Kalman fit. The first
834 possibility, kOther, is a special category of short tracks that use the parametric fitter. The
835 identification choices available for Kalman tracks are kEM (a photon or electron), kLight-
836 Track (typically muons), or kHeavyTracks (protons). Only kEM and kOther particles are
837 passed on to shower reconstruction, which places an inherent dependence on the efficiency
838 of the track particle identification (PID) on any shower based analysis.

839 This analysis is done in two parts. First for a selected sample of stopping tracks (which
840 are most likely muons), the PID variables used in the identification are compared and then
841 used to create a Monte Carlo to data mapping. This mapping is then used to calculate the
842 difference in the efficiencies of selecting the correct hypothesis for true Monte Carlo particles.

843 3.4.1 Stopping Muon Sample

844 In order to create a mapping between data and Monte Carlo PIDs, an easily extractable
845 sample in data must be used. Stopping muons were tagged as such a sample. A muon
846 particle gun was used to model the incoming muons. A sample of 20,000 muons were created
847 for both the water-in and water-out PØD configurations and processed through nd280mc,
848 elecSim, oaCalib, PØDRecon and oaAnalysis. The muons have a linear energy distribution
849 with a gradient of -0.5 MeV goes to zero at 700 MeV. These Monte Carlo muons are shown
850 to roughly agree with the data by studying the track length, see Figure 3.8.

851 The vertex of the muons in the particle gun was placed at (0.0, 0.0, -345.0) cm in a box
852 that was 200 cm by 200 cm by 2 cm. This is upstream of the PØD. Figures 3.9 and 3.10

3.4. P \emptyset D PARTICLE IDENTIFICATION

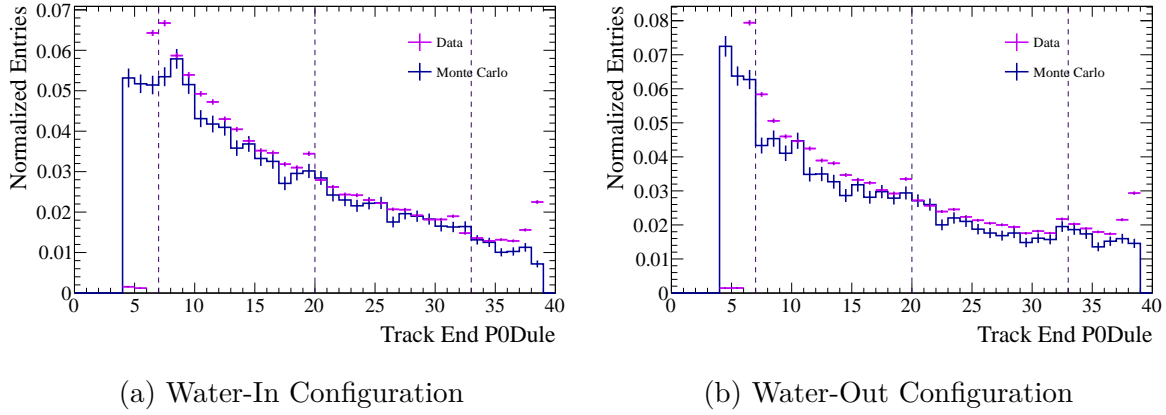


Figure 3.7: The last P \emptyset Dule used in a reconstructed track for muons that enter the front face of the P \emptyset D and do not exit. The dashed lines show the boundaries of the SuperP \emptyset Dules. Note the agreement for mid-range tracks.

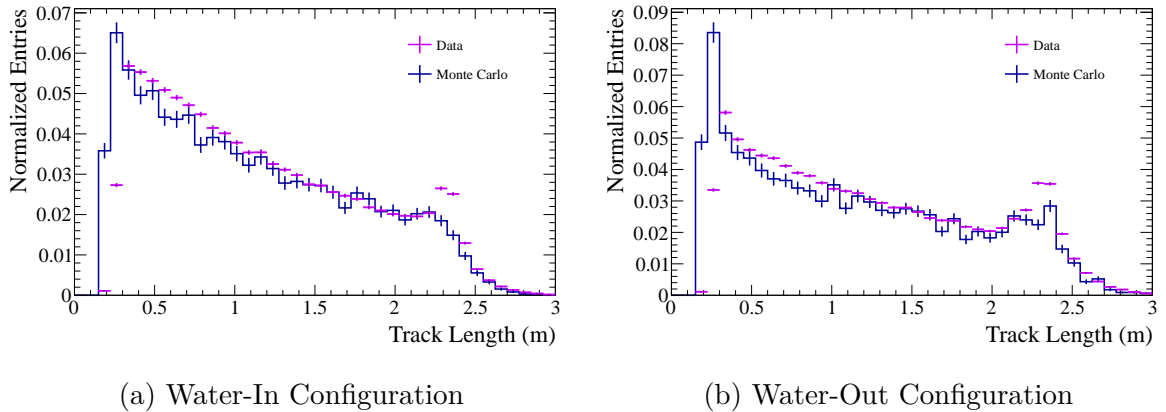


Figure 3.8: The length of the reconstructed tracks for muons that enter the front face of the P \emptyset D and do not exit. Short tracks have historically been difficult to model, but the mid-range tracks have the same shape in data and Monte Carlo.

3.4. P0D PARTICLE IDENTIFICATION

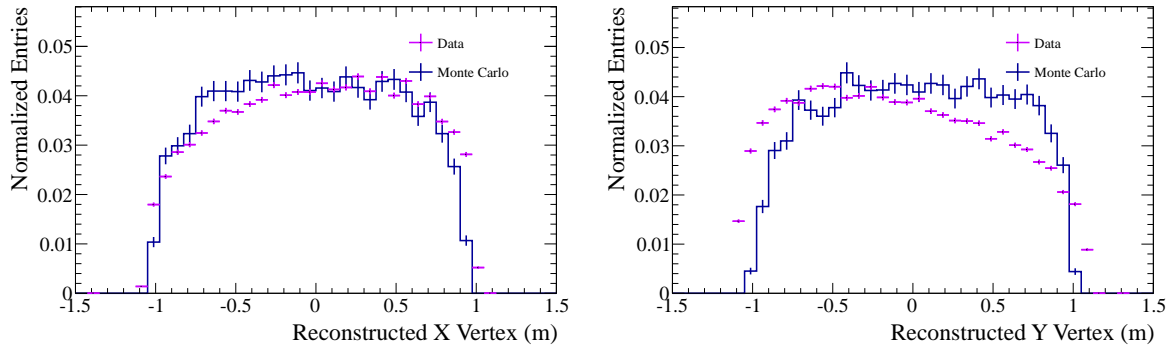


Figure 3.9: For the water-in configuration, the vertex distribution of the stopping muons. Due to the off-axis quality of the neutrino beam, a slight shift in both projections is expected.

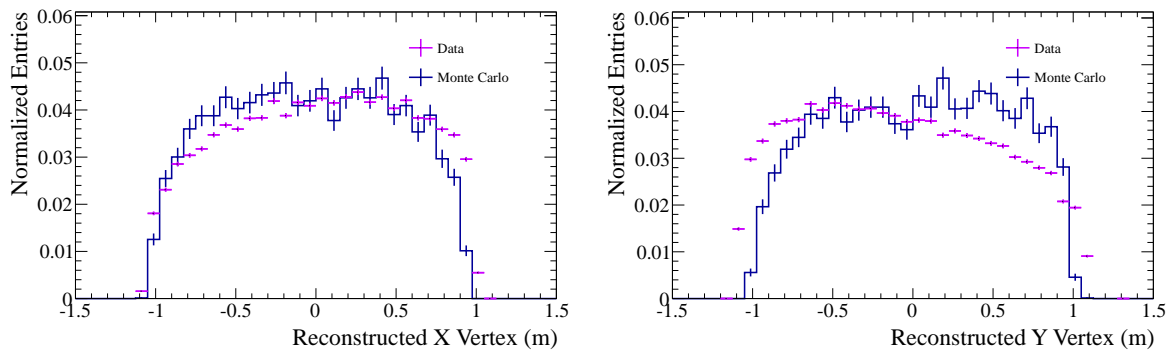


Figure 3.10: For the water-out configuration, the vertex distribution of the stopping muons. Due to the off-axis quality of the neutrino beam, a slight shift in both projections is expected.

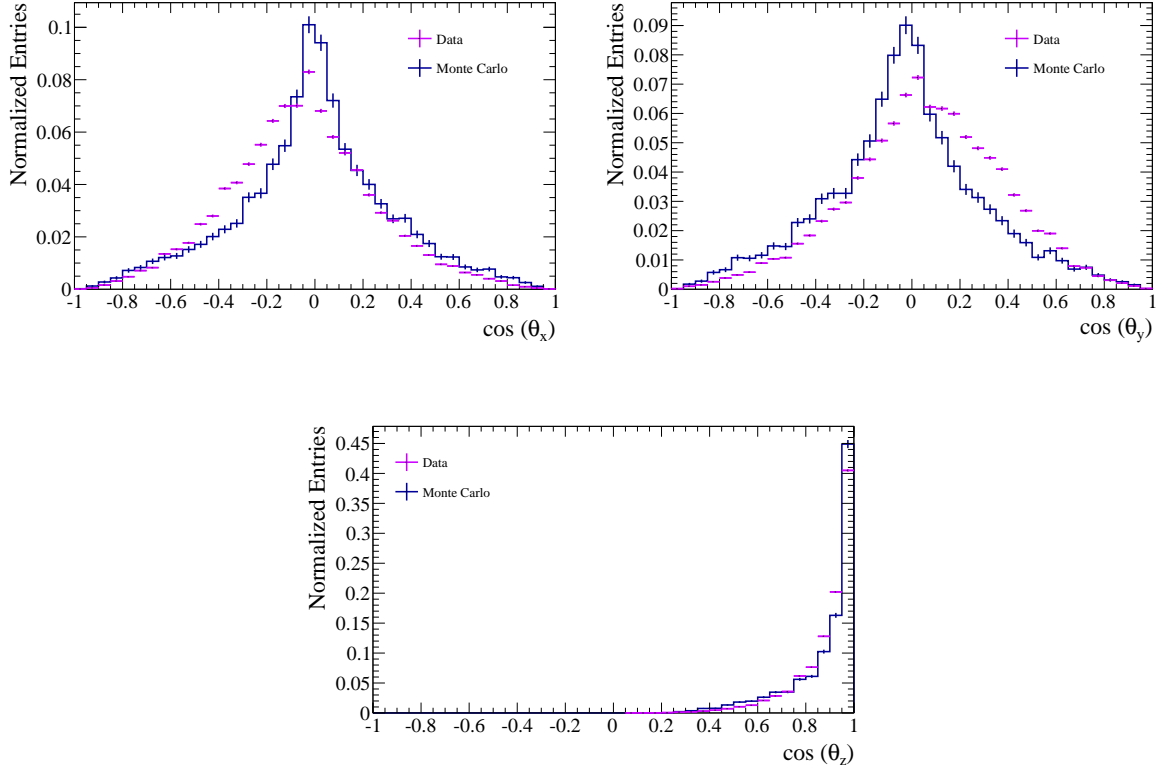


Figure 3.11: For the water-in configuration, the angular distribution of the stopping muons. Due to the off-axis quality of the neutrino beam, a slight shift in x and y is expected.

853 show that the reconstructed vertex is accurate except for the small offset due to the off-axis
 854 nature of the neutrino beam seen in the data.

855 The muons were directed in a one dimensional beam in the z direction with a radial sigma
 856 of 40 degrees. The sigma was hand tuned to match with the data distributions. Figures 3.11
 857 and 3.12 give an idea of the accuracy of this approximation. There is again an offset from
 858 the off-axis nature of the neutrino beam in data. However, these distributions show that the
 859 particle gun created is a fairly good approximation of the stopping muon sample in the data.

860 In order to extract this stopping muon sample, the results from TPØDTrackRecon were
 861 examined. One reconstructed vertex with one track fit by a Kalman fitter is required. The
 862 track must start in the upstream-most PØDule and be contained. A contained object requires
 863 that there is no charge in the edge bars or last PØDule.

864 3.4.2 Creating a Map

865 There are five variables that enter into the Kalman track identification. After a variable
 866 for a track is calculated, PDFs are used to make a log likelihood calculation for each identi-
 867 fication hypothesis. The three hypotheses are compared and the hypothesis with the largest
 868 log likelihood is chosen as the PID.

869 The first variable is three dimensional. It looks at the relative charge that is deposited

3.4. P0D PARTICLE IDENTIFICATION

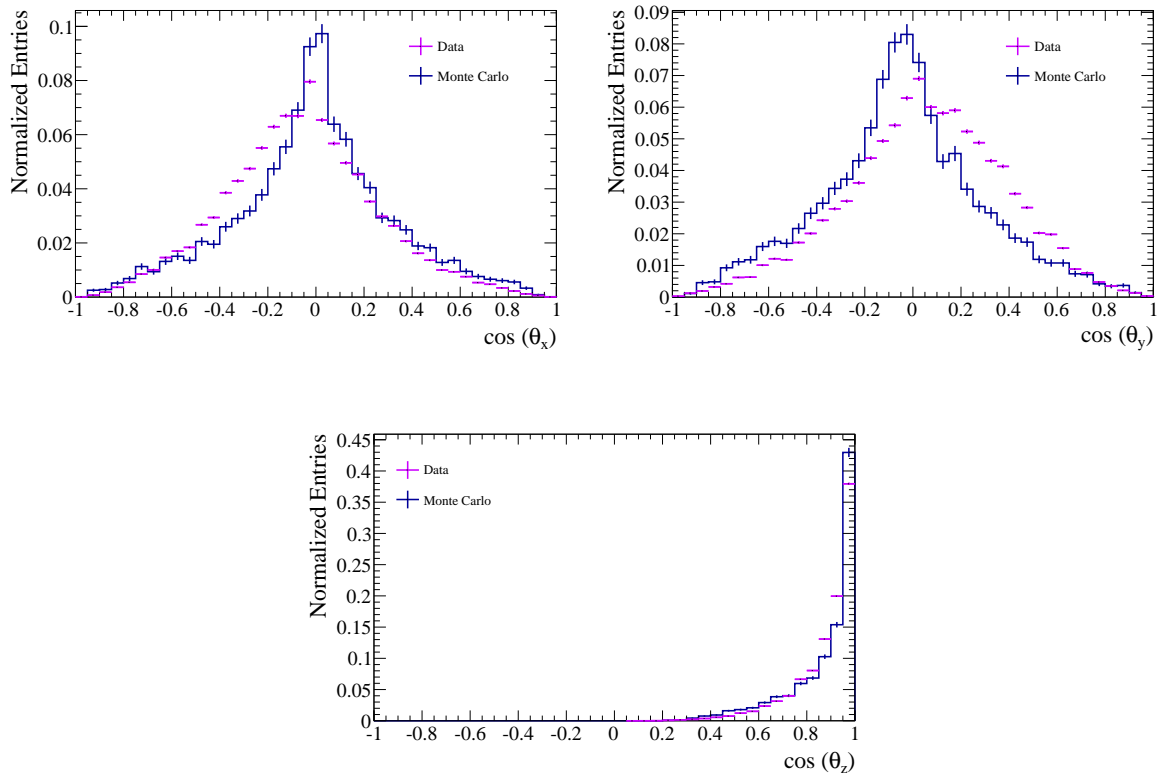
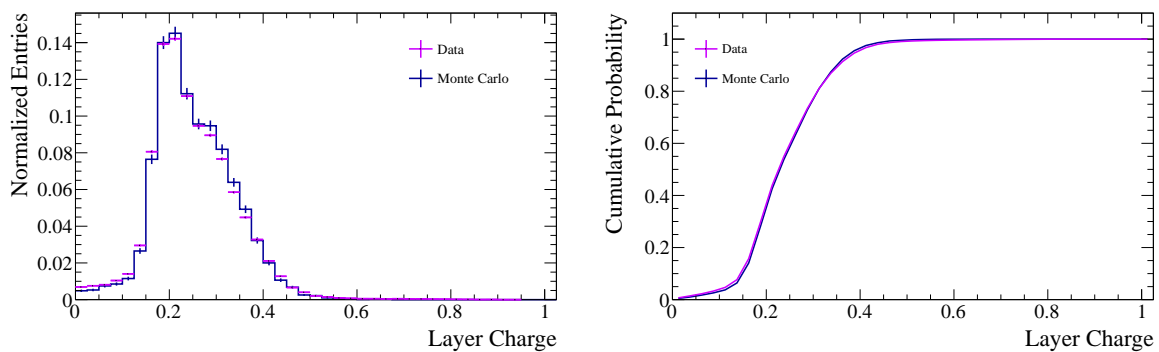


Figure 3.12: For the water-out configuration, the angular distribution of the stopping muons. Due to the off-axis quality of the neutrino beam, a slight shift in x and y is expected.



(a) Variable Distribution

(b) Cumulative Distribution

Figure 3.13: For the water-in configuration, these plots show an example of the distributions of different layer charge ratio variables for the stopping muon sample. This example shows the fractional reconstructed charge in the last layer of the reconstructed track at $\cos\theta_z = (0.9\bar{1}, 1.0)$.

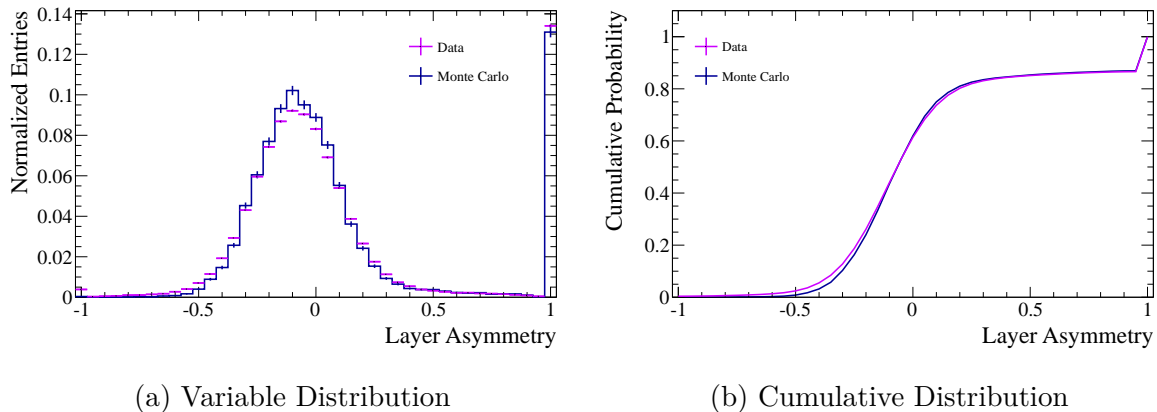


Figure 3.14: For the water-in configuration, these plots show an example of the distributions of variables for the stopping muon sample. This example shows the layer asymmetry in the last P \emptyset Dules of the reconstructed track.

870 in the last five layers of a reconstructed track. For each layer, the angle of the track and the
 871 charge deposited as a fraction of the total charge in the last five layers is saved. The angle,
 872 defined by the $\cos \theta_z$ is split into nine pieces with all events less than 0.2 reassigned to the
 873 $0.2 - 0.2\bar{8}$ bin. This is called the layer charge ratio. An example of the layer charge ratio
 874 distribution for a single layer and a single angle bin can be seen in Figure 3.13.

875 The next variable is the layer asymmetry of the last five P \emptyset Dules. Empty P \emptyset Dules are
 876 assigned an asymmetry value of 2.0, all other P \emptyset Dules have asymmetries (A) calculated by

$$A = \frac{Q_X - Q_Y}{Q_X + Q_Y}, \quad (3.1)$$

877 where Q_X refers to the charge in the X layer and Q_Y refers to the charge in the Y layer. The
 878 last four P \emptyset Dules are placed into separate PDFs, all the other P \emptyset Dules used in the tracks
 879 have asymmetries used in one PDF. An example of the layer asymmetry distribution for the
 880 last P \emptyset Dules of the track can be seen in Figure 3.14.

881 Next, there is the P \emptyset Dule asymmetry of the five pairs of P \emptyset Dules. If there are two
 882 adjacent P \emptyset Dules, the asymmetry is set to 2.0 again. Allowing $Q_i = Q_X + Q_Y$ to be the
 883 total charge in the i th P \emptyset Dule, the asymmetry is

$$A = \frac{Q_i - Q_{i+1}}{Q_i + Q_{i+1}} \quad (3.2)$$

884 The last four pairs of P \emptyset Dules use separate PDFs while all other pairs use the same PDF.
 885 An example of the P \emptyset Dule asymmetry in the last pair of P \emptyset Dules in the track can be seen
 886 in Figure 3.15.

887 Another variable counts the integer number of empty layers in a track. This variable also
 888 divides the tracks into groups by length for use with the PDFs. There are 5 length categories
 889 done by 500 mm sections where anything longer than 2000 mm is grouped together. An

3.4. P \emptyset D PARTICLE IDENTIFICATION

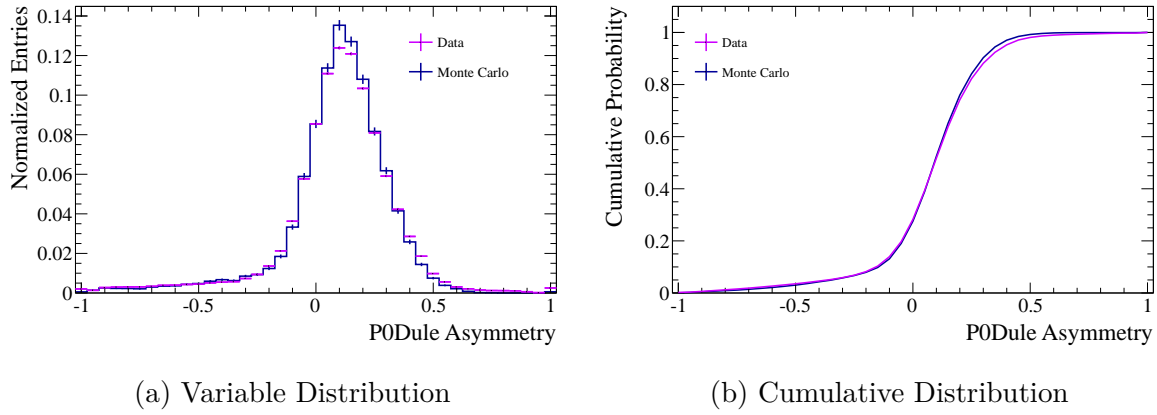


Figure 3.15: For the water-in configuration, these plots show an example of the distributions of variables for the stopping muon sample. This example shows the P \emptyset Dule asymmetry in the last pair of P \emptyset Dules of the reconstructed track.

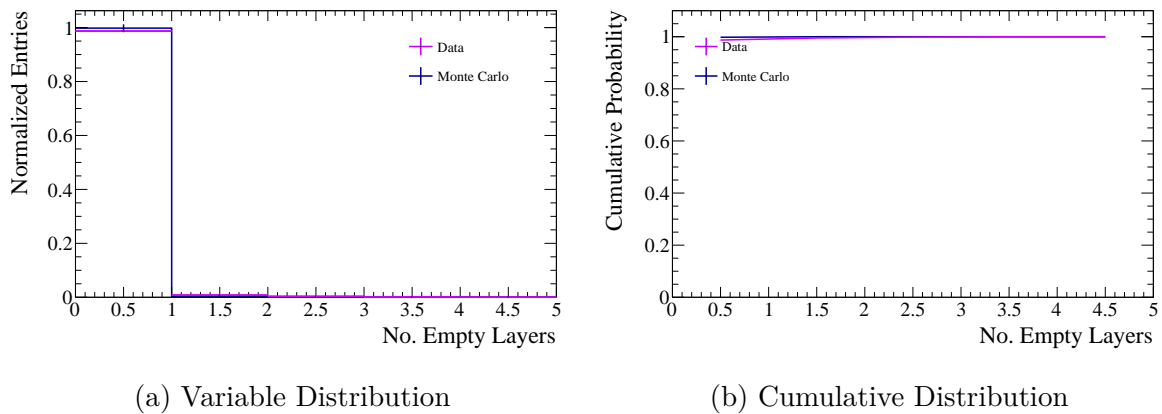


Figure 3.16: For the water-in configuration, these plots show an example of the distributions of variables for the stopping muon sample. This example shows the number of empty layers for short (0-500 mm) reconstructed tracks.

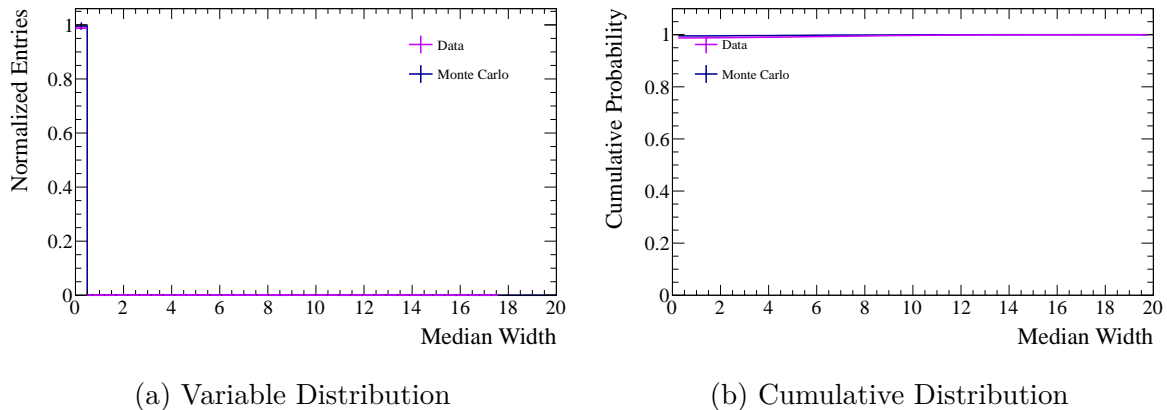


Figure 3.17: For the water-in configuration, these plots show an example of the distributions of variables for the stopping muon sample. This example shows the number of empty layers for short (0-500 mm) reconstructed tracks.

890 example of the distribution of the empty layers for the stopping muon sample is shown in
 891 Figure 3.16

892 The last variable used in the track reconstruction is the median width of the nodes of
 893 the track. Essentially this is a measure of how spread out the track is at each node. For
 894 muons this width should be small. This variable also uses the length of the track to further
 895 differentiate between particles. An example of this distribution of median widths of stopping
 896 muons can be seen in Figure 3.17.

897 With all of the variables accounted for, a mapping from the stopping muon Monte Carlo
 898 sample to the stopping muon data sample is created.

899 3.4.3 Mapping the PID

900 Using the entire Production 5E Monte Carlo, the default and a mapped version of the
 901 PID are compared. Again TP \emptyset DTrackRecon results are examined. A vertex in the fiducial
 902 volume is required with at least one three dimensional track. The true particle is determined
 903 by requiring most of the true charge deposit to be from one type of particle (EM, Muon or
 904 Proton). Next, the PID is calculated using the same PDFs that are found in p \emptyset dRecon. In
 905 addition, the variables are recalculated using the mapping created from the stopped muon
 906 sample. A variable is mapped by calculating its quantile in the Monte Carlo distribution.
 907 That same quantile is found in the data distribution and the variable that matches with it
 908 is used to calculate the PID. This mapping is done for each track.

909 Using the information in Tables 3.5 and 3.7, the difference between the default and
 910 mapped PID can be examined. The efficiency and accuracy of the Track PID can be taken
 911 from Tables 3.6 and 3.8. There is a clear effort put into correctly identifying the true EM
 912 particles. For the P \emptyset D water-in Monte Carlo with statistical Poisson errors, $3.94 \pm 0.02\%$
 913 of the true EM tracks reconstructed with the Kalman method are incorrectly identified
 914 using the default PID. With the mapped PID, this reduces to $2.24 \pm 0.01\%$ which gives

3.4. P \emptyset D PARTICLE IDENTIFICATION

Table 3.5: For the water-in configuration, the track-by-track rates of the default and mapped PID. There were 3922930 parametric tracks reconstructed.

	True Muon	True Electron	True Proton
Default PID			
Reconstructed Light Track	1361381	18624	311993
Reconstructed EM	447099	1064310	689316
Reconstructed Heavy Track	370509	25057	535913
Mapped PID			
Reconstructed Light Track	1112131	8876	238387
Reconstructed EM	564760	1083166	778480
Reconstructed Heavy Track	502098	15949	520355
Total True Events	2178989	1107991	1537222

Table 3.6: For the water-in configuration, the track-by-track efficiencies of the default and mapped PID. One can clearly see a directed effort into correctly identifying the EM sample.

	True Muon	True Electron	True Proton
Default PID			
Reconstructed Light Track	62.5%	1.7%	20.3%
Reconstructed EM	20.5%	96.1%	44.8%
Reconstructed Heavy Track	17.0%	2.3%	34.9%
Mapped PID			
Reconstructed Light Track	51.0%	0.08%	15.5%
Reconstructed EM	25.9%	97.8%	50.6%
Reconstructed Heavy Track	23.0%	1.4%	33.8%

Table 3.7: For the water-out configuration, the track-by-track rates of the default and mapped PID. There were 1864414 parametric tracks reconstructed.

	True Muon	True Electron	True Proton
Default PID			
Reconstructed Light Track	403149	8866	102480
Reconstructed EM	253524	496189	371301
Reconstructed Heavy Track	197261	14247	343162
Mapped PID			
Reconstructed Light Track	361716	5129	100355
Reconstructed EM	296773	504353	421055
Reconstructed Heavy Track	195445	9820	295533
Total True Events	853934	519302	816943

Table 3.8: For the water-out configuration, the track-by-track efficiencies of the default and mapped PID. Again there is evidence of a large effort to separate the true EM sample

	True Muon	True Electron	True Proton
Default PID			
Reconstructed Light Track	47.2%	1.7%	12.5%
Reconstructed EM	29.7%	95.5%	45.5%
Reconstructed Heavy Track	23.1%	2.7%	42.0%
Mapped PID			
Reconstructed Light Track	42.4%	1.0%	12.3%
Reconstructed EM	34.8%	97.1%	51.5%
Reconstructed Heavy Track	22.9%	1.9%	36.2%

3.5. CONVERTING DEPOSITED CHARGE TO ENERGY

915 a $1.70 \pm 0.02\%$ difference in efficiencies. Of all the true EM Kalman tracks in the P \emptyset D
916 water-out Monte Carlo, $4.45 \pm 0.02\%$ are incorrectly identified using the default PID. When
917 using the mapped PID, $2.88 \pm 0.02\%$ are incorrectly identified. This leads to a difference of
918 $1.57 \pm 0.04\%$ for the water-out configuration. However, since the sample used for the map
919 construction is a stopping muon sample, analyses are better served by approximating a PID
920 efficiency by looking at the number of true muons that enter the shower reconstruction. If
921 this definition is used, then there is a $5.40 \pm 0.05\%$ inefficiency difference of muons being
922 misidentified as EM for the water-in configuration and a $5.06 \pm 0.03\%$ inefficiency for the
923 water-out configuration.

924 3.5 Converting Deposited Charge to Energy

925 In order to understand the relationship between the reconstructed charge (PEU) and the
926 true energy (MeV), three samples of photons were generated, water-in water target, water-
927 out water target, and ECal. Each sample shows a different charge to energy response. It was
928 previously assumed that the water-in water target had a comparable energy scale to that of
929 the ECal [27]. However, the water-out water target will have a very different energy scale.
930 This conversion is necessary to provide an accurate energy of any reconstructed photons.

931 3.5.1 Creating a Photon Sample

932 Using Production 5F (ND280 v10r11p21), 200,000 photons were created in the P \emptyset D
933 water-in configuration and again in the P \emptyset D water-out configuration. An additional 100,000
934 photons were created in a special ECal geometry. This special geometry remodels the P \emptyset D as
935 40 ECal layers. The generated particles were uniformly distributed in energy from 1 MeV to 1
936 GeV. The focus of this study is on photons below 200 MeV, a typical energy of a photon from
937 a decaying π^0 . The vertex positions were smeared in a box on the upstream end of the water
938 target, in order to get the best chance of photon conversion in the water target. In addition,
939 the particles were generated isotropically downstream (no upstream going particles) due to
940 reconstruction efficiencies. The simulation process runs events through nd280MC, elecSim,
941 oaCalib, and P \emptyset DRecon.

942 Next, the events were processed through a selection to extract the cleanest sample of
943 reconstructed photons with their true and reconstructed deposited charge. For the truth
944 information, one vertex containing one particle (a photon) is required. Every event should
945 meet this requirement. At least 90% of the true energy deposit must be in the P \emptyset D, to ensure
946 that the particle is relatively contained inside the P \emptyset D. This is calculated by adding up the
947 energy deposit from the individual true hit segments. The total true energy is accessed by
948 examining the total true particle energy adjusted by the fraction of the true energy that is
949 deposited by the Monte Carlo in the P \emptyset D.

950 To access the the reconstructed information, every cycle is checked for a result containing
951 TP \emptyset DShowerRecon/TP \emptyset DShowerPID. This requires that the EM particle is reconstructed
952 correctly as a shower. Once a result is found, all vertices and showers are checked, in order
953 to get all possible information from the event. Every particle is checked and the attenuation
954 corrected charge deposit is added together. While the total charge deposit is added, the

3.5. CONVERTING DEPOSITED CHARGE TO ENERGY

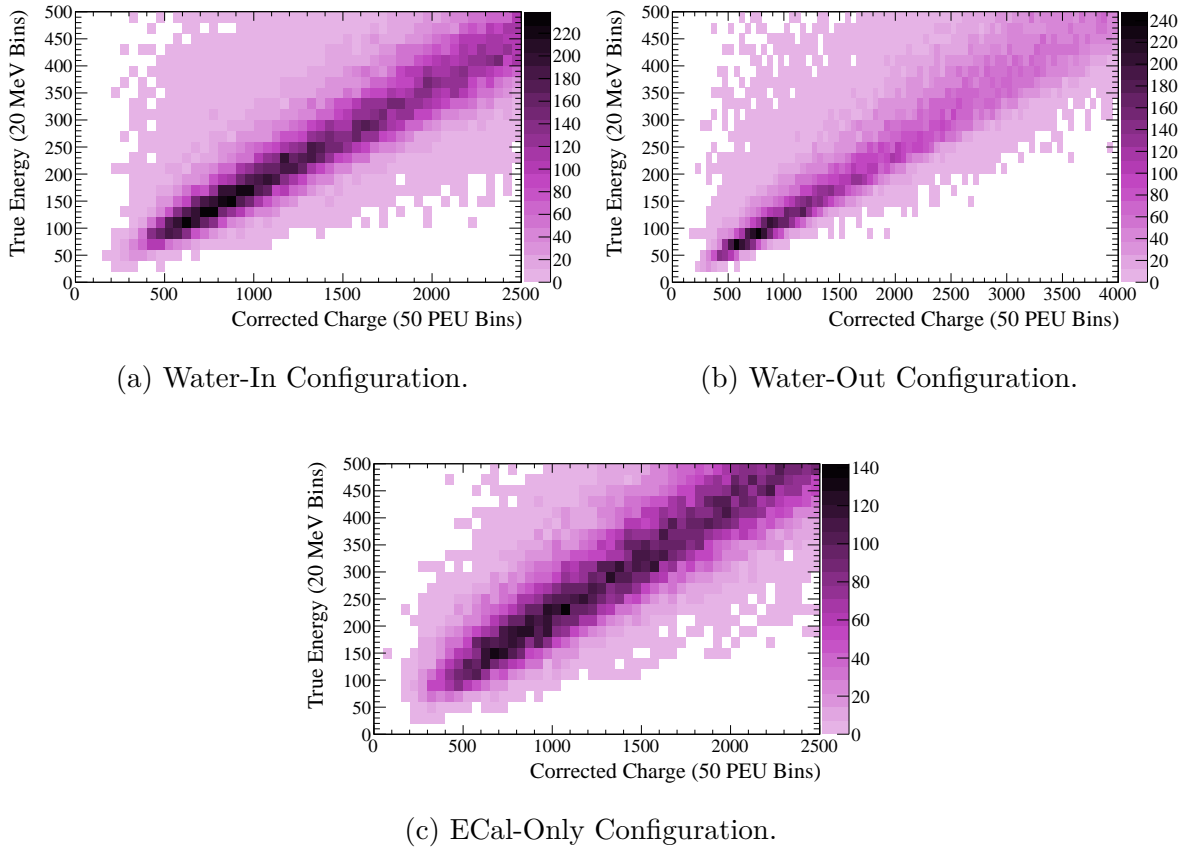


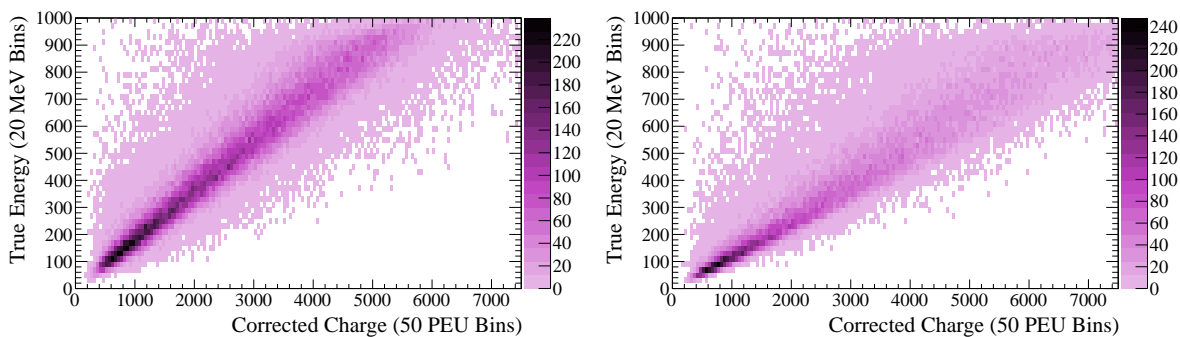
Figure 3.18: The distribution of the relationship between the attenuated corrected charge and the true energy of the photons. The charge is cut off to a region of interest where the true energy is less than 500 MeV. Note that the water-out configuration extends to higher charge region.

955 largest EM particle is extracted. This particle must have three dimensional information as
956 well as containing 90% of the total charge reconstructed in the event. The charge from the
957 reconstructed particle and the energy deposit from the truth information are studied further.
958 Also considered was the fraction of the attenuated charge in the particle that falls within
959 the water target which allows a division of the reconstructed charge.

960 3.5.2 Calculating the PEU to MeV Conversion

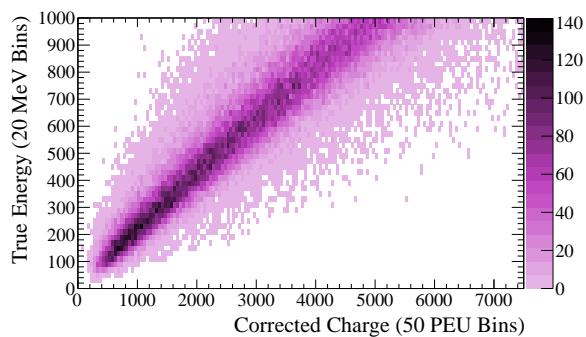
961 The true energy against the attenuation corrected reconstructed charge is plotted in
962 Figure 3.18. For the water target samples, all of the charge of the particle is required to
963 be inside the water target to investigate that piece of the P \emptyset D. Each bin, 20 MeV wide,
964 of the true energy is projected onto a one dimensional histogram. Using Gaussian fits, the
965 peaks of each projection is found. Although on first glance looking at charge bins makes
966 more sense, since the input is a charge and output should be an energy, there is an inherent
967 dependency on the input distribution of the generated energy. For example, if instead of a

3.5. CONVERTING DEPOSITED CHARGE TO ENERGY



(a) Water-In Configuration.

(b) Water-Out Configuration.



(c) ECal-Only Configuration.

Figure 3.19: The distribution of the relationship between the attenuated corrected charge and the true energy of the photons. The full range of the generated energy and the charge is shown.

3.5. CONVERTING DEPOSITED CHARGE TO ENERGY

Table 3.9: The energy scale values from linear fits of Figure 3.23.

	α_0 (MeV/PEU)	α_1 (MeV)
Water In	0.197 ± 0.019	-14.2 ± 14.1
Water Out	0.121 ± 0.011	-1.3 ± 13.0
ECal	0.262 ± 0.025	-29.6 ± 16.0

uniform true energy particle gun, a gaussian energy distribution was generated, the charge bins would have a drastically different shape. There is additionally some shape variation due to the different efficiencies of the detector at different energies. Due to this difference, the energy bin projections are studied with the individual bins only dealing with monoenergetic detector responses.

For the Gaussian fits, the fit range is restricted to one RMS of the distribution around the mean. The result must have at least one degree of freedom and be relatively narrow ($\sigma < 1000$ PEU). In addition the maximum of the function must be within 50% of the maximum of the histogram. Examples of these fits for photons can be seen in Figures 3.20, 3.21, and 3.22. The means of the Gaussian fits are plotted and fitted with a straight line. The errors shown are calculated by using the RMS divided by the square root of the entries. Since the energy bins were projected, the energy was placed on the x-axis. In addition, in order to get a better handle on the low energy photons used in the NC1 π^0 Analysis, the fit was restricted to less than 200 MeV. Finally, the function of energy chosen for the fit was

$$Q = f(E) = \frac{1}{\alpha_0}(E - \alpha_1), \quad (3.3)$$

where α_0 describes a slope and α_1 describes an intercept. This functions was chosen in order to trivially invert the function to a function of charge,

$$E = f^{-1}(Q) = \alpha_0 Q + \alpha_1. \quad (3.4)$$

The fits in Figure 3.23 gives the energy scale parameters for photons and is summarized in Table 3.9.

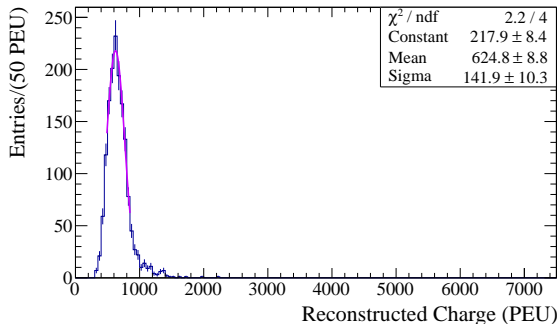
3.5.3 Checking the PEU to MeV Conversion

For a given water target charge, A , and ECal charge, B , a formula to calculate the total energy needs to be established. The formula considers the sum of the contributions of both parts of the detector,

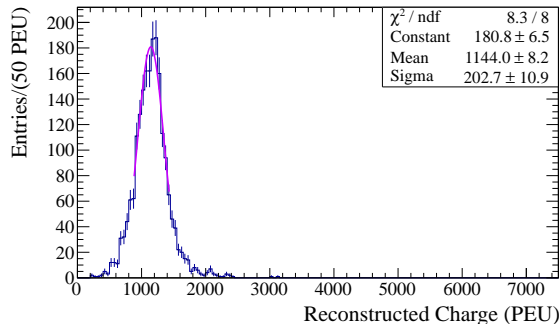
$$E = \alpha_0 \cdot A + \alpha_1 + \beta_0 \cdot B + \beta_1 \quad (3.5)$$

where α and β describe the water target and ECal charge to energy conversion. There are two types of α , one for the water-in configuration, α^{in} , and one for the water-out configuration α^{out} .

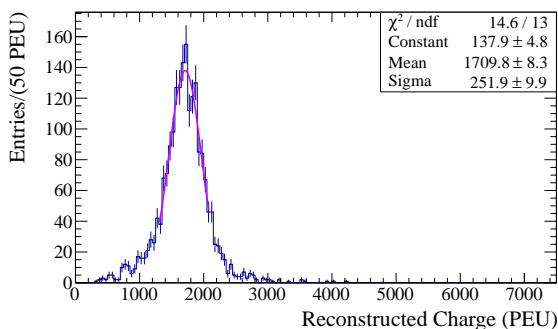
3.5. CONVERTING DEPOSITED CHARGE TO ENERGY



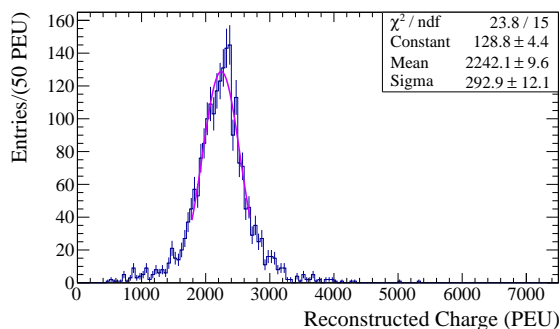
(a) 100 to 120 MeV



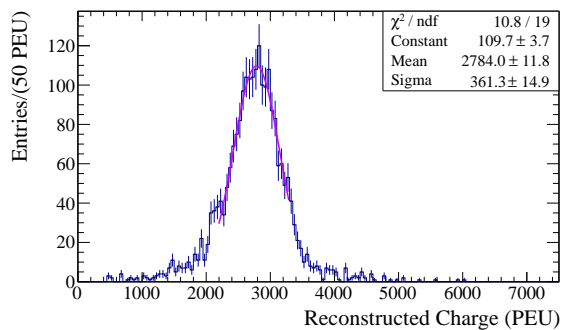
(b) 200 to 220 MeV



(c) 300 to 320 MeV



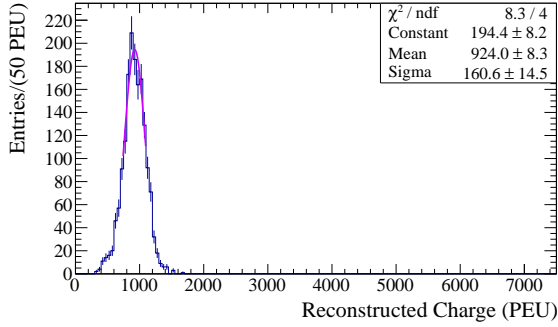
(d) 400 to 420 MeV



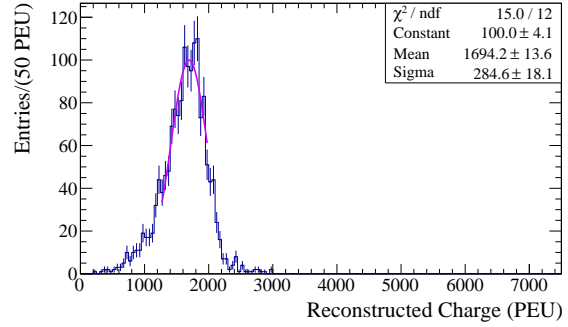
(e) 500 to 520 MeV

Figure 3.20: Examples of the Gaussian fits performed on each energy bin for the water-in-water target configuration.

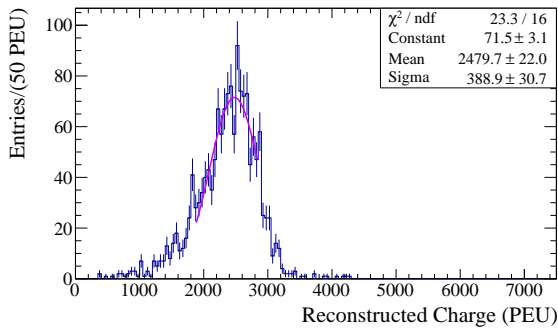
3.5. CONVERTING DEPOSITED CHARGE TO ENERGY



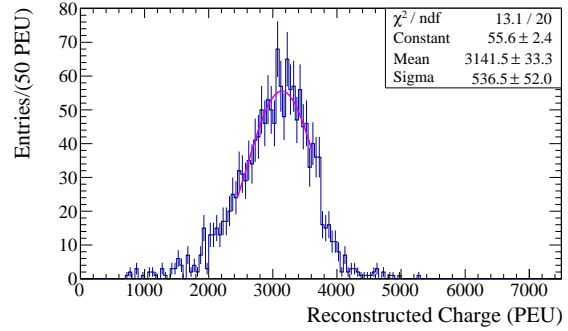
(a) 100 to 120 MeV



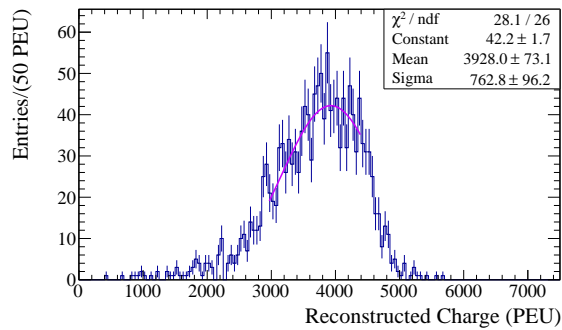
(b) 200 to 220 MeV



(c) 300 to 320 MeV



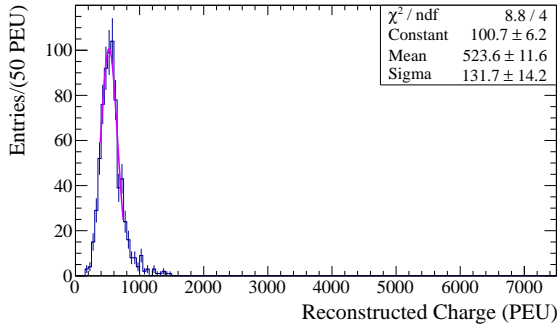
(d) 400 to 420 MeV



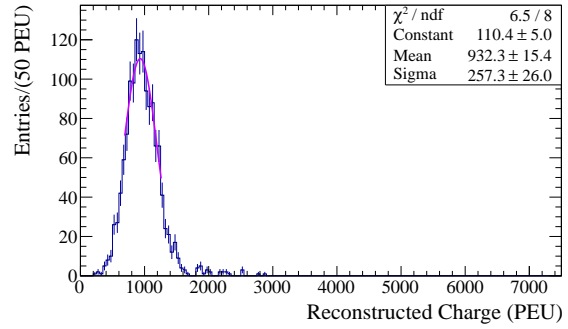
(e) 500 to 520 MeV

Figure 3.21: Examples of the Gaussian fits performed on each energy bin for the water-out water target configuration.

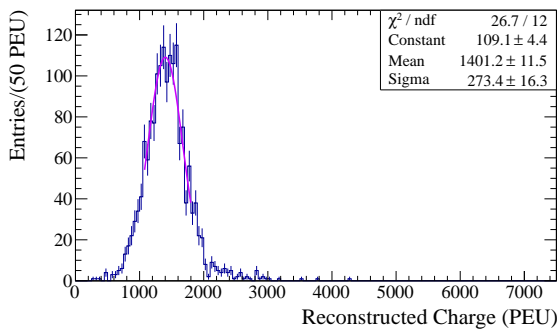
3.5. CONVERTING DEPOSITED CHARGE TO ENERGY



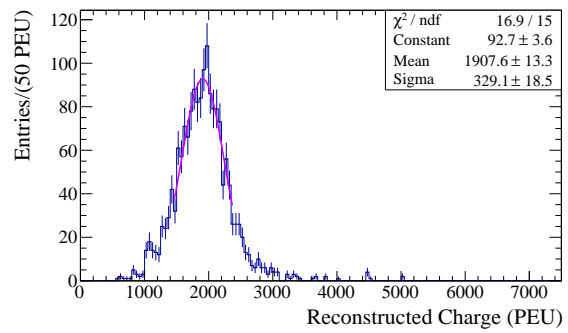
(a) 100 to 120 MeV



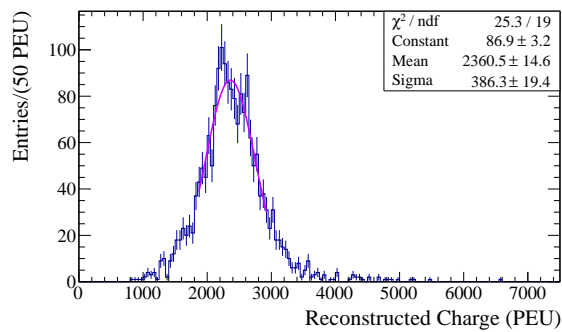
(b) 200 to 220 MeV



(c) 300 to 320 MeV



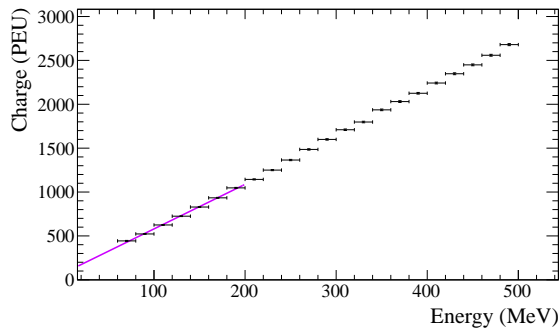
(d) 400 to 420 MeV



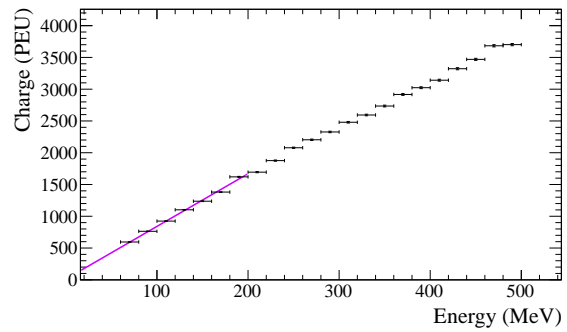
(e) 500 to 520 PEU

Figure 3.22: Examples of the Gaussian fits performed on each energy bin for the ECal-only configuration.

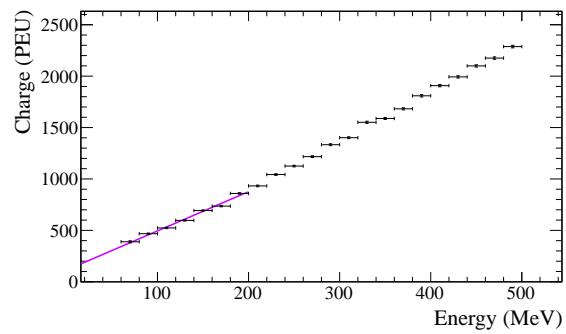
3.5. CONVERTING DEPOSITED CHARGE TO ENERGY



(a) Water-in Configuration



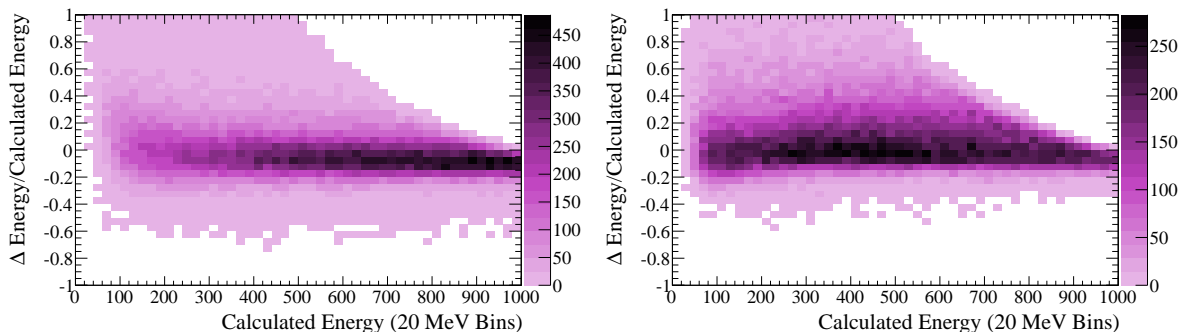
(b) Water-out Configuration



(c) ECal Only Configuration

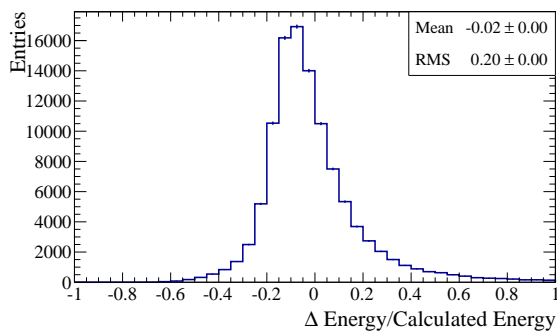
Figure 3.23: The linear fits of the means from the Gaussian fits of the energy bins of Figure 3.18.

3.5. CONVERTING DEPOSITED CHARGE TO ENERGY

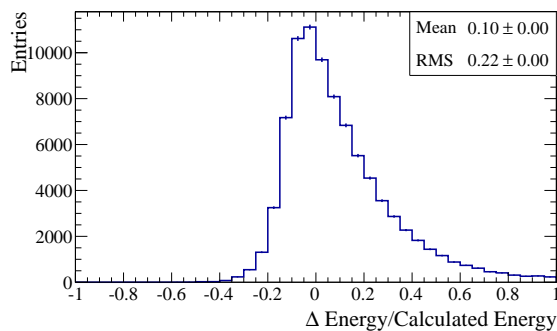


(a) Water-in Configuration.

(b) Water-out Configuration.



(c) Water-in Configuration.



(d) Water-out Configuration.

Figure 3.24: The fractional accuracy of the estimated energy is shown. The two dimensional plots show good consistency throughout the calculated energy scale. There is a long tail due to reconstruction efficiencies present at low energies. The one dimensional plots show an overall mean or peak close to zero as expected, with an RMS of approximately 20%.

993 Resolution

994 Using the energy conversion listed in Table 3.9, the accuracy and resolution of the equa-
 995 tion above can be examined. Figure 3.24 shows the fractional accuracy of the estimated
 996 energy $((E_{est} - E_{true})/E_{est})$ versus the estimated energy for photons. Ideally, for all esti-
 997 mated energies, all points would be at zero on the Y axis, indicating that the estimated
 998 energy is exactly the same as the true energy.

999 Figures 3.25 show the fractional accuracy of the estimation $((E_{true} - E_{est}/E_{est}))$, from
 1000 the Gaussian and median fits respectively, against the true energy for photons. Again this
 1001 distribution should be flat along the null line of the Y axis. A good consistency over the
 1002 true energy range and good approximations of the true value is shown. In particular, the
 1003 low energy values (the range of 50 to 200 MeV) appear to be well predicted, as can be seen
 1004 in the profile plots.

1005 In Figures 3.26, the accuracy of the true energy is plotted against the corrected charge for
 1006 photons. These plots, in conjunction with the one dimensional plots in Figure 3.25 can be
 1007 used to get an idea of the energy resolution. The widths of the one dimensional projections
 1008 show that the energy resolution is around 20%.

1009 Charge Addition

1010 To check the energy scale response for varied positions in the PØD, 20,000 monoenergetic
 1011 events were generated. These events were generated at 200, 300 and 500 MeV for photons.
 1012 The vertices were generated in a smeared box that starts in the upstream-most layer in the
 1013 water target and ends at the downstream end in the ECal for both of the water-in and water-
 1014 out configurations. For these monoenergetic studies, all of the generated charge is required
 1015 to be in the PØD, which leads to a loss of statistics in the ECal due to exiting events. The
 1016 events then go through the same process and selection described in Section 3.5.1. At the
 1017 end of processing, the estimated energy is calculated for the water target portion of the total
 1018 energy and the ECal portion of the total energy. The sum of the energy deposit in the ECal
 1019 and the water target should be the same, no matter what the fraction of the energy is in the
 1020 water target. For the purpose of display, any event that was only in the water target or only
 1021 in the ECal was discarded. In addition, the Z-axis is plotted with a log scale to emphasize
 1022 the shape of the distribution. This allows the topology of the plots to focus on the area of
 1023 interest, the mixture of charge deposit in the water target and in the ECal. The response to
 1024 the mono-energetic study is shown in Figures 3.27 and 3.28.

1025 These results of the monoenergetic study are summarized in Tables 3.10. The overall
 1026 trend of the two dimensional plots shown in Figures 3.27 and 3.28 is linear, showing that
 1027 this method of adding the charge deposit with individual energy conversions is an acceptable
 1028 way to estimate the energy. For the PØD NC1 π^0 analysis, the energy conversion calculated
 1029 here is considered an approximation and a separate energy scale is fit again in the final
 1030 invariant mass fit.

3.5. CONVERTING DEPOSITED CHARGE TO ENERGY

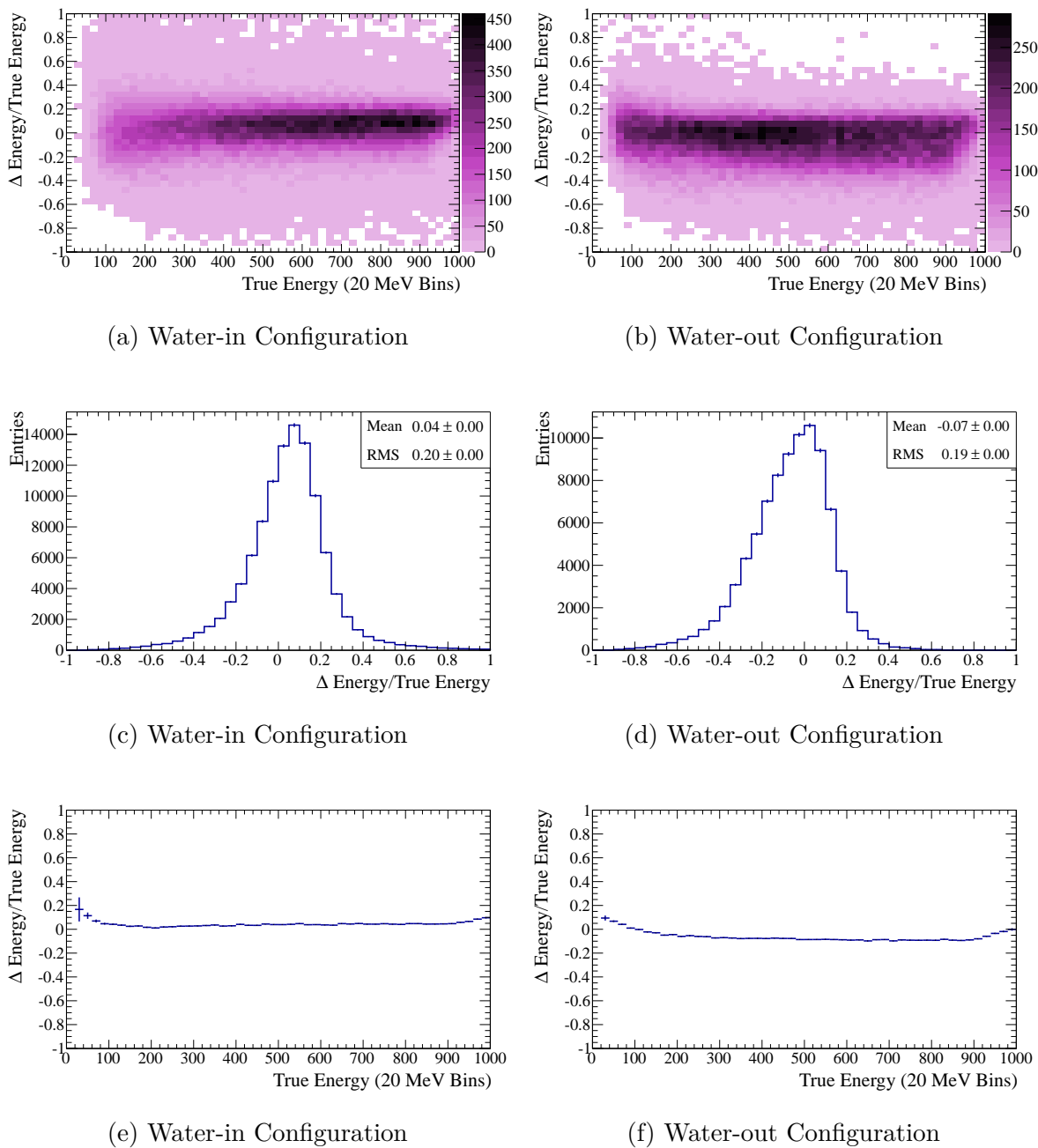


Figure 3.25: The response of the estimation against the true energy. The two dimensional plots show good consistency throughout the true energy scale. The one dimensional plots show an overall mean and peak close to zero as expected, with an RMS of approximately 20%. The profile plots show a slight variation at the low energy region, but energies between 50 and 200 MeV are of most concern to the $\text{NC}1\pi^0$ analysis which appear to be accurate.

3.5. CONVERTING DEPOSITED CHARGE TO ENERGY

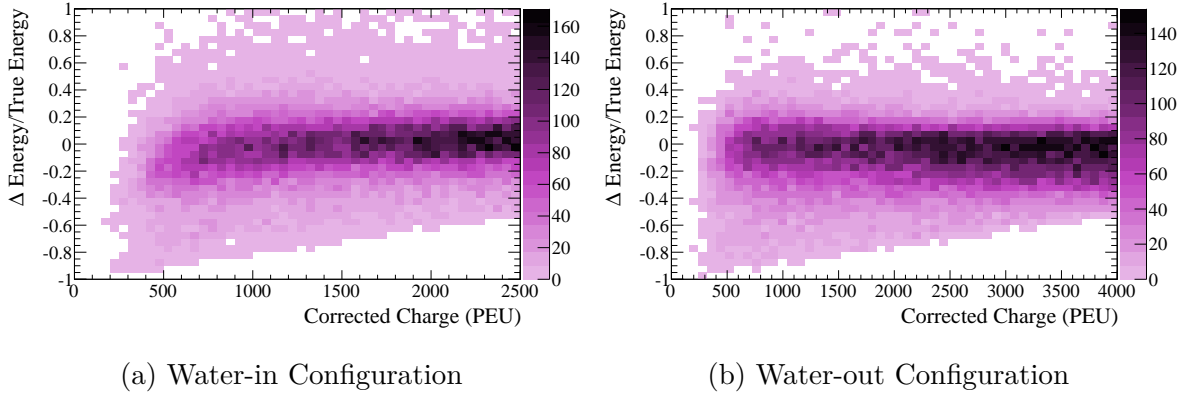


Figure 3.26: The response of the estimation against the corrected charge deposit is shown. The two dimensional plots show good consistency throughout the corrected charge deposit scale for the water-out configuration. Some efficiency loss is shown in the water-in configuration. The one dimensional plots are shown in Figure 3.25.

Table 3.10: A summary of the mono-energetic study. The values for the energy and the RMS columns come from the mean and RMS of the one dimensional plots in Figures 3.27 and 3.28. The accuracy column is the reconstructed mean energy divided by the true energy. The resolution column is the RMS of the reconstructed energy divided by the reconstructed energy. The first row for each configuration show the average accuracy and resolution of the individual mono-energetic studies.

	True Energy (MeV)	Energy (MeV)	RMS (MeV)	Accuracy %	Resolution %
Water In				105.5 ± 0.2	19.4 ± 0.1
	200	207.5 ± 0.7	52.0 ± 0.5	103.8 ± 0.4	25.1 ± 0.3
	300	313.8 ± 1.0	62.7 ± 0.7	104.6 ± 0.3	20.0 ± 0.2
	500	540.0 ± 1.7	70.1 ± 1.2	108.0 ± 0.3	13.0 ± 0.2
Water Out				102.7 ± 0.3	18.3 ± 0.2
	200	204.6 ± 0.8	44.1 ± 0.6	102.3 ± 0.4	21.6 ± 0.3
	300	305.4 ± 1.5	60.7 ± 1.1	101.8 ± 0.5	19.9 ± 0.4
	500	520.7 ± 3.2	69.9 ± 2.3	104.1 ± 0.6	13.4 ± 0.4

3.5. CONVERTING DEPOSITED CHARGE TO ENERGY

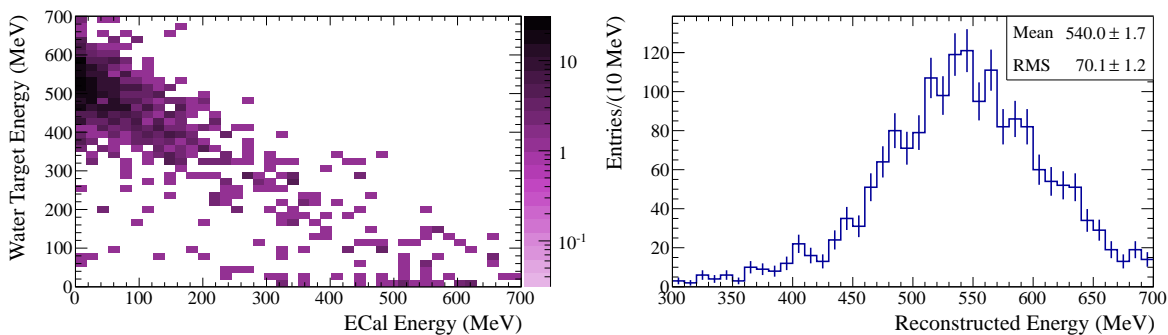
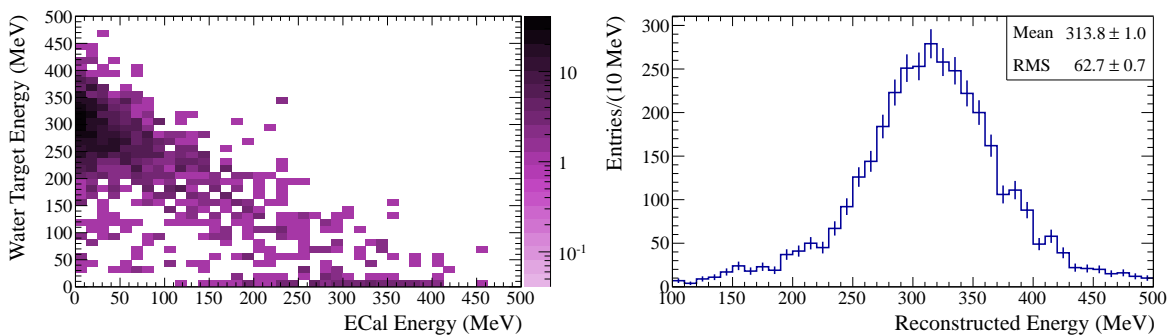
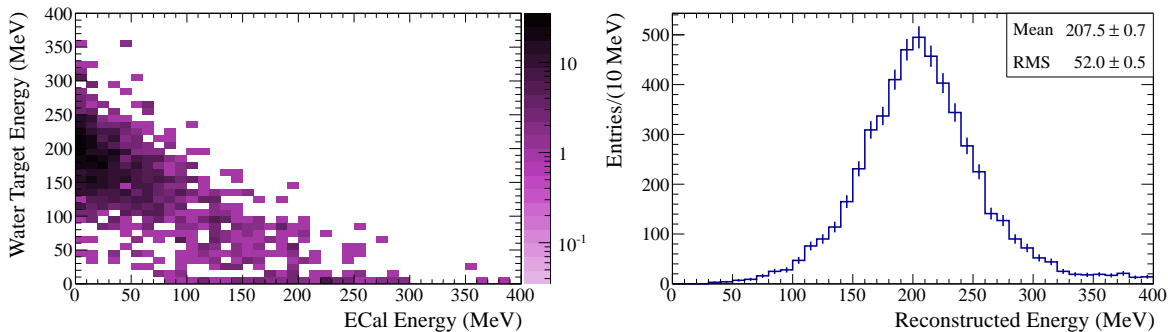
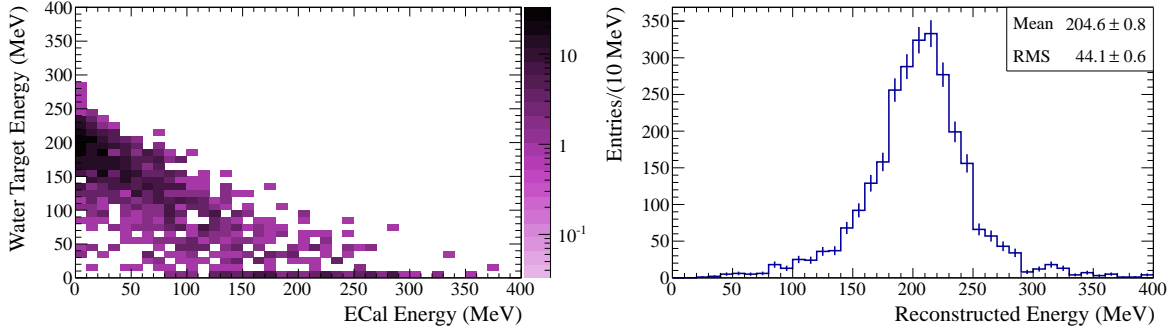
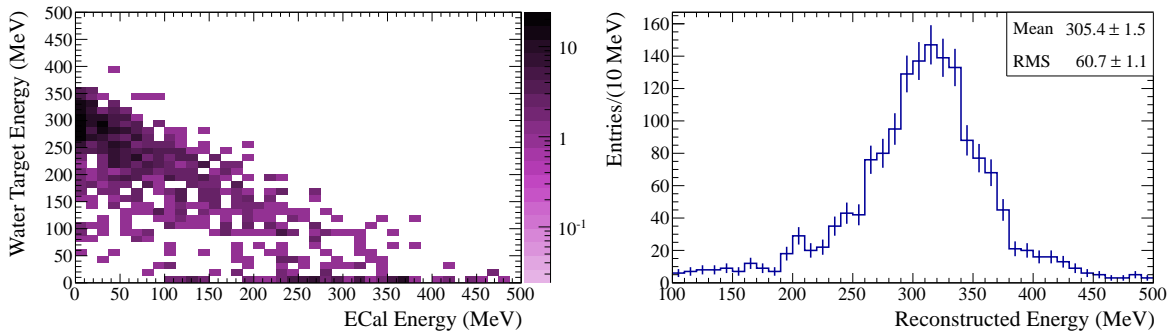


Figure 3.27: The results of the mono-energetic test of the energy scale for the water-in configuration.

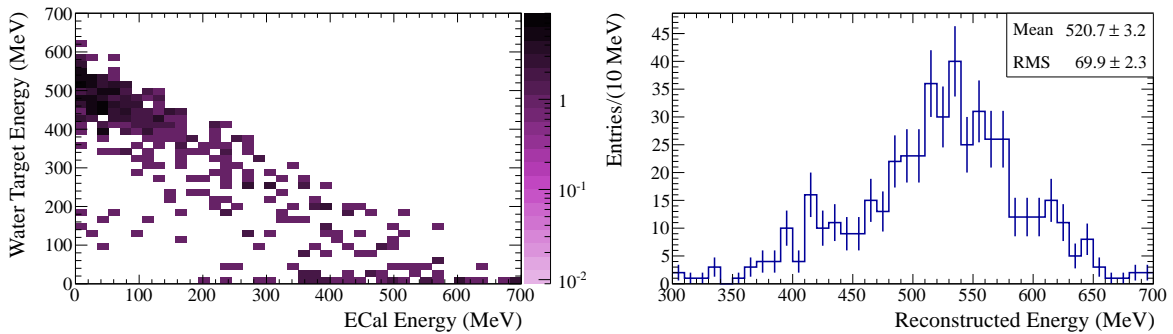
3.5. CONVERTING DEPOSITED CHARGE TO ENERGY



(a) 200 MeV: Sum of Reconstructed Energy (b) 200 MeV: Total Reconstructed Energy



(c) 300 MeV: Sum of Reconstructed Energy (d) 300 MeV: Total Reconstructed Energy



(e) 500 MeV: Sum of Reconstructed Energy (f) 500 MeV: Total Reconstructed Energy

Figure 3.28: The results of the mono-energetic test of the energy scale for the water-out configuration.

1031 3.6 P \emptyset D Alignment

1032 What follows is a description of the methods and validation for the alignment of the P \emptyset D.
 1033 First, the hit resolution of the X and Y layers must be determined to give a limit on the
 1034 alignment precision. The process of finding the hit resolution for both doublet and singlet
 1035 hits is detailed in Section 3.6.1. After that discussion, the method of alignment, including
 1036 the process of selecting events for alignment, is explained. As a cross-check on the alignment
 1037 method, a survey of the external position of the P \emptyset Dules was completed in the fall of 2010.
 1038 The initial alignment study was completed before the Great East Japan Earthquake and
 1039 Disaster in 2011. After which it was necessary to do a brief audit which found that no
 1040 significant displacement of the P \emptyset Dules occurred.

1041 3.6.1 P \emptyset D Layer Resolution

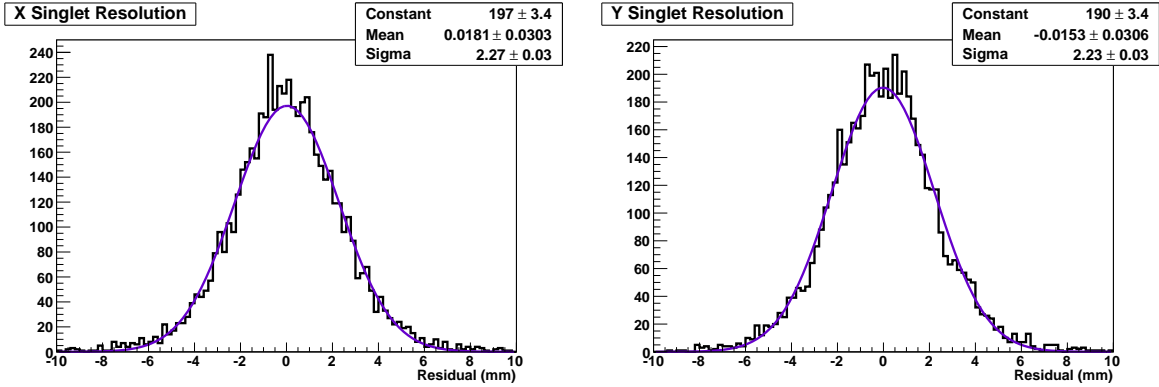
1042 Both the process for finding the single hit resolution and for determining the alignment
 1043 constants use the same event selection. In order to attain straight tracks through the de-
 1044 tector, cosmic ray runs were taken with the UA1 magnet turned off. The first step in the
 1045 selection process it to loop through each active data-taking time cycle recorded. There must
 1046 be one and only one 3D matched track in the P \emptyset D, which reduces noise hits from other tracks
 1047 from interfering with the track of interest. The track must have hits in both the first and
 1048 last P \emptyset Dule, which provides the longest lever arm for alignment and reduces the uncertainty
 1049 in the angle of the track. In order to include as many hits as possible, the unused hits from
 1050 the reconstruction are utilized. The unused hits within one centimeter in the Z direction and
 1051 four centimeters in the X or Y directions of any hit in the reconstructed track, the unused
 1052 hit is saved to the track hit selection. The hits from individual bars are clustered together
 1053 by XZ or YZ layers to form a single charge weighted hit. This single charge-weighted hit
 1054 is required to come from either a singlet or a doublet. A singlet is a hit or charge deposit
 1055 in the detector that occurs in only one bar in a layer. A doublet is a charge deposit in two
 1056 adjacent bars in a layer, the more likely scenario due to bar overlap. Requiring at most two
 1057 hits per layer prevents any biases due to delta rays coming off the track. Additionally, the
 1058 resolutions of singlets and doublets are of the most interest. Every layer must have at most
 1059 one clustered hit which has the benefit of removing delta rays as well as reducing fitting
 1060 error. At this point, the event is saved and will be used to produce alignment constants and
 1061 to study the single hit resolution.

1062 Due to the triangular geometry of the scintillator bars, deriving the ideal resolution is
 1063 difficult. Thus, to find the ideal single hit resolution, a particle gun Monte Carlo was used.
 1064 Using v8r5p13 of the ND280 Software, one thousand 10GeV muon events were generated
 1065 along the Z-axis through the P \emptyset D. The Z-axis was chosen because it will give a minimum
 1066 limit to the resolution of the P \emptyset D since there is a slight angular dependence to the resolution
 1067 and it coincides with the general beam direction. The sample that was used was constructed
 1068 with a perfect geometry. The events were run through Monte Carlo particle gun simulation,
 1069 electronic noise simulation and finally the P \emptyset D reconstruction. A self-made program was
 1070 used to extract the P \emptyset D reconstruction information used in this study.

1071 The clusters of hits, previously explained, are fit to two two-dimensional lines, one in the
 1072 XZ projection and one in the YZ projection. The fit result is used to calculate the residual

Table 3.11: The measured resolutions of both layers for data and Monte Carlo. All errors are statistical.

Layer	Data		Monte Carlo	
	Singlet (mm)	Doublet (mm)	Singlet (mm)	Doublet (mm)
X	2.57 ± 0.11	2.46 ± 0.06	2.27 ± 0.03	2.51 ± 0.02
Y	3.13 ± 0.12	2.78 ± 0.06	2.23 ± 0.03	2.43 ± 0.02



(a) X Layers.

(b) Y Layers.

Figure 3.29: The Monte Carlo predicted resolution of a singlet in the PØD. The errors are purely statistical.

1073 distance to the layer hit. Figures 3.29 and 3.30 show the ideal Monte Carlo singlet and
 1074 doublet resolutions for the X and Y Layers. These values represent the best resolution it is
 1075 possible to achieve. For data, the in situ singlet and doublet resolutions are shown in Figures
 1076 3.31 and 3.32 for the X and Y layers. The results from this study are summarized in Table
 1077 3.11

1078 3.6.2 Internal Alignment

1079 After selecting a 3D track, graphs of the residuals for the hits in each PØDule are
 1080 made. The displacements in X and Y of the PØDules are calculated from the mean of the
 1081 residual distributions. These numbers were saved and uploaded to the database to realign
 1082 the geometry before reconstruction.

1083 To test the accuracy of this method, a particle gun Monte Carlo was used. One thou-
 1084 sand 10GeV muon events were created in the +Z direction and processed with a misaligned
 1085 geometry. The point of this endeavor was to see if this method could extract the correct
 1086 constants. Figure 3.33 presents the results. The graph shows the difference between the
 1087 misalignments programmed into the geometry and the alignment constants that resulted
 1088 from this alignment process. The fluctuation of the difference is related to the systematic
 1089 error of the alignment which is 0.5 mm. The standard deviation of the values is 0.10 mm in

3.6. PØD ALIGNMENT

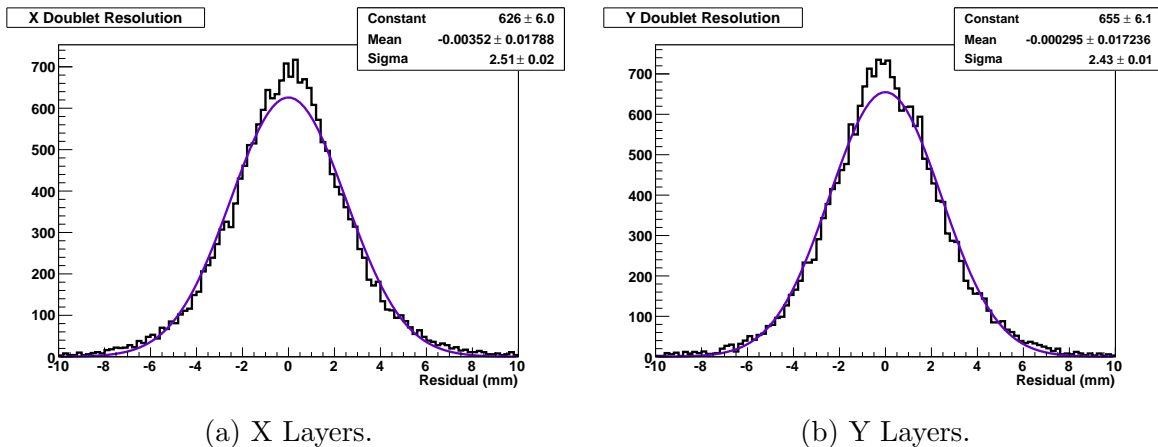


Figure 3.30: The Monte Carlo predicted resolution of a doublet in the PØD. The errors are purely statistical.

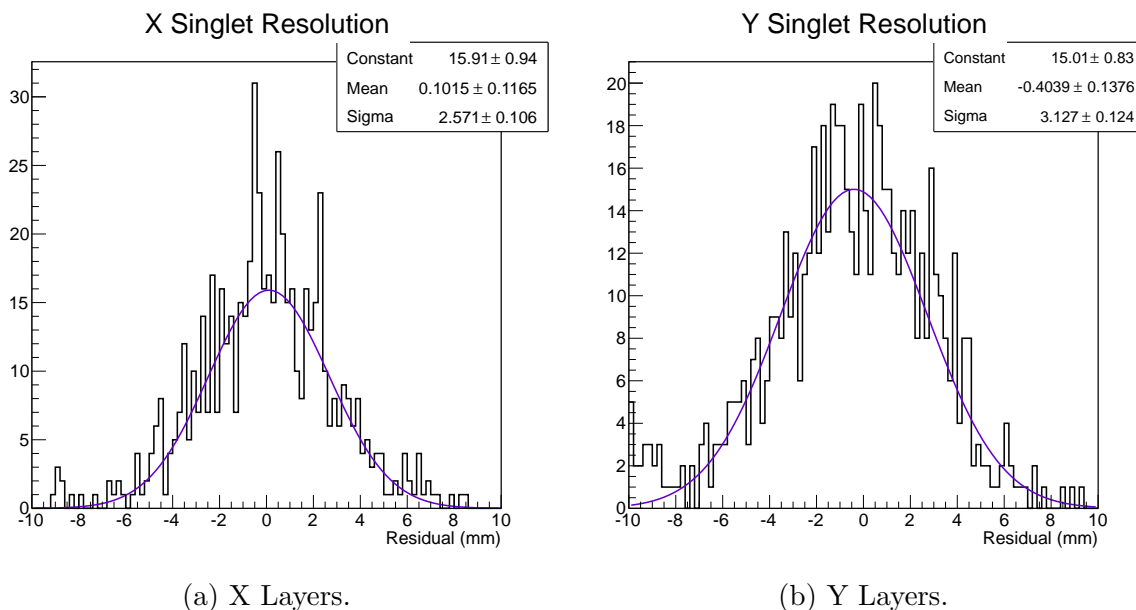


Figure 3.31: The measured data resolution of a singlet in the PØD. The errors are purely statistical.

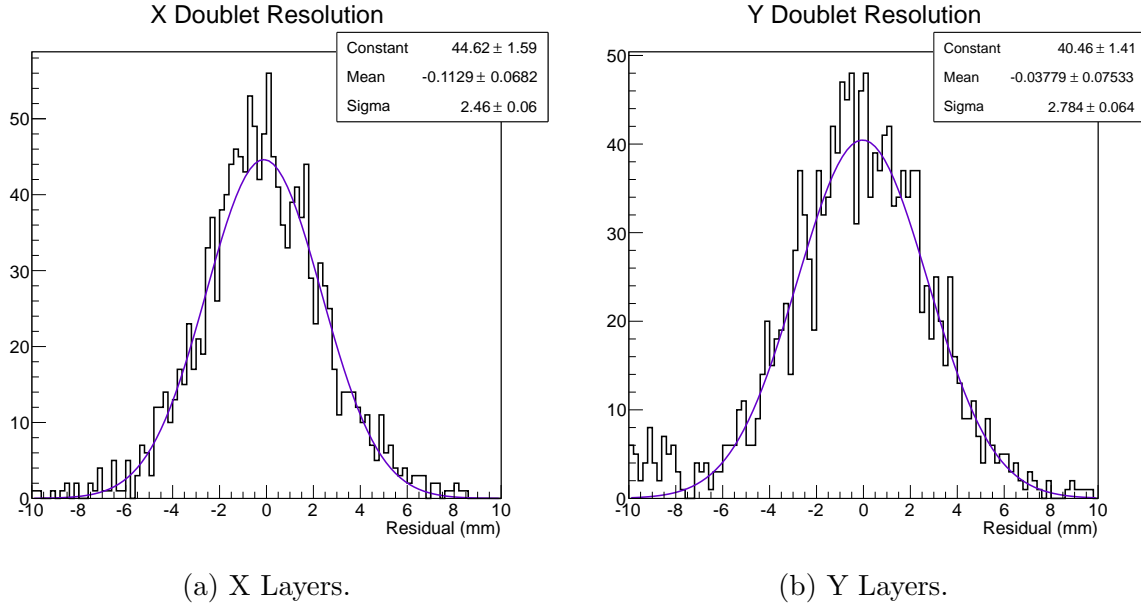


Figure 3.32: The measured data resolution of a doublet in the PØD. The errors are purely statistical.

1090 X and 0.08 mm in Y.

1091 To find the alignment parameters, Run 4863 Subrun 0 was processed through version
 1092 v9r7p9 of the ND280 software. For Run 4863, the magnet was turned off and the trigger
 1093 was set to accept cosmics. Figure 3.34 shows the alignment parameters for the layer by
 1094 layer alignment. The program found fifty-six useful tracks in this subrun, which is around
 1095 30 minutes of data taking. The layer-by-layer variation over the whole PØD is on order with
 1096 the resolution of the detector. This means that in situ, the internal PØD alignment in the
 1097 geometry is close to the ideal resolution of the detector.

1098 3.6.3 Alignment to the TPC

1099 In order to align the PØD to TPC1 (the TPC that is adjacent to the upstream end
 1100 of the PØD), tracks must be selected that cross the barrier between the two detectors.
 1101 Several selection criteria are required. One and only one 3D matched track in one time
 1102 cycle in the PØD is required to reduce noise hits from other tracks interfering with the track.
 1103 The track must start before the CECal and go through last PØDule which increases the
 1104 probability of the track having enough momentum to continue into TPC1. The last node of
 1105 the reconstructed track in the PØD must contain information both in the X and Y directions.
 1106 A node is a reconstructed object that describes the position and direction of the hits in the
 1107 two adjacent layers of the PØDule. One and only one object in TPC1 is allowed. The time,
 1108 position and direction of the last node of the PØD and the first node of the TPC are saved
 1109 from these events.

1110 First, is a cut based on the difference in the Z-direction between the last node of the PØD
 1111 and the first node of the TPC. Next, the events are cut on the angular difference between
 1112 the direction of the PØD node and the TPC node. This is done to prevent any kinks, due to

3.6. PØD ALIGNMENT

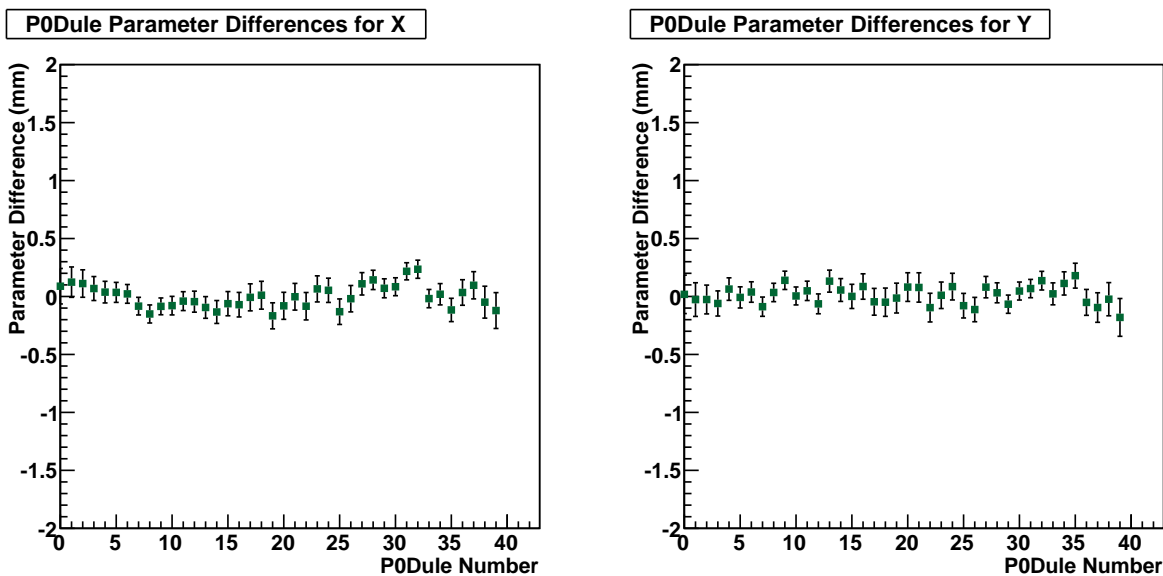
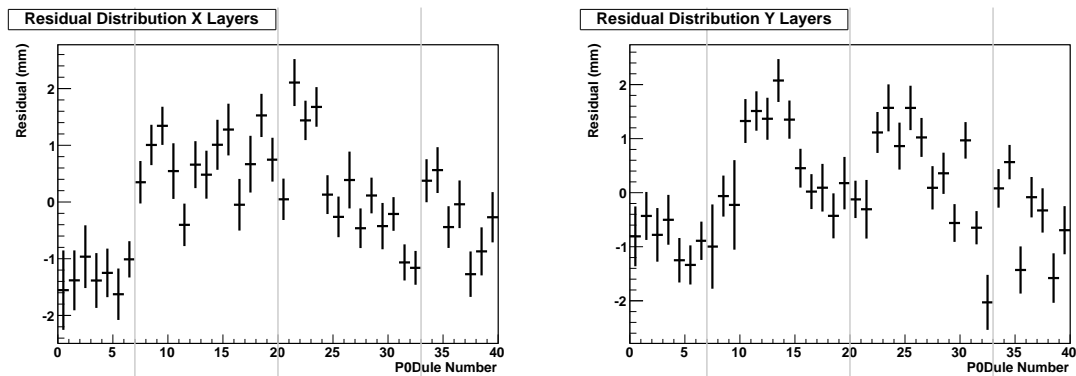


Figure 3.33: The difference between parameters forced on the geometry and the parameters acquired from the full PØD alignment method.



(a) X Layers.

(b) X Layers.

Figure 3.34: Parameters acquired as a result of the PØD alignment method on Run 4863 Subrun 0. The gray lines mark the divisions of the SuperPØDules.

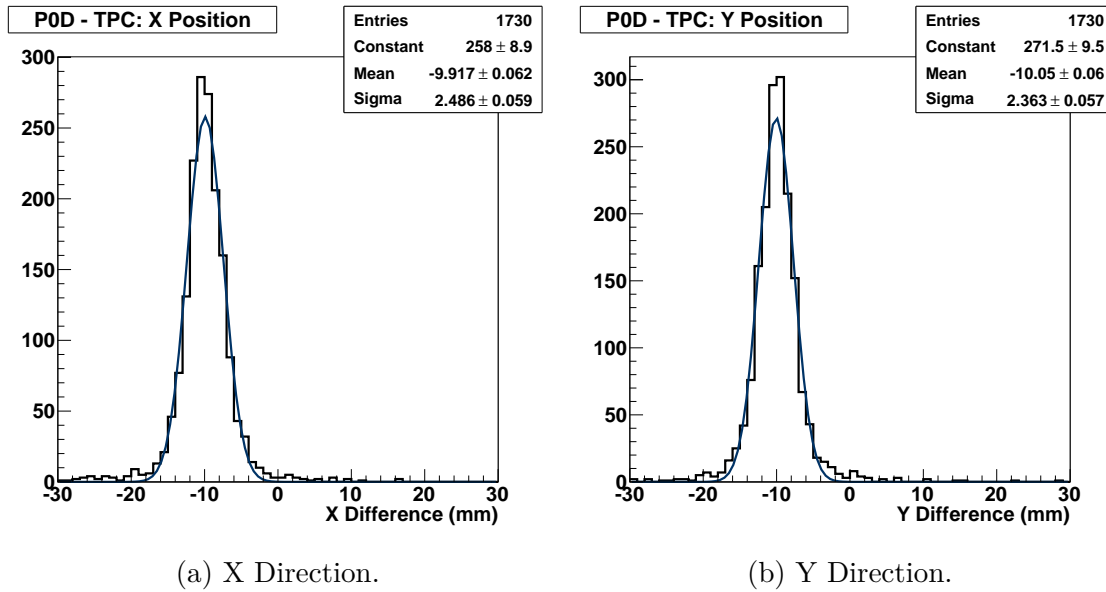


Figure 3.35: The parameters retrieved from the external alignment process using Monte Carlo particle guns after forcing the PØD to be -10 mm in both the X and Y directions.

1113 possible scattering, that might affect the final result. In order to make the final evaluation,
 1114 the TPC node is propagated to the same Z position of the PØD node by extrapolating a
 1115 straight line utilizing the direction associated with the TPC node. The extrapolated TPC
 1116 position is then subtracted from the PØD position and plotted in histograms. The histograms
 1117 are then fit to gaussian curves in order to extract the alignment constants.

1118 To test the matching code, twenty five thousand 1GeV muons were produced in the +Z
 1119 direction using a particle gun monte carlo. At the reconstruction stage, the file was recon-
 1120 structed three times with three different geometries. These geometries have no misalignment,
 1121 a -5 mm offset in both X and Y in the PØD, and a -10 mm offset in both X and Y in the
 1122 PØD. In Figure 3.35, the results from the 10 mm test are shown. The results show that the
 1123 PØD need to be moved $+10.0$ mm in the X direction and $+9.9$ mm in the Y direction to
 1124 return to the original position. A similar accuracy was present in the other trials. Given the
 1125 precision of the trials, a systematic error of ± 0.5 mm is assigned.

1126 Using 382 tracks from Run 4863 Subrun 0, the in situ external alignment was calculated.
 1127 Figure 3.36 shows that in the Monte Carlo geometry, the PØD needs to be moved $3.5 \pm$
 1128 $0.2(\text{stat}) \pm 0.5(\text{sys})$ mm in the -X direction and $13.1 \pm 0.3(\text{stat}) \pm 0.5(\text{sys})$ mm in the -Y
 1129 direction. For Production 5 of the near detector software, the active center of the PØD has
 1130 been moved in the Monte Carlo geometry to the coordinates $(-35.7, -0.7)$.

1131 3.6.4 Alignment Survey Measurements

1132 In the fall of 2010, a survey using a laser level (Stanley 77-154 SP5 FatMax Five Beam
 1133 Laser Kit by CST/Berger) was conducted. The company that made the level claimed an
 1134 accuracy of $\frac{1}{4}$ inch at 100 feet. After some on-site testing, the level was assigned a systematic
 1135 error of 1 mm over six feet. The laser was designed to be self leveling and to have a

3.6. PØD ALIGNMENT

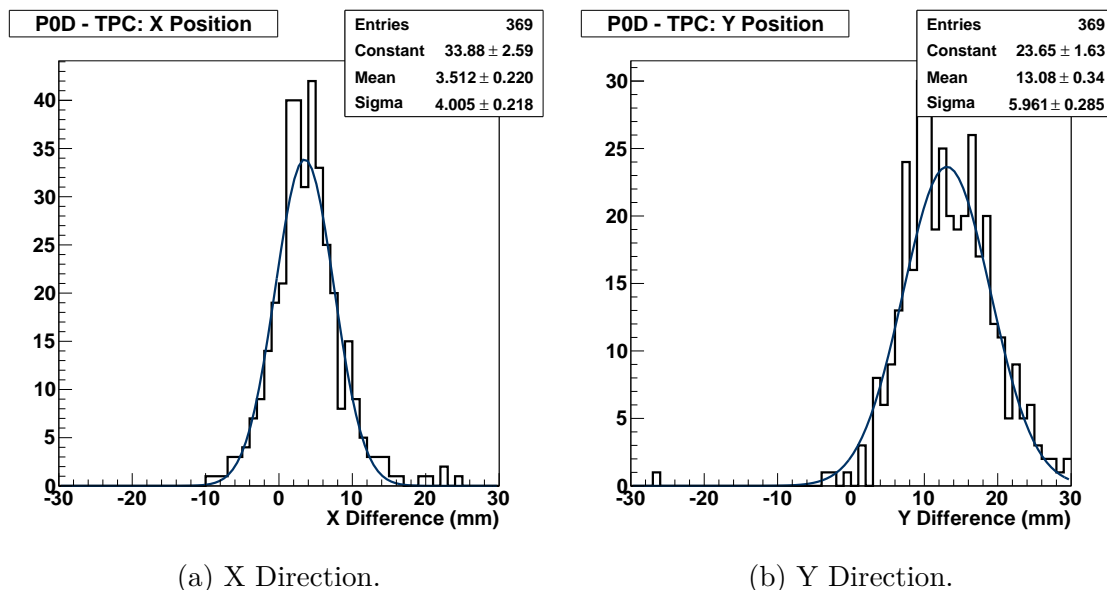


Figure 3.36: Result of TPC-PØD matching on Run 4863 Subrun 0. This indicates that the PØD needs to be moved to the north (-X) 3.5 ± 0.2 mm and down (-Y) 13.1 ± 0.3 mm.

1136 beam emitted in five directions. Measurements of the accessible bottom parts of the PØD
 1137 along the north and south edges and the accessible north side of the PØD were taken. For
 1138 some PØDules, an additional measuring tool was used with an assumed 1 mm systematic
 1139 uncertainty. The measurements made with the ruler had an error of 0.5 mm.

1140 PØD Bottom Survey

1141 There were two surveys conducted of the bottom of the PØD. One survey was a compar-
 1142 ison to fixed points on the TPCs, the other was a comparison within the PØD. The global
 1143 survey was done by sending a laser line down the north side of the detectors and another laser
 1144 was sent down the south side of the detectors. Using a ruler, fixed points on the outer casings
 1145 of the PØD and the TPCs were directly compared. The findings are summarized in Table
 1146 3.12. The measurements of the north and south side were done independently and the error
 1147 on the measurement is 1.1 mm due to the error in the laser and the error in the measurement
 1148 with a ruler. The surveyed positions were the bottom of the first and last PØDules and the
 1149 aluminum bracket on the bottom of the TPCs. The hope was that a prior professional survey
 1150 of the TPCs could be extrapolated to the PØD with these measurements. The north and
 1151 south side measurements were taken independently and are separately normalized.

1152 A more detailed survey of the bottom of the PØD is shown in Figure 3.37. In order to
 1153 conduct this survey, the laser was located at two points: the north-east corner of the PØD
 1154 and the south-east corner of the PØD. Due to the inaccessibility of the part of the bottom of
 1155 the PØD, only eighteen PØDules on the north side and six PØDules on the south side could
 1156 be measured. The error on these measurements is 1.1 mm. In Figure 3.37, the north side,
 1157 the south side and the calculated parameters from Figure 3.34 are presented. The three sets
 1158 are artificially placed so that their averages are zero.

Table 3.12: A P \emptyset D survey taken in reference to the TPC. The Upstream plate of TPC1 was chosen as the reference point. The Upstream(Downstream) measurements are signified by a U(D).

	P \emptyset D		TPC1		TPC2		TPC3	
	U (mm)	D (mm)	U (mm)	D (mm)	U (mm)	D (mm)	U (mm)	D (mm)
North	1	5	0	-2	-3	-3	-4	-4
South	3	3	0	0	-1	-1	-1	-2

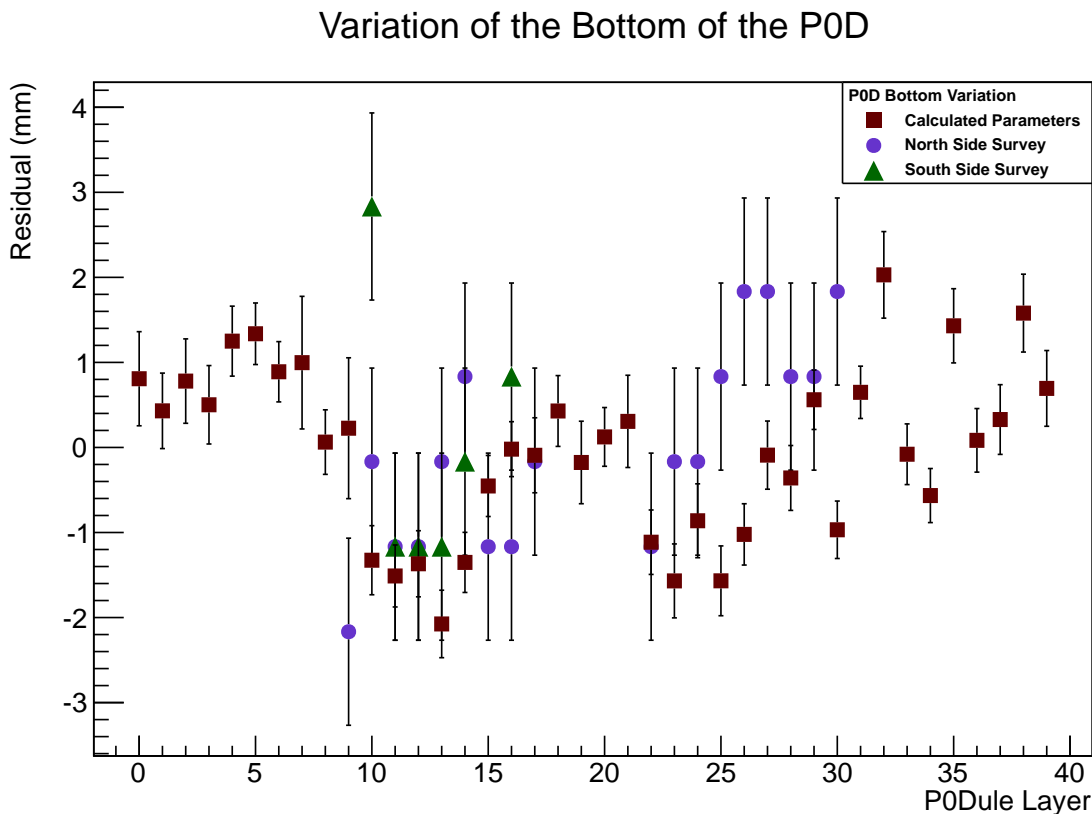


Figure 3.37: Measurements of the variation of the P \emptyset Dules' Y position along the bottom side of the P \emptyset D. The graph includes the north side survey (blue circle), the south side survey (green triangle) and the calculated parameters (red square) from the alignment procedure. The average of each set is artificially fixed at 0mm.

Variation of the Side of the PØD

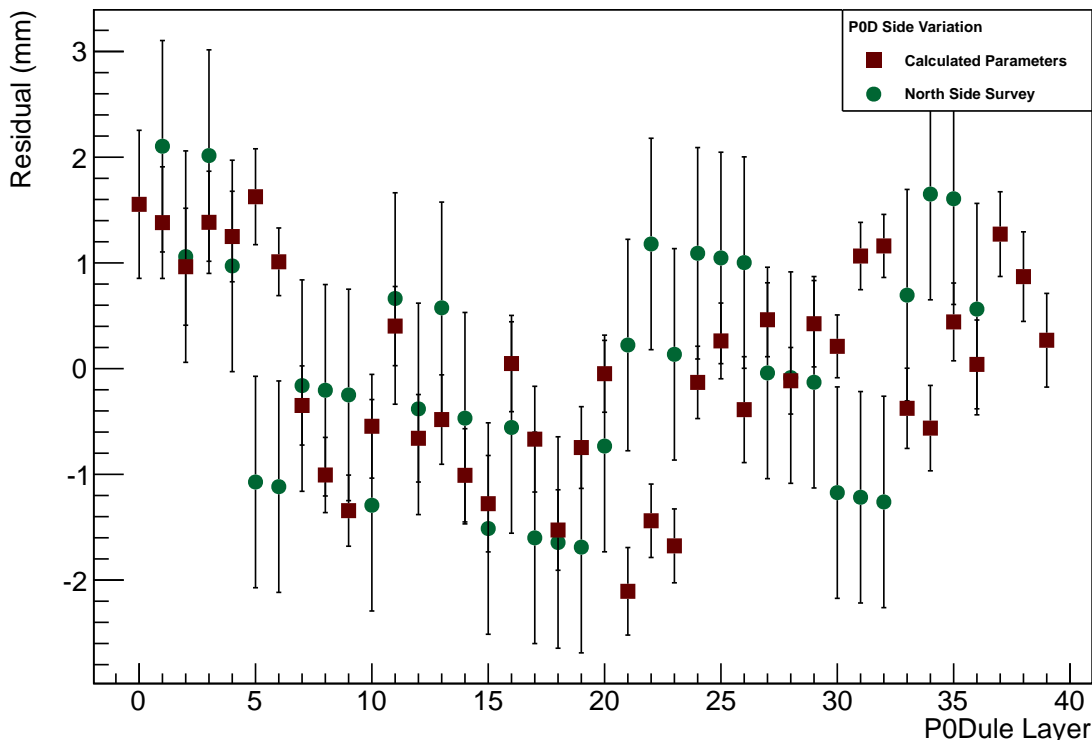


Figure 3.38: Measurements of the variation of the PØDules' X position along the north side of the PØD. The graph includes the survey along the north side (green circle) and the calculated parameters (red square) from the alignment procedure. The average of each set is artificially fixed at 0mm.

1159 **PØD North Side Survey**

1160 For this survey, the laser was set up along the north-west corner, arranged so that the
 1161 beam traveled along the north side of the PØD. Since there was no way to get a laser line
 1162 perfectly parallel to the side of the PØD, this was corrected by subtracting a linear offset
 1163 determined by the distances. This way, the average position of the side of the PØD would be
 1164 zero and the laser line could be artificially adjusted to be parallel to the PØD. Figure 3.38 is
 1165 the result of this manipulation. Overlaid on the survey results are the calculated parameters
 1166 from Figure 3.34.

Chapter 4

NC1 π^0 Rate Measurement

For this analysis, the signal is defined by the final state particles. The final state interactions remain uncorrected by the Monte Carlo. One π^0 particle is required to exit the nucleus with no other leptons or mesons. Any number of protons and neutrons are allowed to be present.

The goal of this analysis is three-fold. The first two goals are to find the ratios of data to Monte Carlo of the rate of NC1 π^0 events that occur on the P \emptyset D water target for both the P \emptyset D water-in and water-out configurations. The number of events in the P \emptyset D water-in and P \emptyset D water-out configurations are represented as $N_{NC1\pi^0, \text{Water-In}}$ and $N_{NC1\pi^0, \text{Water-Out}}$ respectively. These numbers are extracted using an unbinned extended maximum likelihood fit to the reconstructed π^0 invariant mass distribution. The last goal is to find the ratio of data to Monte Carlo of the rate of NC1 π^0 events, $N_{NC1\pi^0, \text{On-Water}}$, that occur on-water from a subtraction of the results of the water-in and water-out measurements.

The general formula for the number of observed events, N_{Obs} can be expressed as

$$N_{\text{Obs}} = \epsilon \cdot \phi \cdot \sigma \cdot t \cdot N_{\text{Target}}, \quad (4.1)$$

where ϵ is the efficiency, ϕ is the flux, σ is the cross section, t is the time exposure, and N_{Target} is the number of target nuclei. The total number of signal events in the water-in configuration can be divided into two parts,

$$N_{\text{Water-In}} = N_{\text{On-Water}} + N_{\text{Not-Water}}, \quad (4.2)$$

where $N_{\text{Not-Water}}$ is the number of single events that occur not on the water in the water-in configuration. This number can be related to the water-out configuration measurement, since the target and cross section are the same. Additionally, the flux times the exposure ϕt can simply be expressed as the number of incident neutrinos, N_ν . However, this number is proportional to the number of protons on target (POT). Given this information, the measurement for the number of signal events in the water-out configuration can be related to the number of not-water signal events in the water-in configuration as

$$\sigma_{\text{Not-Water}} N_{\text{Target, Not-Water}} = \frac{N_{\text{Not-Water}}}{\epsilon_{\text{Not-Water}} N_{\nu, \text{Not-Water}}} = \frac{N_{\text{Water-Out}}}{\epsilon_{\text{Water-Out}} N_{\nu, \text{Water-Out}}}. \quad (4.3)$$

Table 4.1: Summary of beam specifications used in the Monte Carlo generation.

Beam	Power (kW)	Repetition (s)	POT/Spill (x 10 ¹³)	Bunch	Duration (ns)
A	50	3.52	3.6617	6	17
B	120	3.2	7.9891	8	19
C	178	2.56	9.463	8	19

Table 4.2: Summary of Run 1 through Run 4 POT used in this analysis. The beam configurations listed reflect the Monte Carlo sample that is used to model the run.

Run	PØD Water Configuration	Beam Configuration	Run Numbers	POT
1	In	A	4165 - 5115	2.96×10^{19}
2	In	B	6462 - 7663	6.96×10^{19}
2	Out	B	7665 - 7754	3.59×10^{19}
3	Out	B	8360 - 8360	5.65×10^{15}
3	Out	C	8550 - 8753	1.35×10^{20}
4	In	C	8995 - 9413	1.65×10^{20}
4	Out	C	9426 - 9798	1.78×10^{20}

1192 This can be rearranged to

$$N_{\text{Not-Water}} = \frac{\epsilon_{\text{Not-Water}} N_{\nu, \text{Not-Water}}}{\epsilon_{\text{Water-Out}} N_{\nu, \text{Water-Out}}} N_{\text{Water-Out}} = \frac{\epsilon_{\text{Not-Water}} \text{POT}_{\text{Not-Water}}}{\epsilon_{\text{Water-Out}} \text{POT}_{\text{Water-Out}}} N_{\text{Water-Out}}. \quad (4.4)$$

1193 The number of POT for not-water is the same as the number of POT for the water-
 1194 in configuration. Finally, using the efficiencies calculated by the Monte Carlo, the POT
 1195 delivered for the run period, and the results of the fits, the number of on-water vertices can
 1196 be determined by

$$N_{NC1\pi^0, \text{On-Water}} = N_{NC1\pi^0, \text{Water-In}} - \frac{\epsilon_{\text{Not-Water}} \text{POT}_{\text{Not-Water}}}{\epsilon_{\text{Water-Out}} \text{POT}_{\text{Water-Out}}} N_{NC1\pi^0, \text{Water-Out}}. \quad (4.5)$$

1197 The final goal is to compare the data collected to the Monte Carlo prediction. To do this
 1198 a ratio of data to Monte Carlo is examined. The ratio of rates on water is defined as

$$R_{NC1\pi^0, \text{On-Water}} = \frac{N_{NC1\pi^0, \text{On-Water}}^{\text{Data}}}{N_{NC1\pi^0, \text{On-Water}}^{\text{MC}}}. \quad (4.6)$$

1199 This measurement was performed using NEUT Monte Carlo from Production 5E and
 1200 data collected from Run 1 to Run 4 processed with Production 5G. The measurement is
 1201 conducted with the intention of inclusion in the 2014 BANFF oscillation analysis.

1202 For the Monte Carlo simulation, there were three different beam configurations used,
 1203 explained in Table 4.1. Tables 4.2 and 4.3 summarize the POT used in this analysis and

Table 4.3: Summary NEUT Monte Carlo POT used in this analysis.

Run	Monte Carlo Configuration	Beam Configuration	POT
1	2010-02-water	A	9.98×10^{20}
2	2010-11-water	B	1.31×10^{21}
4	2010-11-water	C	4.87×10^{21}
2/3b	2010-11-air	B	1.00×10^{21}
3c	2010-11-air	C	3.01×10^{21}

relates the Run periods to specific beam configurations. It is important to note that the beam A configuration uses 6 bunches per spill where the other configurations use 8 bunches per spill, fundamentally the biggest difference. As such, beam A events are selected under a different pre-selection than those from later periods.

This analysis uses an extended maximum likelihood fit on the invariant mass of the final selected sample selected from 0 to 500 MeV/c². This invariant mass window is chosen in order to extend past the π^0 mass peak in order to be able to fit the shape of the background. The selected events also have a fixed angular cut due to detector reconstruction at $\cos \theta_z > 0.5$. Additionally, this angle was chosen as it describes a track that will cross two of the triangular bars in a layer. Tracks or showers that are perpendicular to the beam direction do not contain as much X-Z and Y-Z information to be reconstructed in three dimensions well. Additionally, the reconstruction always reconstructs a vertex upstream of any activity. It is therefore difficult to reconstruct downstream-going particles and resolving their directions and momentum. In order to provide a better constraint on the shape of the background, the μ -decay sideband invariant mass is fitted simultaneously.

This chapter is split into three main sections. The first section describes the reconstruction efficiencies and resolutions. The next section describes the event selection with the following section describing the selection of which cut to use for the sideband in the fit. Then the discussion moves to the construction of the fit and the results.

4.1 Reconstruction of the NC1 π^0

There were several reconstruction efficiencies of the NC1 π^0 search studied. Of primary concern is the vertex resolution which enters in to the systematic errors discussed in Chapter 5. Figures 4.1 and 4.2 show the vertex resolutions in x, y and z for the water-in and water-

Table 4.4: The vertex position resolution and mean for the saved NC1 π^0 events.

	$\langle x \rangle$ (cm)	σ_x (cm)	$\langle y \rangle$ (cm)	σ_y (cm)	$\langle z \rangle$ (cm)	σ_z (cm)
Water In	-0.06	5.52	0.06	6.06	1.67	8.65
Water Out	0.08	6.77	0.20	7.95	1.72	11.21

4.1. RECONSTRUCTION OF THE $\text{NC1}\pi^0$

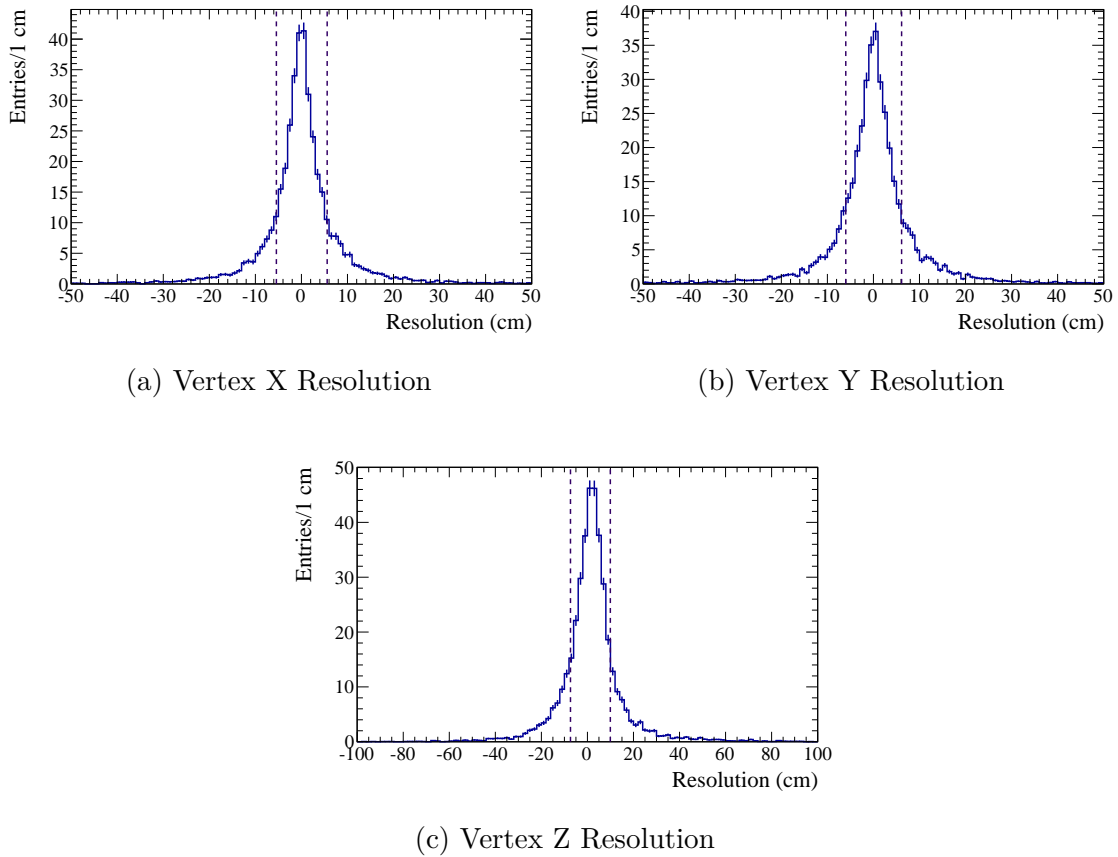


Figure 4.1: The $\text{NC1}\pi^0$ vertex resolution for the water-in configuration. The vertical lines correspond to the 16% and 84% quantiles.

4.1. RECONSTRUCTION OF THE $\text{NC1}\pi^0$

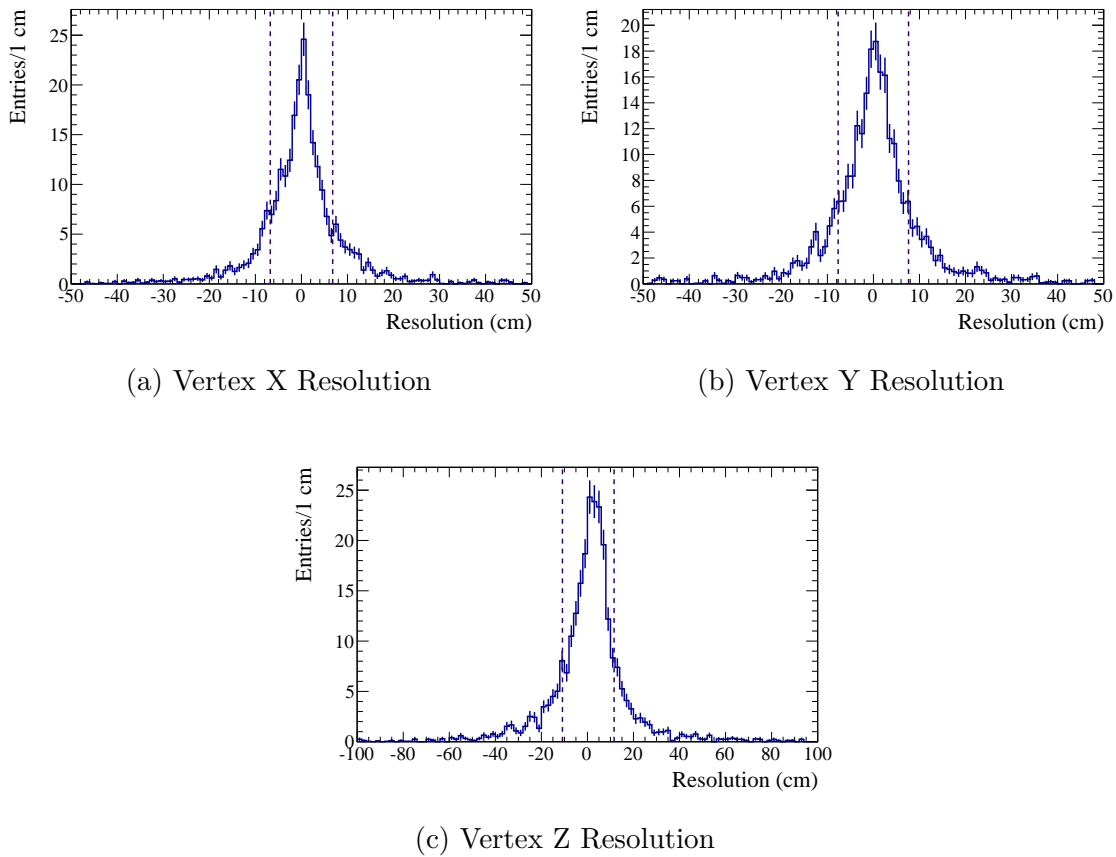


Figure 4.2: The $\text{NC1}\pi^0$ vertex resolution for the water-out configuration. The vertical lines correspond to the 16% and 84% quantiles

4.1. RECONSTRUCTION OF THE $\text{NC1}\pi^0$

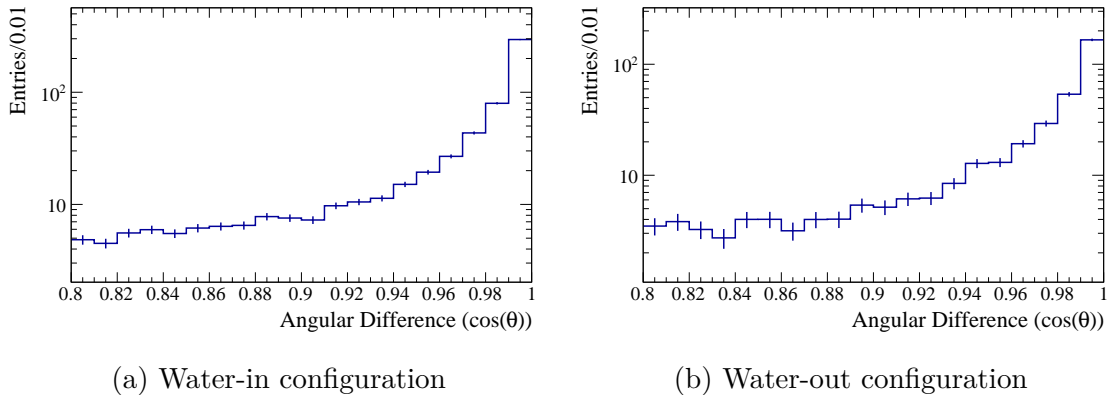


Figure 4.3: The angular difference between the decay photon reconstructed and true directions for selected signal events.

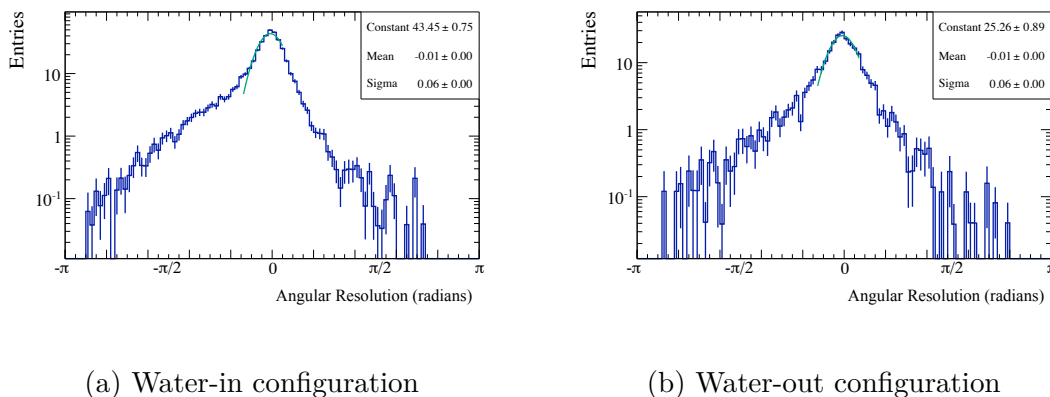


Figure 4.4: The $\text{NC1}\pi^0$ opening angle angle resolution fit to a Gaussian curve.

1227 out configurations of the $\text{P}\emptyset\text{D}$ respectively. The plots are from Monte Carlo studies looking
 1228 at the true $\text{NC1}\pi^0$ events that pass all selection cuts. Due to the non-Gaussian nature of
 1229 the distributions, resolutions were found by taking half the distance from the 16% and 84%
 1230 quantiles which is equivalent to the probability contained in 1σ of a Gaussian distribution.
 1231 They are summarized in Table 4.4.

1232 In addition to the vertex resolution, the $\text{NC1}\pi^0$ photon reconstruction was examined. In
 1233 Figure 4.3, there is sharp peak at $\cos\theta = 1$, θ is the angular difference between the true
 1234 and reconstructed angle. This shows that the decay photons are well reconstructed, thus the
 1235 opening angle is also well reconstructed. Figure 4.4 shows the resolution of the reconstructed
 1236 opening angle in radians. For the $\text{P}\emptyset\text{D}$ water-in configuration, a Gaussian fit gives a mean
 1237 of -0.008 ± 0.001 radians and a sigma of 0.062 ± 0.001 radians. For $\text{P}\emptyset\text{D}$ water-out, the fit
 1238 gives a mean of -0.008 ± 0.002 radians and a sigma of 0.064 ± 0.003 radians.

1239 The momentum resolution of the π^0 was studied as well. In Figure 4.5, the distribution of
 1240 the fractional momentum resolution (the difference of the reconstructed and true momenta

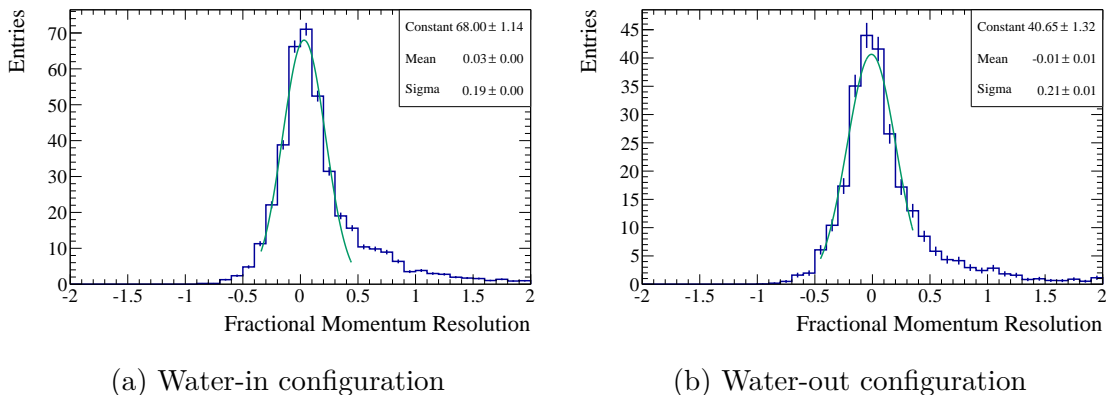


Figure 4.5: The NC1 π^0 fractional momentum resolution is shown fit to a Gaussian distribution here for selected signal events.

1241 divided by the true momentum) was fit to a Gaussian. The mean of the Gaussian is $-3.2 \pm$
 1242 0.3% with a sigma of $18.7 \pm 0.3\%$ for the water-in P \emptyset D. For the P \emptyset D water-out configuration,
 1243 the mean is $-0.8 \pm 0.6\%$ with a sigma of $21.1 \pm 0.6\%$. The means of these fits are considered
 1244 sufficiently close to zero for the energy reconstruction to be considered accurate. The sigmas
 1245 of the fits can be considered as the resolution of the energy.

1246 4.2 Event Selection

1247 The signature of interest is two reconstructed electromagnetic-like objects that are as-
 1248 sumed to be the resulting photons of a π^0 decay after an NC1 π^0 interaction. A cut selection
 1249 was developed in order to emphasize the shape difference between the signal invariant mass
 1250 and the background invariant mass. Motivation for each cut is described below, followed by
 1251 a discussion of how the optimization of the cuts is performed.

1252 This analysis uses the output from the package oaAnalysis and only the reconstruction
 1253 information from p \emptyset dRecon. A description of p \emptyset dRecon is presented in Section 3.3. For
 1254 this analysis, the output of the cycle reconstruction is used, an event is therefore defined as
 1255 a cycle with a reconstructed vertex. Events are split into seven categories: NC1 π^0 , other
 1256 neutral current, charged current with one π^0 , other charged current, events with external
 1257 vertices, events with multiple interactions and noise. Colors listed in parentheses correspond
 1258 to Figures 4.6 to 4.12. There are four categories representing physical interactions of interest
 1259 in the P \emptyset D.

- 1260 • NC1 π^0 (Light Violet)- Signal events. The final state of this interaction contains one
 1261 exiting π^0 , any number of exiting baryons and no other exiting particles.
- 1262 • NC Other (Yellow Green)- This background contains all other neutral current events
 1263 defined by no exiting charged leptons.
- 1264 • CC1 π^0 (Pink)- These events contain a single exiting muon and a single exiting pion.

4.2. EVENT SELECTION

Table 4.5: Definition of the P \emptyset D fiducial volume. Column 2 shows the center position for all three dimensions in global coordinates. Column 3 shows the half-widths of the box. Columns 3 and 4 give the minimum and maximum positions.

Coordinate	Center (mm)	Half-Width (mm)	Minimum (mm)	Maximum (mm)
X	-36	800	-836	764
Y	-1	870	-871	869
Z	-2116	852.5	-2969	-1264

- 1265 • CC Other (Green)- All other events with a charged lepton exiting the nucleus.

1266 In addition to these physics categories, there are categories based on the topologies of the
 1267 events. Since this is a P \emptyset D only analysis, events that originate in the P \emptyset D are examined, thus
 1268 any external events are placed in the background sample. The cleanest set of reconstruction
 1269 results is desired, so a single true vertex in each cycle of p \emptyset dRecon is required. Lastly, the
 1270 Production 5 Monte Carlo has implemented a more accurate estimation of the noise that
 1271 will be present in the data. The noise is defined as any event that has reconstructed P \emptyset D
 1272 information, but no true vertex, or the true vertex is not found. A true vertex may not
 1273 be saved if it occurs far outside the detector or if it doesn't have any daughter trajectories
 1274 that leave an energy deposit in the P \emptyset D. Plots are examined that display a cut variable's
 1275 distribution for events passing all cuts with the cut of interest not applied. These are called
 1276 N-1 plots. For cleaner and clearer plots, the N-1 plots are produced with a single other
 1277 category (Blue) that contains the external vertices, the noise, and the multi-vertex events.

1278 There are eight selection cuts implemented: preselection, fiducial volume, P \emptyset D contain-
 1279 ment, muon decay, charge in shower, PID, π^0 direction and shower separation. Three of the
 1280 cuts are considered optimizable due to semi-continuous natures: charge in shower, shower
 1281 separation, and PID weight. Several optimization methods were considered, the one chosen
 1282 is explained after the cuts are described. First, a flat tree is constructed that saves all events
 1283 with P \emptyset D activity. In the flat tree, all the cut variables are calculated for each event as well
 1284 as any auxiliary information we consider necessary.

1285 The first cut is a preselection cut. A single 3D vertex in the P \emptyset D is required. For Run
 1286 1, each beam spill contained six bunches. At the start of Run 2, this was increased to
 1287 eight bunches per spill. For the rest of the running period, the beam has been sent in eight
 1288 bunches. For the event to be a beam event, the vertex must occur within the spill window,
 1289 which corresponds to cycles 4 to 9(11) for Run 1(2-4) of the detector readout.

1290 The next cut is that the 3D vertex is in the fiducial volume, shown in Figure 4.6. This
 1291 cut is necessary to have fewer reconstruction failures, less energy leakage and better vertex
 1292 resolution. The fiducial volume is defined in Table 4.5, originally considered as ~ 25 cm
 1293 from the edge of the active volume. This volume is described and motivated in Section 3.1.

1294 In addition to the fiducial volume cut, a containment cut was constructed. In order
 1295 to accurately reconstruct the charge deposited from the event in the detector, we require
 1296 that it does not leave the P \emptyset D. In p \emptyset dRecon, exiting particles are treated differently from

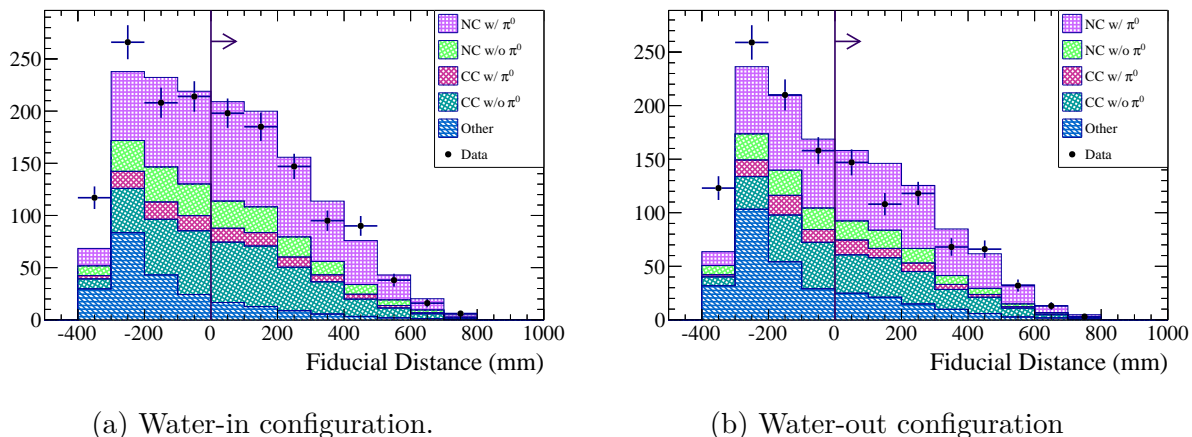


Figure 4.6: The N-1 plots of the fiducial volume cut, area normalized to emphasize any shape differences. The fiducial volume parameter is calculated as the minimum distance between the vertex and a fiducial boundary. Positive values indicate that the vertex is inside the fiducial volume. The cut value is set at 0 mm.

1297 contained particles with respect to reconstruction and particle identification. The particle
 1298 identification present in Production 5 is not as well understood for exiting particles. The
 1299 same exiting definition as the reconstruction is used. Any particle that has a hit in the last
 1300 layer of the P \emptyset D or in the outer two bars of any layer that is above a 2 PEU threshold is
 1301 considered as exiting.

1302 In order to remove charged current ν_μ events, a muon decay cut is employed, shown in
 1303 Figure 4.7. For this selection, each cycle during and after the main event was examined for
 1304 a muon decay cluster. The original algorithm to find these decay clusters was developed by
 1305 Phoc Trung Le [28]. If a muon decay cluster is found in or after the time of the vertex of
 1306 interest, the event is discarded.

1307 In order to compensate for reconstruction of separate delta rays or any other recon-
 1308 struction inefficiencies, a cut was constructed on the fraction of event charge in the two
 1309 decay gamma candidates. In order to do this, we loop through every particle (both re-
 1310 constructed tracks and showers) reconstructed in the event, which is then the total event
 1311 charge $Q_{tot} = \sum Q_{shower} + \sum Q_{track}$. The decay photon candidates are considered to be up
 1312 to two reconstructed showers with the greatest amount of deposited charge in the event
 1313 $Q_{\gamma\gamma} = \sum_1^2 Q_{shower}$. The N-1 cut distribution for the shower charge, $Q_{\gamma\gamma}/Q_{tot}$, is shown in
 1314 Figure 4.8.

1315 Until this point, only the information on whether a particle was reconstructed as a shower
 1316 is necessary. At the shower reconstruction stage of p \emptyset dRecon, after the tracks have been
 1317 removed, there are two possible particle identifications, kEM (photons and electrons) and
 1318 kOther (not EM particles). The parameter of interest for cutting on this particle identi-
 1319 fication is the difference of the log likelihoods of the EM and Other shower PIDs. The
 1320 distribution of this parameter is shown in Figure 4.9.

1321 The π^0 direction cut is based on detector performance. In general, due to the P \emptyset D

4.2. EVENT SELECTION

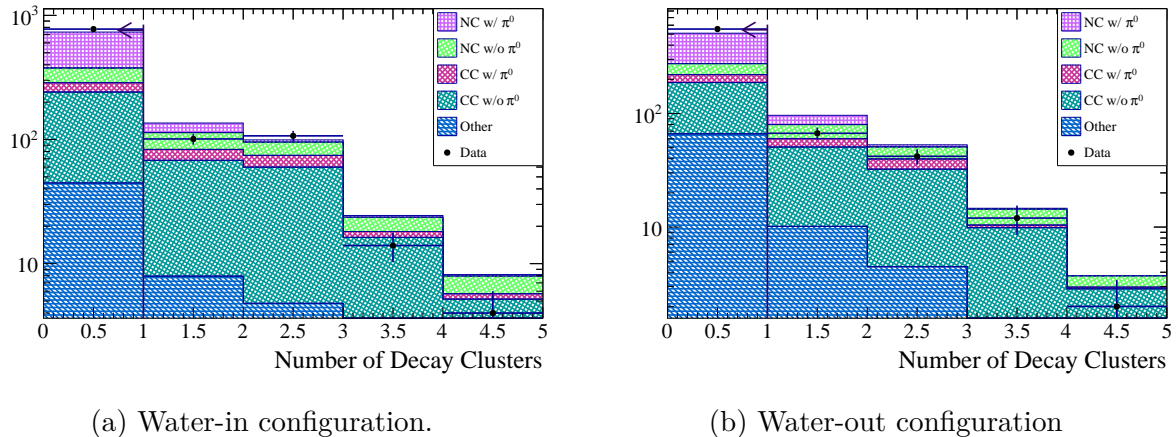


Figure 4.7: The N-1 plots of the muon decay cut, area normalized to emphasize any shape differences.

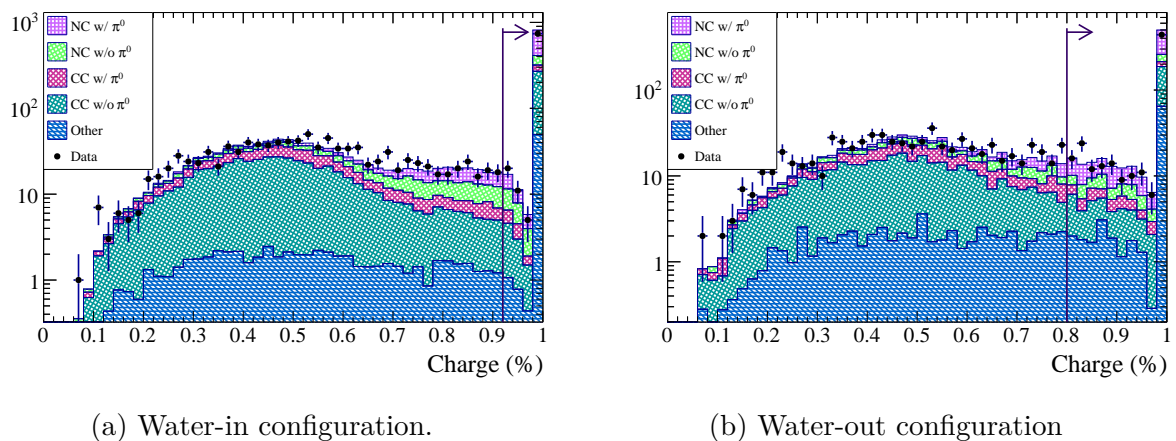


Figure 4.8: The N-1 plots of the event shower charge distribution cut, area normalized to emphasize any shape differences. To pass this cut 92% of the charge must be EM-like for the P \emptyset D water-in configuration. For the P \emptyset D water-out configuration, the cut is placed at 80%.

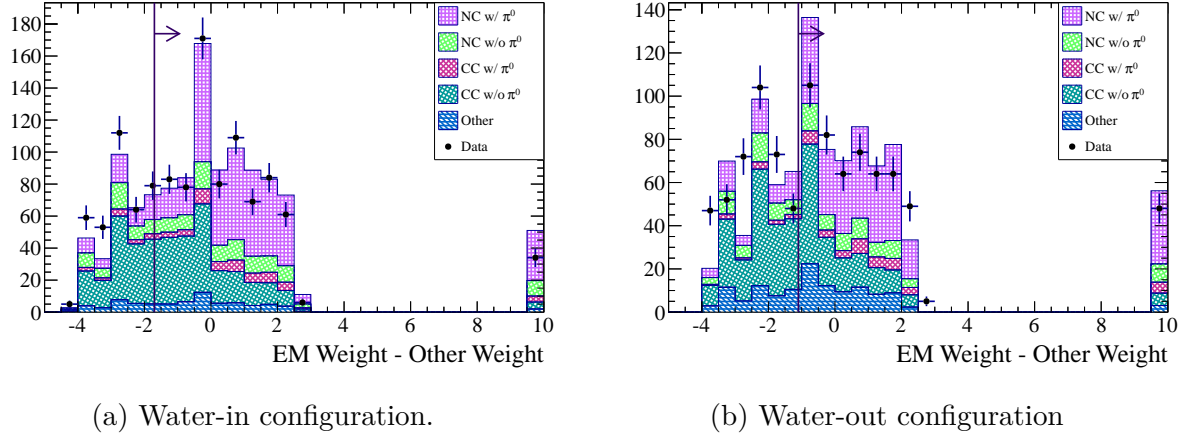


Figure 4.9: The N-1 plots of the PID weight cut, area normalized to emphasize any shape differences. The events that fall in the last bin are a special case from the reconstruction that will always be labelled as EM particles. The cut value is set at -1.7 for the P \emptyset D water-in configuration and -1.1 for the P \emptyset D water-out configuration.

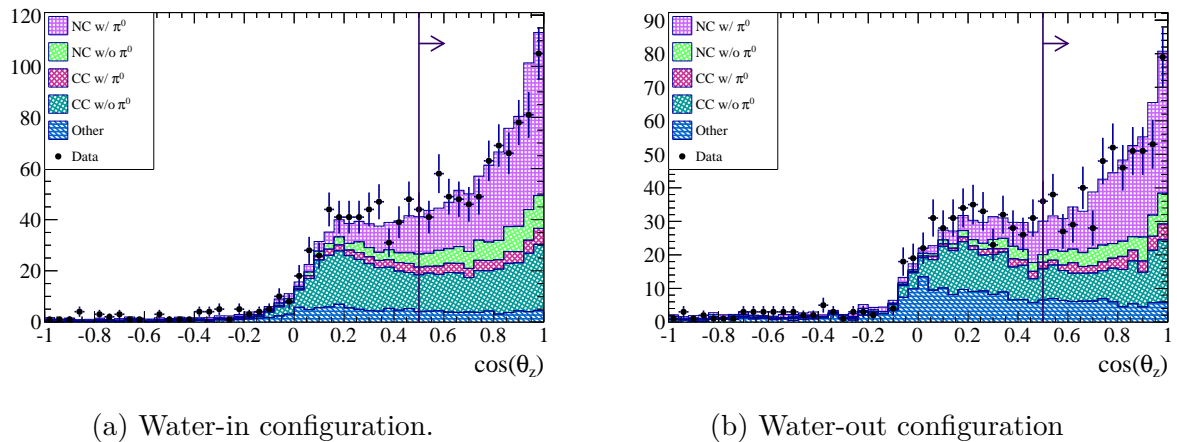


Figure 4.10: The N-1 plots of the π^0 direction cut, area normalized to emphasize any shape differences. The cut value is set at $\cos \theta > 0.5$.

4.2. EVENT SELECTION

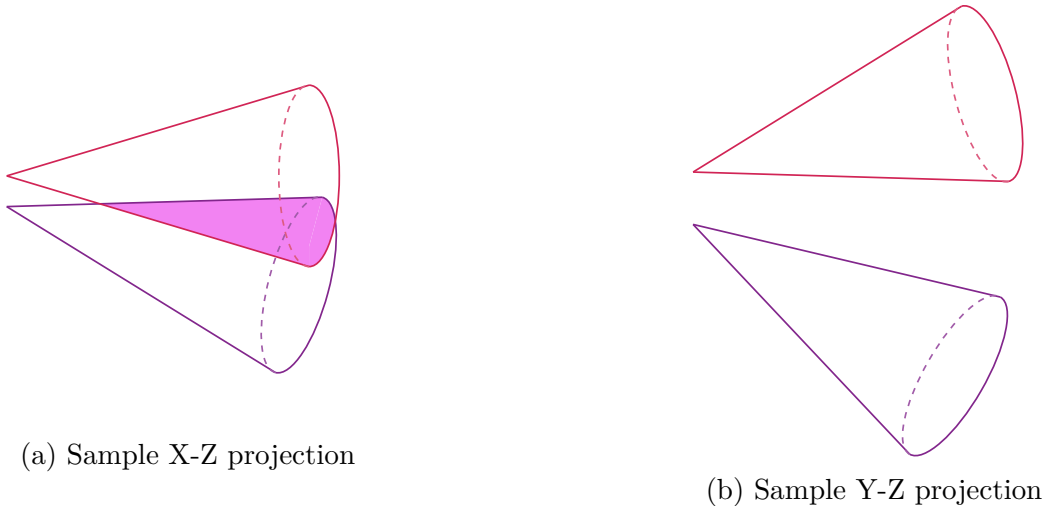


Figure 4.11: In Subfigure 4.11a, the two dimensional projections of the 3D showers overlap. The hit distances calculated in that projection will be at most the size of one or two bars. However, the showers are completely separated in 3D, which is apparent in the Y-Z projection shown in Subfigure 4.11b.

1322 geometry, the reconstruction performs well up to 75° from the z axis. As such, we fixed the
 1323 direction of the π^0 to be less than 60° from the z axis or $\cos\theta_z > 0.5$, as shown in Figure
 1324 4.10.

1325 Part of the ability to reconstruct two complete decay photons depends on the separation
 1326 between the two reconstructed objects. In order to get the cleanest reconstruction result,
 1327 a cut on the separation of the decay photon candidates is imposed. This cut is calculated
 1328 by finding the distance between the two closest hits of the photon showers, ignoring hits
 1329 with less than 2 PEU, in the X-Z and Y-Z dimensions. Since it is possible to reconstruct
 1330 two separate three dimensional objects when the two dimensional projections overlap, the
 1331 maximum of the X-Z and Y-Z distances is taken as the cut variable, see Figure 4.11. The
 1332 distribution for this variable is shown in Figure 4.12.

1333 At this point, there are three tunable cuts: charge in shower, shower separation, and
 1334 particle identification weight. An optimization had to be performed for both water-in and
 1335 water-out configurations using a sample that has already passed all other cuts. The final
 1336 goal of the optimization was to assure that there would be two distinct invariant mass
 1337 distributions, one for the signal and one for the background, which can then be fit. The
 1338 figure of merit chosen was $\pi^2 \cdot \epsilon$, where π is the purity and ϵ is the efficiency, in order to
 1339 have an optimization parameter that emphasizes the shape differences in the invariant mass.
 1340 The optimization method was focused on optimizing the π^0 mass peak window, 90 MeV to
 1341 170 MeV. In addition, π^0 particles with a momentum larger than 200 MeV comprise the ν_e
 1342 appearance background in Super-K that are of the most interest.

1343 A histogram with three axes, one for each of the optimizable cuts, was constructed. For
 1344 the PID weight difference, based on the initial distribution of the tuning histograms, a range
 1345 of possible cuts from -4.0 to 4.0 at 0.1 intervals was studied. For the shower separation cut,
 1346 cuts from 0 to 150 mm at 10 mm intervals were studied. Note that the width of a bar is

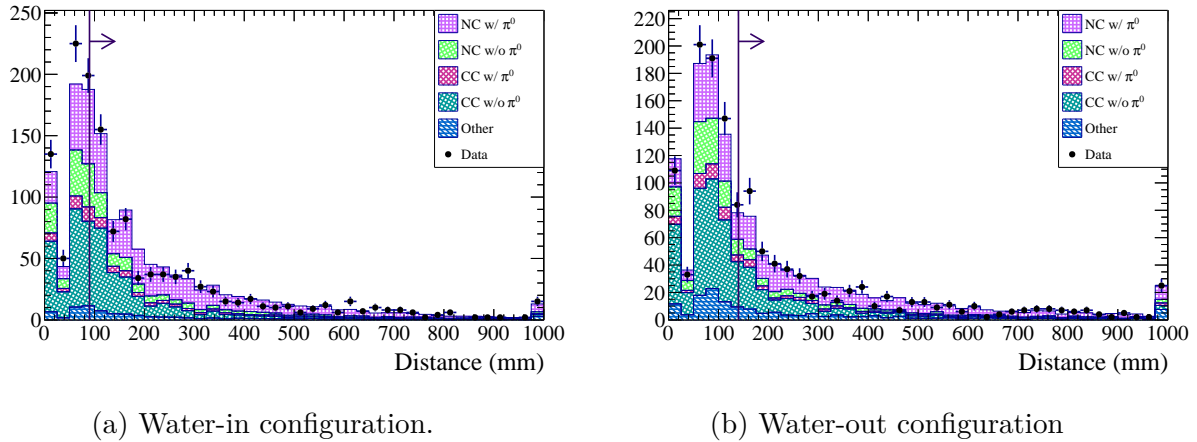
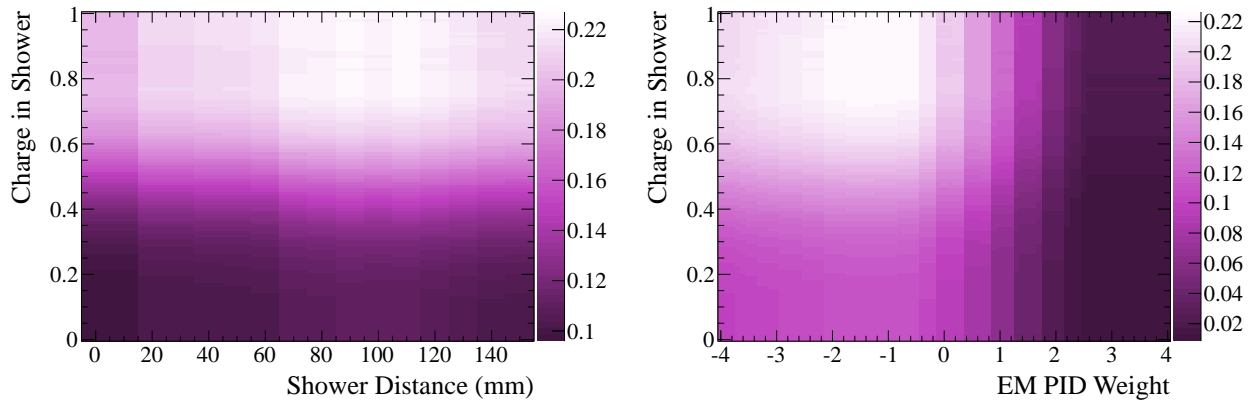


Figure 4.12: The N-1 plots of the shower separation cut, area normalized to emphasize any shape differences. The cut value is set at 90 mm for the P \emptyset D water-in configuration and 140 mm for the P \emptyset D water-out configuration.

1347 approximately 16 mm, so the step size was small enough to see each bar interval. Lastly, the
 1348 shower charge cut values encompassed the entire possible range, 0.0 to 1.0 at 0.01 intervals.
 1349 Using a subsample of the Monte Carlo events that pass all but these three cuts the figure
 1350 of merit (the efficiency times the square of the purity) is calculated for each bin. The bin
 1351 position of the maximum value was then used as the optimized cut values.

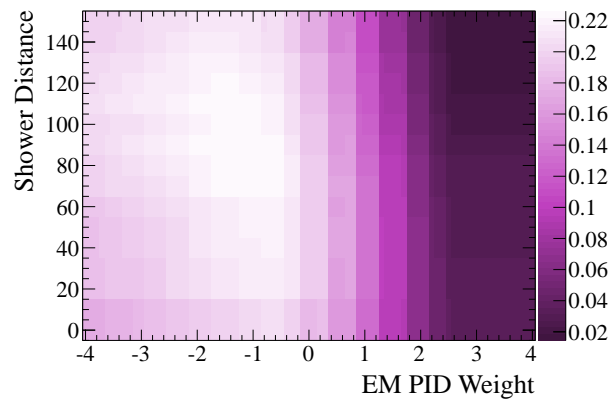
1352 There is a dependence on the energy scale within this optimization. The energy scale
 1353 did undergo a reevaluation to improve the energy conversion at low energies. It was decided
 1354 to preserve the cuts as optimized before looking at the data. The optimization method is
 1355 highly sensitive to statistical fluctuations. To show that the previous optimized cuts are still
 1356 applicable, the two dimensional projections at the cut values of the three dimensional figure
 1357 of merit histogram are shown in Figures 4.13 and 4.14. The cut values fall on the maximum
 1358 plateaus of the two dimensional projections and are therefore held as still applicable.

4.2. EVENT SELECTION



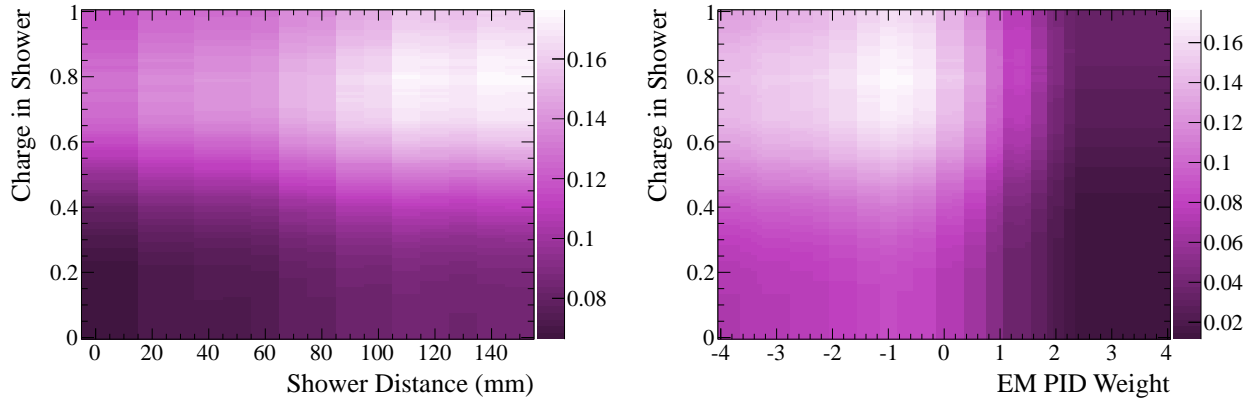
(a) Two dimensional comparison of the charge in shower and shower separation cuts with the particle identification cut fixed at -1.7.

(b) Two dimensional comparison of the charge in shower and particle identification cuts with the shower separation cut fixed at 90 mm.



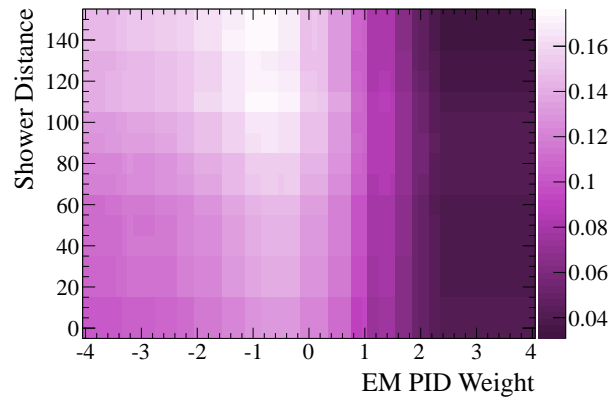
(c) Two dimensional comparison of the shower separation and particle identification cuts with the percent of charge in showers fixed at 92%.

Figure 4.13: The chosen significance, $\pi^2 \cdot \epsilon$, distributions over the ranges for the cut values for the water-in configuration. Each plot shows the 2D projection of the 3D optimization space at a fixed optimized cut. These plots show the figure of merit calculated from the revamped PEU to MeV energy conversion.



(a) Two dimensional comparison of the charge in shower and shower separation cuts with the particle identification cut fixed at -1.1.

(b) Two dimensional comparison of the charge in shower and particle identification cuts with the shower separation cut fixed at 140 mm.



(c) Two dimensional comparison of the shower separation and particle identification cuts with the percent of charge in showers fixed at 80%.

Figure 4.14: The chosen significance, $\pi^2 \cdot \epsilon$, distributions over the ranges for the cut values for the water-out configuration. Each plot shows the 2D projection of the 3D optimization space at a fixed optimized cut. These plots show the figure of merit calculated from the revamped PEU to MeV energy conversion.

4.3 Sideband Selection

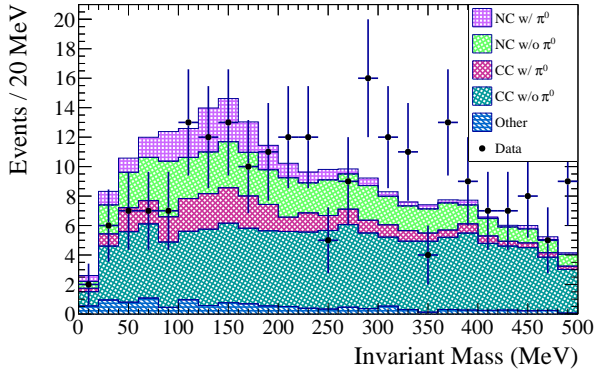
There are several possibilities for a sideband selection. In order to pick the best sideband to use in simultaneous fit to constrain the backgrounds in the various possibilities are compared. In the end, the muon decay sideband was chosen for use in the simultaneous fit because it has relatively low purity and a similar background composition to that in the selected events. There are eight cuts and eight possible $N - 1$ sidebands. Three of the cuts are discarded, Preselection, Fiducial Volume and Containment, due to the lack of information present in the sideband and the unknown nature of the data to Monte Carlo comparisons. The π^0 direction cut is based on reconstruction efficiencies so its sideband is also not well understood. The remaining possible sidebands are compared in three ways. First, the shape of the sidebands between data and Monte Carlo is compared. Without a reasonable shape match, these sidebands will not be useful to constrain the shape of the background. Figures 4.15 through 4.18 show the area normalized comparisons of the data to the Monte Carlo.

The second item to check is to compare the content of the sideband background and the selected region background. Tables 4.6 and 4.8 show the composition of the background. The composition of the muon decay sideband most closely matches with the content of the background of the selected region. Tables 4.7 and 4.9 list the purities of the different sidebands. It is best to focus on a low signal purity sideband in order to remove the interaction intended for measurement. The goal of the sideband is to effectively constrain the cross section of the background. As such, the sidebands comparing the PID weight, the reconstructed direction of the π^0 , and the shower separation, may not be ideal samples. Although the charge in shower sideband has a relatively low purity, the content of this sideband is heavily influenced by the $CC1\pi^0$ channel.

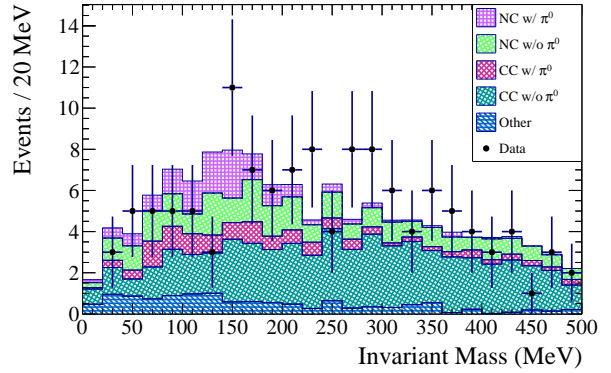
The third item of interest is to compare the shapes of the sideband background and the selected region background. Figures 4.19 through 4.22 show the area normalized Monte Carlo predictions of the backgrounds in the selected region and the sideband regions. Visually, the muon decay sideband, Figure 4.19, most closely matches the shape of the selected region background. In addition, the muon decay sideband is composed of the same types of interactions as the selected region background. As such, the muon decay sideband is used to constrain the selected region background in this analysis.

Table 4.6: For the $P\emptyset D$ water-in configuration, the summary of the composition of the background of the sidebands for events with a reconstructed invariant mass less than 500 MeV. For comparison, the first row contains the composition of the selected events. All numbers are in terms of the percent of the total background.

Sideband	NC Other (%)	CC π^0 (%)	CC Other (%)	External (%)	Multiple (%)	Noise (%)
Selected	23.9 ± 0.2	12.1 ± 0.1	52.1 ± 0.2	8.6 ± 0.1	3.3 ± 0.0	0.0 ± 0.0
Muon Decay	24.8 ± 0.2	13.3 ± 0.1	56.1 ± 0.3	3.1 ± 0.0	2.7 ± 0.0	0.0 ± 0.0
Shower Charge	16.0 ± 0.1	20.2 ± 0.1	56.6 ± 0.2	3.3 ± 0.0	3.9 ± 0.0	0.0 ± 0.0
PID Weight	19.1 ± 0.2	5.6 ± 0.1	65.4 ± 0.3	7.5 ± 0.1	2.3 ± 0.0	0.0 ± 0.0
Nearest Shower	26.6 ± 0.2	7.8 ± 0.1	58.3 ± 0.3	5.4 ± 0.1	1.9 ± 0.0	0.0 ± 0.0

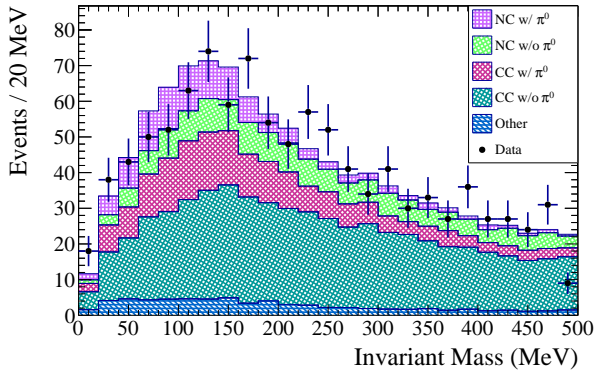


(a) Water-in configuration.

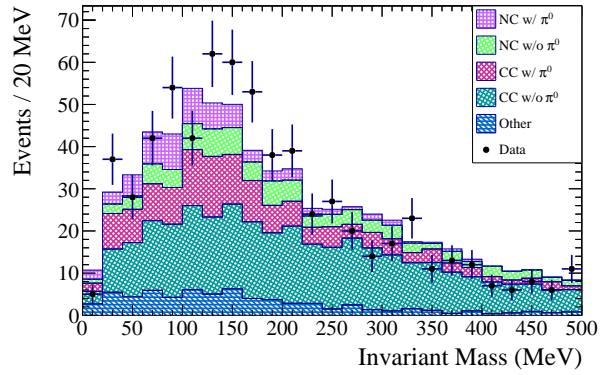


(b) Water-out configuration

Figure 4.15: The comparison between the area normalized muon decay sideband data and Monte Carlo.



(a) Water-in configuration.



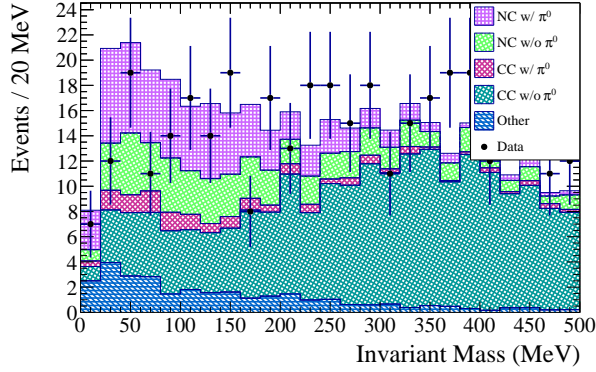
(b) Water-out configuration

Figure 4.16: The comparison between the area normalized charge in shower sideband data and Monte Carlo.

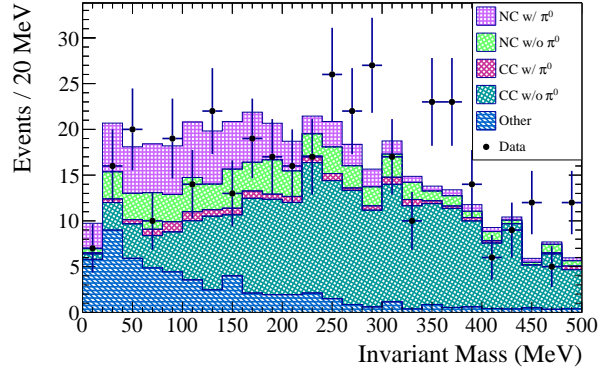
Table 4.7: For the P0D water-in configuration, the summary of the purities in the sideband selections for a reconstructed invariant mass less than 500 MeV. For comparison, the selected event purity is listed in the first column. All numbers are in percent.

Selected	Muon Decay (%)	Shower Charge (%)	PID Weight (%)	Nearest Shower (%)
48.7 ± 0.2	10.1 ± 0.1	10.4 ± 0.1	19.0 ± 0.2	26.7 ± 0.2

4.3. SIDEBAND SELECTION

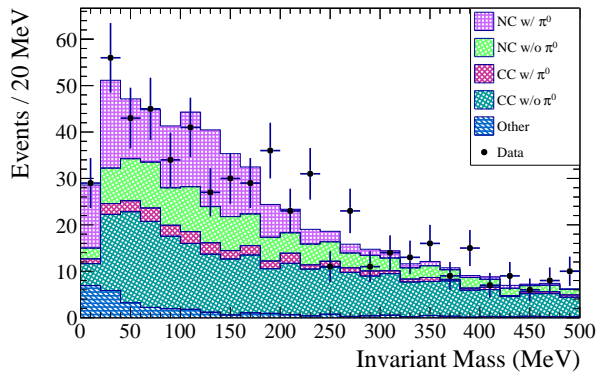


(a) Water-in configuration.

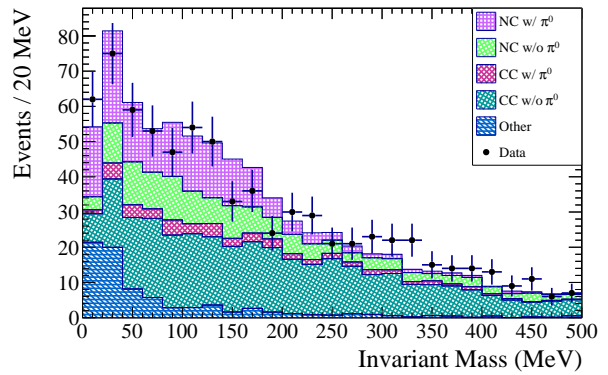


(b) Water-out configuration

Figure 4.17: The comparison between the area normalized PID weight sideband data and Monte Carlo.



(a) Water-in configuration.



(b) Water-out configuration

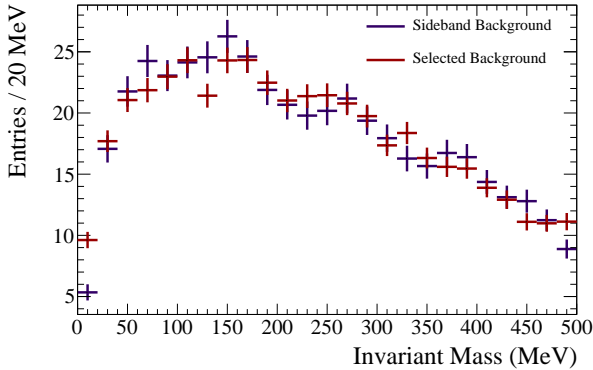
Figure 4.18: The comparison between the area normalized shower separation sideband data and Monte Carlo.

Table 4.8: For the P \emptyset D water-out configuration, the summary of the composition of the background of the sidebands for events with a reconstructed invariant mass less than 500 MeV. For comparison, the first row contains the composition of the selected events. All numbers are in terms of the percent of the total background.

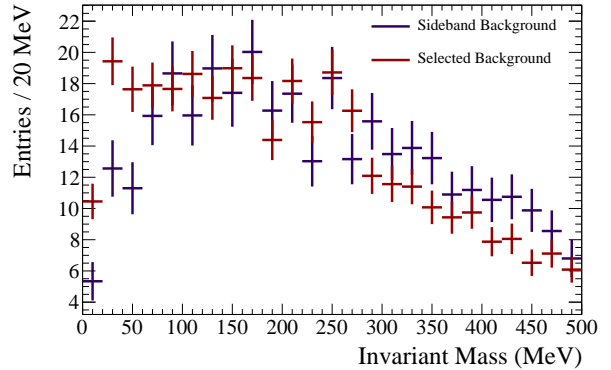
Sideband	NC Other (%)	CC π^0 (%)	CC Other (%)	External (%)	Multiple (%)	Noise (%)
Selected	20.0 ± 0.3	11.8 ± 0.2	44.1 ± 0.4	20.8 ± 0.3	3.3 ± 0.1	0.0 ± 0.0
Muon Decay	24.1 ± 0.4	11.6 ± 0.2	53.5 ± 0.6	7.3 ± 0.2	3.6 ± 0.1	0.0 ± 0.0
Shower Charge	13.6 ± 0.2	22.4 ± 0.2	52.7 ± 0.3	6.2 ± 0.1	5.1 ± 0.1	0.0 ± 0.0
PID Weight	16.5 ± 0.3	3.8 ± 0.1	62.3 ± 0.4	15.0 ± 0.2	2.3 ± 0.0	0.0 ± 0.0
Nearest Shower	22.5 ± 0.2	7.4 ± 0.1	56.6 ± 0.3	11.3 ± 0.1	2.2 ± 0.0	0.0 ± 0.0

Table 4.9: For the P \emptyset D water-out configuration, the summary of the purities in the sideband selections for a reconstructed invariant mass less than 500 MeV. For comparison, the selected event purity is listed in the first column. All numbers are in percent.

Selected	Muon Decay (%)	Shower Charge (%)	PID Weight (%)	Nearest Shower (%)
46.1 ± 0.3	11.2 ± 0.2	9.5 ± 0.1	17.3 ± 0.2	22.7 ± 0.2



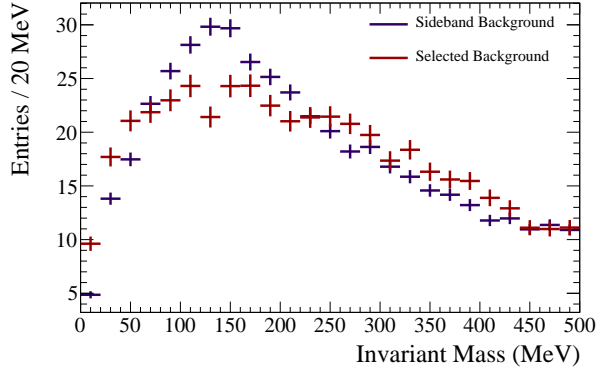
(a) Water-in configuration.



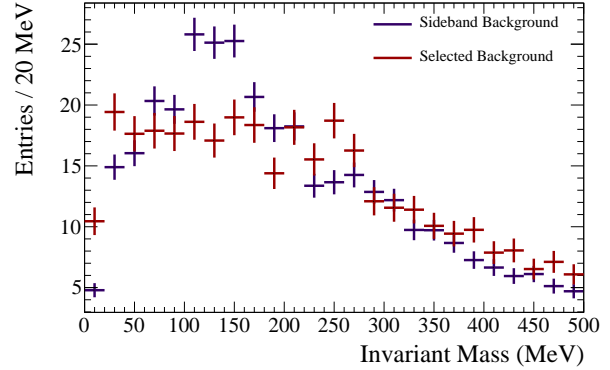
(b) Water-out configuration

Figure 4.19: The comparison between the area normalized selected region predicted background and the muon decay sideband predicted background.

4.3. SIDEBAND SELECTION

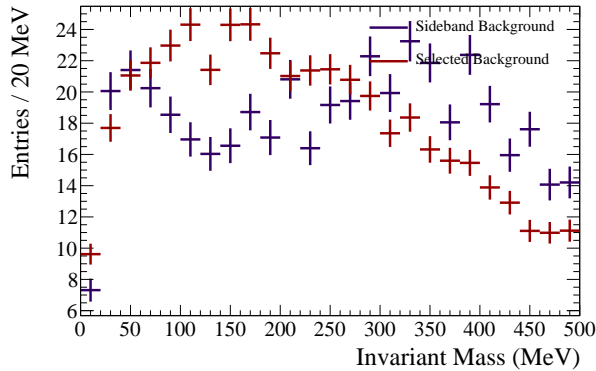


(a) Water-in configuration.

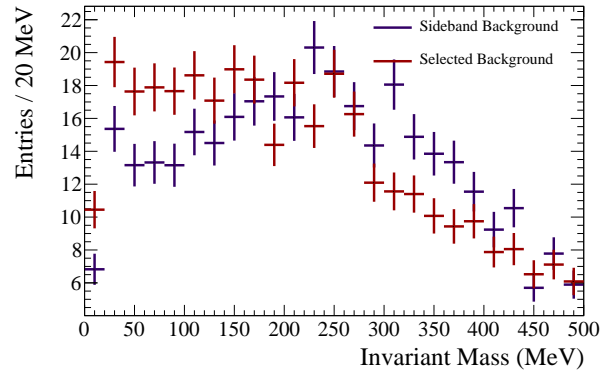


(b) Water-out configuration

Figure 4.20: The comparison between the area normalized selected region predicted background and the charge in shower sideband predicted background.



(a) Water-in configuration.



(b) Water-out configuration

Figure 4.21: The comparison between the area normalized selected region predicted background and the PID weight sideband predicted background.

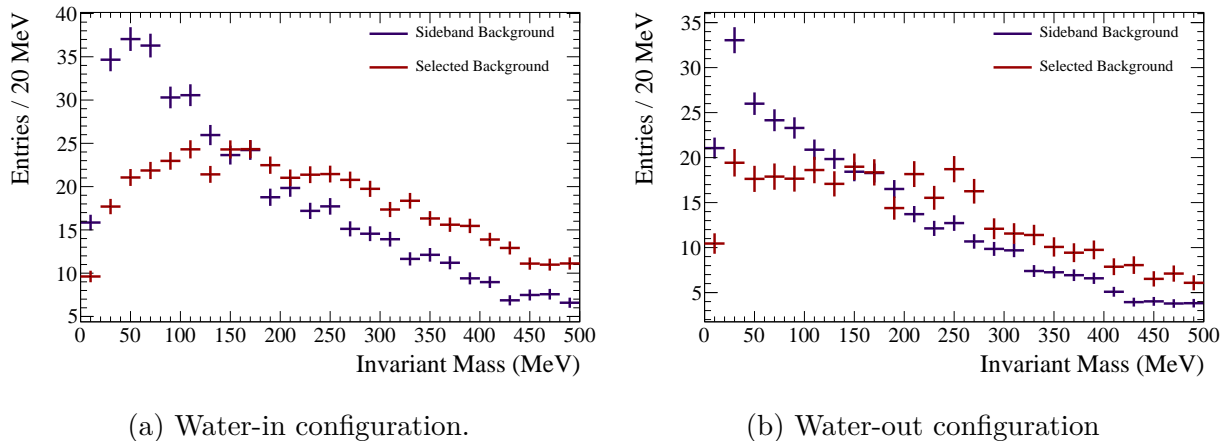


Figure 4.22: The comparison between the area normalized selected region predicted background and the shower separation sideband predicted background.

4.4 Analysis

The event signature of the search is that of two photons, the π^0 decay signature. In order to examine those photons, the invariant mass, $M_{\gamma\gamma}$ is reconstructed using

$$M_{\gamma\gamma} = \sqrt{2E_{\gamma_1}E_{\gamma_2}(1 - \cos\theta_{\gamma\gamma})}, \quad (4.7)$$

where E_{γ_i} is the energy of the i th photon and $\theta_{\gamma\gamma}$ is the angle between the decay photons. The invariant mass of the two photons would ideally match the mass of the π^0 particle, 135.0 MeV. The equation depends on the reconstructed energy of the two decay photon candidates and their opening angle. Hence the invariant mass peak will be smeared due to reconstruction inefficiencies. Figure 4.23 shows the area normalized result of the selection.

4.4.1 Final Sample Cross Checks

Tables 4.10 and 4.11 summarize the effect of each cut on the final sample of NC1 π^0 candidate events. The tables contain the number of data events passing each cut as well as the number of simulated events and the number of simulated signal events that make it into the final sample. There is a discrepancy in the efficiency of the fiducial volume cut that is due to sand muons not being modeled in the default NEUT Monte Carlo.

Tables 4.12 and 4.13 show the breakdown of the signal and background present in the final Monte Carlo sample. Tables 4.14 and 4.15 show the breakdown of the signal and background present in the final Monte Carlo muon decay sideband sample. Table 4.16 describes the composition of the events that are used in the analysis that have a reconstructed invariant mass above 500 MeV. All event numbers in Tables 4.10 through 4.16 have been reweighted by the P0D fiducial mass difference between data and Monte Carlo, the relative data and Monte Carlo POT, and by the flux, using version 11b 3.2 released by the beam group.

There are two efficiencies quoted in Table 4.17. The first, ϵ_{ff} , is introduced as an absolute efficiency of the final selected sample compared to the total number of NC1 π^0 events

4.4. ANALYSIS

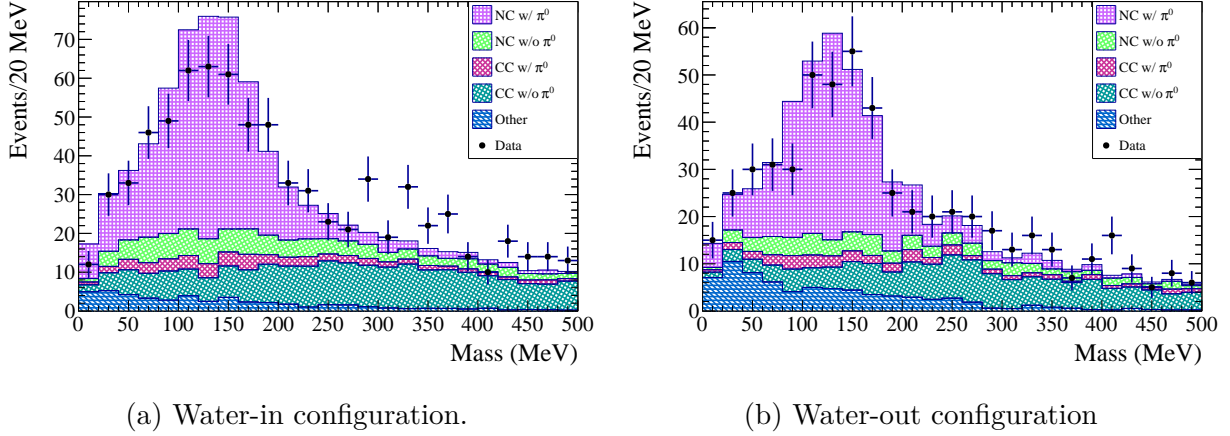


Figure 4.23: The distribution of the invariant mass of the selected events.

Table 4.10: The number of events passing each cut for the P \emptyset D water-in configuration. The first column lists the cut variable names, the second gives the number of events found in the detector. The third and fourth column show the number of events predicted in the Monte Carlo and its relative efficiencies. The last two column show the number of signal events predicted in the Monte Carlo and its relative efficiencies.

Cut	Events	Rel. Eff (%)	Expected	Rel. Eff (%)	Signal	Rel. Eff (%)
Preselection	1255802	N/A	643150.9	N/A	15208.7	N/A
Fiducial	149099	11.9	159698.7	24.8	5857.0	38.5
Contained	121505	81.5	129904.5	81.3	4290.3	73.2
Muon Decay	94043	77.4	93628.7	72.1	3904.2	91.0
Shower Charge	24222	25.8	24065.6	25.7	2915.2	74.7
PID Weight	15138	62.5	15153.5	63.0	1967.4	67.5
π^0 Direction	6325	41.8	6468.1	42.7	1320.0	67.1
Shower Separation	775	12.3	893.0	13.8	434.9	32.9

Table 4.11: The number of events passing each cut for the P \emptyset D water-out configuration. The first column lists the cut variable names, the second gives the number of events found in the detector. The third and fourth column show the number of events predicted in the Monte Carlo and its relative efficiencies. The last two column show the number of signal events predicted in the Monte Carlo and its relative efficiencies.

Cut	Events	Rel. Eff (%)	Expected	Rel. Eff (%)	Signal	Rel. Eff (%)
Preselection	1608938	N/A	793152.1	N/A	16341.7	N/A
Fiducial	158055	9.8	164475.9	20.7	5432.5	33.2
Contained	124235	78.6	127160.1	77.3	3653.3	67.2
Muon Decay	99953	80.5	95570.4	75.2	3329.0	91.1
Shower Charge	30508	30.5	28804.5	30.1	2347.5	70.5
PID Weight	17959	58.9	16902.6	58.7	1495.8	63.7
π^0 Direction	9134	50.9	8046.6	47.6	1000.9	66.9
Shower Separation	555	6.1	629.6	7.8	290.3	29.0

Table 4.12: The breakdown of the final sample in the Monte Carlo for the P \emptyset D water-in configuration.

Data	775
Monte Carlo Expectation	893.0 ± 6.1
Signal	434.9 ± 4.3
Background	458.2 ± 4.4
Neutral Current	109.5 ± 2.2
Charged Current w/ π^0	55.5 ± 1.5
Charged Current Other	238.8 ± 3.2
External	39.2 ± 1.3
Multiple	15.1 ± 0.8
Noise	$0.0 \pm \text{-nan}$

4.4. ANALYSIS

Table 4.13: The breakdown of the final sample in the Monte Carlo for the P \emptyset D water-out configuration.

Data	555
Monte Carlo Expectation	629.6 ± 8.0
Signal	290.3 ± 5.4
Background	339.3 ± 5.9
Neutral Current	67.8 ± 2.7
Charged Current w/ π^0	40.1 ± 2.0
Charged Current Other	149.7 ± 3.9
External	70.6 ± 2.8
Multiple	11.1 ± 1.1
Noise	$0.0 \pm \text{-nan}$

Table 4.14: The breakdown of the muon decay sideband in the Monte Carlo for the P \emptyset D water-in configuration.

Data	227
Monte Carlo Expectation	330.6 ± 3.8
Signal	33.2 ± 1.2
Background	297.3 ± 3.6
Neutral Current	73.9 ± 1.8
Charged Current w/ π^0	39.4 ± 1.3
Charged Current Other	166.9 ± 2.6
External	9.1 ± 0.6
Multiple	8.0 ± 0.6
Noise	$0.0 \pm \text{-nan}$

Table 4.15: The breakdown of the muon decay sideband in the Monte Carlo for the P \emptyset D water-out configuration.

Data	123
Monte Carlo Expectation	210.4 ± 4.6
Signal	23.5 ± 1.6
Background	186.8 ± 4.3
Neutral Current	45.0 ± 2.2
Charged Current w/ π^0	21.6 ± 1.5
Charged Current Other	99.9 ± 3.2
External	13.6 ± 1.2
Multiple	6.7 ± 0.8
Noise	$0.0 \pm \text{-nan}$

Table 4.16: A summary of the events that pass all selection cuts and events that fall in the μ -decay sideband, but have a reconstructed invariant mass greater than 500 MeV for both the P \emptyset D water-in and water-out configurations.

	Water-In		Water-Out	
	Selected	Sideband	Selected	Sideband
Data	138	49	50	25
NC1 π^0	6.6 ± 0.1	1.7 ± 0.2	2.5 ± 0.2	0.8 ± 0.4
NC Other	24.6 ± 0.0	18.9 ± 0.0	12.2 ± 0.1	8.7 ± 0.1
CC1 π^0	7.3 ± 0.1	4.5 ± 0.1	2.7 ± 0.2	2.9 ± 0.2
CC Other	69.5 ± 0.0	53.9 ± 0.0	27.2 ± 0.1	22.1 ± 0.1
External	1.2 ± 0.2	0.9 ± 0.2	2.6 ± 0.2	0.8 ± 0.4
Multiple Vertices	2.8 ± 0.1	2.3 ± 0.1	1.1 ± 0.3	1.8 ± 0.2
Noise	$0.0 \pm \text{-nan}$	$0.0 \pm \text{-nan}$	$0.0 \pm \text{-nan}$	$0.0 \pm \text{-nan}$

Table 4.17: A summary of the efficiencies (ϵ) and purity (π) found for both the water-in and water-out configurations given the event selection described in Section 4.2.

	ϵ_{ff} (%)	ϵ_A (%)	π (%)
Water In	6.01 ± 0.01	12.42 ± 0.04	48.7 ± 0.17
Water Out	4.79 ± 0.02	11.00 ± 0.06	46.1 ± 0.3

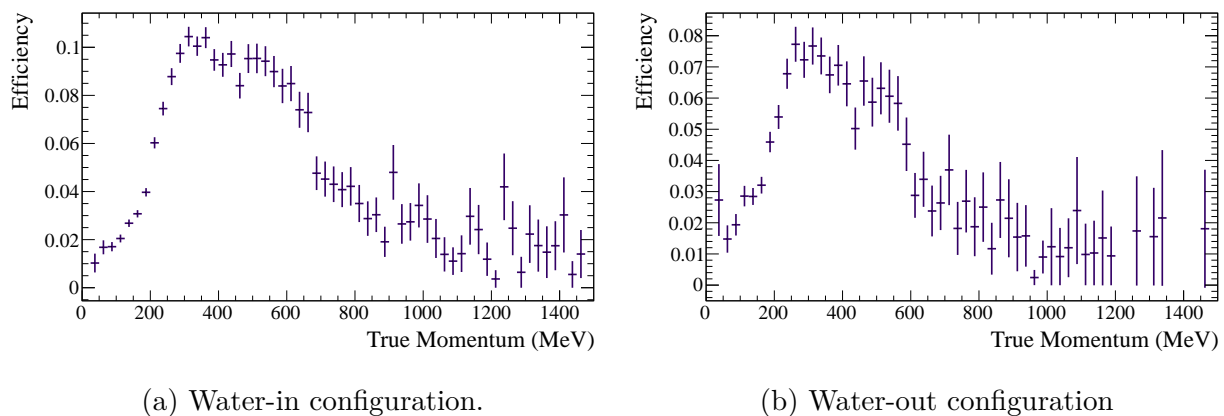


Figure 4.24: The efficiency of the NC1 π^0 analysis as a function of the momentum of the π^0 .

4.4. ANALYSIS

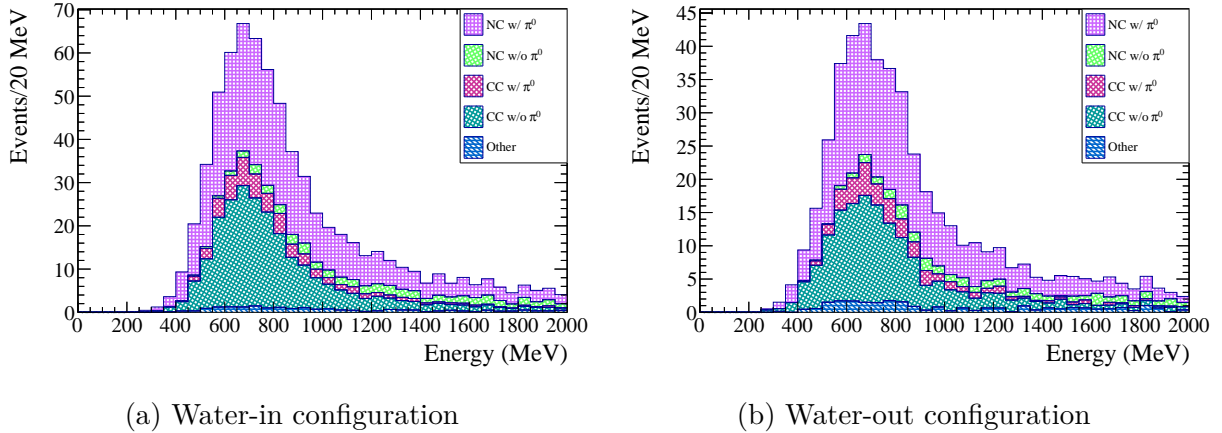


Figure 4.25: The distribution of the true neutrino energy for the saved Monte Carlo events.

1412 generated in the fiducial volume of the P \emptyset D. There is a difference between the P \emptyset D water-in
 1413 and water-out configuration efficiencies which can be contributed to the difference in masses
 1414 between the two configurations. The reduced mass of the P \emptyset D water-out configuration means
 1415 that photons travel further and are therefore harder to reconstruct. This makes the π^0 harder
 1416 to reconstruct as well. The second, ϵ_A , is the efficiency of this analysis's topology. It is an
 1417 efficiency of the final selected sample compared to the sample of events that is preselected,
 1418 fully contained, with a reconstructed fiducial vertex. The purity quoted is based of the final
 1419 state of the interaction with one π^0 exiting the nucleus and no other mesons or leptons com-
 1420 pared to the total number of saved events. The efficiency as a function of the true momentum
 1421 of the π^0 is shown in Figure 4.24 and the distribution of the true neutrino energy is shown
 1422 in Figure 4.25. The low momentum efficiency drop is due to the lower energy photon falling
 1423 below the reconstruction threshold. The higher end of the momentum also drops as the π^0
 1424 is boosted enough to lead to the decay photons overlapping and not resolving separately in
 1425 the reconstruction.

1426 In the data, 775 events were saved for the water-in configuration and 555 events were saved
 1427 for the water-out configuration of the P \emptyset D. Figure 4.26 shows the number of π^0 candidate
 1428 events as a function of POT for each configuration. Figures 4.27 and 4.28 show the timing of
 1429 the selected events for the separate runs in the detector. The vertex distributions are shown
 1430 in one dimensional projections in Figures 4.29 and 4.30 and in two dimensional projections
 1431 in Figures 4.31 and 4.32. Lastly a comparison of the reconstructed energy between data and
 1432 Monte Carlo is shown in Figure 4.33.

1433 4.4.2 Definition of Likelihood

1434 Using Minuit, the selected region (passing all cuts) and the muon decay sideband region
 1435 (passing all cuts, but failing the muon decay cut) are fit simultaneously using an unbinned
 1436 extended maximum likelihood. The shape of each sample is defined by a selection of PDFs.
 1437 Two PDFs describe the Monte Carlo prediction for the signal and background shape in the
 1438 selected region, denoted $\rho_{\text{Sig}}^{\text{Selected}}$ and $\rho_{\text{Bkg}}^{\text{Selected}}$. These PDFs are shown in Figures 4.34 and

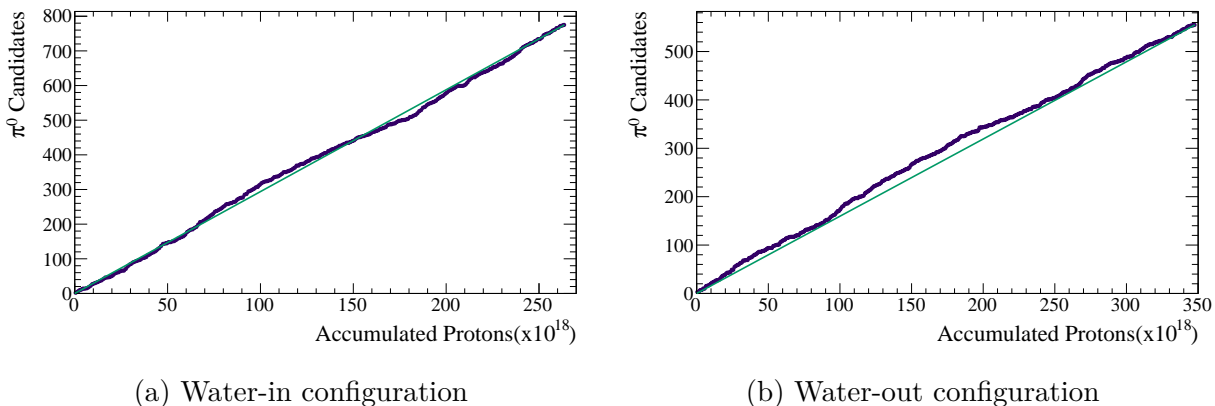


Figure 4.26: The rate of π^0 candidates observed in the P \emptyset D. The event rate is 2.94 candidates/ 10^{18} POT for the P \emptyset D water-in configuration and 1.60 candidates/ 10^{18} POT for the P \emptyset D water-out configuration. A K-S test was performed on each sample. The P \emptyset D water-in configuration has a probability of 0.78 and a maximum distance of 0.03. The P \emptyset D water-out configuration has a probability of 0.35 with a maximum distance of 0.06.

1439 4.35. The other two PDFs describe the prediction for the signal and background shape in the
 1440 sideband region, denoted $\rho_{\text{Sig}}^{\text{Sideband}}$ and $\rho_{\text{Bkg}}^{\text{Sideband}}$ and are also seen in Figures 4.34 and 4.35.

1441 The overall signature to save is that of two photons in an event. For both the selected
 1442 and sideband regions, the number of two photon events ($N_{\gamma\gamma}$) is a sum of the true signal
 1443 events (N_{Sig}) and the background events (N_{Bkg}). There is a fixed relationship between the
 1444 number of signal events in the signal region and the sideband region. The same holds true
 1445 for the number of background events. Using the Monte Carlo, that relationship is fixed by
 1446 $\alpha = N_{\text{Sig}}^{\text{Sideband}}/N_{\text{Sig}}^{\text{Selected}}$ and $\beta = N_{\text{Bkg}}^{\text{Sideband}}/N_{\text{Bkg}}^{\text{Selected}}$ to give

$$N_{\gamma\gamma}^{\text{Selected}} = N_{\text{Sig}}^{\text{Selected}} + N_{\text{Bkg}}^{\text{Selected}} \quad (4.8a)$$

$$N_{\gamma\gamma}^{\text{Sideband}} = N_{\text{Sig}}^{\text{Sideband}} + N_{\text{Bkg}}^{\text{Sideband}} \quad (4.8b)$$

$$= \alpha \cdot N_{\text{Sig}}^{\text{Selected}} + \beta \cdot N_{\text{Bkg}}^{\text{Selected}}. \quad (4.8c)$$

1447 Breaking the likelihood equations down,

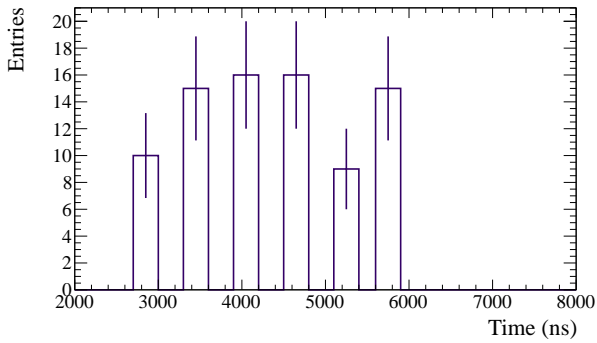
$$\mathcal{L}_{\text{Signal}} = \mathcal{L}(N_{\text{Sig}}^{\text{Selected}}, N_{\text{Bkg}}^{\text{Selected}})_{\text{Norm}} \times \mathcal{L}(e, N_{\text{Sig}}^{\text{Selected}}, N_{\text{Bkg}}^{\text{Selected}})_{\text{Shape}} \quad (4.9a)$$

$$\mathcal{L}_{\text{Sideband}} = \mathcal{L}(N_{\text{Sig}}^{\text{Sideband}}, N_{\text{Bkg}}^{\text{Sideband}})_{\text{Norm}} \times \mathcal{L}(e, N_{\text{Sig}}^{\text{Sideband}}, N_{\text{Bkg}}^{\text{Sideband}})_{\text{Shape}} \quad (4.9b)$$

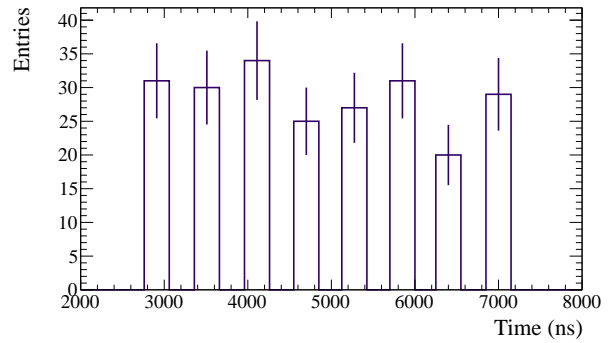
$$\mathcal{L}_{\text{Total}} = \mathcal{L}_{\text{Signal}} \times \mathcal{L}_{\text{Sideband}} \times \mathcal{L}_{\text{Sys}}(N_{\text{Sig}}^{\text{Selected}}, N_{\text{Bkg}}^{\text{Selected}}, N_{\text{Sig}}^{\text{Sideband}}, N_{\text{Bkg}}^{\text{Sideband}}). \quad (4.9c)$$

1448 The total likelihood depends on the number of signal and background in the signal
 1449 region ($N_{\text{Sig}}^{\text{Selected}}$ and $N_{\text{Bkg}}^{\text{Selected}}$), the number of signal and background in the sideband region
 1450 ($N_{\text{Sig}}^{\text{Sideband}}$ and $N_{\text{Bkg}}^{\text{Sideband}}$) and the energy scale (e) which is common to both samples. In order
 1451 to simultaneously fit the signal and sideband regions, the likelihoods must be minimized at
 1452 the same time with the constraint term, Equation 4.9c.

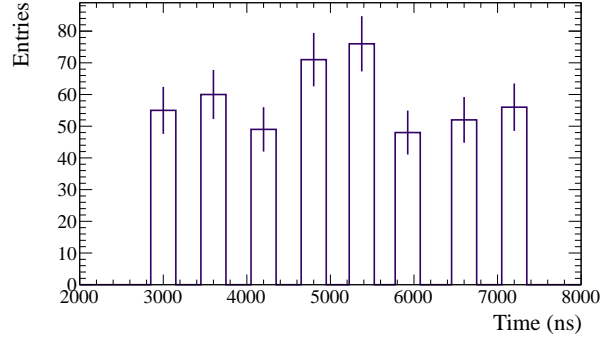
4.4. ANALYSIS



(a) Run 1

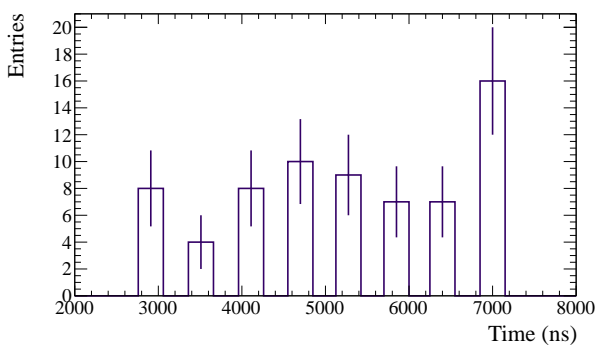


(b) Run 2

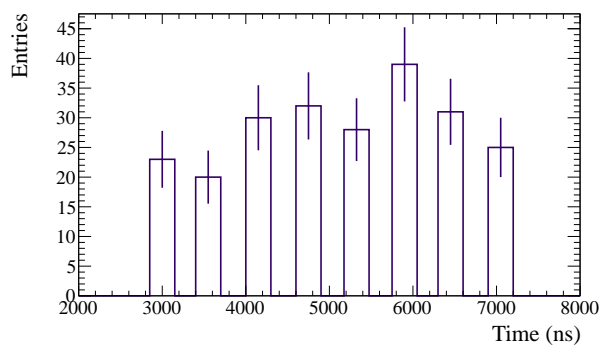


(c) Run 4

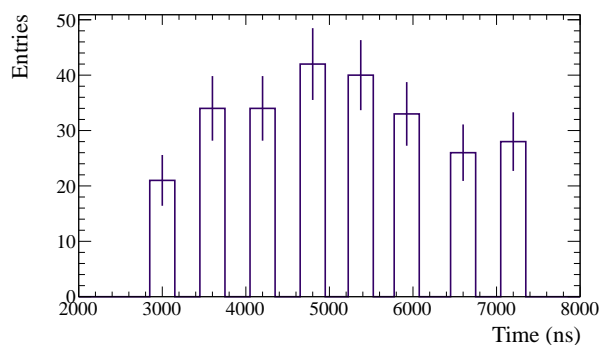
Figure 4.27: The bunch timing of the observed candidates in the P \emptyset D in the water-in configuration. There were 81 selected events in Run 1, 227 events in Run 2 and 467 events in Run 4.



(a) Run 2



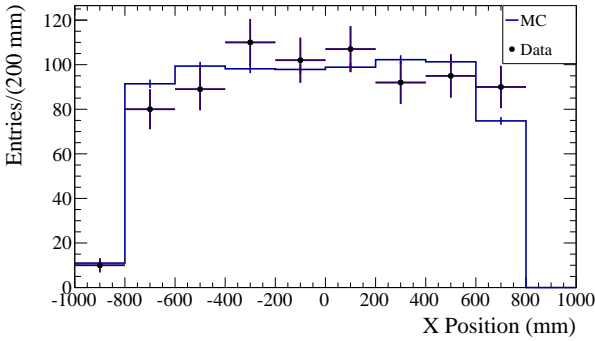
(b) Run 3



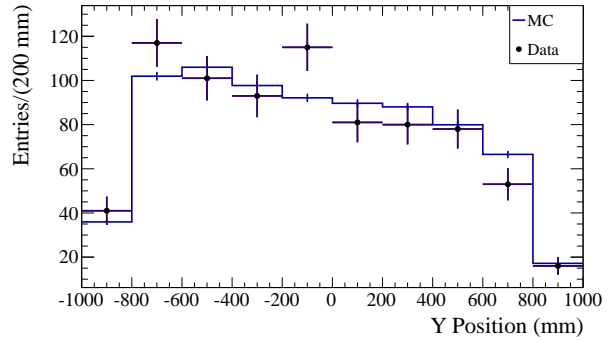
(c) Run 4

Figure 4.28: The bunch timing of the observed candidates in the P \emptyset D in the water-out configuration. There were 69 selected events in Run 2, 228 events for Run 3 and 258 events in Run 4.

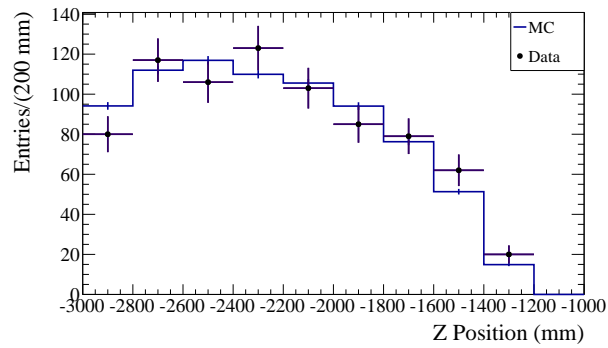
4.4. ANALYSIS



(a) X projection

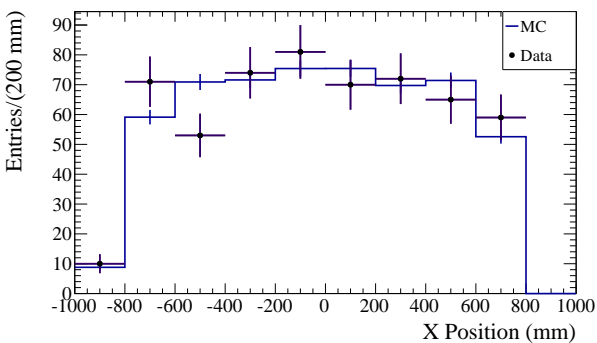


(b) Y projection

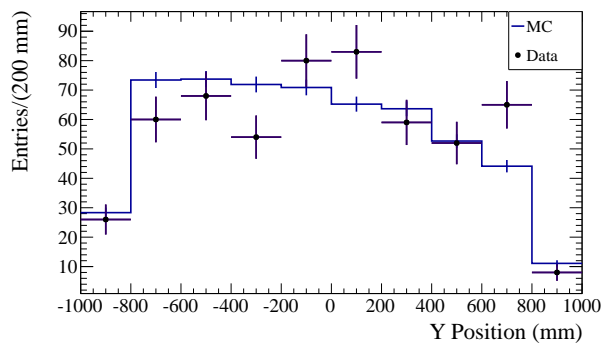


(c) Z projection

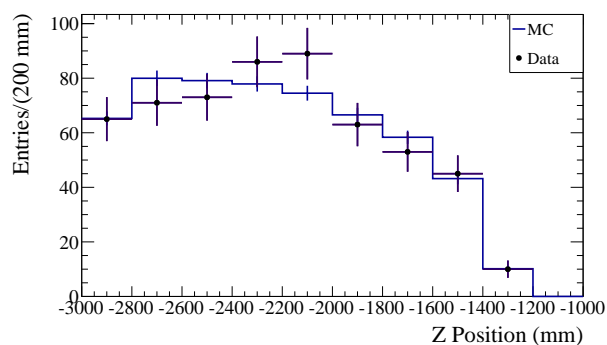
Figure 4.29: Comparison of the one-dimensional vertex distributions of candidate events in the $P\bar{0}D$ in the water-in configuration. Monte Carlo events are weighted by the mass difference between the Monte Carlo geometry and the as-built measurements, the POT, and the flux.



(a) X projection



(b) Y projection



(c) Z projection

Figure 4.30: Comparison of the one-dimensional vertex distributions of candidate events in the P \emptyset D in the water-out configuration. Monte Carlo events are weighted by the mass difference between the Monte Carlo geometry and the as-built measurements, the POT, and the flux.

4.4. ANALYSIS

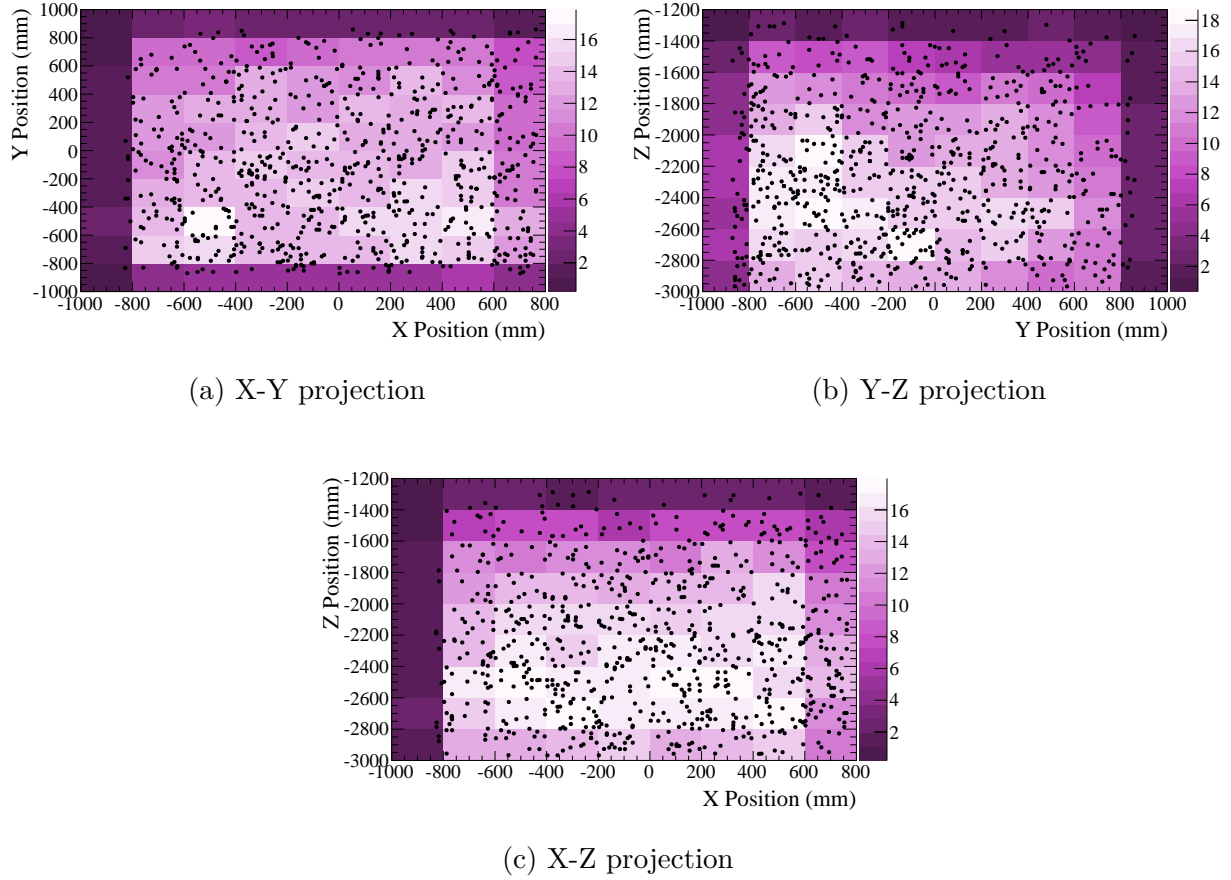
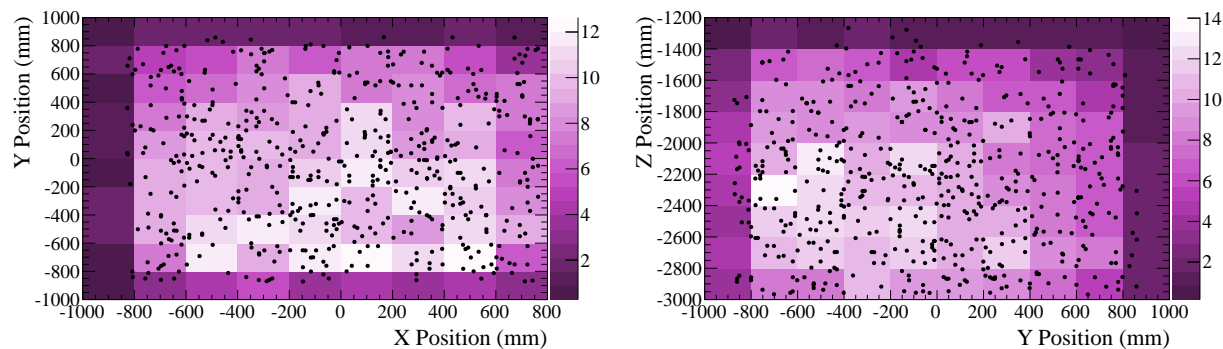
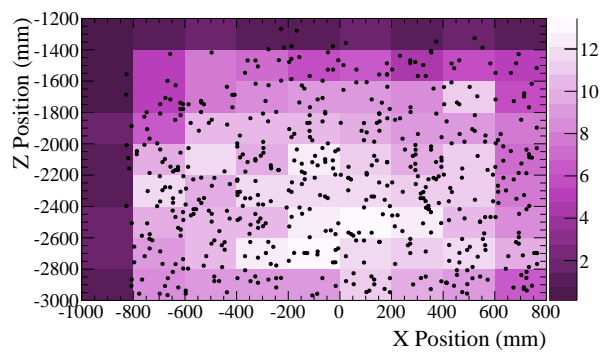


Figure 4.31: Comparison of the two-dimensional vertex distributions of candidate events in the PØD in the water-in configuration. Monte Carlo events are weighted by the mass difference between the Monte Carlo geometry and the as-built measurements, the POT, and the flux.



(a) X-Y projection

(b) Y-Z projection



(c) X-Z projection

Figure 4.32: Comparison of the two-dimensional vertex distributions of candidate events in the P \emptyset D in the water-out configuration. Monte Carlo events are weighted by the mass difference between the Monte Carlo geometry and the as-built measurements, the POT, and the flux.

4.4. ANALYSIS

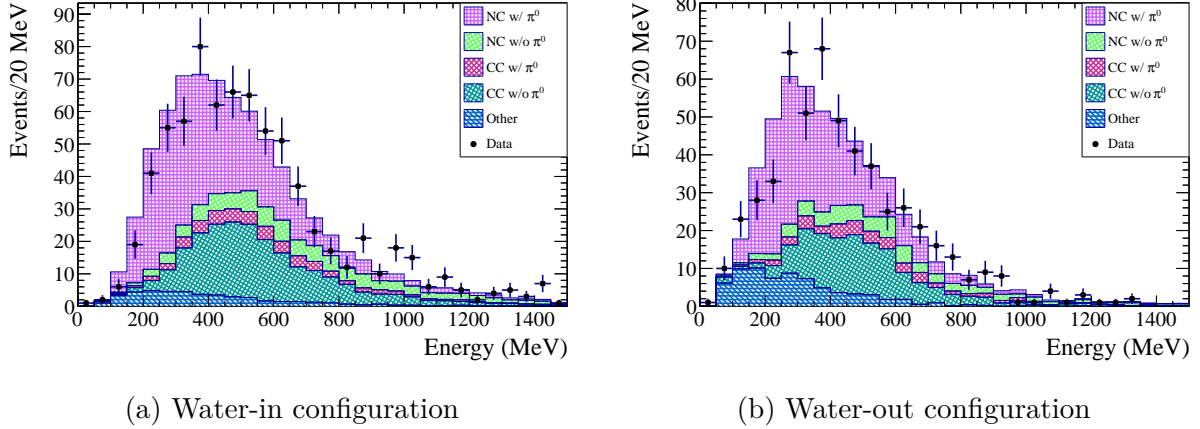


Figure 4.33: The reconstructed π^0 energy for events passing all selection cuts. The Monte Carlo events are flux, mass and POT weighted, then the overall distribution is area normalized to the data distribution in order to emphasize any shape differences.

1453 The normalization terms for the selected region and the sideband region are defined as
 1454 Poisson distributions,

$$\mathcal{L}(N_{\text{Sig}}^{\text{Selected}}, N_{\text{Bkg}}^{\text{Selected}})_{\text{Norm}} \sim \frac{(N_{\text{Sig}}^{\text{Selected}} + N_{\text{Bkg}}^{\text{Selected}}) N_{\text{Obs}}^{\text{Selected}} e^{-(N_{\text{Sig}}^{\text{Selected}} + N_{\text{Bkg}}^{\text{Selected}})}}{N_{\text{Obs}}^{\text{Selected}}!} \quad (4.10)$$

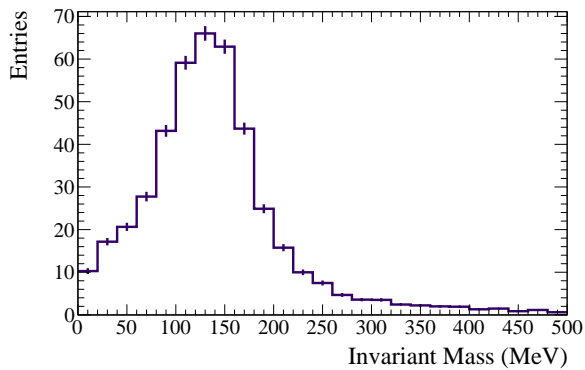
$$\mathcal{L}(N_{\text{Sig}}^{\text{Sideband}}, N_{\text{Bkg}}^{\text{Sideband}})_{\text{Norm}} \sim \frac{(N_{\text{Sig}}^{\text{Sideband}} + N_{\text{Bkg}}^{\text{Sideband}}) N_{\text{Obs}}^{\text{Sideband}} e^{-(N_{\text{Sig}}^{\text{Sideband}} + N_{\text{Bkg}}^{\text{Sideband}})}}{N_{\text{Obs}}^{\text{Sideband}}!}. \quad (4.11)$$

1455 with the number of observed events, N_{Obs} , remaining constant through the fitting procedure.

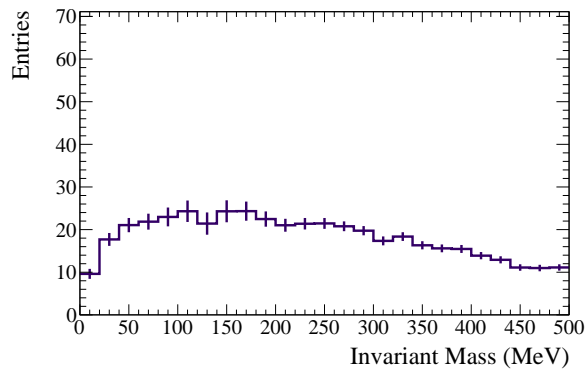
1456 The likelihood of the shape of the distributions, $\mathcal{L}(e, N_{\text{Sig}}^{\text{Selected}}, N_{\text{Bkg}}^{\text{Selected}})_{\text{Shape}}$ and $\mathcal{L}(e,$
 1457 $N_{\text{Sig}}^{\text{Sideband}}, N_{\text{Bkg}}^{\text{Sideband}})_{\text{Shape}}$, are defined by the four non-parametric PDFs shown in Figures
 1458 4.34 and 4.35. These PDFs are first normalized to one, then the linear interpolated value at
 1459 the energy scale shifted invariant mass is pulled as the likelihood from the PDFs. Since the
 1460 mass of the data events (m_i) is shifted by the energy scale, an addition multiplication of the
 1461 likelihood by e is needed. The shape likelihood becomes

$$\mathcal{L}(e, N_{\text{Sig}}^{\text{Selected}}, N_{\text{Bkg}}^{\text{Selected}})_{\text{Shape}} \sim \prod_i e \cdot \left(\frac{N_{\text{Sig}}^{\text{Selected}}}{N_{\text{Sig}}^{\text{Selected}} + N_{\text{Bkg}}^{\text{Selected}}} \cdot \rho_{\text{Sig}}^{\text{Selected}}(e \cdot m_i) + \frac{N_{\text{Bkg}}^{\text{Selected}}}{N_{\text{Sig}}^{\text{Selected}} + N_{\text{Bkg}}^{\text{Selected}}} \cdot \rho_{\text{Bkg}}^{\text{Selected}}(e \cdot m_i) \right) \quad (4.12)$$

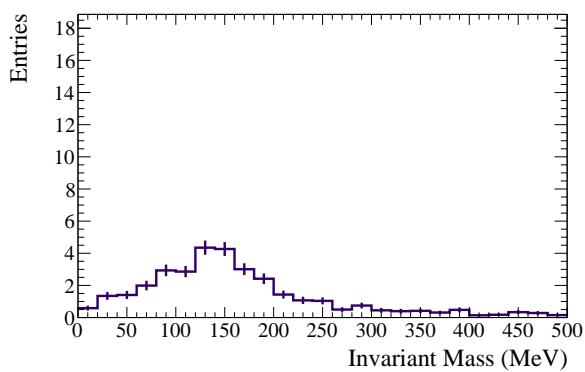
$$\mathcal{L}(e, N_{\text{Sig}}^{\text{Sideband}}, N_{\text{Bkg}}^{\text{Sideband}})_{\text{Shape}} \sim \prod_i e \cdot \left(\frac{N_{\text{Sig}}^{\text{Sideband}}}{N_{\text{Sig}}^{\text{Sideband}} + N_{\text{Bkg}}^{\text{Sideband}}} \cdot \rho_{\text{Sig}}^{\text{Sideband}}(e \cdot m_i) + \frac{N_{\text{Bkg}}^{\text{Sideband}}}{N_{\text{Sig}}^{\text{Sideband}} + N_{\text{Bkg}}^{\text{Sideband}}} \cdot \rho_{\text{Bkg}}^{\text{Sideband}}(e \cdot m_i) \right). \quad (4.13)$$



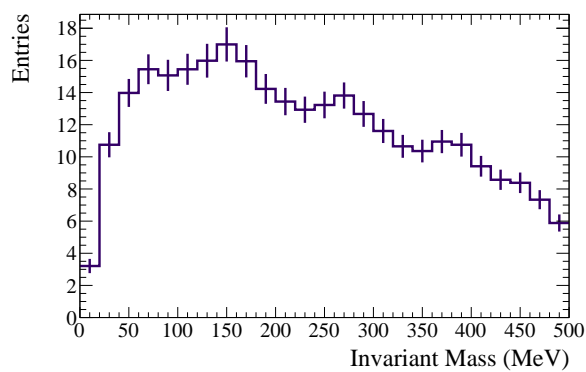
(a) Signal PDF of Selected Events.



(b) Background PDF of Selected Events.



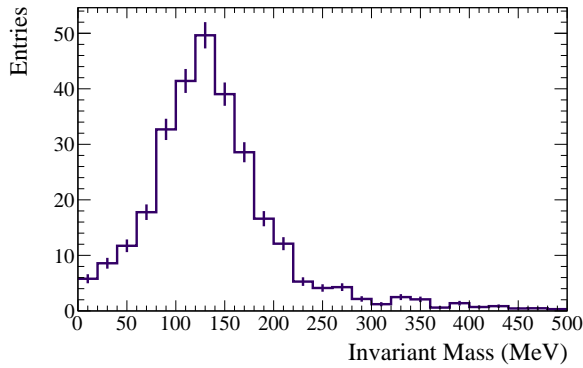
(c) Signal PDF of Sideband Events.



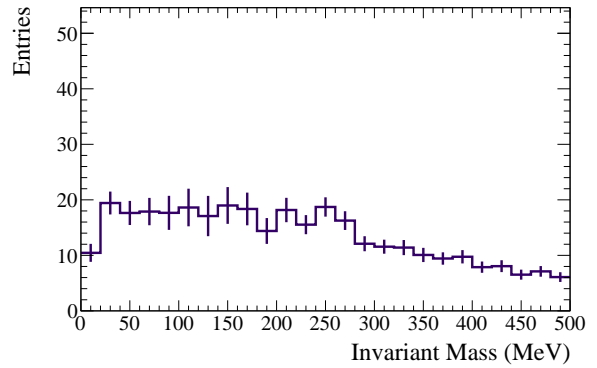
(d) Background PDF of Sideband Events.

Figure 4.34: The input PDFs for the $P\bar{0}D$ water-in configuration. Shown are the signal and sideband events. These PDFs are normalized to one to be used in the extended maximum likelihood.

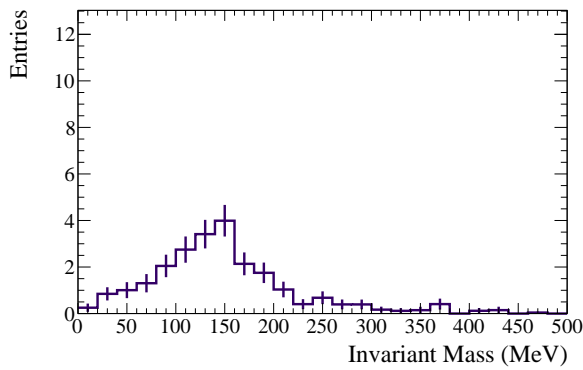
4.4. ANALYSIS



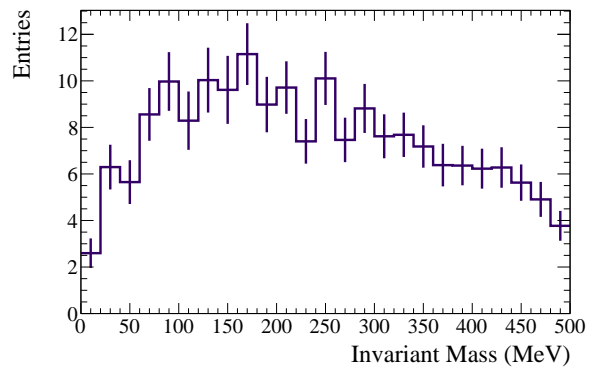
(a) Signal PDF of Selected Events.



(b) Background PDF of Selected Events.



(c) Signal PDF of Sideband Events.



(d) Background PDF of Sideband Events.

Figure 4.35: The input PDFs for the P \emptyset D water-out configuration. Shown are the signal and sideband events. The plots use the flux-weighted NEUT Monte Carlo as their normalization. These PDFs are normalized to one to be used in the extended maximum likelihood.

1462 The last piece of the likelihood comes from constraints on the parameters on the fit. To
 1463 that end, a covariance matrix, \mathbb{C} , was constructed to attempt to minimize the correlations
 1464 between the individual values. The vector $\Delta\mathbf{X}$ represents the deviation from the nominal
 1465 values. These constraints are added to the likelihood through

$$\mathcal{L}(N_{\text{Sig}}^{\text{Selected}}, N_{\text{Bkg}}^{\text{Selected}}, N_{\text{Sig}}^{\text{Sideband}}, N_{\text{Bkg}}^{\text{Sideband}}) \sim \exp\left(-\frac{1}{2}\Delta\mathbf{X}^T\mathbb{C}^{-1}\Delta\mathbf{X}\right), \quad (4.14)$$

1466 with

$$\mathbf{X} = \begin{pmatrix} \frac{N_{\text{Sig}}^{\text{Sideband}}}{N_{\text{Sig}}^{\text{Selected}}} & \frac{N_{\text{Bkg}}^{\text{Sideband}}}{N_{\text{Bkg}}^{\text{Selected}}} \end{pmatrix}. \quad (4.15)$$

1467 The constraint placed on the ratio of the sideband signal to the selected signal comes from
 1468 the difference in data and Monte Carlo of the fake rate of muon decay cluster reconstruction
 1469 which is detailed in the Subsection 5.7.3. The constraint placed on the ratio of the sideband
 1470 background to the selected background comes from the difference in data and Monte Carlo
 1471 muon decay cluster reconstruction efficiency also detailed in the Subsection 5.7.3.

1472 Removing Model Dependencies

1473 As an auxiliary analysis, an attempt at removing the dependency on the NEUT model
 1474 background was made. This was performed by an addition of a shape affecting term, g .
 1475 The least well known part of the background pdf occurs underneath the π^0 invariant mass
 1476 peak. In order to compensate for this region, an extra shape moderated by g is added into
 1477 the fit. Although any normalizable shape can be applied, the worst case scenario is that
 1478 the background appears as a peak in the selected region, or reproduces the selected signal
 1479 shape. If the background had the same appearance as the signal, the measurement could be
 1480 a drastic overestimate or underestimate of the signal. The total number of selected events
 1481 is equal to the sum of the bins in the selected signal and selected background histogram as

$$N_{\gamma\gamma}^{\text{Selected}} = \sum_i^{\text{bins}} \rho_{\text{Sig}}^{\text{Selected}}(i) + \sum_i^{\text{bins}} \rho_{\text{Bkg}}^{\text{Selected}}(i) \quad (4.16a)$$

$$\sum_i^{\text{bins}} \rho_{\text{Sig}}^{\text{Selected}}(i) = N_{\text{Sig}}^{\text{Selected}} + g \cdot N_{\text{Bkg}}^{\text{Selected}} \quad (4.16b)$$

$$\sum_i^{\text{bins}} \rho_{\text{Bkg}}^{\text{Selected}}(i) = N_{\text{Bkg}}^{\text{Selected}} - g \cdot N_{\text{Bkg}}^{\text{Selected}}. \quad (4.16c)$$

1482 The normalization of the selected signal histogram is the number of signal plus the g
 1483 factor times the number of background. It is here that the background is varied by the
 1484 shape of the selected signal histogram, with a normalization of $g \cdot N_{\text{Bkg}}^{\text{Selected}}$. The background
 1485 histogram contribution to the total number of selected events needs to then be modified by
 1486 this g factor to retain the overall normalization. In the sideband set of equations,

4.4. ANALYSIS

$$N_{\gamma\gamma}^{\text{Sideband}} = \sum_i^{\text{bins}} \rho_{\text{Sig}}^{\text{Sideband}}(i) + \sum_i^{\text{bins}} \rho_{\text{Sig}}^{\text{Selected}}(i) + \sum_i^{\text{bins}} \rho_{\text{Bkg}}^{\text{Sideband}}(i) \quad (4.17a)$$

$$\sum_i^{\text{bins}} \rho_{\text{Sig}}^{\text{Sideband}}(i) = \alpha \cdot N_{\text{Sig}}^{\text{Selected}} \quad (4.17b)$$

$$\sum_i^{\text{bins}} \rho_{\text{Sig}}^{\text{Selected}}(i) = \beta \cdot g \cdot N_{\text{Bkg}}^{\text{Selected}} \quad (4.17c)$$

$$\sum_i^{\text{bins}} \rho_{\text{Bkg}}^{\text{Sideband}}(i) = \beta \cdot N_{\text{Bkg}}^{\text{Selected}} - \beta \cdot g \cdot N_{\text{Bkg}}^{\text{Selected}}, \quad (4.17d)$$

1487 the application of the shape variation is more apparent. The number of sideband events is
 1488 equal to the sum of the normalization of three histograms: the sideband signal histogram,
 1489 the shape variation histogram, and the sideband background histogram.

1490 The variable g allows the fit to be flexible in the peak area. The g factor is allowed to
 1491 be positive or negative, which means that the shape histogram could have add or subtract
 1492 from the total shape whilst retaining the overall normalization. Adding the g factor turns
 1493 the overall likelihood into

$$\mathcal{L}_{\text{Signal}} = \mathcal{L}(N_{\text{Sig}}^{\text{Selected}}, N_{\text{Bkg}}^{\text{Selected}})_{\text{Norm}} \times \mathcal{L}(e, g, N_{\text{Sig}}^{\text{Selected}}, N_{\text{Bkg}}^{\text{Selected}})_{\text{Shape}} \quad (4.18a)$$

$$\mathcal{L}_{\text{Sideband}} = \mathcal{L}(N_{\text{Sig}}^{\text{Sideband}}, N_{\text{Bkg}}^{\text{Sideband}})_{\text{Norm}} \times \mathcal{L}(e, g, N_{\text{Sig}}^{\text{Sideband}}, N_{\text{Bkg}}^{\text{Sideband}})_{\text{Shape}} \quad (4.18b)$$

$$\mathcal{L}_{\text{Total}} = \mathcal{L}_{\text{Signal}} \times \mathcal{L}_{\text{Sideband}} \times \mathcal{L}_{\text{Sys}}(e, g, N_{\text{Sig}}^{\text{Selected}}, N_{\text{Bkg}}^{\text{Selected}}, N_{\text{Sig}}^{\text{Sideband}}, N_{\text{Bkg}}^{\text{Sideband}}). \quad (4.18c)$$

1494 The normalization terms for the selected region and the sideband region are not affected
 1495 by this additional shape term. Neither is the constraint term, since g is allowed to float
 1496 freely.

1497 The likelihood of the shape of the distributions, $\mathcal{L}(e, g, N_{\text{Sig}}^{\text{Selected}}, N_{\text{Bkg}}^{\text{Selected}})_{\text{Shape}}$ and $\mathcal{L}(e, g,$
 1498 $N_{\text{Sig}}^{\text{Sideband}}, N_{\text{Bkg}}^{\text{Sideband}})_{\text{Shape}}$ must be adjusted for the g factor. For the selected region, the signal
 1499 PDF is used for the signal prediction. However, the signal PDF is used again in conjunction
 1500 with the background PDF to predict the overall shape of the background. This is where the
 1501 power of the g factor comes in, it allows the background PDF to be varied in a predictable
 1502 way underneath the signal peak. For the sideband region, the sideband signal PDF is used
 1503 for the signal prediction, but the selected signal PDF is used as a variation on the sideband
 1504 background. In this way, the shape of the sideband constrains the possibilities for the g
 1505 factor which then effects the background shape in the selected region. The shape likelihood
 1506 becomes

Table 4.18: The results of running the fit for both the P0D water-in and P0D water-out configurations.

	$N_{\text{Sig}}^{\text{Selected}}$	$N_{\text{Bkg}}^{\text{Selected}}$	$N_{\text{Sig}}^{\text{Sideband}}$	$N_{\text{Bkg}}^{\text{Sideband}}$	e (%)
Water-In	341.6 ± 32.6	388.1 ± 25.5	26.9 ± 2.6	245.4 ± 14.9	89.45 ± 3.44
Water-Out	246.5 ± 26.0	270.6 ± 21.7	20.4 ± 2.2	140.6 ± 10.7	96.71 ± 0.62

Table 4.19: The Monte Carlo prediction for the P0D water-in and P0D water-out configurations adjusted by the fitted energy scale.

	$N_{\text{Sig}}^{\text{Selected}}$	$N_{\text{Bkg}}^{\text{Selected}}$	$N_{\text{Sig}}^{\text{Sideband}}$	$N_{\text{Bkg}}^{\text{Sideband}}$
Water-In	432.6 ± 4.3	428.6 ± 4.3	32.6 ± 1.2	278.4 ± 3.4
Water-Out	290.1 ± 5.4	334.9 ± 5.9	23.5 ± 1.6	184.3 ± 4.3

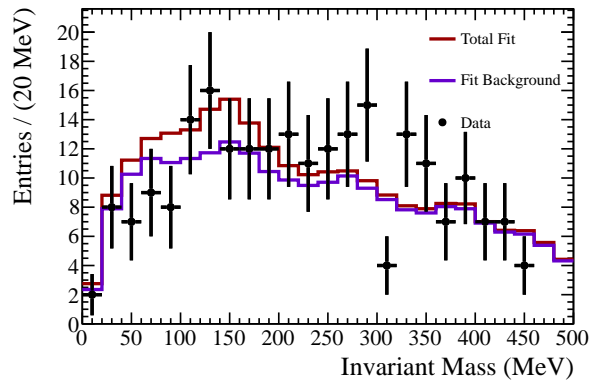
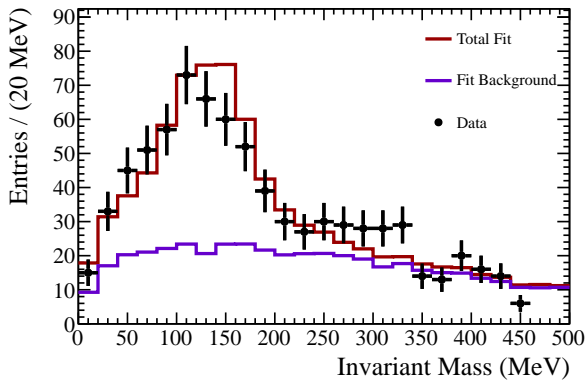
$$\begin{aligned}
\mathcal{L}(e, g, N_{\text{Sig}}^{\text{Selected}}, N_{\text{Bkg}}^{\text{Selected}})_{\text{Shape}} \sim \prod_i e \cdot & \left(\frac{N_{\text{Sig}}^{\text{Selected}}}{N_{\text{Sig}}^{\text{Selected}} + N_{\text{Bkg}}^{\text{Selected}}} \cdot \rho_{\text{Sig}}^{\text{Selected}}(e \cdot m_i) \right. \\
& + \frac{N_{\text{Bkg}}^{\text{Selected}}}{N_{\text{Sig}}^{\text{Selected}} + N_{\text{Bkg}}^{\text{Selected}}} \cdot g \cdot \rho_{\text{Sig}}^{\text{Selected}}(e \cdot m_i) \\
& \left. + \frac{N_{\text{Bkg}}^{\text{Selected}}}{N_{\text{Sig}}^{\text{Selected}} + N_{\text{Bkg}}^{\text{Selected}}} \cdot (1 - g) \cdot \rho_{\text{Bkg}}^{\text{Selected}}(e \cdot m_i) \right)
\end{aligned} \tag{4.19}$$

$$\begin{aligned}
\mathcal{L}(e, g, N_{\text{Sig}}^{\text{Sideband}}, N_{\text{Bkg}}^{\text{Sideband}})_{\text{Shape}} \sim \prod_i e \cdot & \left(\frac{N_{\text{Sig}}^{\text{Sideband}}}{N_{\text{Sig}}^{\text{Sideband}} + N_{\text{Bkg}}^{\text{Sideband}}} \cdot \rho_{\text{Sig}}^{\text{Sideband}}(e \cdot m_i) \right. \\
& + \frac{N_{\text{Bkg}}^{\text{Sideband}}}{N_{\text{Sig}}^{\text{Sideband}} + N_{\text{Bkg}}^{\text{Sideband}}} \cdot g \cdot \rho_{\text{Sig}}^{\text{Selected}}(e \cdot m_i) \\
& \left. + \frac{N_{\text{Bkg}}^{\text{Sideband}}}{N_{\text{Sig}}^{\text{Sideband}} + N_{\text{Bkg}}^{\text{Sideband}}} \cdot (1 - g) \cdot \rho_{\text{Bkg}}^{\text{Sideband}}(e \cdot m_i) \right).
\end{aligned} \tag{4.20}$$

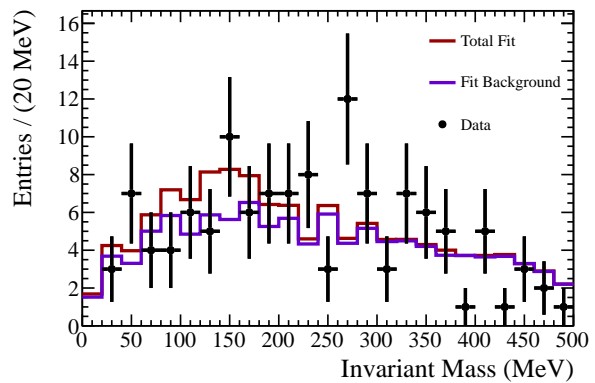
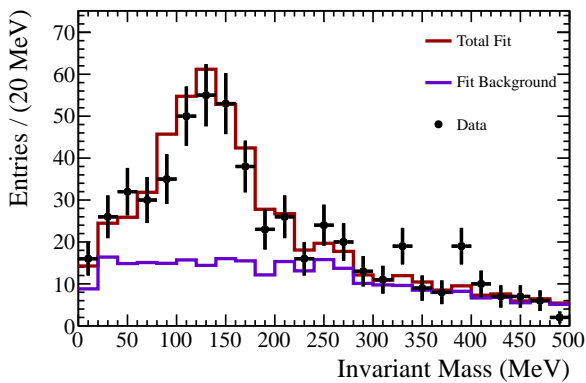
Table 4.20: The number of signal events found in the fit for both the water-in and water-out configurations. The errors listed come from the fit and are statistical.

	Observed	Expected	Ratio
Water-In	341.6 ± 32.6	432.6 ± 4.3	0.790 ± 0.076
Water-Out	246.5 ± 26.0	290.1 ± 5.4	0.850 ± 0.091

4.4. ANALYSIS



(a) Water-in Configuration



(b) Water-out Configuration

Figure 4.36: The $P\bar{0}D$ water-in and water-out configuration simultaneous invariant mass fit.

Table 4.21: The results of running the fit for both the P \emptyset D water-in and P \emptyset D water-out configurations with an unconstrained g factor.

	$N_{\text{Sig}}^{\text{Selected}}$	$N_{\text{Bkg}}^{\text{Selected}}$	$N_{\text{Sig}}^{\text{Sideband}}$	$N_{\text{Bkg}}^{\text{Sideband}}$	e (%)	g
Water-In	408.7 ± 32.9	341.2 ± 23.6	32.2 ± 2.7	220.1 ± 14.5	91.15 ± 0.74	-0.27 ± 0.07
Water-Out	321.0 ± 28.6	214.3 ± 20.6	26.6 ± 2.4	116.1 ± 10.7	98.00 ± 0.61	-0.39 ± 0.09

Table 4.22: The Monte Carlo prediction for the P \emptyset D water-in and P \emptyset D water-out configurations adjusted by the fitted energy scale.

	$N_{\text{Sig}}^{\text{Selected}}$	$N_{\text{Bkg}}^{\text{Selected}}$	$N_{\text{Sig}}^{\text{Sideband}}$	$N_{\text{Bkg}}^{\text{Sideband}}$
Water-In	432.8 ± 4.3	433.5 ± 4.3	32.7 ± 1.2	282.3 ± 3.5
Water-Out	290.2 ± 5.4	336.3 ± 5.9	23.5 ± 1.6	185.6 ± 4.3

1507 4.4.3 Fit Results

1508 Figure 4.36 show the results of the simultaneous unbinned extended maximum likelihood
 1509 fit. The first 22 bins of each region are used to calculate the χ^2 . The last three bins
 1510 are removed because they can potentially be affected by the energy scale. There are five
 1511 parameters in the fit leading to a 39 degrees of freedom. The χ^2 value for the P \emptyset D water-in
 1512 configuration is 40.4 for 39 degrees of freedom, leading to a p-value of 0.41. The χ^2 value
 1513 for the P \emptyset D water-out configuration is 53.5 for 39 degrees of freedom, leading to a p-value
 1514 of 0.06. The results of fitting the invariant mass spectrum are listed in Table 4.18. The
 1515 energy scale adjusted Monte Carlo prediction is listed in Table 4.19. In order to calculate a
 1516 systematic from this, first the data to Monte Carlo ratio of the number of signal events must
 1517 be calculated. Table 4.20 summarizes the data to Monte Carlo ratios with statistical errors.
 1518 To see the negative log likelihood curves from the fits, please look in Appendix A.

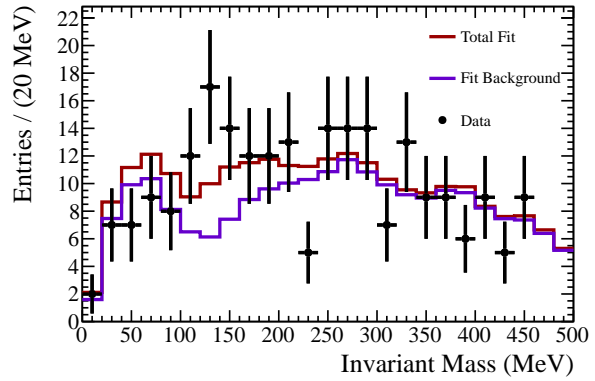
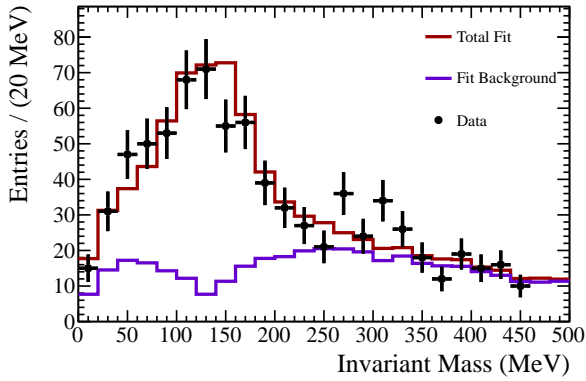
1519 Removing Model Dependencies

1520 The result of fitting the data with this method is shown in Figure 4.37. The first 22 bins
 1521 of each region are used to calculate the χ^2 . The last three bins are removed because they can
 1522 potentially be affected by the energy scale. There are six parameters in the fit leading to a
 1523 38 degrees of freedom. The χ^2 value for the P \emptyset D water-in configuration is 47.5 for 38 degrees
 1524 of freedom, leading to a p-value of 0.14. The χ^2 value for the P \emptyset D water-out configuration

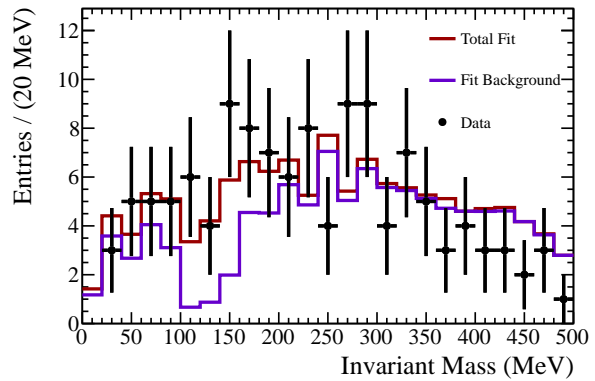
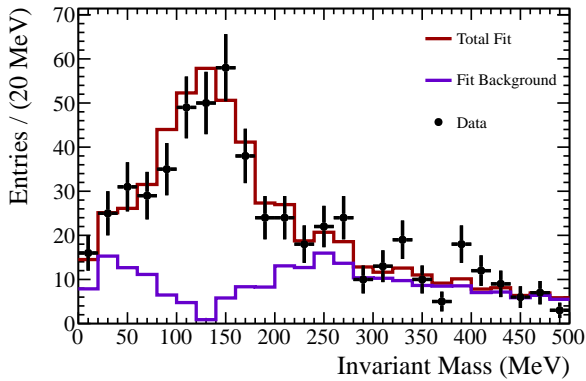
Table 4.23: The number of signal events found in the fit for both the water-in and water-out configurations with an unconstrained g factor. The errors listed come from the fit and are statistical.

	Observed	Expected	Ratio
Water-In	408.7 ± 32.5	432.8 ± 4.3	0.944 ± 0.076
Water-Out	321.0 ± 28.6	290.2 ± 5.4	1.107 ± 0.100

4.4. ANALYSIS



(a) Water-in Configuration



(b) Water-out Configuration

Figure 4.37: The P \emptyset D water-in and water-out configuration simultaneous invariant mass fit with an unconstrained g factor.

Table 4.24: Listed are the efficiencies (ϵ) and the purity (π) of the selection. The total efficiencies are shown as well as the specific on-water and not-water efficiencies. Note that the P \emptyset D water-out configuration has an effective on-water efficiency of 0.0 since there is no water in the P \emptyset D.

	ϵ_{ff}	ϵ_A	π
Water-In			
Total	6.097 ± 0.014	12.419 ± 0.038	48.69 ± 0.17
On-Water	6.205 ± 0.024	12.663 ± 0.064	56.16 ± 0.30
Not-Water	6.037 ± 0.017	12.284 ± 0.047	45.28 ± 0.21
Water-Out			
Total	4.790 ± 0.019	10.996 ± 0.061	46.12 ± 0.32

Table 4.25: The number of Monte Carlo predicted signal NC1 π^0 events for each run with a true vertex on water. Note that the entirety of Run 3 was in the P \emptyset D water-out configuration, so it would have no on-water vertices.

Run 1	Run 2	Run 4	Total
18.3 ± 0.8	41.4 ± 1.6	97.5 ± 1.9	157.2 ± 2.5

1525 is 38.7 for 38 degrees of freedom, leading to a p-value of 0.44.

1526 There is a very large distortion present in the shape of the background under the peak.
 1527 Although this may initially cause some concern, the distortion is accounted for in the system-
 1528 atics. In addition, the normalization is the information extracted, not the shape information,
 1529 to perform the ratio calculations. For the data to Monte Carlo ratios of the P \emptyset D water-in
 1530 and water-out configurations, the fractional difference between the $g \neq 0$ and $g = 0$ is added
 1531 in quadrature with the rest of the systematics. Tables 4.21 and 4.22 show the breakdown of
 1532 the numbers of expected and observed events in both the signal region and in the sideband
 1533 region. Table 4.23 lists the number of signal events expected and observed and the data to
 1534 Monte Carlo ratio with statistical errors. The P \emptyset D water-in configuration data to Monte
 1535 Carlo ratio of NC1 π^0 events with systematics is $0.944 \pm 0.076(\text{stat}) \pm 0.231(\text{sys})$. For the
 1536 P \emptyset D water-out configuration data to Monte Carlo ratio is $1.107 \pm 0.101(\text{stat}) \pm 0.316(\text{sys})$.
 1537 To see the negative log likelihood curves from the fits, please look in Appendix A.

1538 4.4.4 On-Water Calculation

1539 Six numbers are necessary for the on-water calculation described in Equation 4.5, the
 1540 POT, efficiency and the observed signal in the signal region for both the water-in and water-
 1541 out configurations. As a sanity check, the calculation of Equation 4.5 was done with the
 1542 Monte Carlo using the number of expected events. The Monte Carlo predictions for the
 1543 efficiencies, broken down into on-water and not-water events, are summarized in Table 4.24.
 1544 The not-water efficiency must be used due to the construction of the subtraction. A count
 1545 of the Monte Carlo NC1 π^0 events on water was done by checking if the location of each

4.5. T2KREWEIGHT

1546 true vertex was in a water target, the results are shown in Table 4.25. This Monte Carlo
1547 count predicts 157.2 ± 2.5 signal events to be on-water. If the subtraction is performed
1548 on the Monte Carlo expectations of the number of water-in and water-out signal events,
1549 the prediction becomes $157.9 \pm 6.8(\text{stat})$. This is a discrepancy of 0.7 events which within
1550 statistical errors is consistent with zero. For the data to Monte Carlo comparison of on-water
1551 events, the number of directly counted events is used because the difference is negligible and
1552 it has a smaller statistical error. Using the subtraction method as described in Equation
1553 4.5 on the data, $106.4 \pm 41.0(\text{stat}) \pm 72.6(\text{sys})$ ($106.4 \pm 41.0(\text{stat}) \pm 71.9(\text{sys})$) events were
1554 calculated, with pre-(post-)BANFF fit systematic errors. The final ratio of data to NEUT
1555 Monte Carlo of the on-water $\text{NC}1\pi^0$ is calculated as $0.677 \pm 0.261(\text{stat}) \pm 0.462(\text{sys})$, with pre-
1556 BANFF fit systematic errors. The final ratio of data to NEUT Monte Carlo of the on-water
1557 $\text{NC}1\pi^0$ is calculated as $0.677 \pm 0.261(\text{stat}) \pm 0.457(\text{sys})$, with post-BANFF fit systematic
1558 errors. A detailed discussion of the systematic error is in Section 5.

1559 Removing Model Dependencies

1560 This secondary analysis uses an unconstrained g shape variation factor, which has been
1561 presented in this section in detail. This result allows the background to be modified within
1562 a variation allowed by the muon decay sideband and provides a less model dependent value.
1563 Using the subtraction method as described in Equation 4.5 on the data, $102.4 \pm 42.5(\text{stat}) \pm$
1564 $90.4(\text{sys})$ ($102.4 \pm 42.5(\text{stat}) \pm 89.3(\text{sys})$) events were calculated, with pre-(post-)BANFF fit
1565 systematic errors. The calculated number of events on-water using the shape variation is
1566 very close to the default method. The final ratio of data to NEUT Monte Carlo of the on-
1567 water $\text{NC}1\pi^0$ is calculated as $0.652 \pm 0.270(\text{stat}) \pm 0.576(\text{sys})$, with pre-BANFF fit systematic
1568 errors. The final ratio of data to NEUT Monte Carlo of the on-water $\text{NC}1\pi^0$ is calculated as
1569 $0.652 \pm 0.270(\text{stat}) \pm 0.569(\text{sys})$, with post-BANFF fit systematic errors. Further discussion
1570 of the systematic error applied to the result is in Section 5.

1571 4.5 T2KReWeight

1572 Although the analysis has been in comparison to the NEUT Monte Carlo, T2K has an
1573 additional tool that can be used to reweight the Monte Carlo given global and ND280 fits
1574 constructed by the Beam and Neutrino Flux Task Force (BANFF), an internal working
1575 group at T2K. This reweighting can provide different central values for the PDFs that have
1576 been constructed. The central values of the pre-BANFF fits are based on other cross section
1577 measurements, such as those done by MiniBooNE and other flux measurements, such as those
1578 done by NA61. These external restrictions provide a different central value than the nominal
1579 flux-weighted NEUT Monte Carlo initially provides. There are additionally different central
1580 values from the post-BANFF fits that incorporate ND280 analyses into the constraints. The
1581 invariant mass shape prediction differs between the flux-weighted NEUT, the pre-BANFF fit
1582 and post-BANFF fit Monte Carlos. This can be seen in Figures 4.38 and 4.39. Additionally,
1583 Figures 4.40 and 4.41 show the extent of the variance from the central values over 1000
1584 throws of T2KReWeight.

1585 Tweaking the cross section and flux dials will change the total number of expected events

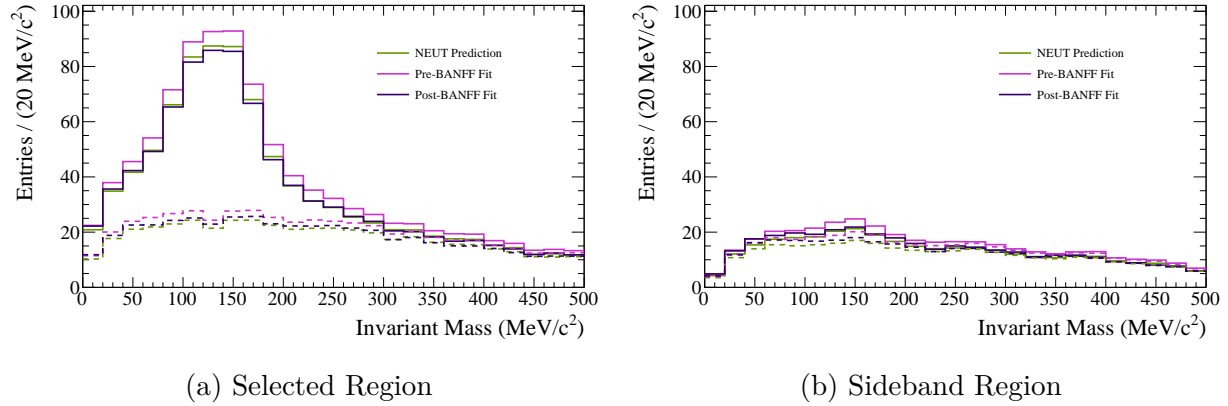


Figure 4.38: For the P \emptyset D water-in configuration, the variation between the central values of the flux-weighted NEUT prediction, the pre-BANFF fit prediction and the post-BANFF fit prediction. The solid lines show the prediction of the shape of the invariant mass for all events. The dashed lines are the prediction of the background shape.

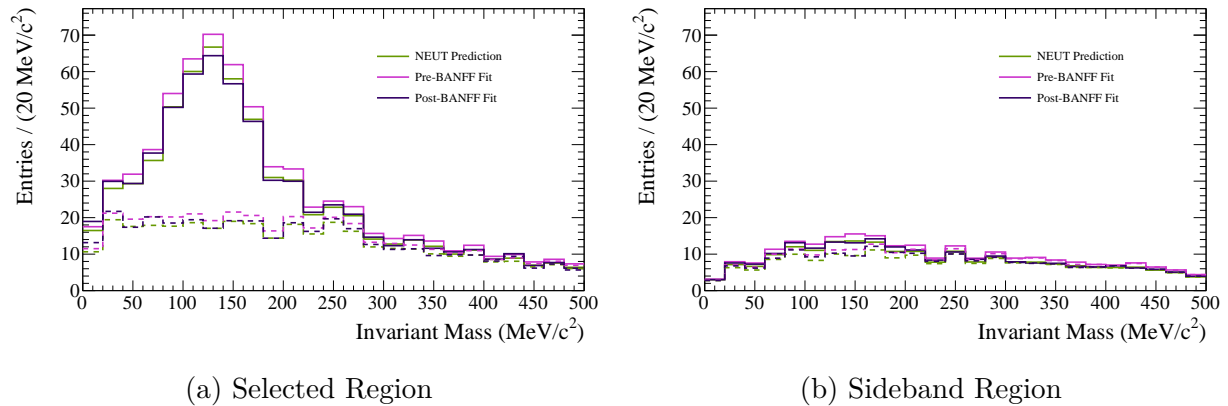


Figure 4.39: For the P \emptyset D water-out configuration, the variation between the central values of the flux-weighted NEUT prediction, the pre-BANFF fit prediction and the post-BANFF fit prediction. The solid lines show the prediction of the shape of the invariant mass for all events. The dashed lines are the prediction of the background shape.

4.5. T2KREWEIGHT

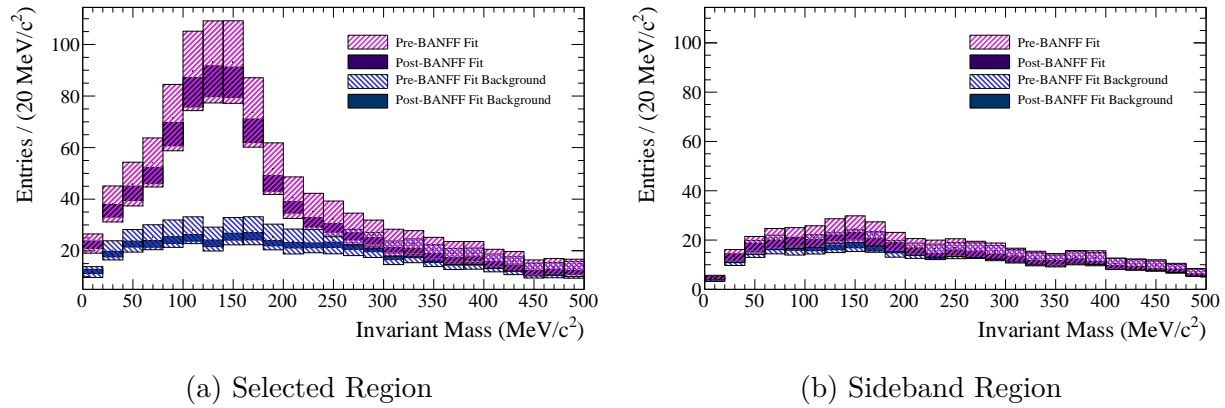


Figure 4.40: For the P \emptyset D water-in configuration, the spread of the errors on the pre-BANFF fit prediction and the post-BANFF fit prediction. The length of the boxes represent the variance from the mean of the repeated throws of T2KReWeight. Both the variance for the total Monte Carlo and for the background Monte Carlo are shown.

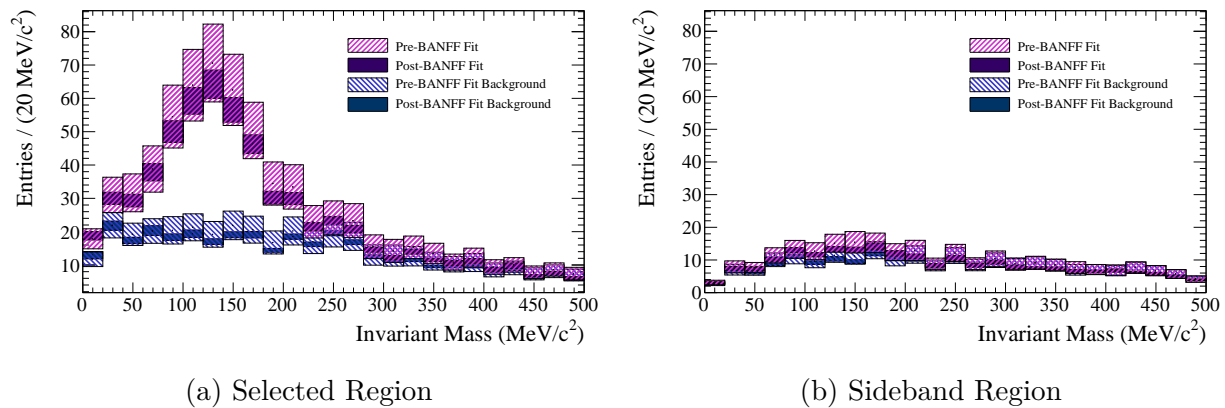


Figure 4.41: For the P \emptyset D water-out configuration, the spread of the errors on the pre-BANFF fit prediction and the post-BANFF fit prediction. The length of the boxes represent the variance from the mean of the repeated throws of T2KReWeight. Both the variance for the total Monte Carlo and for the background Monte Carlo are shown.

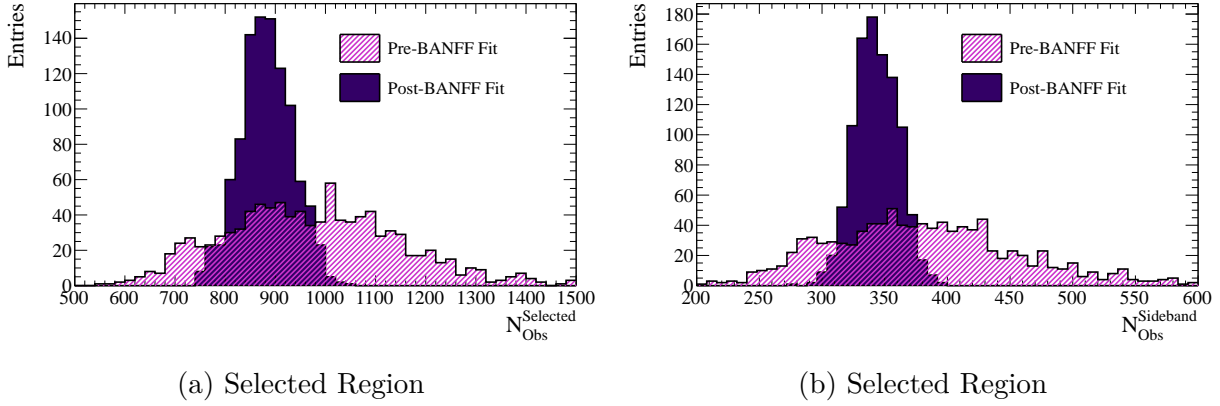


Figure 4.42: For the $P\bar{0}D$ water-in configuration, the spread of the expectation of the number of observed events in the selected and sideband regions pulled from throws of the pre- and post-BANFF fit T2KReWeight.

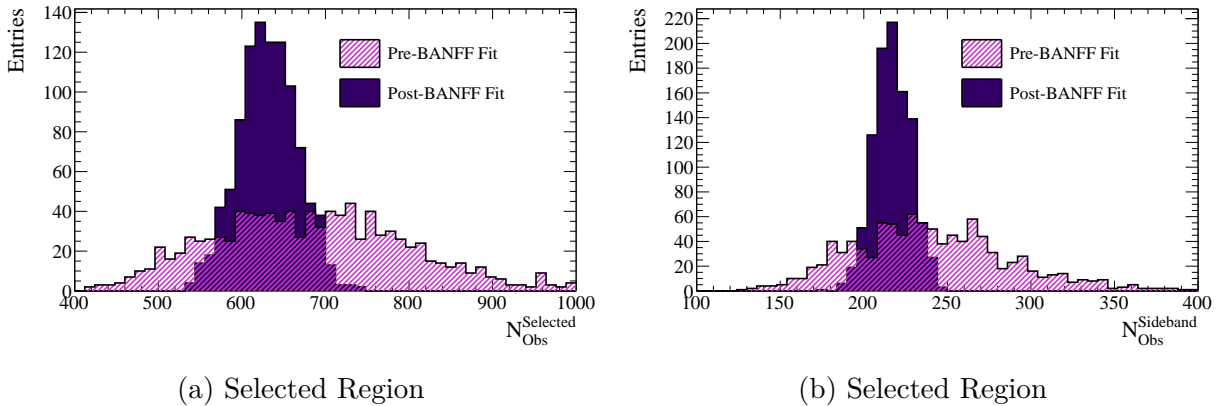


Figure 4.43: For the $P\bar{0}D$ water-out configuration, the spread of the expectation of the number of observed events in the selected and sideband regions pulled from throws of the pre- and post-BANFF fit T2KReWeight.

4.5. T2KREWEIGHT

Table 4.26: The results of running the fit for both the P \emptyset D water-in and P \emptyset D water-out configurations with the T2KReWeight pre-BANFF fit central values.

	$N_{\text{Sig}}^{\text{Selected}}$	$N_{\text{Bkg}}^{\text{Selected}}$	$N_{\text{Sig}}^{\text{Sideband}}$	$N_{\text{Bkg}}^{\text{Sideband}}$	e
Water-In	352.6 ± 30.2	376.8 ± 23.6	29.2 ± 2.5	243.5 ± 14.3	87.79 ± 1.11
Water-Out	249.5 ± 24.3	266.3 ± 23.6	21.5 ± 2.1	140.7 ± 11.1	96.74 ± 0.90

Table 4.27: The expected number of events from the pre-BANFF fit central values for both the P \emptyset D water-in and P \emptyset D water-out configurations.

	$N_{\text{Sig}}^{\text{Selected}}$	$N_{\text{Bkg}}^{\text{Selected}}$	$N_{\text{Sig}}^{\text{Sideband}}$	$N_{\text{Bkg}}^{\text{Sideband}}$
Water-In	452.7 ± 4.5	479.2 ± 4.8	35.8 ± 1.3	318.6 ± 4.0
Water-Out	302.3 ± 5.6	373.7 ± 6.6	25.5 ± 1.7	210.9 ± 4.9

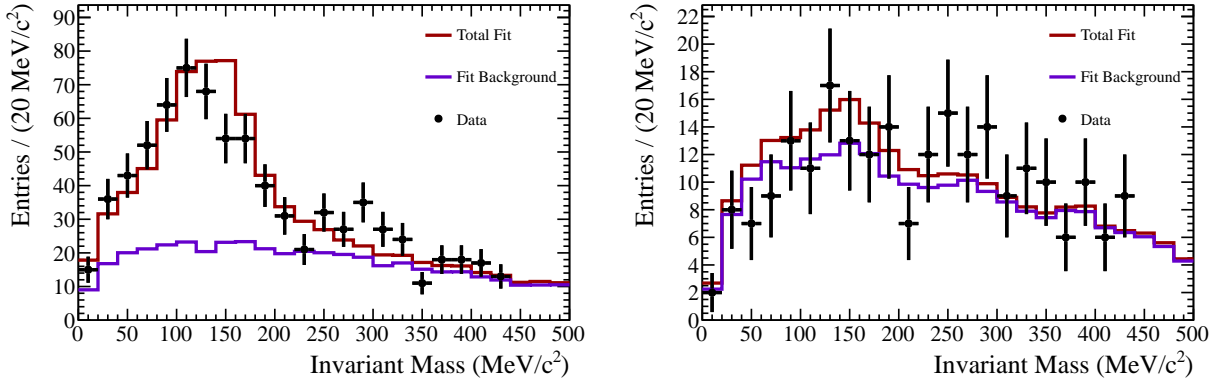
1586 as well. To get an idea of this variation, Figures 4.42 and 4.43 show the spread in the expected
 1587 number of selected and sideband events. As is evident, the pre-BANFF fit throws show a
 1588 wide range of possible expectations and the post-BANFF fit values show a more constrained
 1589 expectation. However, as is explained in Subsection 5.6, the spread of the expectation is
 1590 simply a normalization effect that is mostly removed by the fit.

1591 4.5.1 Fit Results

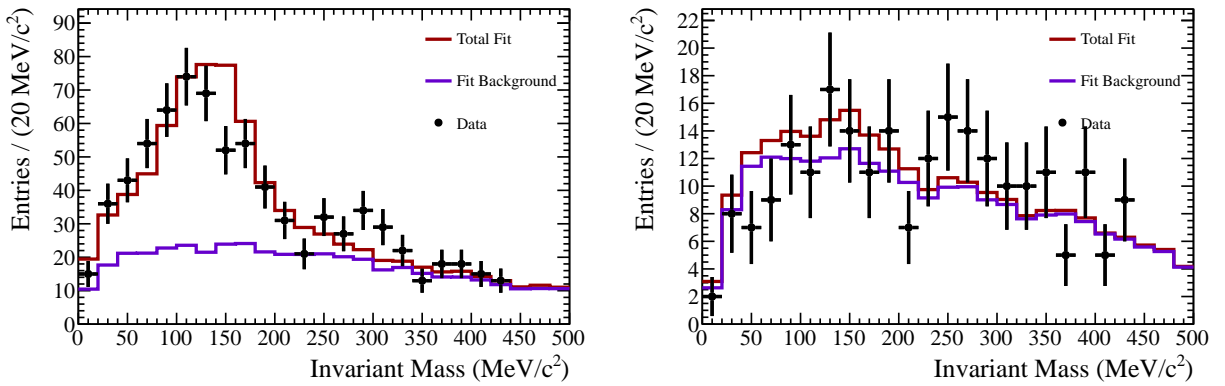
1592 Given that T2KReWeight changes the PDFs that enter into the simultaneous unbinned
 1593 maximum likelihood fit, the fit is run with both post-BANFF and pre-BANFF values. Tables
 1594 4.26 and 4.28 describe the fit parameter results from running the fit with the pre- and post-
 1595 BANFF central value PDFs. Tables 4.27 and 4.29 describe the expected reweighted Monte
 1596 Carlo events from pre- and post-BANFF central value PDFs. Figures 4.44 and 4.45 show
 1597 the results of the fit on the P \emptyset D water-in and water-out configurations with both the pre-
 1598 and post-BANFF fit central values. Given the results of the fit and assuming the same
 1599 systematic errors as listed in Table 5.24, the P \emptyset D water-in configuration ratio becomes
 1600 $0.779 \pm 0.067(\text{stat}) \pm 0.141(\text{sys})$ ($0.837 \pm 0.073(\text{stat}) \pm 0.151(\text{sys})$) for the pre-(post-)BANFF
 1601 fit reweighted NEUT Monte Carlo. For the P \emptyset D water-out configuration ratio, $0.825 \pm$
 1602 $0.082(\text{stat}) \pm 0.133(\text{sys})$ ($0.893 \pm 0.091(\text{stat}) \pm 0.141(\text{sys})$) is found. Counting the number of
 1603 reweighted expected on-water events, there are 164.4 ± 2.7 (149.3 ± 2.4) NC1 π^0 events are
 1604 expected. Using the fit results, the on-water value is calculated. For the pre-BANFF fit,

Table 4.28: The results of running the fit for both the P \emptyset D water-in and P \emptyset D water-out configurations with the T2KReWeight post-BANFF fit central values.

	$N_{\text{Sig}}^{\text{Selected}}$	$N_{\text{Bkg}}^{\text{Selected}}$	$N_{\text{Sig}}^{\text{Sideband}}$	$N_{\text{Bkg}}^{\text{Sideband}}$	e
Water-In	342.6 ± 29.5	385.5 ± 23.3	25.9 ± 2.3	248.1 ± 14.1	87.52 ± 0.70
Water-Out	249.7 ± 25.0	268.6 ± 21.1	19.3 ± 2.0	140.5 ± 10.4	96.71 ± 0.51



(a) Pre-BANFF Fit



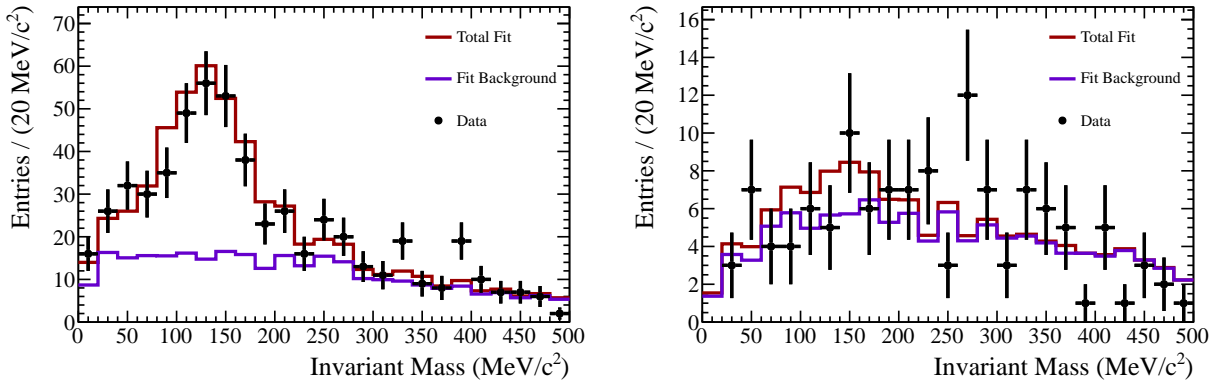
(b) Post-BANFF Fit

Figure 4.44: For the $P\bar{0}D$ water-in configuration, the result after fitting the data to the pre- and post-BANFF fit adjusted Monte Carlo. The pre-BANFF fit result has a total χ^2 of 45.1 with 39 degrees of freedom. This leads to a probability of 0.232. The post-BANFF fit result has a total χ^2 of 49.2 with 39 degrees of freedom and a 0.127 probability.

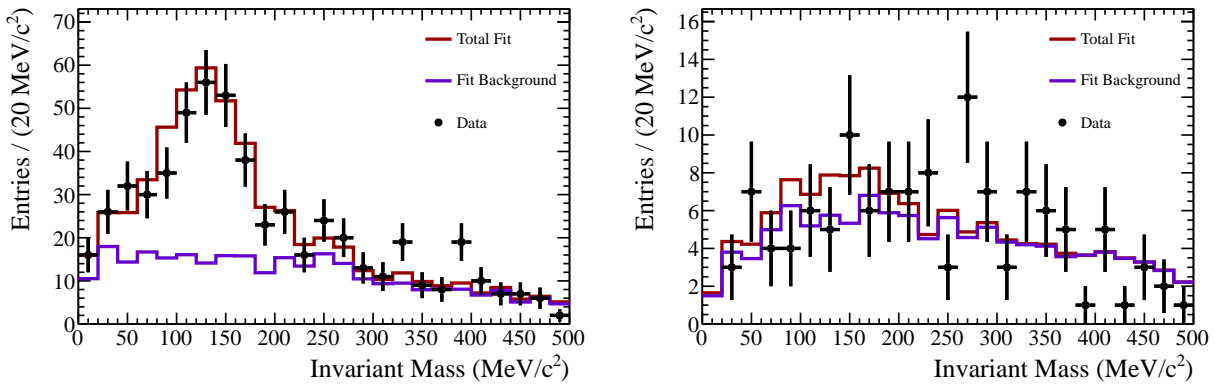
Table 4.29: The expected number of events from the post-BANFF fit central values for both the $P\bar{0}D$ water-in and $P\bar{0}D$ water-out configurations.

	$N_{\text{Sig}}^{\text{Selected}}$	$N_{\text{Bkg}}^{\text{Selected}}$	$N_{\text{Sig}}^{\text{Sideband}}$	$N_{\text{Bkg}}^{\text{Sideband}}$
Water-In	409.5 ± 4.0	438.1 ± 4.4	29.5 ± 1.1	291.7 ± 3.6
Water-Out	279.6 ± 5.2	348.9 ± 6.1	21.2 ± 1.4	193.5 ± 4.5

4.5. T2KREWEIGHT



(a) Pre-BANFF Fit



(b) Post-BANFF Fit

Figure 4.45: For the P \emptyset D water-out configuration, the result after fitting the data to the pre- and post-BANFF fit adjusted Monte Carlo. The pre-BANFF fit result has a total χ^2 of 54.7 with 39 degrees of freedom. This leads to a probability of 0.049. The post-BANFF fit result has a total χ^2 of 53.6 with 39 degrees of freedom and a 0.060 probability.

Table 4.30: The results of running the fit for both the P \emptyset D water-in and water-out configurations with the T2KReWeight pre-BANFF fit central values with an unconstrained g factor.

	$N_{\text{Sig}}^{\text{Selected}}$	$N_{\text{Bkg}}^{\text{Selected}}$	$N_{\text{Sig}}^{\text{Sideband}}$	$N_{\text{Bkg}}^{\text{Sideband}}$	e	g
Water-In	419.9 ± 32.2	329.9 ± 23.5	34.8 ± 2.9	217.4 ± 14.6	90.25 ± 0.64	-0.30 ± 0.08
Water-Out	326.4 ± 29.9	208.4 ± 21.7	28.2 ± 2.7	115.0 ± 11.4	98.45 ± 0.72	-0.42 ± 0.11

Table 4.31: The expected number of events from the pre-BANFF fit central values for both the P \emptyset D water-in and water-out configurations with an unconstrained g factor.

	$N_{\text{Sig}}^{\text{Selected}}$	$N_{\text{Bkg}}^{\text{Selected}}$	$N_{\text{Sig}}^{\text{Sideband}}$	$N_{\text{Bkg}}^{\text{Sideband}}$
Water-In	453.3 ± 4.5	485.9 ± 4.8	35.9 ± 1.3	324.7 ± 4.0
Water-Out	302.4 ± 5.6	375.9 ± 6.6	25.5 ± 1.7	212.6 ± 5.0

1605 the on-water rate is $114.6 \pm 38.1(\text{stat}) \pm 74.6(\text{sys})$ leading to a ratio of $0.697 \pm 0.232(\text{stat}) \pm$
 1606 $0.454(\text{sys})$. For the post-BANFF fit, the on-water rate is $104.4 \pm 40.0(\text{stat}) \pm 72.3(\text{sys})$ leading
 1607 to a ratio of $0.699 \pm 0.254(\text{stat}) \pm 0.484(\text{sys})$.

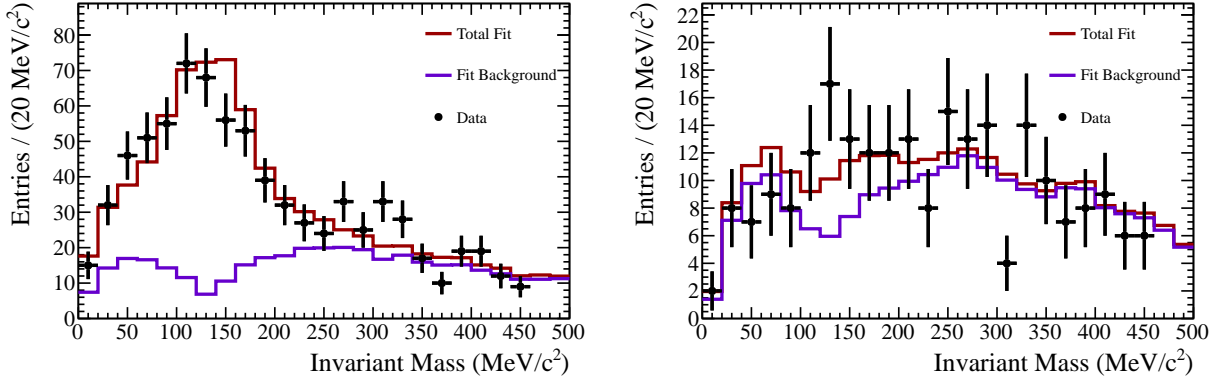
1608 Removing Model Dependencies

1609 This section describes the results when the g factor is unconstrained. Tables 4.30 and 4.32
 1610 describe the fit parameter results from running the fit with the pre- and post-BANFF central
 1611 value PDFs. Tables 4.31 and 4.33 describe the expected reweighted Monte Carlo events from
 1612 pre- and post-BANFF central value PDFs. Figures 4.46 and 4.47 show the results of the
 1613 fit on the P \emptyset D water-in and water-out configurations with both the pre- and post-BANFF
 1614 fit central values. Given the results of the fit and assuming the same systematic errors as
 1615 listed in Table 5.26, the P \emptyset D water-in configuration ratio becomes $0.926 \pm 0.072(\text{stat}) \pm$
 1616 $0.227(\text{sys})$ ($0.992 \pm 0.081(\text{stat}) \pm 0.242(\text{sys})$) for the pre-(post-)BANFF fit reweighted NEUT
 1617 Monte Carlo. For the P \emptyset D water-out configuration ratio, $1.079 \pm 0.101(\text{stat}) \pm 0.308(\text{sys})$
 1618 ($1.152 \pm 0.106(\text{stat}) \pm 0.327(\text{sys})$) is found. Counting the number of reweighted expected
 1619 on-water events, there are 164.4 ± 2.7 (149.3 ± 2.4) NC1 π^0 events are expected. Using the
 1620 fit results, the on-water value is calculated. For the pre-BANFF fit, the on-water rate is
 1621 $108.5 \pm 43.0(\text{stat}) \pm 92.5(\text{sys})$ leading to a ratio of $0.660 \pm 0.262(\text{stat}) \pm 0.566(\text{sys})$. For

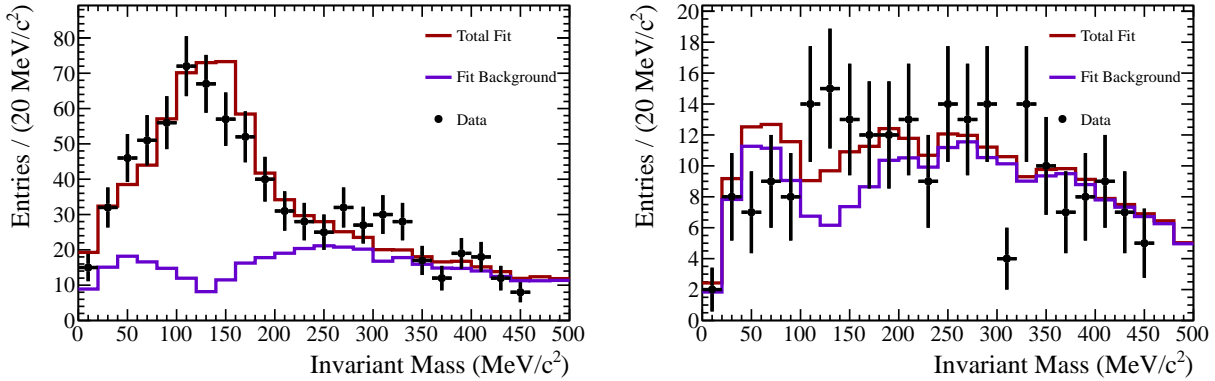
Table 4.32: The results of running the fit for both the P \emptyset D water-in and water-out configurations with the T2KReWeight post-BANFF fit central values with an unconstrained g factor.

	$N_{\text{Sig}}^{\text{Selected}}$	$N_{\text{Bkg}}^{\text{Selected}}$	$N_{\text{Sig}}^{\text{Sideband}}$	$N_{\text{Bkg}}^{\text{Sideband}}$	e	g
Water-In	406.8 ± 32.9	340.8 ± 23.7	30.8 ± 2.5	223.7 ± 14.7	90.09 ± 1.24	-0.28 ± 0.07
Water-Out	322.1 ± 29.1	214.2 ± 21.9	24.9 ± 2.3	116.8 ± 11.2	97.58 ± 0.59	-0.38 ± 0.10

4.5. T2KREWEIGHT



(a) Pre-BANFF Fit

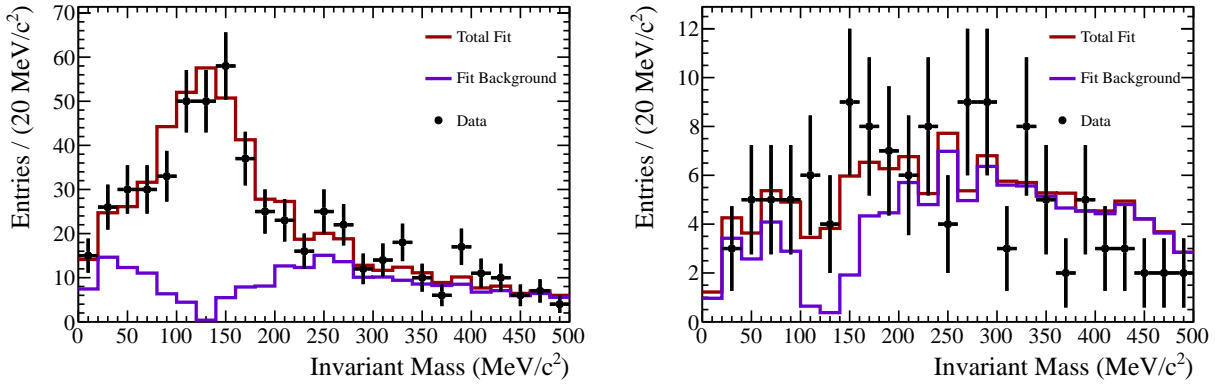


(b) Post-BANFF Fit

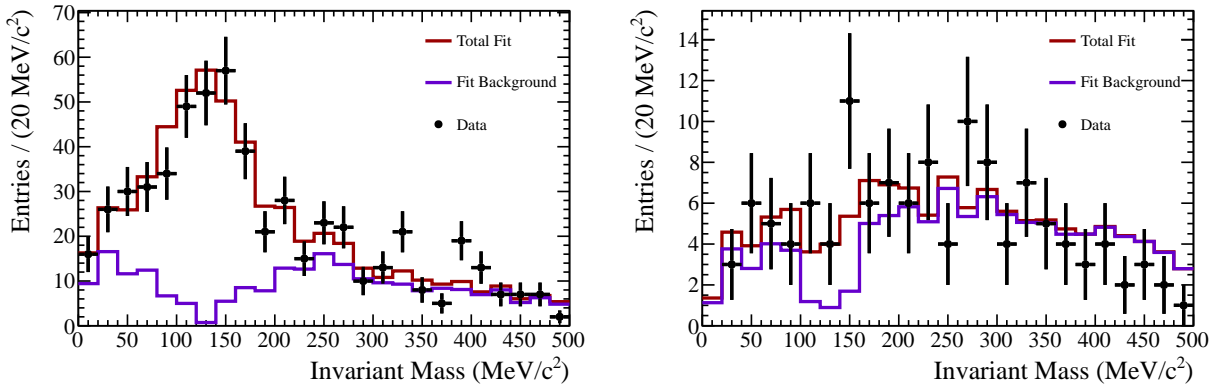
Figure 4.46: For the P \emptyset D water-in configuration, the result after fitting the data to the pre- and post-BANFF fit adjusted Monte Carlo. These fits are performed with an unconstrained g factor. The pre-BANFF fit result has a total χ^2 of 46.3 with 38 degrees of freedom. This leads to a probability of 0.167. The post-BANFF fit result has a total χ^2 of 42.2 with 38 degrees of freedom and a 0.294 probability.

Table 4.33: The expected number of events from the post-BANFF fit central values for both the P \emptyset D water-in and water-out configurations with an unconstrained g factor.

	$N_{\text{Sig}}^{\text{Selected}}$	$N_{\text{Bkg}}^{\text{Selected}}$	$N_{\text{Sig}}^{\text{Sideband}}$	$N_{\text{Bkg}}^{\text{Sideband}}$
Water-In	409.9 ± 4.0	444.8 ± 4.4	29.6 ± 1.1	297.0 ± 3.7
Water-Out	279.6 ± 5.2	349.8 ± 6.1	21.2 ± 1.4	194.6 ± 4.5



(a) Pre-BANFF Fit



(b) Post-BANFF Fit

Figure 4.47: For the $P\bar{0}D$ water-out configuration, the result after fitting the data to the pre- and post-BANFF fit adjusted Monte Carlo. These fits are performed with an unconstrained g factor. The pre-BANFF fit result has a total χ^2 of 38.0 with 38 degrees of freedom. This leads to a probability of 0.469. The post-BANFF fit result has a total χ^2 of 51.2 with 38 degrees of freedom and a 0.075 probability.

4.5. T2KREWEIGHT

Table 4.34: Summary of the P \emptyset D water-in and water-out configuration data to Monte Carlo ratios. The ratios are based on the fits of the data to the nominal flux-weighted NEUT Monte Carlo, the pre-BANFF fit reweighted Monte Carlo and the post-BANFF fit reweighted Monte Carlo. The top half of the table summarizes the results of the default fit while the bottom half shows the results from the unconstrained g fit.

	g	Water-In	Water-Out
NEUT (Pre)	No	$0.790 \pm 0.076(\text{stat}) \pm 0.143(\text{sys})$	$0.850 \pm 0.091(\text{stat}) \pm 0.137(\text{sys})$
NEUT (Post)	No	$0.790 \pm 0.076(\text{stat}) \pm 0.142(\text{sys})$	$0.850 \pm 0.091(\text{stat}) \pm 0.134(\text{sys})$
Pre-BANFF	No	$0.779 \pm 0.067(\text{stat}) \pm 0.141(\text{sys})$	$0.825 \pm 0.082(\text{stat}) \pm 0.133(\text{sys})$
Post-BANFF	No	$0.837 \pm 0.073(\text{stat}) \pm 0.151(\text{sys})$	$0.893 \pm 0.091(\text{stat}) \pm 0.141(\text{sys})$
NEUT (Pre)	Yes	$0.944 \pm 0.076(\text{stat}) \pm 0.231(\text{sys})$	$1.107 \pm 0.101(\text{stat}) \pm 0.316(\text{sys})$
NEUT (Post)	Yes	$0.944 \pm 0.076(\text{stat}) \pm 0.230(\text{sys})$	$1.107 \pm 0.101(\text{stat}) \pm 0.314(\text{sys})$
Pre-BANFF	Yes	$0.926 \pm 0.072(\text{stat}) \pm 0.227(\text{sys})$	$1.079 \pm 0.101(\text{stat}) \pm 0.308(\text{sys})$
Post-BANFF	Yes	$0.992 \pm 0.081(\text{stat}) \pm 0.242(\text{sys})$	$1.152 \pm 0.106(\text{stat}) \pm 0.327(\text{sys})$

Table 4.35: Summary of the predictions for the number of NC1 π^0 on-water vertices. The pre- and post-BANFF fit reweightings predict a slightly different number of events than the flux-weighted NEUT Monte Carlo.

NEUT	Pre-BANFF	Post-BANFF
157.2 ± 2.5	164.4 ± 2.7	149.3 ± 2.4

1622 the post-BANFF fit, the on-water rate is $99.5 \pm 43.1(\text{stat}) \pm 89.1(\text{sys})$ leading to a ratio of
 1623 $0.697 \pm 0.232(\text{stat}) \pm 0.454(\text{sys})$.

1624 4.5.2 Comparing Fit Results

1625 Table 4.34 lists the possible P \emptyset D water-in and water-out configuration ratios for the rate
 1626 of NC1 π^0 interactions. Listed are both the results for the default fits and the unconstrained
 1627 g factor fits. With the reweighting of the pre- and post-BANFF fit central values, the Monte
 1628 Carlo prediction for the number of NC1 π^0 events on-water in the P \emptyset D will shift, this is

Table 4.36: Summary of the on-water NC1 π^0 event rate calculations for the P \emptyset D. The first column are based on the results of the unconstrained g factor fits. The second column are based on the results of the default fits.

	$g \neq 0$	$g = 0$
NEUT (Pre)	$102.4 \pm 42.5(\text{stat}) \pm 90.4(\text{sys})$	$106.4 \pm 41.0(\text{stat}) \pm 72.6(\text{sys})$
NEUT (Post)	$102.4 \pm 42.5(\text{stat}) \pm 89.3(\text{sys})$	$106.4 \pm 41.0(\text{stat}) \pm 71.9(\text{sys})$
Pre-BANFF	$108.5 \pm 43.0(\text{stat}) \pm 92.5(\text{sys})$	$114.6 \pm 38.1(\text{stat}) \pm 74.6(\text{sys})$
Post-BANFF	$99.5 \pm 43.1(\text{stat}) \pm 89.1(\text{sys})$	$104.4 \pm 40.0(\text{stat}) \pm 72.3(\text{sys})$

Table 4.37: Summary of the data to Monte Carlo ratios of the rate of NC1 π^0 interactions in the P \emptyset D. The first column are based on the results of the unconstrained g factor fits. The second column are based on the results of the default fits.

	$g \neq 0$	$g = 0$
NEUT (Pre)	$0.652 \pm 0.270(\text{stat}) \pm 0.576(\text{sys})$	$0.677 \pm 0.261(\text{stat}) \pm 0.462(\text{sys})$
NEUT (Post)	$0.652 \pm 0.270(\text{stat}) \pm 0.569(\text{sys})$	$0.677 \pm 0.261(\text{stat}) \pm 0.457(\text{sys})$
Pre-BANFF	$0.660 \pm 0.262(\text{stat}) \pm 0.566(\text{sys})$	$0.697 \pm 0.232(\text{stat}) \pm 0.454(\text{sys})$
Post-BANFF	$0.666 \pm 0.289(\text{stat}) \pm 0.599(\text{sys})$	$0.699 \pm 0.254(\text{stat}) \pm 0.484(\text{sys})$

1629 described in Table 4.35. These values can then be compared to the air subtracted on-water
 1630 values listed in Table 4.36 in order to calculate the final data to Monte Carlo ratios shown
 1631 in Table 4.37. Curiously, even though the P \emptyset D water-in and water-out configuration ratios
 1632 of data to Monte Carlo show a large discrepancy between the default fits and unconstrained
 1633 g factor fits, the final on-water ratio is not greatly affected.

Chapter 5

Systematics

The following chapter describes the systematic uncertainties as they will be applied to the water-in and water-out $\text{NC1}\pi^0$ ratios. The first section covers the effect of the energy scale on the analysis, including effects from the geometry differences, the Monte Carlo and data photoelectron peak discrepancies, and the error on the number of signal due to the fitted energy scale. The next section describes the variation in $\text{P}\emptyset\text{D}$ response over time. Following that are the errors that come from the uncertainty in the knowledge of the mass and alignment. Next the fiducial volume uncertainties are explained. There are two uncertainties, one dealing with how the result will change if Monte Carlo and data are scaled together and one dealing with what happens when there is a systematic shift between data and Monte Carlo. After that, the systematic uncertainties that arise using T2KReWeight on the flux and cross sections are explained. The reconstruction uncertainties are then examined. First, a look at the systematic shift between data and Monte Carlo of the Track PID reconstruction is taken. Then, the optimized cuts are studied for any data to Monte Carlo shifts. Lastly, a description of the the muon decay fake identification rate and the efficiency for finding a muon decay is taken and used as a constraint in the constraint matrix of the simultaneous extended maximum likelihood fit. The last section deals with the systematic on the background shape, which is done by examining the result of fixing the g factor to zero. This systematic is only dealt with in the case of an unconstrained g factor.

5.1 Energy Scale

There are a few ways the energy scale can be affected. The first relies on any density differences in the detector in the as-built and Monte Carlo geometries. This can affect the efficiency of the detector. Next, an issue was found with low charge deposit between data and Monte Carlo. There was a large difference in the appearance of the photoelectric (PE) peaks expected by the MPPCs. Lastly, the error on the energy scale result of the fit needs to be accounted for and applied to the error on the number of signal events fit.

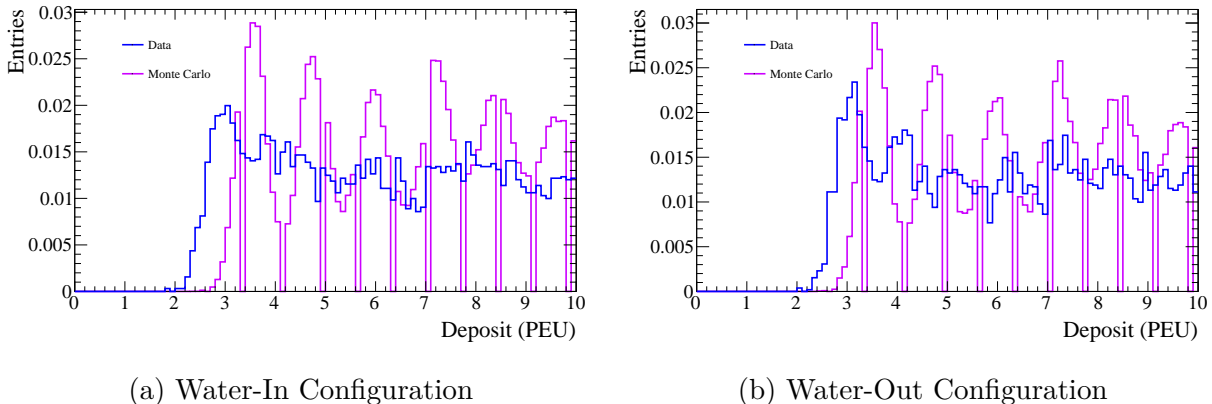


Figure 5.1: The distributions of the charge of hits that contribute to the selected sample. The Monte Carlo shows some digitization (where the plot goes to zero) as expected from the electronics simulation.

1661 5.1.1 Geometry Differences

1662 In order to see how changing the detector density changes the efficiency, the P \emptyset D water-in
 1663 and water-out configuration's efficiency and mass can be used as an approximation. Using
 1664 the efficiencies listed in Table 4.17, the percent change in efficiency from the P \emptyset D water-out
 1665 configuration to the P \emptyset D water-in configuration is $127.3 \pm 2.7(\text{stat})\%$. Using the values of the
 1666 water mass listed in Table 3.4, there is a mass of 1924.08 ± 0.11 kg in the Monte Carlo and
 1667 1902 ± 16 kg in the as-built approximation. Combining the systematic difference between
 1668 the Monte Carlo and as-built masses (22.08 ± 16 kg) with its statistical uncertainty gives
 1669 a conservative estimate of the total error on the difference between the P \emptyset D water-in and
 1670 water-out configurations. This total error is calculated to be 27.3 kg. Given that the dry mass
 1671 of the P \emptyset D is completely correlated between the water-in and water-out configurations, the
 1672 percent change in the mass is $155.5 \pm 0.03(\text{stat}) \pm 0.79(\text{sys})\%$. Next the fractional systematic
 1673 error of the mass, which is 0.51%, is applied to the efficiency. This makes the percent change
 1674 in efficiency from the P \emptyset D water-out to P \emptyset D water-in configuration $127.3 \pm 2.7(\text{stat}) \pm$
 1675 $0.65(\text{sys})\%$. Adding the statistical and systematic errors in quadrature gives 2.8% which is
 1676 then used as a conservative estimate of the systematic due to any geometric differences or
 1677 density fluctuations.

1678 5.1.2 PE Peak Uncertainty

1679 In Production 5, the Monte Carlo incorrectly modeled the photo-electron (PE) peaks
 1680 expected. There were several implementation issues found, the PE peak values, the spread
 1681 of the peaks etc. This issue appears in both the P \emptyset D water-in and water-out configurations,
 1682 as seen in Figure 5.1. For a 3D shower to be reconstructed, the minimum requirement for
 1683 hits is that there be at least one hit in each projection and that there be at least 5 hits in
 1684 either projection. An example of this is seen in Figure 5.2. In order to estimate the effect
 1685 this has on the NC1 π^0 analysis, the final sample of selected events is studied. A cut is placed

5.1. ENERGY SCALE

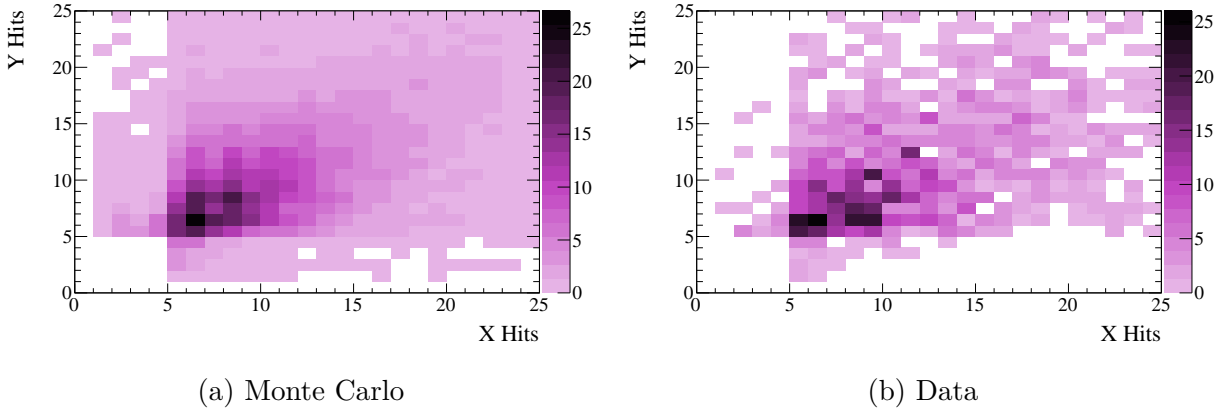


Figure 5.2: These plots demonstrate the unmodified number of hits in the X-Z and Y-Z projections for the P \emptyset D water-in configuration.

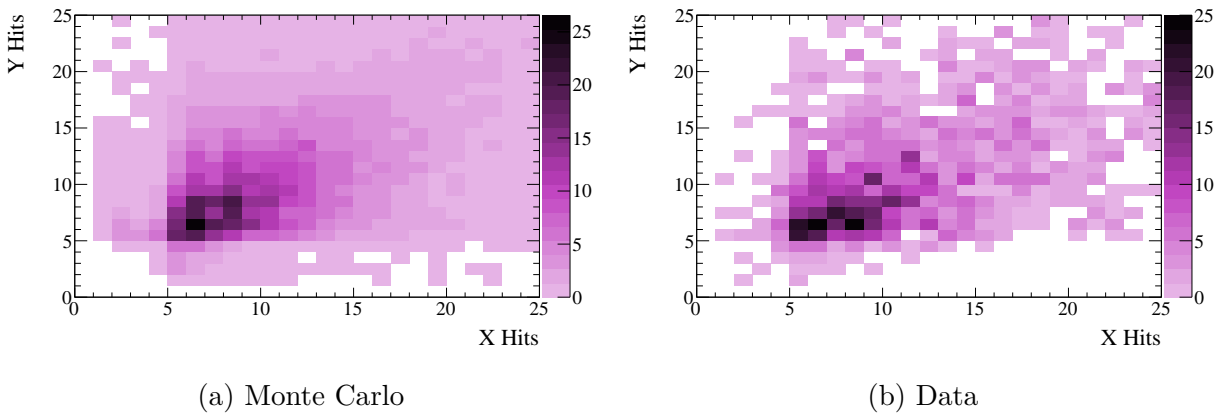


Figure 5.3: These plots demonstrate the number of hits in the X-Z and Y-Z projections for the P \emptyset D water-in configuration after a cut has been applied at 3.5 PEU.

Table 5.1: A summary of the loss in events for various charge deposit cuts for the P \emptyset D water-in configuration. The first column lists the charge deposit cut used. The next two columns list the number of events passing the two shower requirement for both data and Monte Carlo. The two columns after that list the percentage of the total events that are lost due to the charge deposit cut. The last column lists the difference between the percent lost of the data and Monte Carlo.

Cut	MC	Data	MC Lost (%)	Data Lost (%)	Difference (%)
0.0	893.0	775	0.0	0.0	0.0
3.0	892.8	770	0.03	0.65	0.62
3.5	891.3	768	0.20	0.90	0.71
4.0	888.0	766	0.57	1.16	0.59
4.5	886.7	765	0.71	1.29	0.58
5.0	884.5	764	0.96	1.42	0.46
5.5	882.8	763	1.15	1.55	0.40
6.0	881.0	760	1.34	1.94	0.59
10.0	860.0	743	3.63	4.13	0.50

Table 5.2: A summary of the loss in events for various charge deposit cuts for the P \emptyset D water-out configuration. The first column lists the charge deposit cut used. The next two columns list the number of events passing the two shower requirement for both data and Monte Carlo. The two columns after that list the percentage of the total events that are lost due to the charge deposit cut. The last column lists the difference between the percent lost of the data and Monte Carlo.

Cut	MC	Data	MC Lost (%)	Data Lost (%)	Difference (%)
0.0	629.4	555	0.0	0.0	0.0
3.0	629.4	555	0.0	0.0	0.0
3.5	628.5	552	0.14	0.54	0.40
4.0	626.5	552	0.46	0.54	0.08
4.5	626.2	549	0.51	1.08	0.57
5.0	623.6	548	0.93	1.26	0.34
5.5	622.7	546	1.07	1.62	0.56
6.0	620.9	545	1.35	1.80	0.45
10.0	607.4	538	3.51	3.06	0.45

5.1. ENERGY SCALE

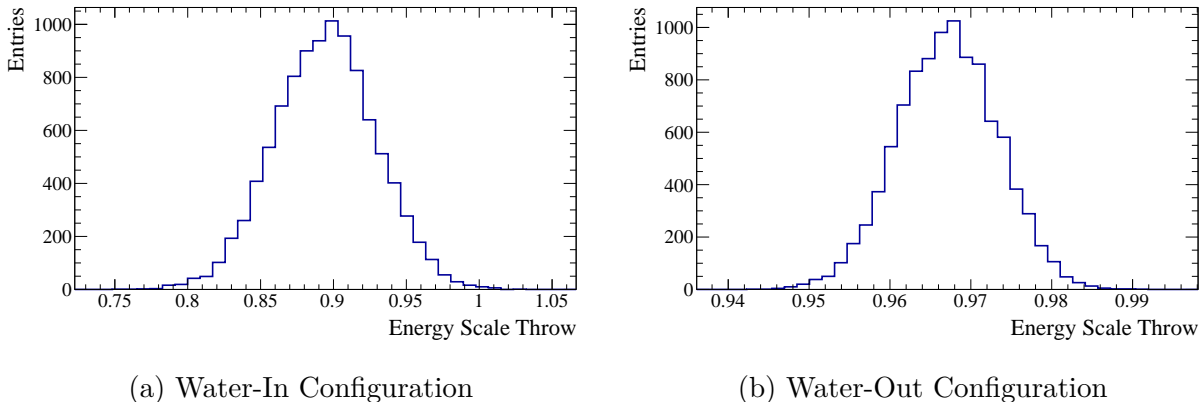


Figure 5.4: The distribution of the throws of the energy scale values. The mean and sigma of the distributions come from the analysis fits.

Table 5.3: The systematic result from the error on the energy scale output from the fit. The first column is the number of Monte Carlo predicted events. The next two columns describe the distribution after throwing the energy scale. The last three columns are the result of calculated the fractional shift from nominal, the fractional RMS of the distribution and the final systematic error.

	Signal	Mean	RMS	Shift (%)	Shift Error (%)	Total Error (%)
Water-In	434.9	411.4	8.6	-5.4	2.1	5.8
Water-Out	290.3	287.8	0.4	-0.9	0.1	0.9

1686 on the charge deposit and the hits are counted. An example of the effect of the charge cut set
 1687 at 3.5 PEU for the P \emptyset D water-in configuration is shown in Figure 5.3 where a migration to
 1688 the lower left corner is seen. If the shower fails the requirement for five hits in one projection
 1689 and some hits in both, the event is failed. The percentage of failed data events is compared
 1690 to the percentage of failed Monte Carlo events in order to extract a systematic error. The
 1691 effect of various charge deposit cuts is listed in Tables 5.1 and 5.2. There is a small turn
 1692 on effect of the cut, so in order to get a systematic, the average of the data to Monte Carlo
 1693 difference is taken for all cuts above 3.5 PEU. This gives a final systematic of 0.6% for the
 1694 P \emptyset D water-in configuration and a 0.4% systematic for the P \emptyset D water-out configuration.

1695 5.1.3 Energy Scale

1696 After the fit has been completed, the energy scale was modeled as a Gaussian using the
 1697 value and error from the fit as the mean and sigma. The goal is to turn this error on the
 1698 energy scale and map it to an error on the number of selected signal events. The effect
 1699 of this scale and its error need to be quantified on the final event rate. Then the NC1 π^0
 1700 efficiency curve, ϵ , as a function of momentum, \vec{p} , was calculated, see Figure 4.24. In order

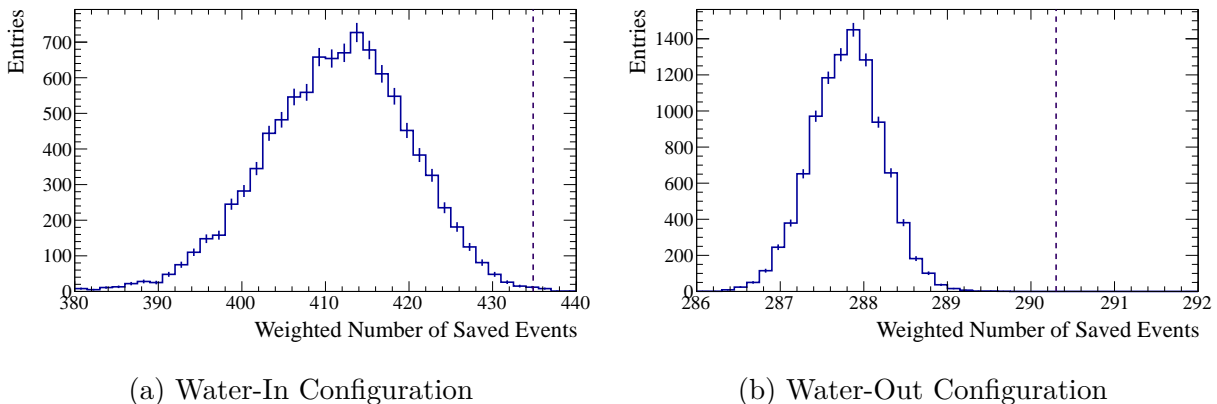


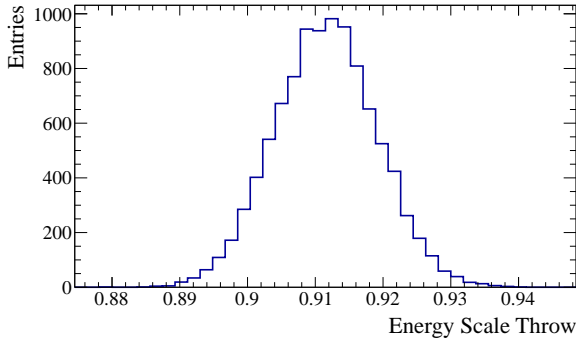
Figure 5.5: The distribution of the weighted signal events from throws of the energy scale values. The vertical dashed line represents the nominal number of Monte Carlo signal weighted events.

Table 5.4: The systematic result from the error on the energy scale output from the fit with an unconstrained g factor. The first column is the number of Monte Carlo predicted events. The next two columns describe the distribution after throwing the energy scale. The last three columns are the result of calculated the fractional shift from nominal, the fractional RMS of the distribution and the final systematic error.

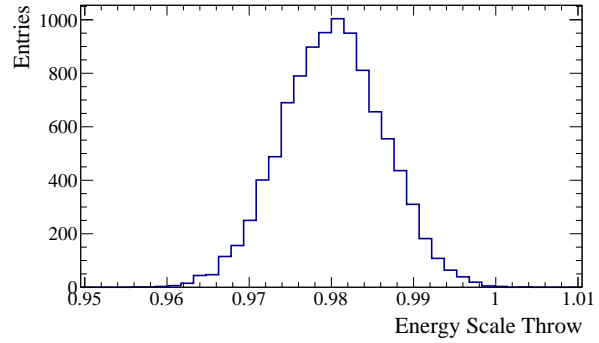
	Signal	Fit Mean	Fit Sigma	Shift (%)	Shift Error (%)	Total Error (%)
Water-In	434.9	415.9	1.8	-4.4	0.4	4.4
Water-Out	290.3	288.7	0.5	-0.5	0.2	0.6

1701 to understand this systematic, the efficiency curve was shifted by a random throw of the
1702 energy scale, e , i.e. $\epsilon(|\vec{p}|) \rightarrow \epsilon(|\vec{p}| \cdot e)$. Taking the ratio of the shifted efficiency curve to
1703 the nominal efficiency curve results in a new event weighting. Using this new weighting,
1704 the number of saved signal events in the Monte Carlo is calculated for each of many throws
1705 of the energy scale and stored in a histogram. The mean and RMS of the distribution is
1706 extracted to be used as a systematic error. The shift from the nominal number of Monte
1707 Carlo $\text{NC}1\pi^0$ saved events and the fractional size of the RMS are components of the final
1708 systematic error. The shift and the error are added in quadrature to extract the systematic
1709 value. The distribution of the ten thousand throws of the energy scale are shown in Figure
1710 5.4. The effect of the energy scale on the weighted sum is shown in Figure 5.5 and listed
1711 in Table 5.3. The $\text{P}\emptyset\text{D}$ water-in and water-out configurations are expected to have different
1712 resolutions, which is reflected by the difference in the values of the systematic errors, due to
1713 a different fraction of active material.

5.1. ENERGY SCALE

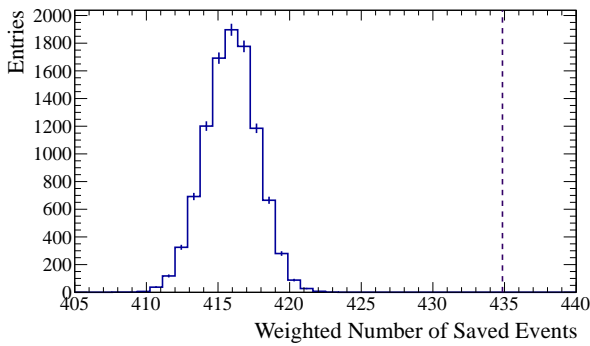


(a) Water-In Configuration

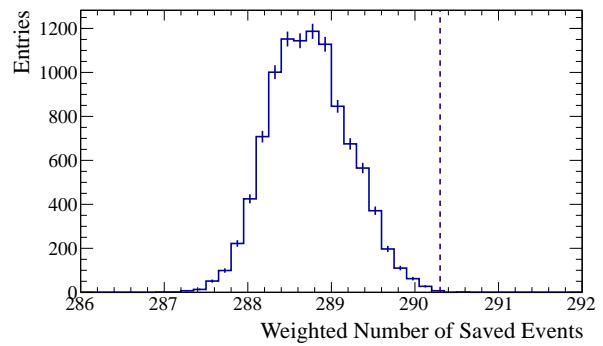


(b) Water-Out Configuration

Figure 5.6: The distribution of the throws of the energy scale values from the unconstrained g factor fit. The mean and sigma of the distributions come from the analysis fits.



(a) Water-In Configuration



(b) Water-Out Configuration

Figure 5.7: The distribution of the weighted signal events from throws of the energy scale values from the unconstrained g factor fit. The vertical dashed line represents the nominal number of Monte Carlo signal weighted events.

1714 Removing Model Dependencies

1715 The energy scale for the unconstrained g factor fit differs from that in the default fit,
 1716 therefore, this systematic needs to be dealt with separately. The distribution of the ten
 1717 thousand throws of the energy scale are shown in Figure 5.6. The effect of the energy scale
 1718 on the weighted sum is shown in Figure 5.7 and listed in Table 5.4.

1719 5.2 Detector Variations

1720 In Production 4, an extensive study of the channel-to-channel variations was performed.
 1721 The end result was that this provided a negligible effect to the overall systematics ($< 1\%$)
 1722 [27]. Additionally, a study smearing the Monte Carlo deposit by 15%, this value was chosen
 1723 in a data comparison study, was performed. After the smearing, the energy scale was found
 1724 to be effected by 0.1% which is negligible compared to the other systematics.

1725 Variation in P \emptyset D Response Over Time

1726 The P \emptyset D charge deposit response varies over time. Most of the variation is removed at
 1727 the calibration stage. However, the remaining, small, variations lead to this systematic which
 1728 are studied by a subsample of the data containing through-going muons. The Monte Carlo
 1729 fixes the MIP peak at 37 which the data MIP peaks need to be corrected to match. The
 1730 MIP peak is extracted by plotting the charge deposit for each hit from events with a single
 1731 track that crosses the P \emptyset D. The distributions are then fit to Landau Gaussian convolutions.

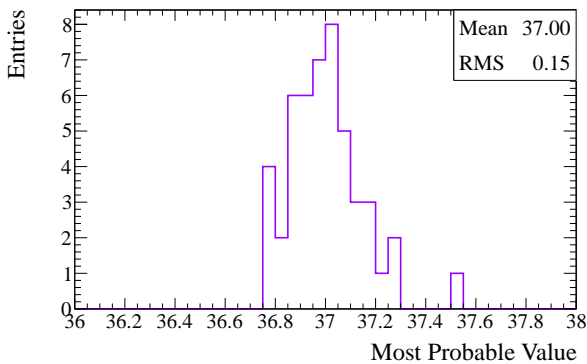
1732 For good fits, selected with a reduced $\chi^2 < 25$, the most probable values are saved. Runs
 1733 1-3 are processed with all appropriate calibration (RDP- real data processing) and therefore
 1734 get an average correction to 37 by run. Run 4 the calibration has not been fully processed
 1735 (FPP- first pass processing) and each week gets a separate calibration constant.

1736 The systematic uncertainty assigned to this correction, which is also applied in the NC1 π^0
 1737 analysis, is calculated from the mean and RMS or the spread of the post-correction peak
 1738 values. This is shown in Figure 5.8 and is summarized in Table 5.5. Two errors are considered,
 1739 one uses the RMS of the distribution, the other uses the more conservative value of the total
 1740 spread of the distribution. This analysis will use the conservative error of 1.8%.

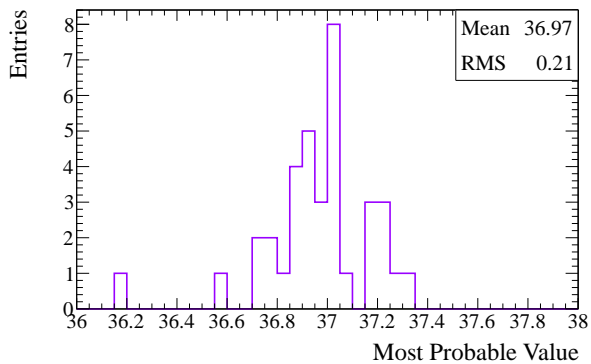
Table 5.5: A summary of the post-correction data. The mean and RMS are from the distributions in Figure 5.8. The width is the width of the distributions disregarding outliers.

	Mean	RMS	Width	Error	Conservative
	(PEU)	(PEU)	(PEU)	(%)	Error (%)
X Layers	37.00	0.15	0.55	0.40	1.49
Y Layers	36.97	0.21	0.65	0.58	1.76
Combined	36.99	0.18	0.65	0.48	1.76

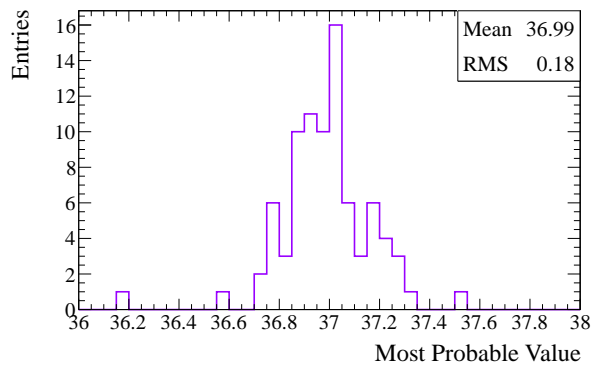
5.2. DETECTOR VARIATIONS



(a) X Layers



(b) Y Layers



(c) X and Y Layers Combined

Figure 5.8: The MIP peak values after correction. Each entry in the histograms represent one continuous week of data. There are outliers due to low statistic weeks, but these are not considered when calculating the systematic error.

5.3 Mass Uncertainty

A detailed mass calculation was done for the as-built mass as well as the mass in the Monte Carlo in Section 3.1. At the time of writing, an analysis of the fiducial mass of the water for Run 4 was unavailable, so this analysis is applying the previously calculated information from Run 2. A summary of the pertinent masses is in Table 3.4.

Two corrections are applied depending where the true vertex is located. If the true vertex is not on-water, it gets weighted by the averaged dry mass. If the true vertex is on-water, and the P \emptyset D is in the water-in configuration, then the vertex is weighted by the water mass.

However some added complexity falls into the P \emptyset D dry mass correction. Between Runs 1 and 2, the entire water sensor system was replaced leading to a slight difference in the fiducial mass, which is handled by Run. It should be noted, most of the Monte Carlo to as-built difference stems from the water target dead material not being modeled in the Monte Carlo. In order to understand the systematic error that arises from the mass, 10,000 Gaussian throws are done of the mass correction factors. The Gaussian distribution for the throws have the mean and sigma pulled from the values in Table 5.6. An example of a series of throws done for the P \emptyset D water-in fit is shown in Figure 5.9. The fit is rerun with these different correction factors applied to Monte Carlo. Since the energy scale is handled separately, the energy scale is fixed to the nominal fit value, all other variables are allowed to float freely. The fitted data to Monte Carlo ratio is then fit to a Gaussian distribution, see Figure 5.10. The results of the fits are described in Table 5.7. The systematic errors are taken as the sigmas of the fitted distributions. The P \emptyset D water-in configuration has a systematic error of 0.5% and the P \emptyset D water-out configuration has a systematic of 0.9%.

Removing Model Dependencies

As the output of this systematic depends on the results of the fit, the systematic is calculated again for the unconstrained g factor fit. The fitted data to Monte Carlo ratio is then fit to a Gaussian distribution, see Figure 5.11. The results of the fits are described in Table 5.8. The P \emptyset D water-in configuration has a systematic error of 0.4% and the P \emptyset D water-out configuration has a systematic of 0.6%.

Table 5.6: The correction factor of the mass for the running period for both the on-water and off-water components.

Run Period	On-Water (%)	Off-Water (%)
Run 1	98.9 ± 0.8	102.6 ± 1.0
Run 2+	98.9 ± 0.8	103.1 ± 1.0

5.3. MASS UNCERTAINTY

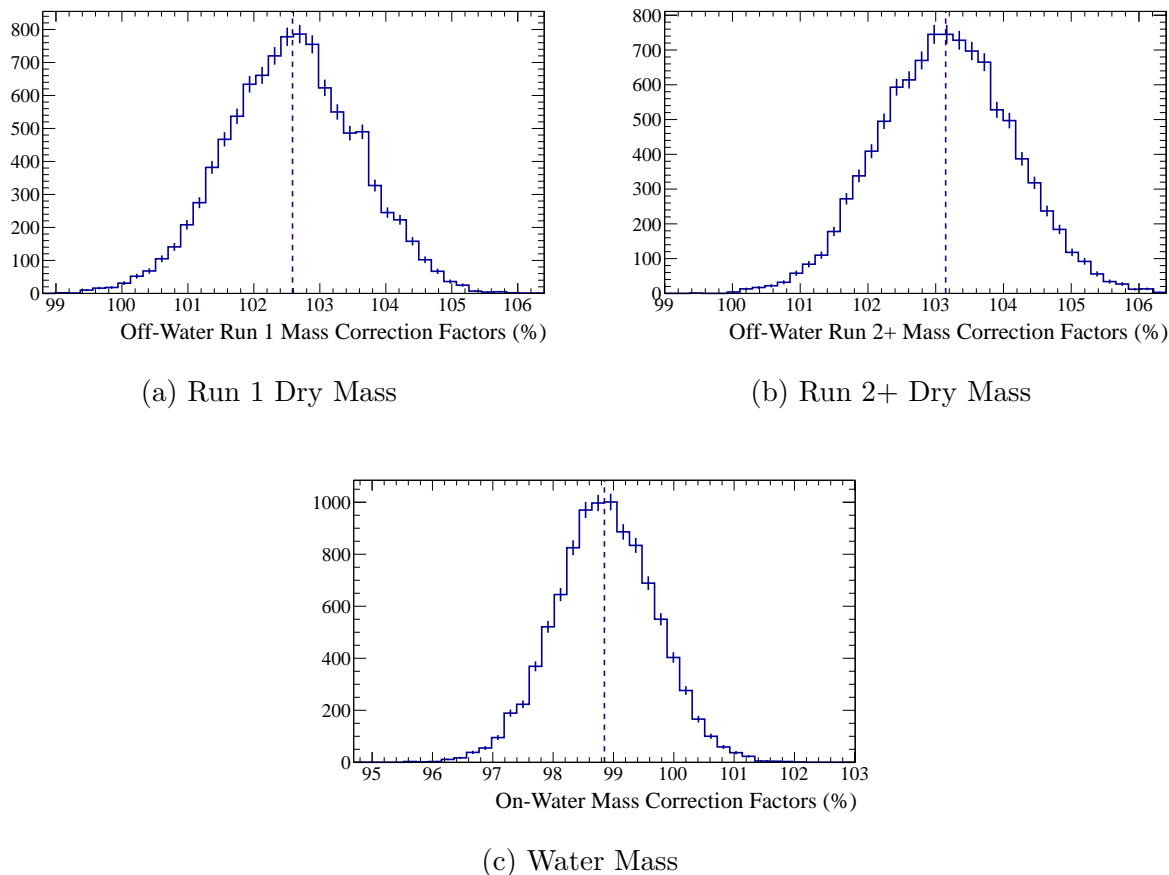


Figure 5.9: An example of the throws of the mass corrections. These were used to reweight the Monte Carlo events before fitting to the data. The vertical line marks the central values given in Table 5.6.

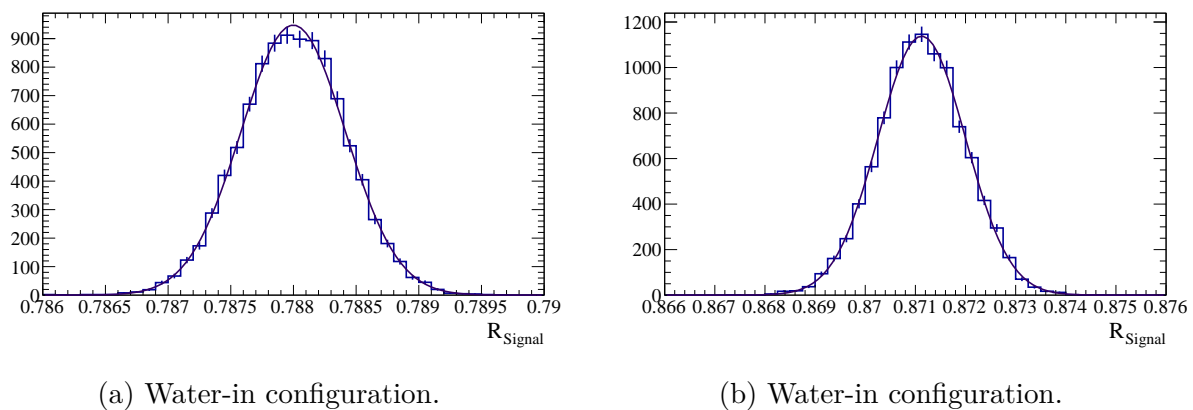
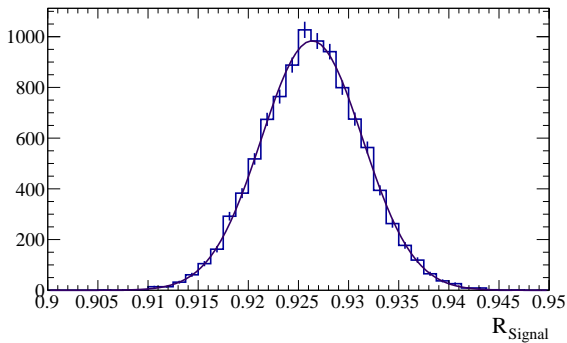


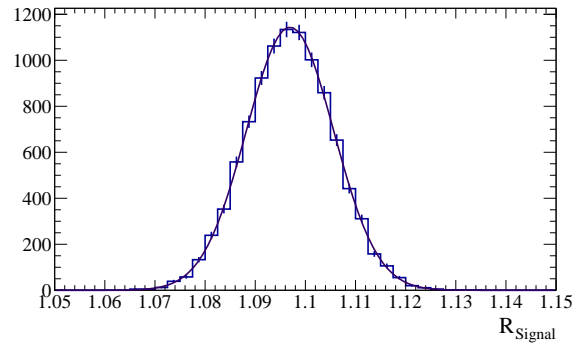
Figure 5.10: The data to Monte Carlo ratios of the fitted signal after 10,000 throws of the mass corrections. Shown are the distributions for both the P \emptyset D water-in and P \emptyset D water-out configurations.

Table 5.7: The summary of the Gaussian fits in Figure 5.10. Listed are the fitted values, for the data to Monte Carlo ratio of the number of signal events in the P \emptyset D water-in and P \emptyset D water-out configuration. The mean is the ratio and the sigma is taken as the systematic error.

	Constant	Mean (%)	Sigma (%)
Water-In	1222.9 ± 15.0	77.4 ± 0.0	0.41 ± 0.00
Water-Out	1264.8 ± 15.5	84.2 ± 0.0	0.63 ± 0.00



(a) Water-in configuration.



(b) Water-out configuration.

Figure 5.11: The data to Monte Carlo ratios of the fitted signal after 10,000 throws of the mass corrections. Shown are the distributions for both the P \emptyset D water-in and P \emptyset D water-out configurations.

Table 5.8: The summary of the Gaussian fits in Figure 5.11. Listed are the fitted values for the data to Monte Carlo ratio of the number of signal events in the P \emptyset D water-in and P \emptyset D water-out configuration. The mean is the ratio and the sigma is taken as the systematic error.

	Constant	Mean (%)	Sigma (%)
Water-In	983.8 ± 12.1	92.6 ± 0.0	0.51 ± 0.00
Water-Out	1143.9 ± 14.0	109.7 ± 0.0	0.87 ± 0.01

1769 5.4 Alignment

1770 The shifts on the alignment are less than 2 mm, as reported in Section 3.6. The ap-
 1771 proximate resolution of the detector in X and Y is 2.5 mm. Due to the construction of the
 1772 fiducial volume, the Z boundaries of the volume occur in the middle of a PØDule, so align-
 1773 ment shifts in Z will have little to no effect on this analysis. If the fiducial volume is scaled
 1774 by the resolution in X and Y, there is a 0.31% change in the fiducial volume. If instead, the
 1775 fiducial volume is scaled by the maximum alignment parameter, a 0.24% change is found.
 1776 Of primary concern is the change due to alignment, so the difference is considered as the
 1777 systematic, 0.07%.

1778 5.5 Fiducial Volume

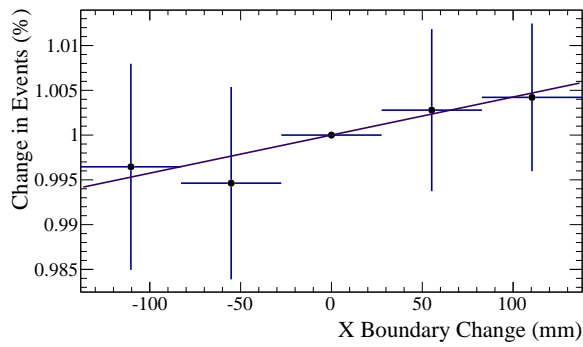
1779 Two concerns were addressed when examining the fiducial volume. The first was how
 1780 data and Monte Carlo scaled together. The second was how the data can shift or scale
 1781 separately from the Monte Carlo fiducial volume.

1782 5.5.1 Fiducial Volume Scaling

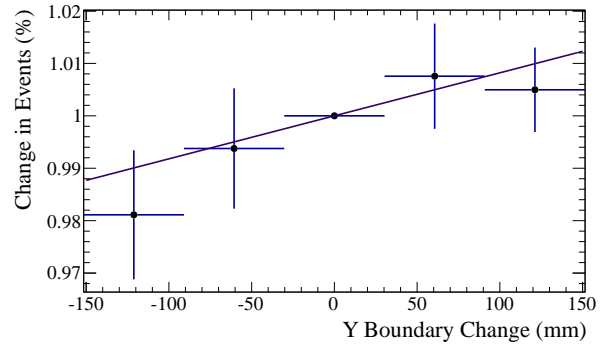
1783 The vertex resolutions discussed in Section 4.1 are used as the step size to expand and
 1784 contract the fiducial volume. The concern for this systematic is the migration of selected
 1785 events into and out of the fiducial volume if the volume definition changes. First, the number
 1786 of events in data and Monte Carlo are counted for varying sizes of the fiducial volume. The
 1787 fiducial volume is varied in the X, Y, Z Downstream, and Z Upstream independently and
 1788 the results are combined for the final systematic error. The Z upstream and Z downstream
 1789 refer to the edges of the fiducial volume that are perpendicular to the Z axis. The upstream
 1790 and downstream edges are considered separately because a large difference in the statistics
 1791 of the vertices that make it to the final sample at each edge is expected. A vertex that is
 1792 created at the upstream edge is more likely to make it to the final sample than one at the
 1793 downstream edge due to the containment cut. The nominal volume is considered as the
 1794 reference point, so the ratio of data to Monte Carlo events is set to 1.0 with an error of 0.0.
 1795 For the $\pm 1\sigma$ and $\pm 2\sigma$ steps, the number of events added or subtracted from the previous
 1796 step (either nominal for 1σ or 1σ values for 2σ) is calculated. The ratio of this excess or
 1797 deficiency is calculate and appropriate Poisson errors are assigned. A linear fit is performed
 1798 on this set of five points, see Figures 5.12 and 5.13. The fit parameters and their errors
 1799 are accessed. At 1σ from the nominal fiducial volume, the change in the data to Monte

Table 5.9: Summary of the fiducial scaling systematic errors.

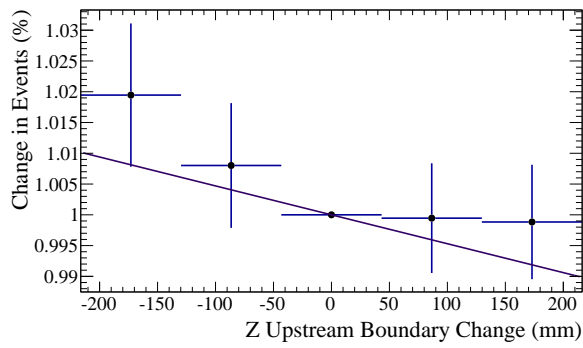
Coordinate	X (%)	Y (%)	Z-Upstream (%)	Z-Downstream (%)
Water-In	0.54	0.80	0.73	1.02
Water-Out	1.17	0.51	1.13	0.00



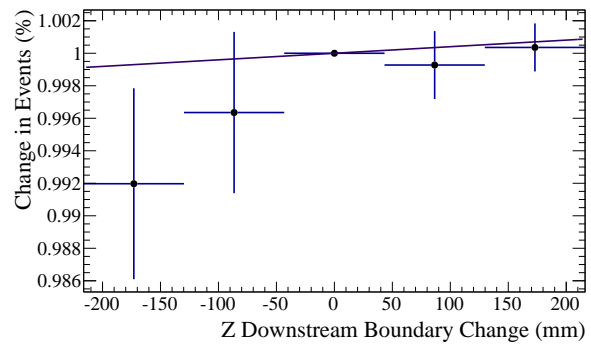
(a) X Fiducial Boundary



(b) Y Fiducial Boundary



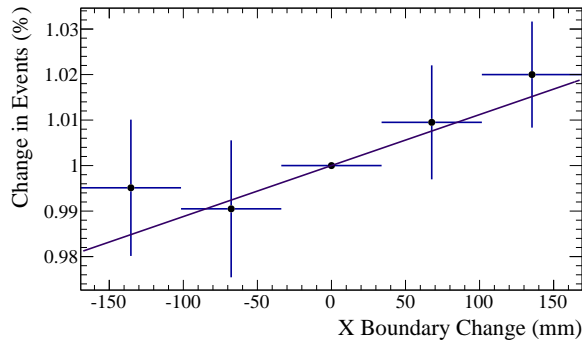
(c) Z Upstream Fiducial Boundary



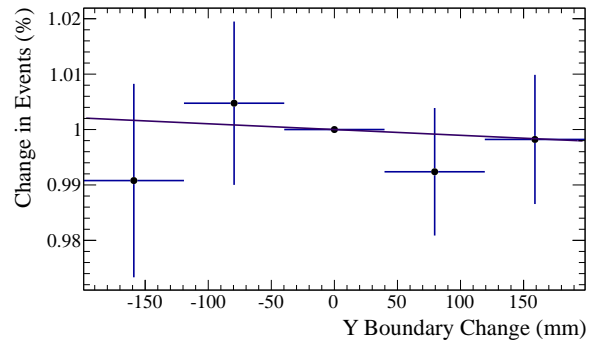
(d) Z Downstream Fiducial Boundary

Figure 5.12: The ratios of data to Monte Carlo candidate events at the edge of the fiducial volume for the water-in configuration.

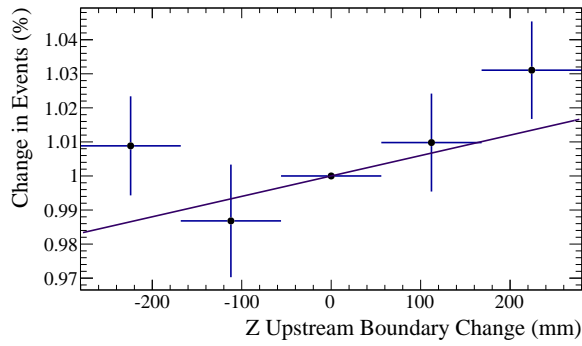
5.5. FIDUCIAL VOLUME



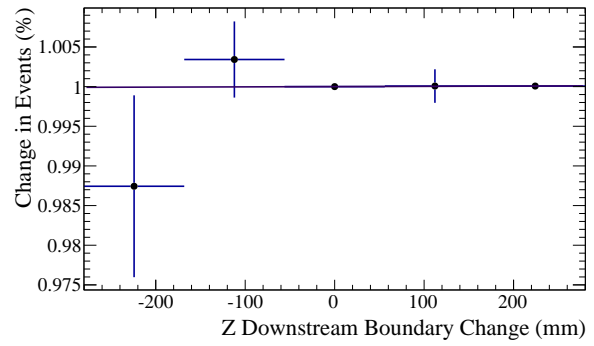
(a) X Fiducial Boundary



(b) Y Fiducial Boundary



(c) Z Upstream Fiducial Boundary



(d) Z Downstream Fiducial Boundary

Figure 5.13: The ratios of data to Monte Carlo candidate events at the edge of the fiducial volume for the water-out configuration.

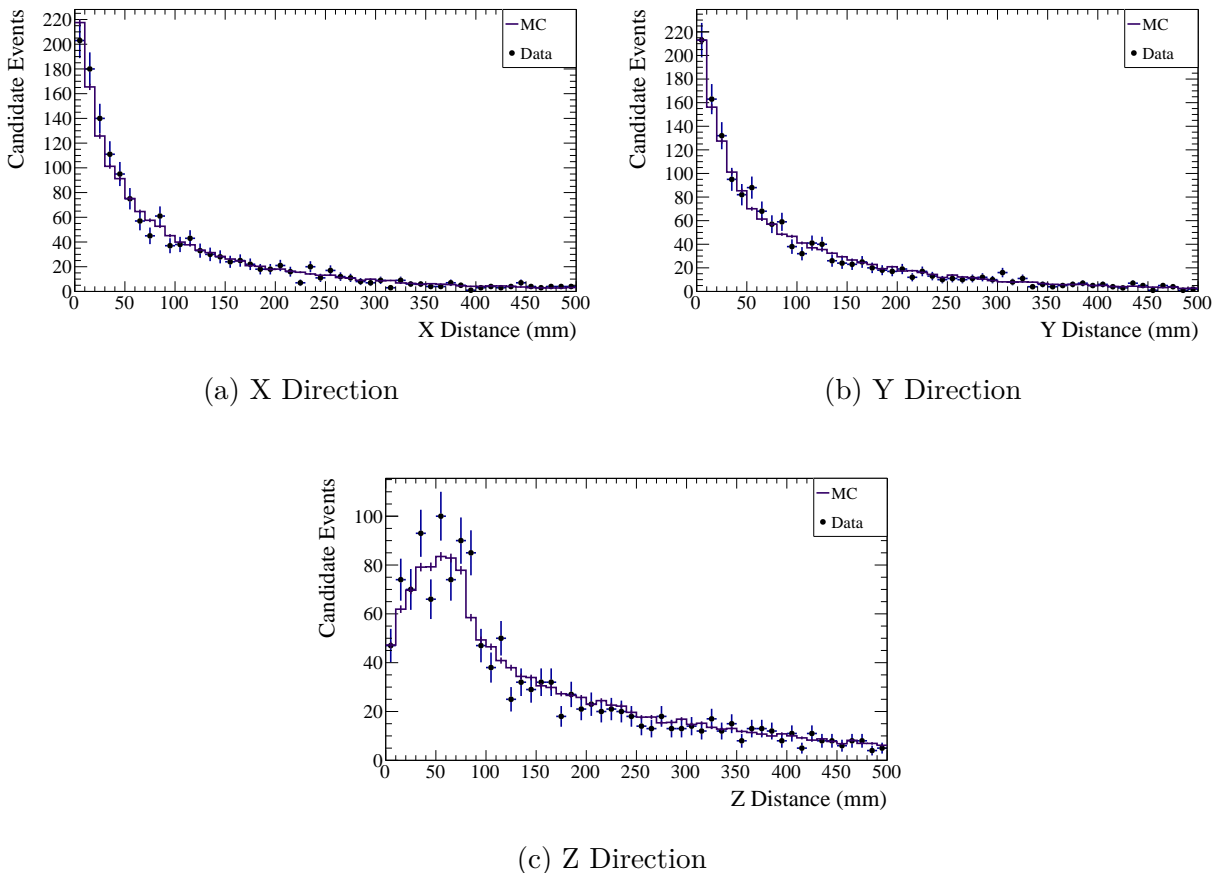


Figure 5.14: The bias between data and Monte Carlo is judged by the difference in the average distance from the π^0 vertex and the reconstructed photon vertices. These plots show the distributions for the P \emptyset D water-in configuration.

1800 Carlo ratio is calculated. The error on the change in the data to Monte Carlo is calculated
 1801 using the errors extracted from the fit. The slope and additional error are added together
 1802 to be utilized as the systematic error. The X and Y fiducial systematics are added linearly
 1803 then combined with the rest of the errors in quadrature. The result is a systematic error of
 1804 1.5% from fiducial volume scaling for the P \emptyset D water-in configuration and 2.0% for the P \emptyset D
 1805 water-out configuration.

1806 5.5.2 Fiducial Volume Shift

1807 The previous systematic dealt with data and Monte Carlo scaling together. This system-
 1808 atic addresses the case where the Monte Carlo scales different from the data (or vice versa).
 1809 In order to understand if the reconstruction is biased between the data and Monte Carlo,
 1810 the distance between the reconstructed π^0 vertex and the decay photons were measured in
 1811 X, Y and Z, shown in Figures 5.14 and 5.15. A summary of the bias values is in Table 5.10.
 1812 If these are compared to the vertex resolution in Tables 4.1 and 4.2, these biases are found

5.5. FIDUCIAL VOLUME

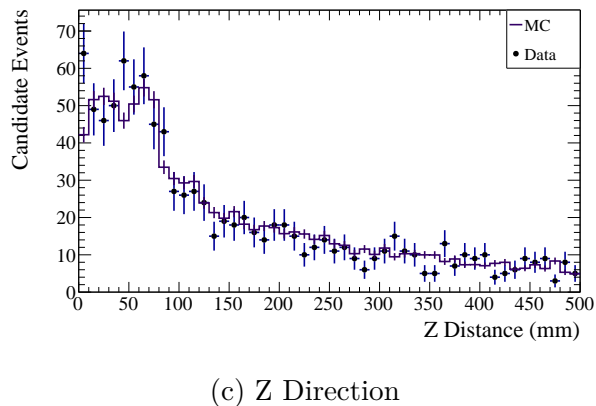
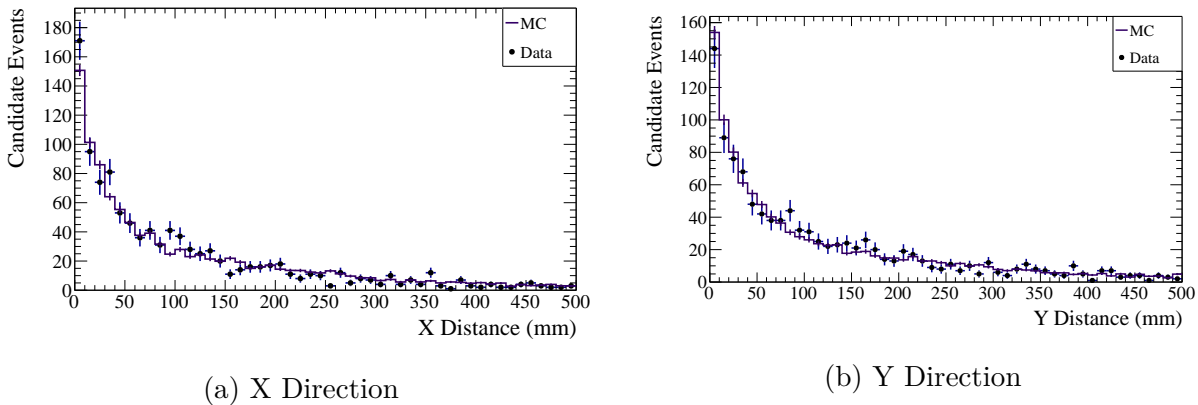


Figure 5.15: The bias between data and Monte Carlo is judged by the difference in the average distance from the π^0 vertex and the reconstructed photon vertices. These plots show the distributions for the P \emptyset D water-out configuration.

Table 5.10: Summary of the bias between data and Monte Carlo as measured by the distance between reconstructed vertex and the reconstruction photons.

	X (mm)	Y (mm)	Z (mm)
Water-In	1.5 ± 2.8	2.3 ± 2.8	6.3 ± 3.3
Water-Out	9.3 ± 3.6	1.0 ± 3.8	5.6 ± 4.4

1813 to be relatively small. The difference in the means of the distributions is taken as the bias
 1814 between data and Monte Carlo. The number of selected events is assumed to scale linearly
 1815 with the target area. The volume is recalculated scaling all three lengths up and down by
 1816 the bias and its error. The fractional change in the volume from the nominal fiducial volume
 1817 is calculated and the larger fluctuation is used as the systematic error. For the P \emptyset D water-in
 1818 configuration, the systematic error is 1.1% and for the P \emptyset D water-out configuration, the
 1819 error is 1.7%.

1820 5.6 Flux and Event Generator Uncertainties

1821 The information from T2KReWeight is accessed in two ways. The first way provides con-
 1822 straints for the covariance matrix in the fit. The second uses the reweighted Monte Carlo
 1823 invariant mass spectrum to rerun the fit multiple times in order to get a systematic error for
 1824 flux and cross section on the final fit result.

1825 The flux parameters and their errors are listed in Table 5.11. This analysis ignores the
 1826 Super Kamiokande related flux errors, so there are only 25 parameters of interest. The
 1827 energy binning of the flux errors is described in Table 5.12. The cross section parameters
 1828 and their errors are listed in Table 5.13. The energy binning of the binned cross section
 1829 errors is shown in Table 5.14. There are 21 input parameters defined by the BANFF matrix.
 1830 A small subsample of cross section parameter contains an energy binning and that binning
 1831 is described in Table 5.13. These parameters were used in the 2013a oscillation analyses
 1832 [20]. The errors on all 46 parameters can be seen visually in Figure 5.17. There is a clear
 1833 improvement on the understanding of the parameter errors after the BANFF fit has been
 1834 performed. The correlations between the parameters are shown in Figure 5.16.

1835 After fixing the MC sample of selected events, the RooTracker Vertices for those events
 1836 are found and saved in a tree. Using those skimmed vertices, the selected events are passed
 1837 into T2KReWeight. The parameters described above are then tweaked and new weights are
 1838 created for every event.

1839 The majority of the T2KReWeight parameters are normalization factors. In order to
 1840 understand the sensitivity of the fit to T2KReWeight, the input PDFs are reweighted with
 1841 the tweaked values in each throw. After reweighting the PDFs, the fit is rerun. There were
 1842 1000 throws of the parameters. Each reweighted fit result is compared to the T2KReWeight
 1843 nominal Monte Carlo prediction, post- or pre-BANFF fit. The nominal T2KReWeight values
 1844 are discussed in Section 4.5. Figures 5.18 and 5.19 show the spread of the results after running
 1845 the fit. The distributions are summarized in Table 5.15. Taking the sum in quadrature of the
 1846 sigma and its error of the output fit gives the final systematic error. For the pre-BANFF fit,
 1847 the error is 2.9% and 3.7% for the P \emptyset D water-in and water-out configurations respectively.
 1848 For the post-BANFF fit, the error is 1.5% and 1.9% respectively. The size of these errors
 1849 indicate that the fit is relatively independent of the cross section normalizations.

1850 Removing Model Dependencies

1851 As the systematic depends on the output of the fit, to calculate the systematic for the shape
 1852 varying fit, the procedure is run again, freeing the g factor. Figures 5.20 and 5.21 show

5.6. FLUX AND EVENT GENERATOR UNCERTAINTIES

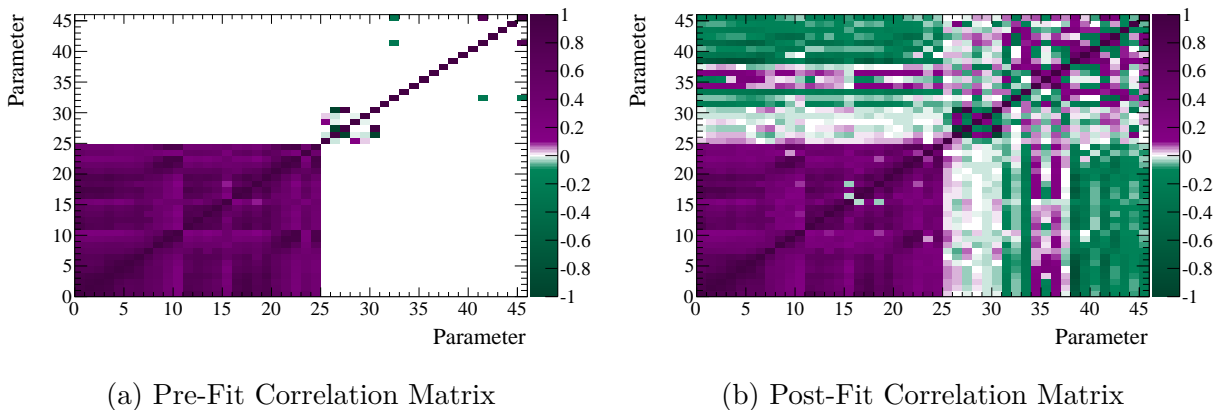


Figure 5.16: The input BANFF correlation matrices for the beam flux (parameters 0-24) and cross section (parameters 25-45) for the 2013 T2K oscillation analyses. Shown are the correlation matrices before and after the BANFF fit.

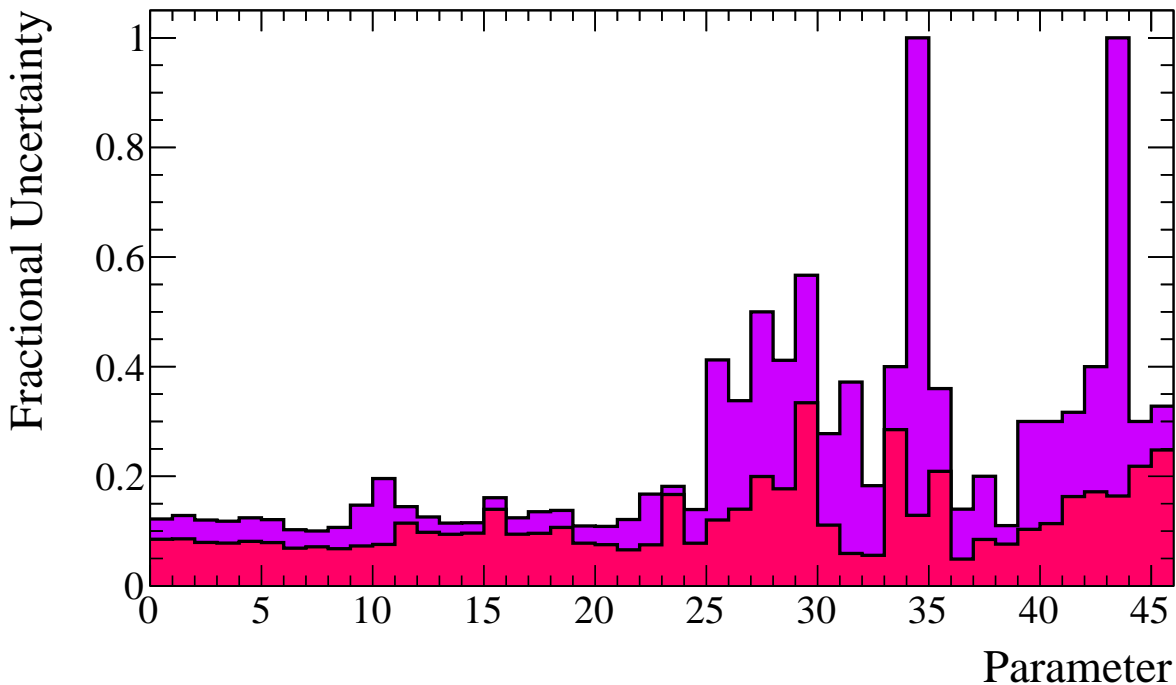


Figure 5.17: The input errors for the beam flux (parameters 0-24) and cross section (parameters 25-45) for the 2013 T2K oscillation analyses. The larger violet histogram shows the errors on the pre-BANFF fit parameters. The red overlay shows the errors on the post-BANFF fit parameters. Shown are the covariance matrices before and after the BANFF fit.

5.6. FLUX AND EVENT GENERATOR UNCERTAINTIES

Table 5.11: Summary of beam flux systematic errors used in T2K Reweight in the 2013 T2K oscillation analyses.

Parameter	Index	BANFF Pre-Fit	BANFF Post-Fit
ν_μ flux E0	0	1.000 ± 0.122	1.027 ± 0.085
ν_μ flux E1	1	1.000 ± 0.128	1.012 ± 0.086
ν_μ flux E2	2	1.000 ± 0.120	0.994 ± 0.079
ν_μ flux E3	3	1.000 ± 0.118	0.965 ± 0.078
ν_μ flux E4	4	1.000 ± 0.124	0.934 ± 0.081
ν_μ flux E5	5	1.000 ± 0.121	0.972 ± 0.079
ν_μ flux E6	6	1.000 ± 0.102	1.027 ± 0.069
ν_μ flux E7	7	1.000 ± 0.100	1.059 ± 0.071
ν_μ flux E8	8	1.000 ± 0.107	1.039 ± 0.068
ν_μ flux E9	9	1.000 ± 0.147	0.980 ± 0.073
ν_μ flux E10	10	1.000 ± 0.196	0.960 ± 0.076
$\bar{\nu}_\mu$ flux E0	11	1.000 ± 0.145	1.030 ± 0.114
$\bar{\nu}_\mu$ flux E1	12	1.000 ± 0.126	1.010 ± 0.098
$\bar{\nu}_\mu$ flux E2	13	1.000 ± 0.115	0.997 ± 0.094
$\bar{\nu}_\mu$ flux E3	14	1.000 ± 0.115	1.015 ± 0.096
$\bar{\nu}_\mu$ flux E4	15	1.000 ± 0.161	1.039 ± 0.140
ν_e flux E0	16	1.000 ± 0.124	1.024 ± 0.094
ν_e flux E1	17	1.000 ± 0.135	1.020 ± 0.096
ν_e flux E2	18	1.000 ± 0.138	0.988 ± 0.107
ν_e flux E3	19	1.000 ± 0.109	0.995 ± 0.078
ν_e flux E4	20	1.000 ± 0.109	1.015 ± 0.075
ν_e flux E5	21	1.000 ± 0.121	0.997 ± 0.066
ν_e flux E6	22	1.000 ± 0.167	0.947 ± 0.075
$\bar{\nu}_e$ flux E0	23	1.000 ± 0.182	1.014 ± 0.167
$\bar{\nu}_e$ flux E1	24	1.000 ± 0.139	0.953 ± 0.078

Table 5.12: The bin divisions in true neutrino energy for the binned beam flux parameters in the 2013 T2K oscillation analyses.

Parameter	Bins	True Neutrino Energy Bin Divisions (GeV)
ν_μ	11	0.0 - 0.4 - 0.5 - 0.6 - 0.7 - 1.0 - 1.5 - 2.5 - 3.5 - 5.0 - 7.0 - 30.0
$\bar{\nu}_\mu$	5	0.0 - 0.7 - 1.0 - 1.5 - 2.5 - 30.0
ν_e	7	0.0 - 0.5 - 0.7 - 0.8 - 1.5 - 2.5 - 4.0 - 30.0
$\bar{\nu}_e$	2	0.0 - 2.5 - 30.0

5.6. FLUX AND EVENT GENERATOR UNCERTAINTIES

Table 5.13: Summary of event generator systematic errors used in T2K Reweight in the 2013 T2K oscillation analyses.

Parameter	Index	BANFF Pre-Fit	BANFF Post-Fit
FSI inelastic low	25	0.000 ± 0.412	0.118 ± 0.120
FSI inelastic high	26	0.000 ± 0.338	0.445 ± 0.140
FSI π production	27	0.000 ± 0.500	-0.685 ± 0.200
FSI π absorption	28	0.000 ± 0.412	-0.270 ± 0.177
FSI charge exchange low	29	0.000 ± 0.567	0.360 ± 0.334
FSI charge exchange high	30	0.000 ± 0.278	-0.381 ± 0.111
M_a^{QE}	31	1.000 ± 0.372	1.025 ± 0.059
M_a^{RES}	32	1.163 ± 0.183	0.797 ± 0.056
DIS/Multi- π Shape	33	0.000 ± 0.400	0.225 ± 0.285
Spectral Function	34	0.000 ± 1.000	0.240 ± 0.129
E_b	35	1.000 ± 0.360	1.236 ± 0.209
p_F	36	1.000 ± 0.140	1.227 ± 0.049
π -less Δ decay	37	0.000 ± 0.200	0.006 ± 0.085
CCQE E0	38	1.000 ± 0.110	0.966 ± 0.076
CCQE E1	39	1.000 ± 0.300	0.931 ± 0.103
CCQE E2	40	1.000 ± 0.300	0.852 ± 0.114
CC1 π E0	41	1.154 ± 0.317	1.265 ± 0.163
CC1 π E1	42	1.000 ± 0.400	1.122 ± 0.172
CC Coherent	43	1.000 ± 1.000	0.449 ± 0.164
NC Other	44	1.000 ± 0.300	1.410 ± 0.218
NC1 π^0	45	0.963 ± 0.328	1.135 ± 0.248

Table 5.14: The bin divisions in true neutrino energy for the binned cross section parameters in the 2013 T2K oscillation analyses.

Parameter	Bins	True Neutrino Energy Bin Divisions (GeV)
CCQE	3	0.0 - 1.5 - 3.5 - 30.0
CC1 π	2	0.0 - 2.5 - 30.0

Table 5.15: The Gaussian fit results of Figures 5.18 and 5.19. The systematic error is taken from the spread of the distribution.

		Constant	Mean	Sigma
Water-In	Pre-BANFF	129.3 ± 5.6	74.2 ± 0.1	2.48 ± 0.07
Water-In	Post-BANFF	315.8 ± 12.6	80.1 ± 0.0	1.08 ± 0.03
Water-Out	Pre-BANFF	115.2 ± 4.7	81.5 ± 0.1	3.27 ± 0.08
Water-Out	Post-BANFF	260.7 ± 10.3	88.5 ± 0.0	1.49 ± 0.03

5.6. FLUX AND EVENT GENERATOR UNCERTAINTIES

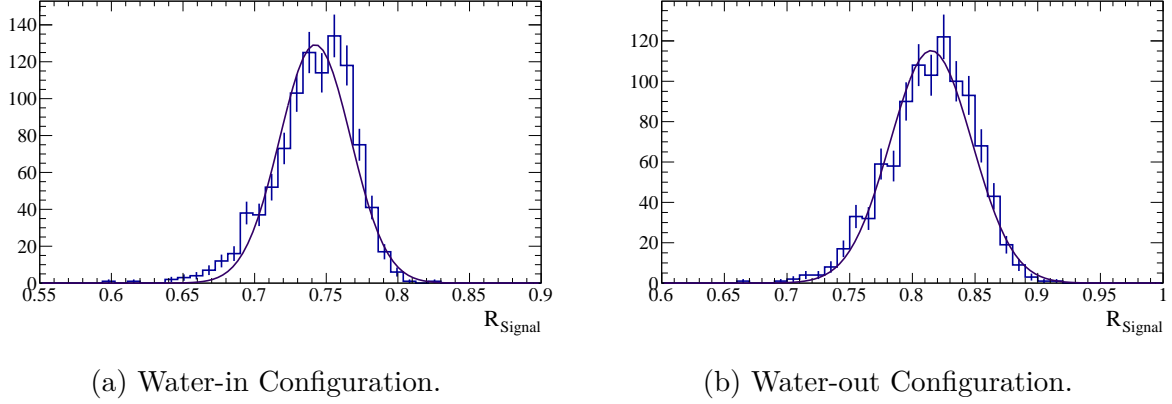


Figure 5.18: The distribution of the ratio of signal in the selected region based on multiple fits using the T2KReWeight pre-BANFF fit throws. The P \emptyset D water-in configuration had a 98.0% convergence rate and the P \emptyset D water-out configuration had a 97.8% convergence rate.

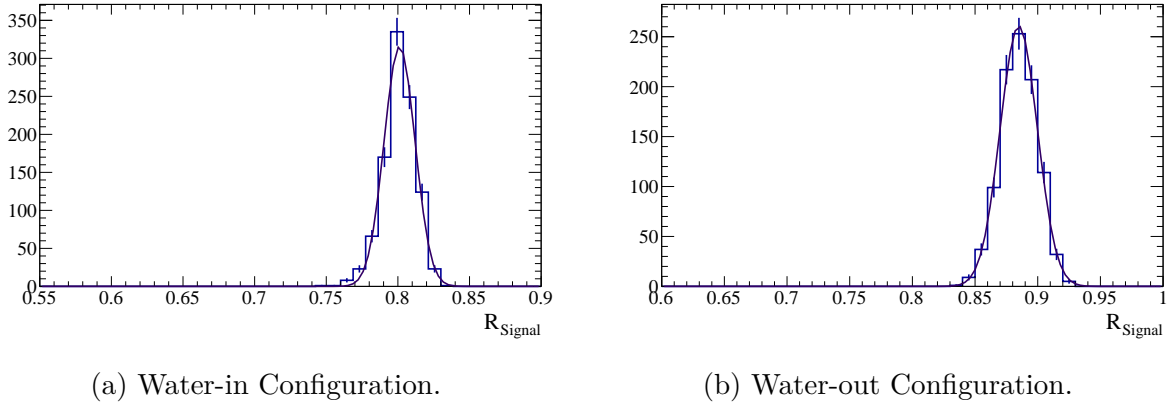


Figure 5.19: The distribution of the ratio of signal in the selected region based on multiple fits using the T2KReWeight post-BANFF fit throws. The P \emptyset D water-in configuration had a 100.0% convergence rate and the P \emptyset D water-out configuration had a 97.3% convergence rate.

Table 5.16: The Gaussian fit results of Figures 5.20 and 5.21 with unconstrained g factors. The systematic error is taken from the spread of the distribution.

		Constant	Mean	Sigma
Water-In	Pre-BANFF	126.7 ± 5.4	89.5 ± 0.1	2.94 ± 0.08
Water-In	Post-BANFF	267.8 ± 11.2	97.0 ± 0.0	1.46 ± 0.04
Water-Out	Pre-BANFF	101.0 ± 4.4	106.3 ± 0.1	3.71 ± 0.11
Water-Out	Post-BANFF	201.1 ± 8.1	114.1 ± 0.1	1.91 ± 0.05

5.6. FLUX AND EVENT GENERATOR UNCERTAINTIES

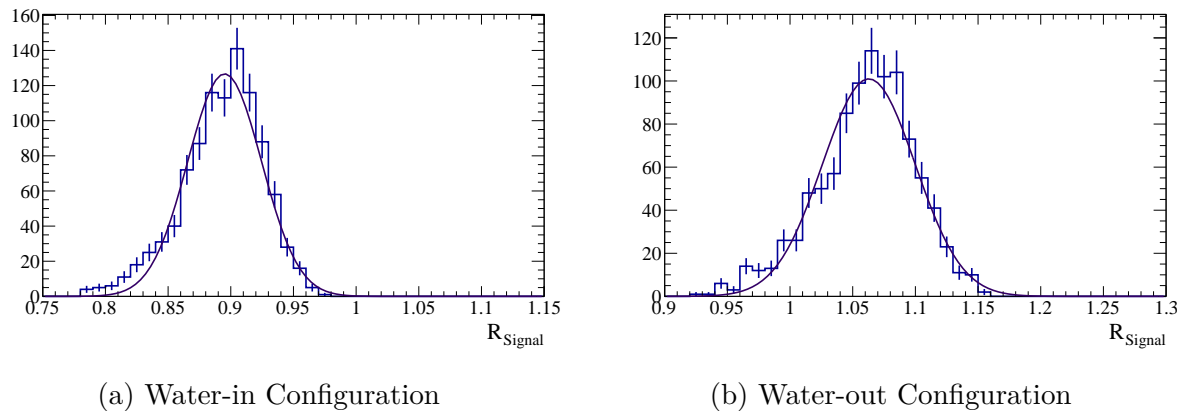


Figure 5.20: The distribution of the ratio of signal in the selected region based on multiple fits using the T2KReWeight pre-BANFF fit throws with an unconstrained g factor. The $P\bar{\nu}D$ water-in configuration had a 98.3% convergence rate and the $P\bar{\nu}D$ water-out configuration had a 97.5% convergence rate.

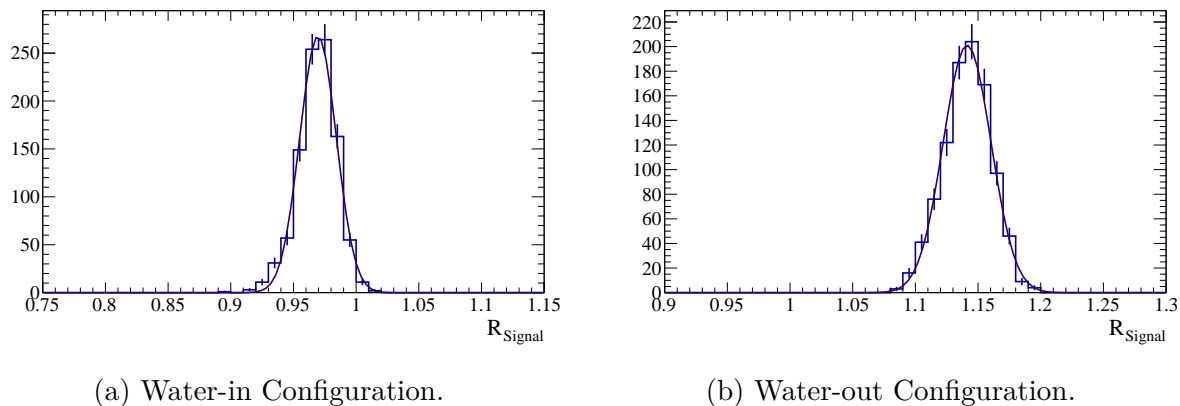


Figure 5.21: The distribution of the ratio of signal in the selected region based on multiple fits using the T2KReWeight post-BANFF fit throws with an unconstrained g factor. The $P\bar{\nu}D$ water-in configuration had a 100.0% convergence rate and the $P\bar{\nu}D$ water-out configuration had a 97.3% convergence rate.

1853 the spread of the results after running the fit. The distributions are summarized in Table
 1854 5.16. Taking the sum in quadrature of the sigma and its error of the output fit gives the
 1855 final systematic error. For the pre-BANFF fit, the error is 2.5% and 3.3% for the P \emptyset D
 1856 water-in and water-out configurations respectively. For the post-BANFF fit, the error is
 1857 1.1% and 1.5% respectively. Again, the size of these errors indicate that the fit is relatively
 1858 independent of the cross section normalizations.

1859 5.7 Reconstruction Uncertainties

1860 There are three types of reconstruction uncertainties of concern. The first issue is the
 1861 efficiency of an event getting to the shower reconstruction, where most of the selection cuts
 1862 are geared toward. The second is the data to Monte Carlo discrepancy in the cuts depending
 1863 on the reconstruction, such as the PID weight, the charge in the showers and the shower
 1864 separation. The third issue, has two parts: how well the Monte Carlo predicts muon decay
 1865 and how accurate that reconstruction is.

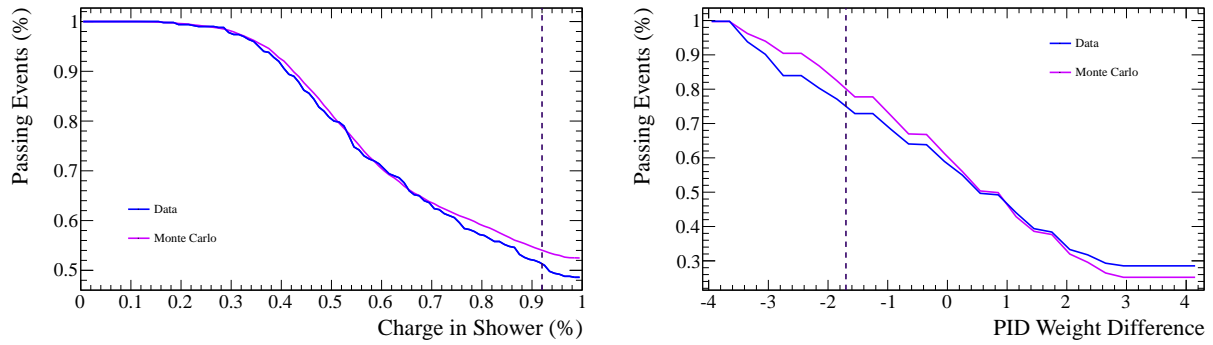
1866 5.7.1 Track PID Efficiency

1867 The analysis for this systematic is detailed in Section 3.4. There is a 5.4% inefficiency
 1868 difference of muons being misidentified as EM for the water-in configuration and a 5.1%
 1869 inefficiency for the water-out configuration.

1870 5.7.2 Continuous Distribution Cuts

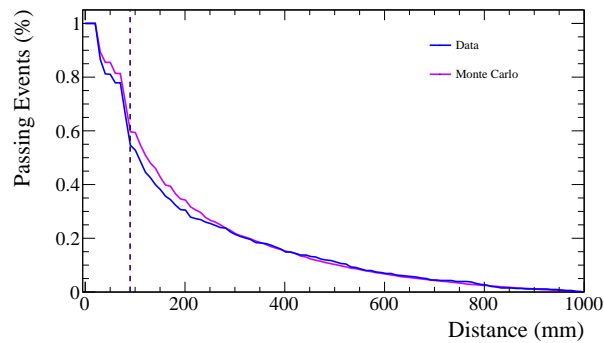
1871 There are three optimized cuts: Charge in Shower, Shower Separation and PID Weight
 1872 Difference. In order to study the systematic effect of these continuous cuts, double sideband
 1873 plots are examined. For example, to look at Shower Separation, events that fail the Charge
 1874 in Shower and PID Weight Difference, but pass all other cuts. This way the events come
 1875 from a low purity sample and are not effected by any data to Monte Carlo signal difference.
 1876 The purities of the samples are summarized in Table 5.19. The percent of saved events for
 1877 varying cuts is shown in Figures 5.22 and 5.23 and the values are interpolated from the
 1878 histograms. The systematic error extracted is the difference of the percent of saved events in
 1879 data and Monte Carlo divided by the Monte Carlo value at the cut. This systematic error has
 1880 an intrinsic statistical error from the binomial error on the interpolated values. Assuming
 1881 the statistical errors on the percent of saved events are Gaussian, the statistical error can be
 1882 propagated through to apply to the systematic. At this point, the systematic and statistical
 1883 errors are added in quadrature and the final systematic error is extracted. A summary of
 1884 these systematic errors are shown in Tables 5.17 and 5.18. After adding the continuous cut
 1885 systematics in quadrature, the systematic error on the efficiency due to the continuous cuts
 1886 is 13.0% for the P \emptyset D water-in configuration and 12.3% for the P \emptyset D water-out configuration.

5.7. RECONSTRUCTION UNCERTAINTIES



(a) Charge in Shower

(b) PID Weight



(c) Nearest Shower

Figure 5.22: Percent of events passing continuous cuts. These distributions show the difference between data and Monte Carlo in the N-2 sidebands for the P0D water-in configuration.

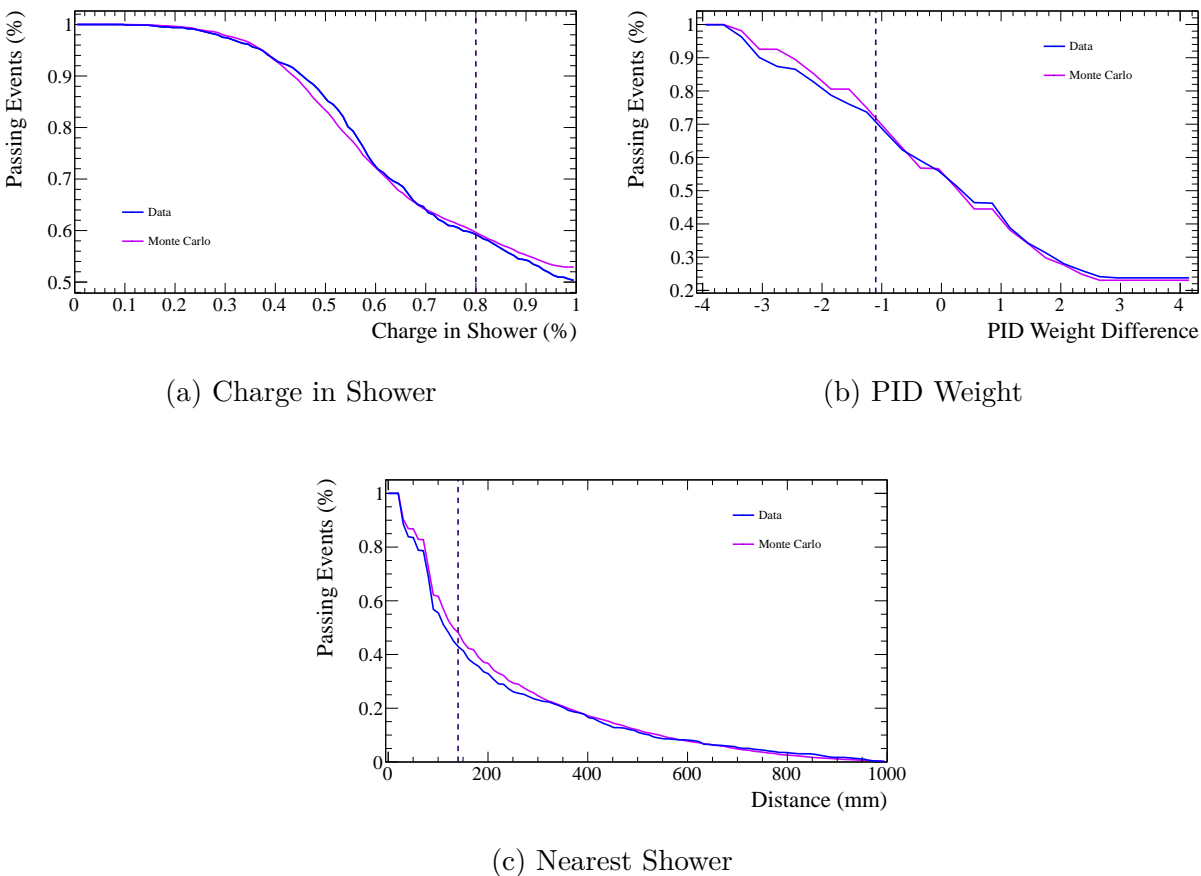


Figure 5.23: Percent of events passing continuous cuts. These distributions show the difference between data and Monte Carlo in the N-2 sidebands for the $P\bar{0}D$ water-out configuration.

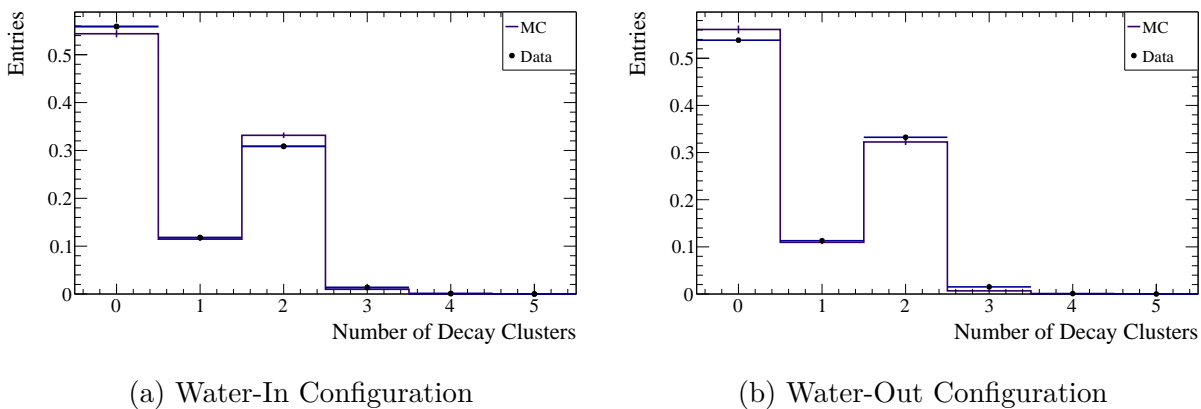


Figure 5.24: For the stopping muon sample, the number of muon decay clusters reconstructed. Data and Monte Carlo histograms are shown normalized to one.

5.7. RECONSTRUCTION UNCERTAINTIES

Table 5.17: The summary of the systematic error on the optimizable cuts for the P \emptyset D water-in configuration. The columns divide the three continuous cuts of interest. The first two rows summarize the interpolated values of the efficiencies at the cut value. The next row contains the systematic difference between the data and Monte Carlo efficiencies. The next two rows summarize the statistical error of the data and Monte Carlo efficiency values. The penultimate row describes the statistical error on the systematic difference between data and Monte Carlo. The last row shows the combined systematic shift and statistical error, which is used as the total systematic error for the cuts.

	Charge in Shower	Shower Separation	PID Weight
Monte Carlo Cut Efficiency	54.0	60.2	80.1
Data Cut Efficiency	51.3	55.18	75.0
Systematic Error	5.1	8.3	6.4
Monte Carlo Statistical Error	0.5	0.5	0.3
Data Statistical Error	2.2	2.1	1.4
Statistical Error	4.2	3.6	1.8
Total Systematic Error	6.6	9.1	6.6

Table 5.18: The summary of the systematic error on the optimizable cuts for the P \emptyset D water-out configuration. The columns divide the three continuous cuts of interest. The first two rows summarize the interpolated values of the efficiencies at the cut value. The next row contains the systematic difference between the data and Monte Carlo efficiencies. The next two rows summarize the statistical error of the data and Monte Carlo efficiency values. The penultimate row describes the statistical error on the systematic difference between data and Monte Carlo. The last row shows the combined systematic shift and statistical error, which is used as the total systematic error for the cuts.

	Charge in Shower	Shower Separation	PID Weight
Monte Carlo Cut Efficiency	59.6	48.2	71.8
Data Cut Efficiency	59.2	43.0	70.7
Systematic Error	0.7	10.8	1.6
Monte Carlo Statistical Error	0.6	0.7	0.5
Data Statistical Error	1.7	2.0	1.4
Statistical Error	3.0	4.3	2.0
Total Systematic Error	3.1	11.6	2.6

Table 5.19: A summary of the purities predicted in the double sidebands for the P0D water-in and water-out configurations.

	Charge in Shower	Shower Separation	PID Weight
Water-In	9.7 ± 0.3	6.7 ± 0.3	7.1 ± 0.2
Water-Out	7.7 ± 0.3	4.3 ± 0.3	5.9 ± 0.3

Table 5.20: The efficiency of finding a muon decay for a reconstructed muon in a stopping muon sample. The first column describes the P0D water status. The second and third column list the efficiency of finding any muon decay cluster in both the Monte Carlo stopping muon particle gun and in the data. The final column describes the fractional difference between data and Monte Carlo. This is used as the constraint on the ratio of background events in the sideband region to background events in the selected region. All numbers are listed in percentage.

Configuration	ϵ_{MC}	ϵ_{Data}	$(\epsilon_{Data} - \epsilon_{MC})/\epsilon_{MC}$
Water-In	45.6 ± 0.5	44.1 ± 0.5	3.3 ± 0.7
Water-Out	43.9 ± 0.6	46.2 ± 0.6	5.2 ± 0.8

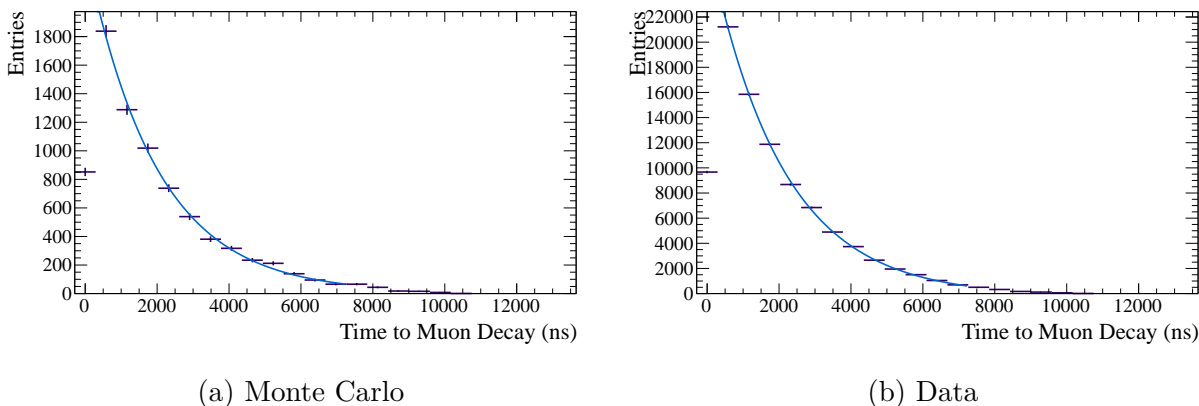


Figure 5.25: For the stopping muon sample, the time difference between the neutrino interaction and the muon decay clusters for the P0D water-in configuration

Table 5.21: The result of the fit to Equation 5.1 to the muon decay time curve in Figure 5.25 for the P0D water-in configuration stopping muons.

Parameter	Monte Carlo	Data
a	2405.7 ± 56.4	28368.3 ± 28368.3
b	$1.96 \pm 0.07 \mu s$	$2.05 \pm 0.02 \mu s$
c	6.6 ± 11.9	-224.6 ± 42.5

5.7. RECONSTRUCTION UNCERTAINTIES

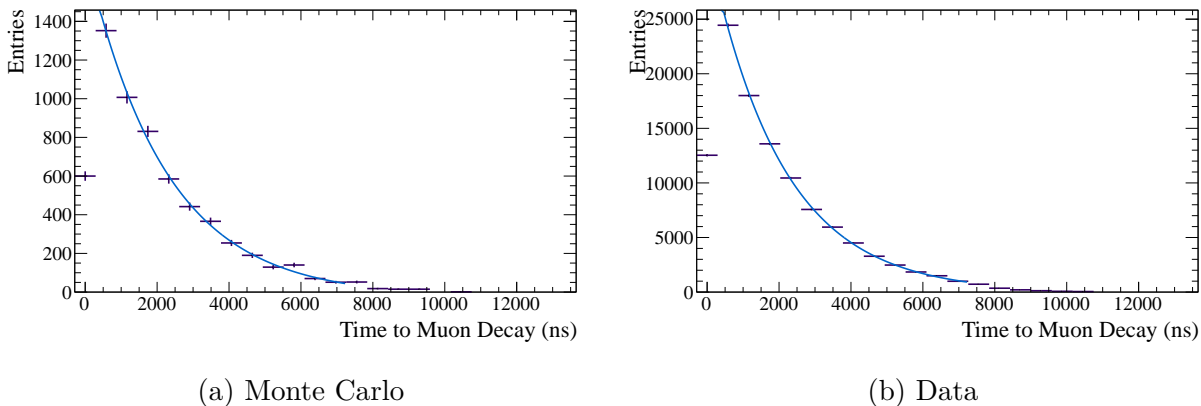


Figure 5.26: For the stopping muon sample, the time difference between the neutrino interaction and the muon decay clusters for the P \emptyset D water-in configuration

Table 5.22: The result of the fit to Equation 5.1 to the muon decay time curve in Figure 5.26 for the P \emptyset D water-out configuration stopping muons.

Parameter	Monte Carlo	Data
a	1783.8 ± 43.3	32150.8 ± 32150.8
b	$2.21 \pm 0.09 \mu\text{s}$	$2.05 \pm 0.02 \mu\text{s}$
c	-23.7 ± 12.9	-24.4 ± 48.7

5.7.3 Muon Decay Systematic

The behavior of the muon decay finding is used in two different ways as input constraints to the fit. The probability of an event with a muon (a background event) entering the selected region rather than the sideband region is determined by the efficiency of detecting a muon decay. The probability of a neutral current event (a signal event) entering the sideband region is determined by the false rate of finding muon decay clusters. For both studies a sample of stopping muons was used. The same sample used for the Track PID efficiency study, described in 3.4 was repurposed for these studies.

For the ratio of the backgrounds, the efficiency of finding a muon decay was examined. For all tracks satisfying the requirement for a stopping muon, the number of muon decay clusters that occur after the neutrino interaction are counted. In Figure 5.24, the number of muon decay clusters found is shown. The data and Monte Carlo histograms are area normalized to one. The efficiency of the reconstruction is calculated from the number of events that have any muon decay clusters and the total number events. The fractional difference between data and Monte Carlo is added in quadrature to its statistical error and used as the constraint on the ratio. This constraint is 3.4% for the P \emptyset D water-in configuration and 5.2% for the P \emptyset D water-out configuration. A summary of the efficiencies is in Table 5.20.

For a constraint on the ratio of the signal in the selected and sideband regions, the rate of fake muon decay clusters is considered. The fake muon decay clusters occur when there are decay clusters reconstructed when there isn't a precursor muon. Figures 5.25 and 5.26 show the time difference between all muon decay clusters and their associated neutrino vertex interaction. The histograms are binned in units of the cycle length. There is a clear exponential decay representing the correctly reconstructed muon decays. The range of interest is from a one cycle difference to a twelve cycle difference. Although there are twenty-three cycles, the beam spill only occurs between cycles four and eleven. If an interaction occurred in cycle 11, there are 12 succeeding cycles in which is it possible to reconstruct a muon decay cluster. If the range above a difference of twelve is examined, then there would be an additional loss of reconstructed muon decays due to late cycle interactions. This is clearly shown when Figures 5.25 and 5.26 are plotted on a log scale. In addition, there is an issue with looking at the number of same cycle events. For these reasons, the exponential decay function,

$$y = ae^{-\frac{1}{b}x} + c, \quad (5.1)$$

is fit to the subrange of time difference from one cycle to twelve. Equation 5.1 has two parts. The first half of the equation describes a simple decay with a normalization of a and a muon decay lifetime of b . The parameter c describes an additional offset due to a possible fake muon decay rate. The results of the fits are listed in Tables 5.21 and 5.22. As verification, one can see that the muon decay lifetime represented by parameter b approaches $2.2\mu s$. Parameter c , normalized by parameter a , is used to extract the fake rate. Then the absolute value of that difference between data and Monte Carlo is used to quantify the constraint. For the P \emptyset D water-in configuration there is a $1.1 \pm 0.5\%$ difference which sums in quadrature to a 1.6% constraint. For the P \emptyset D water-out configuration there is a $1.3 \pm 0.7\%$ difference which sums in quadrature to a 2.0% constraint.

A summary of the constraints the muon decay efficiency and fake reconstruction rate

5.8. G FACTOR

1929 is present in Table 5.25. These describe the input constraints on the fit performed in the
1930 Analysis section.

1931 **5.8 g Factor**

1932 There are two parts to this systematic. One is the statistical error on g as the output
1933 to the fit, the other is the systematic difference due to the inclusion of the g factor in the
1934 fit. There appears to be a correlation between using the g and not using it in the on-water
1935 subtraction. As such, the systematic difference is only used as a systematic error on the
1936 individual P \emptyset D water-in and P \emptyset D water-out configuration ratios. The statistical error gets
1937 passed through the subtraction to be applied to the on-water result.

1938 **5.8.1 Statistical g Contribution**

1939 The calculation of the statistical contribution to the number of signal events is approached
1940 in much the same way as the energy scale error was evaluated. After constructing the fit, the
1941 resulting value of g and its error are used to pull 10,000 times from a Gaussian distribution,
1942 see Figure 5.27. Using the pulls, the number of signal events was recalculated, shown in
1943 Figure 5.28. The mean and RMS of the resulting distribution are used to calculate the effect
1944 of the statistical error on g on the final number of selected signal events. The results of the
1945 statistical effect is summarized in Table 5.23.

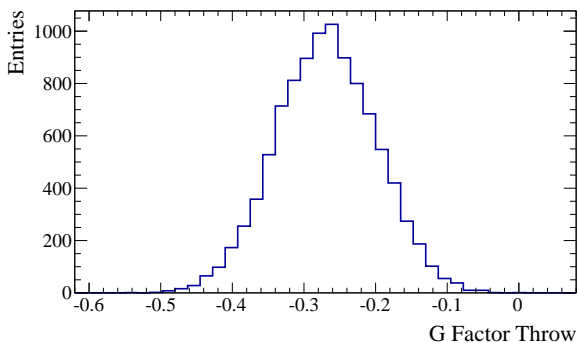
1946 **5.8.2 Systematic g Contribution**

1947 In order to try to understand the effect of the g factor on the simultaneous fit, a com-
1948 parison was made between the default fit and the unconstrained g factor fit. Section 4.4.3
1949 describes the results of both fits. The error is the fractional difference between the $g = 0$ and
1950 $g \neq 0$ which is 16.4% for the P \emptyset D water-in configuration and 23.2% for the P \emptyset D water-out
1951 configuration.

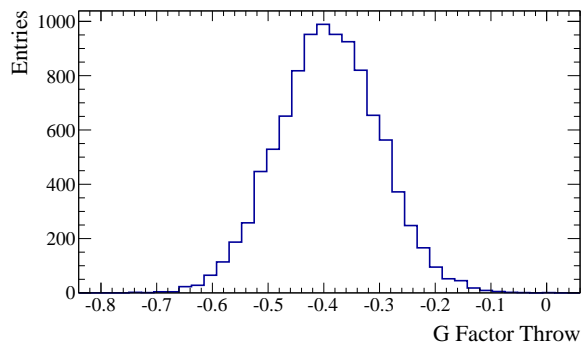
1952 This systematic is not propagated through the on-water subtraction due to a correlation
1953 between the P \emptyset D water-in and water-out configurations with and without the g factor.
1954 The on-water calculation without using the g factor gives $106.4 \pm 41.0(\text{stat}) \pm 72.6(\text{sys})$

Table 5.23: The systematic result from the error on the g factor output from the fit. The first column is the number of Monte Carlo predicted events. The next two columns describe the distribution after throwing the g factor. The last three columns are the result of calculated the fractional shift from nominal, the fractional RMS of the distribution and the final systematic error.

	Signal	Mean	RMS	Shift (%)	Shift Error (%)	Total Error (%)
Water-In	532.3	531.0	19.9	-0.2	3.8	3.8
Water-Out	385.5	384.7	16.1	-0.2	4.2	4.2

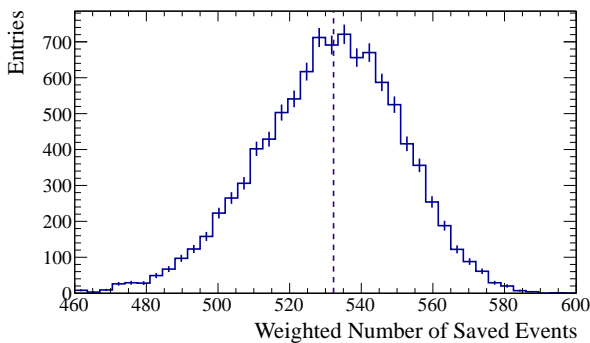


(a) Water-in Configuration

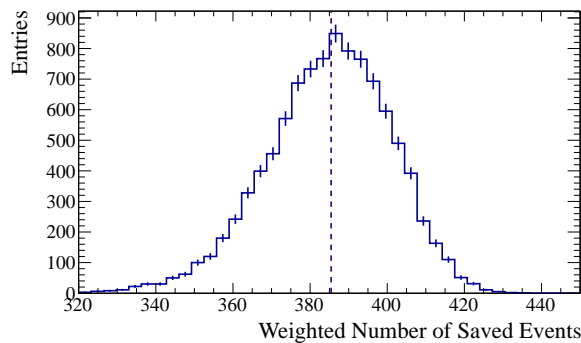


(b) Water-out Configuration

Figure 5.27: The distribution of the throws of the g factor. The mean and sigma of the base distribution come from the fit results.



(a) Water-in Configuration



(b) Water-out Configuration

Figure 5.28: The distribution of the weighted signal events using the g factor throws. The vertical dashed line represents the nominal number of Monte Carlo signal weighted events.

5.9. SUMMARY OF SYSTEMATIC ERRORS

1955 events where processing the fit with g gives $102.4 \pm 42.5(\text{stat}) \pm 90.4(\text{sys})$. Propagating this
1956 information through implies a fractional systematic error of 3.9% on the on-water result.
1957 This is added in quadrature to the other systematic errors after calculating the on-water
1958 data to Monte Carlo ratio.

1959 **5.9 Summary of Systematic Errors**

1960 The systematic errors are summarized in Table 5.24. The muon decay cluster reconstruc-
1961 tion systematics that are used as constraints on the fit are listed in Table 5.25. For more
1962 details on how the muon decay cluster reconstruction contributes to the constraints on the
1963 fit, please see Subsection 5.7.3.

1964 **Removing Model Dependencies**

1965 The g factor systematic error is applied directly to the data to Monte Carlo ratio for
1966 the P \emptyset D water-in and water-out configurations. It is not propagated with the remaining
1967 systematic errors through to the on-water result. Instead, the fractional difference between
1968 the $g = 0$ and $g \neq 0$ on-water data to Monte Carlo ratio is taken as the systematic error
1969 due to g on the final number. The error is passed through the subtraction as an error on the
1970 number of reconstructed data events.

Table 5.24: Summary of Systematic errors.

Parameter	Uncertainty	
	Water-In	Water-Out
Geometry Differences	2.8%	2.8%
PE Peak Discrepancy	0.6%	0.4%
Energy Scale	5.8%	0.9%
Detector Variations	< 0.1%	< 0.1%
P \emptyset D Response	1.8%	1.8%
Mass Uncertainty	0.5%	0.9%
Alignment	< 0.1%	< 0.1%
Fiducial Volume Scaling	1.5%	2.0%
Fiducial Volume Shift	1.1%	1.7%
Flux and Event Generator	2.9%(1.5%)	3.7%(1.9%)
Track PID Efficiency	5.4%	5.1%
Shower Separation	10.9%	13.5%
PID Weight	8.1%	3.4%
Charge In Shower	7.8%	3.0%
Total Systematic	18.1%(18.0%)	16.1%(15.8%)

Table 5.25: Summary of the constraints to be applied in the fit. The first column describes the source of the constraint. The second column lists the parameter that the constraint is used for. The last two columns list the constraints used for the P \emptyset D water-in and water-out configurations.

Error	Parameter	Parameter Value	
		Water-In	Water-Out
Muon Decay Fake Rate	$N_{\text{Sig}}^{\text{Sideband}} / N_{\text{Sig}}^{\text{Selected}}$	1.6%	2.0%
Muon Decay Efficiency	$N_{\text{Bkg}}^{\text{Sideband}} / N_{\text{Bkg}}^{\text{Selected}}$	3.4%	5.2%

5.9. SUMMARY OF SYSTEMATIC ERRORS

Table 5.26: Summary of Systematic errors with an unconstrained g factor. There are two values listed for the Flux and Event Generator errors. The first are the pre-BANFF fit systematic errors, the latter are the post-BANFF fit systematic errors. The penultimate line is the sum in quadrature of all previous systematics. The g factor systematic is listed separately as it will be handled separately in the analysis.

Parameter	Uncertainty	
	Water-In	Water-Out
Geometry Differences	2.8%	2.8%
PE Peak Discrepancy	0.6%	0.4%
Energy Scale	4.4%	0.6%
Detector Variations	< 0.1%	< 0.1%
P \emptyset D Response	1.8%	1.8%
Mass Uncertainty	0.4%	0.6%
Alignment	< 0.1%	< 0.1%
Fiducial Volume Scaling	1.5%	2.0%
Fiducial Volume Shift	1.1%	1.7%
Flux and Event Generator	2.5% (1.1%)	3.3% (1.5%)
Track PID Efficiency	5.4%	5.1%
Shower Separation	10.9%	13.5%
PID Weight	8.1%	3.4%
Charge In Shower	7.8%	3.0%
g Factor (statistical)	3.8%	4.2%
Total Systematic	18.2%(18.0%)	16.7%(16.4%)
g Factor (systematic)	16.4%	23.2%

Chapter 6

Conclusion

An on-water $\text{NC}1\pi^0$ rate analysis has been performed using T2K Run 1, Run 2 and Run 4 water-in data with 2.64×10^{20} POT and Run 2, Run 3, and Run 4 water-out data with 3.49×10^{20} POT. An enriched sample of $\text{NC}1\pi^0$ events was selected with an efficiency of $6.01 \pm 0.01\%$ ($4.79 \pm 0.02\%$) and a purity of $48.7 \pm 0.17\%$ ($46.1 \pm 0.3\%$) for the water-in (water-out) sample. The Monte Carlo expects 432.8 ± 4.3 signal events for the water-in configuration and 290.2 ± 5.4 signal events for the water-out configuration. An extended maximum likelihood fit was performed, using Minuit, on each sample with the invariant mass window limited to 0-500 MeV. There were two versions of the analysis conducted.

In order to directly compare the result to the NEUT Monte Carlo, the background shape is not allowed to vary. This background shape fixed analysis found 341.6 ± 32.6 observed signal events on $\text{P}\emptyset\text{D}$ water-in data and 246.5 ± 26.0 observed signal events on $\text{P}\emptyset\text{D}$ water-out data. Using the T2KReWeight pre-BANFF fit correlation matrix, the flux and cross section systematic errors are estimated in conjunction with detector systematic errors. The resulting data to Monte Carlo ratios are $0.790 \pm 0.076(\text{stat}) \pm 0.143(\text{sys})$ for water-in and $0.850 \pm 0.091(\text{stat}) \pm 0.137(\text{sys})$ for water-out. The NEUT Monte Carlo predicts 157.2 ± 2.5 signal events. Using the ratio of the water-in and water-out POT and efficiencies, there were $106.4 \pm 41.0(\text{stat}) \pm 72.6(\text{sys})$ signal on-water events observed. This leads to an on-water production rate ratio of $0.677 \pm 0.261(\text{stat}) \pm 0.462(\text{sys})$ in the $\text{P}\emptyset\text{D}$.

The secondary analysis allows the shape to be constrained and modified by the muon decay sideband. This background shape varying analysis found 408.7 ± 32.5 observed signal events on $\text{P}\emptyset\text{D}$ water-in data and 324.1 ± 28.6 observed signal events on $\text{P}\emptyset\text{D}$ water-out data. Using the T2KReWeight pre-BANFF fit correlation matrix, the flux and cross section systematic errors are estimated in conjunction with detector systematic errors. The resulting data to Monte Carlo ratios are $0.944 \pm 0.076(\text{stat}) \pm 0.231(\text{sys})$ for water-in and $1.107 \pm 0.101(\text{stat}) \pm 0.316(\text{sys})$ for water-out. Using the ratio of the water-in and water-out POT and efficiencies, there were $102.4 \pm 42.5(\text{stat}) \pm 90.4(\text{sys})$ signal on-water events observed. This leads to an on-water production rate ratio of $0.652 \pm 0.270(\text{stat}) \pm 0.576(\text{sys})$ in the $\text{P}\emptyset\text{D}$.

Although there is a large difference between the default analysis and the model independent analysis, the on-water result seems to be relatively unaffected with a difference between the data and Monte Carlo ratios at 0.025 which is a tenth of the statistical error.

2004 6.1 Future Improvements

2005 There are many ways to improve this analysis, which is the first of its kind. Due to
 2006 the subtraction method, the errors on the water-in and water-out measurements combine to
 2007 become quite large on the on-water calculation. As of now, T2K has received only 8% of the
 2008 total expected POT. With more data, the statistical errors will be reduced. In particular,
 2009 the muon decay sideband sample will gain more statistical power and, therefore, will have
 2010 more strength to regulate the background shape.

2011 A concerted effort must be undertaken to reduce the systematic errors on the mea-
 2012 surements. In Table 5.24, the largest errors come from the optimized cut errors (shower
 2013 separation, PID weight, and charge in shower). When the cuts were optimized, the potential
 2014 systematic errors introduced were not considered. However, the cut values can be reevalu-
 2015 ated and reduced by considering the size of these errors. Additionally, improvements have
 2016 been made on the reconstruction for Production 6, the next version of the ND280 software.
 2017 Among those, are improvements in the shower PID of which Production 5 contained a beta
 2018 version. The improvements would also reflect on the track PID, another high systematic
 2019 error. However, more improvements can be made to the reconstruction by trying to extract
 2020 a clean sample of reconstructed electrons and photons to compare between data and Monte
 2021 Carlo. Up to now, the driving force behind the PID and reconstruction came from the
 2022 stopping and through-going muon samples.

2023 Another change that could be made to the analysis, is the definition of the shower sep-
 2024 aration cut. As it is written now, it is susceptible to noise in the detector. A more robust
 2025 definition, perhaps comparing the second or third nearest hit, should be employed. Or even
 2026 a distance between the ellipsoid surface of the three dimensional clusters in the shower.

2027 Further studies can be made on the shape independent fit. Although this analysis chose
 2028 the selected signal shape as a shape variation, there are many other choices. One shape
 2029 of interest is a linearly adjusted muon decay background shape which would allow for the
 2030 suppression of the low energy background but leave the high tail unaffected. By looking at
 2031 a collection of different shapes, a better understanding of the effect of the shape and the
 2032 ability to remove the NEUT model shape dependency is possible.

2033 Overall, the errors considered were evaluated on the conservative side to provide an upper
 2034 limit on the possible values for the rate of the $\text{NC}1\pi^0$ interaction. Future analyses will be able
 2035 to reduce and improve the systematic error on the water-in and water-out measurements,
 2036 thereby increasing the power of the final on-water measurement.

2037

Bibliography

- 2038 [1] Particle Data Group. The Review of Particle Physics. <http://pdg.lbl.gov/index.html>, May 2014.
- 2039
- 2040 [2] K. Zuber. *Neutrino physics*. CRC Press, 2011.
- 2041 [3] W. Pauli. Excerpt from a Letter. <http://www.physics.ucdavis.edu/~svoboda/doublechooz/bkg/pauli.html>, June 2006.
- 2042
- 2043 [4] F. Wilson. Fermi's theory of beta decay. *American Journal of Physics*, 36(12):1150–1160, 1968.
- 2044
- 2045 [5] G. Rodeback and J. Allen. Neutrino Recoils Following the Capture of Orbital Electrons in A 37. *Physical Review*, 86(4):446, 1952.
- 2046
- 2047 [6] M. Goldhaber, L. Grodzins, and A. Sunyar. Helicity of neutrinos. *Physical review*, 109(3):1015, 1958.
- 2048
- 2049 [7] F. Reines and C. Cowan Jr. Free antineutrino absorption cross section. I. Measurement of the free antineutrino absorption cross section by protons. *Physical Review*, 113(1):273, 1959.
- 2050
- 2051
- 2052 [8] G. Danby et al. Observation of high-energy neutrino reactions and the existence of two kinds of neutrinos. *Physical Review Letters*, 9(1):36–44, 1962.
- 2053
- 2054 [9] K. Kodama et al. Observation of tau neutrino interactions. *Physics Letters B*, 504(3):218–224, 2001.
- 2055
- 2056 [10] SLD Electroweak, LEP Electroweak Working Group, et al. Precision electroweak measurements on the Z resonance. *Physics Reports*, 427:257, 2006.
- 2057
- 2058 [11] R. Davis Jr. Attempt to Detect the Antineutrinos from a Nuclear Reactor by the Cl 37 ($\bar{\nu}$, e^-) A 37 Reaction. *Physical Review*, 97(3):766, 1955.
- 2059
- 2060 [12] J. Bahcall. Solar Neutrinos. I. Theoretical. *Phys. Rev. Lett.*, 12:300–302, Mar 1964.
- 2061 [13] R. Davis. Solar Neutrinos. II. Experimental. *Phys. Rev. Lett.*, 12:303–305, Mar 1964.
- 2062 [14] R. Davis Jr, D. Harmer, and K. Hoffman. Search for neutrinos from the sun. *Physical Review Letters*, 20(21):1205, 1968.
- 2063

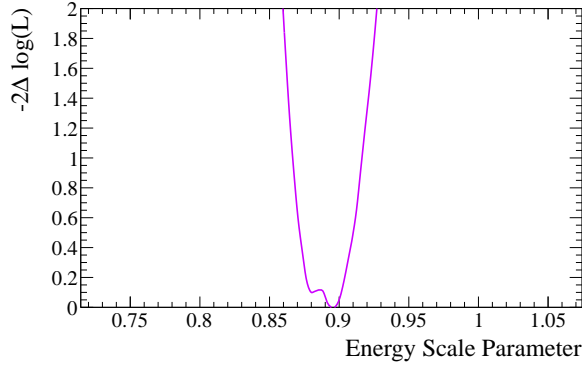
BIBLIOGRAPHY

- 2064 [15] J. Bahcall, N. Bahcall, and G. Shaviv. Present Status of the Theoretical Predictions for
2065 the Cl^{37} Solar-Neutrino Experiment. *Physical Review Letters*, 20(21):1209–1212, 1968.
- 2066 [16] K. Hirata et al. Observation in the Kamiokande-II detector of the neutrino burst from
2067 supernova SN1987A. *Physical Review D*, 38(2):448, 1988.
- 2068 [17] Y. Fukuda et al. Evidence for oscillation of atmospheric neutrinos. *Physical Review
2069 Letters*, 81(8):1562, 1998.
- 2070 [18] Q. Ahmad et al. Measurement of the Rate of $\nu_e + d \rightarrow p + p + e^-$ Interactions Produced
2071 by B 8 Solar Neutrinos at the Sudbury Neutrino Observatory. *Physical Review Letters*,
2072 87(7):071301, 2001.
- 2073 [19] Q. Ahmad et al. Direct evidence for neutrino flavor transformation from neutral-
2074 current interactions in the Sudbury Neutrino Observatory. *Physical Review Letters*,
2075 89(1):011301, 2002.
- 2076 [20] K. Abe et al. Observation of Electron Neutrino Appearance in a Muon Neutrino Beam.
2077 *Phys. Rev. Lett.*, 112:061802, Feb 2014.
- 2078 [21] E. Worcester. Observation of electron antineutrino disappearance by the Daya Bay Re-
2079 actor Neutrino Experiment. In *Proceedings of the DPF 2013 Meeting of the American
2080 Physical Society Division of Particles and Fields, Santa Cruz, California, August 13-17,
2081 2013*, Oct 2013.
- 2082 [22] S. Nakayama et al. Measurement of single production π^0 in neutral current neutrino
2083 interactions with water by a 1.3 gev wide band muon neutrino beam. *Physics Letters
2084 B*, 619(3À4):255 – 262, 2005.
- 2085 [23] T2K collaboration. Tokai-to-Kamiokande (T2K) Long Baseline Neutrino Oscillation
2086 Experiment Proposal, 2006.
- 2087 [24] K. Abe et al. T2K neutrino flux prediction. *Physical Review D*, 87(1):012001, 2013.
- 2088 [25] K. Abe et al. The T2K experiment. *Nuclear Instruments and Methods in Physics
2089 Research Section A: Accelerators, Spectrometers, Detectors and Associated Equipment*,
2090 659(1):106–135, 2011.
- 2091 [26] S. Assylbekov et al. The T2K ND280 off-axis π^0 detector. *Nuclear Instruments and
2092 Methods in Physics Research Section A: Accelerators, Spectrometers, Detectors and As-
2093 sociated Equipment*, 686:48–63, 2012.
- 2094 [27] Glenn Lopez. *Measurement of the Single Neutral Pion Production Cross Section in
2095 Neutral-Current Neutrino Interactions in the T2K Pi-zero Detector*. PhD thesis, Stony
2096 Brook University, Stony Brook, NY, 2012.
- 2097 [28] Phoc Trung Le. *Event reconstruction and energy calibration using cosmic muons for
2098 the T2K π^0 detector*. PhD thesis, Stony Brook University, Stony Brook, NY, 2009.

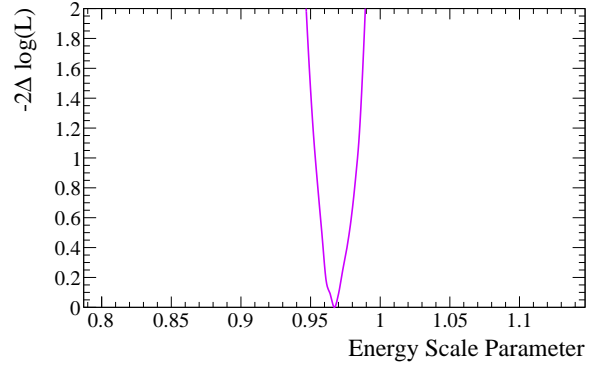
2099 **Appendix A**

2100 **Supporting Plots for Fit Result**

2101 The following plots show the supporting information for the default fit result. There are
2102 the negative log likelihood curves for the five parameters that are fit as well as the two
2103 dimensional likelihood contours of the number of signal and background in both the selected
2104 and sideband regions. The one-dimensional negative log likelihood curves are shown as
2105 well as the two dimensional comparison between the number of signal and the number of
2106 background events in the selected and sideband regions. The two-dimensional contours give
2107 a visual sense of the correlation between the normalization of the signal and the background.

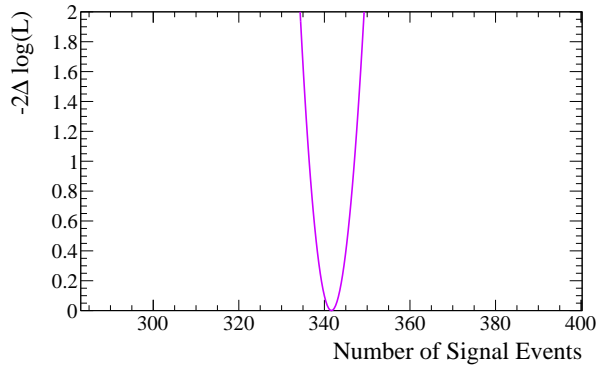


(a) Water-in Configuration

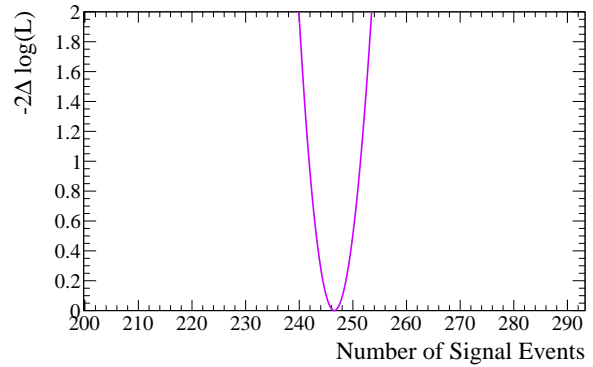


(b) Water-out Configuration

Figure A.1: The negative log likelihood curves for the energy scale parameter for both the P \emptyset D water-in and water-out configurations.

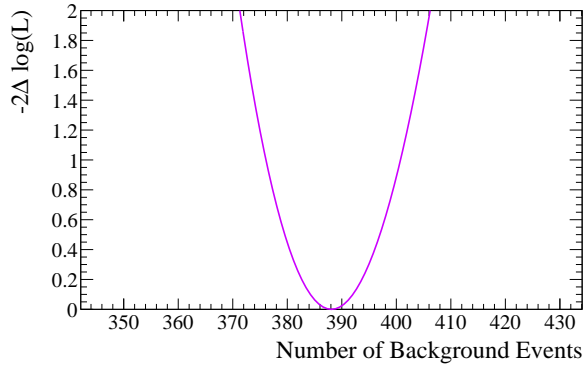


(a) Water-in Configuration

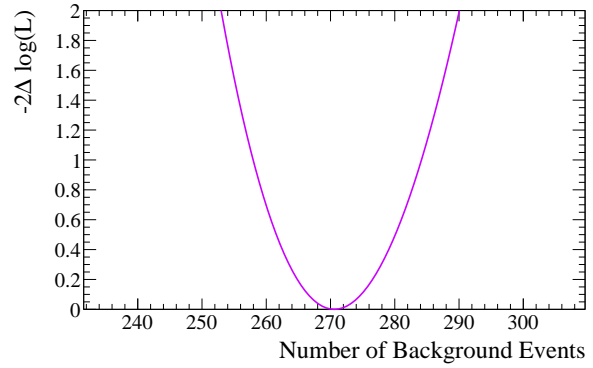


(b) Water-out Configuration

Figure A.2: The negative log likelihood curves for the number of signal events in the selected region for both the P \emptyset D water-in and water-out configurations.

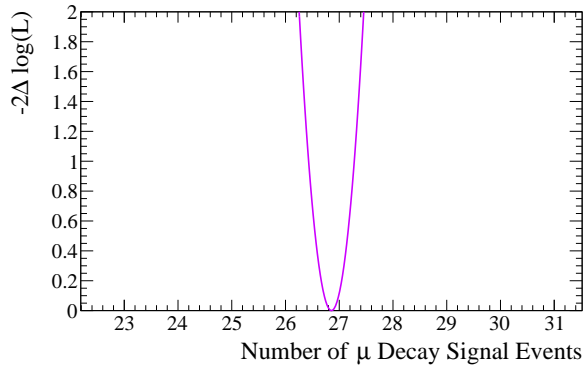


(a) Water-in Configuration

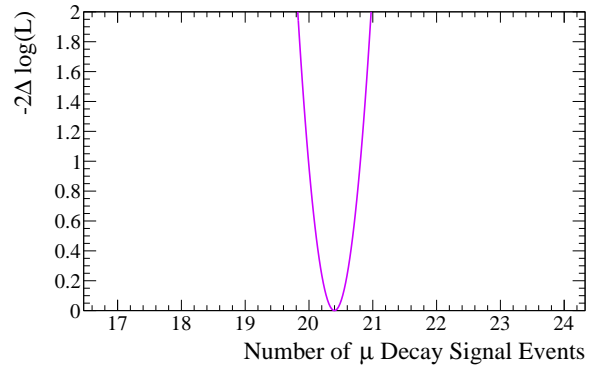


(b) Water-out Configuration

Figure A.3: The negative log likelihood curves for the number of background events in the selected region for both the $P\bar{0}D$ water-in and water-out configurations.

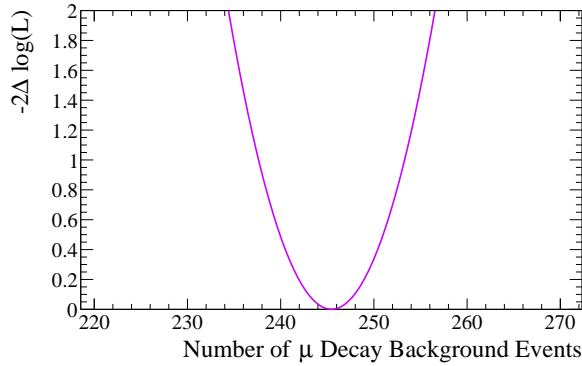


(a) Water-in Configuration

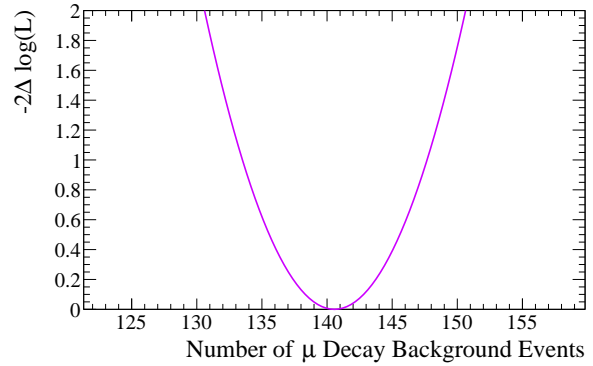


(b) Water-out Configuration

Figure A.4: The negative log likelihood curves for the number of signal events in the sideband region for both the $P\bar{0}D$ water-in and water-out configurations.

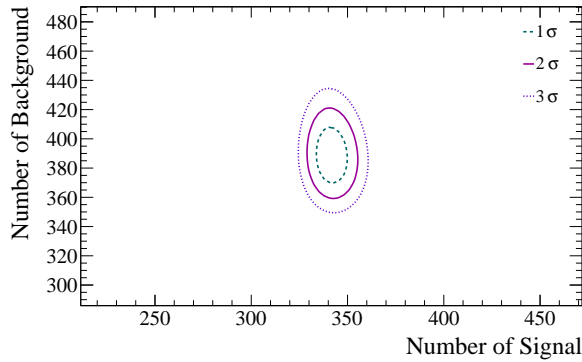


(a) Water-in Configuration

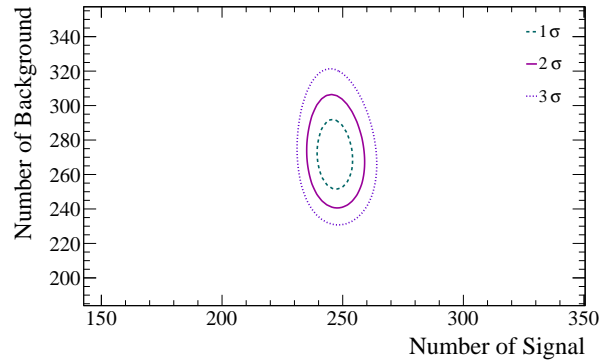


(b) Water-out Configuration

Figure A.5: The negative log likelihood curves for the number of background events in the sideband region for both the P \emptyset D water-in and water-out configurations.



(a) Water-in Configuration



(b) Water-out Configuration

Figure A.6: The negative log likelihood curves for the number of signal events in the sideband region for both the P \emptyset D water-in and water-out configurations.

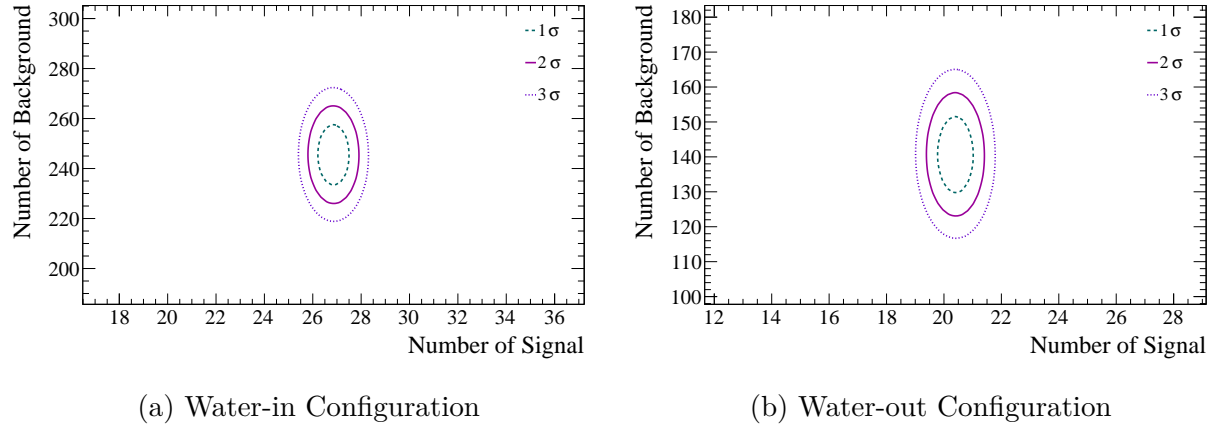
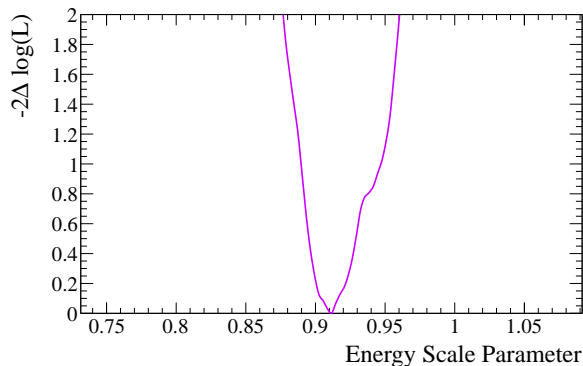


Figure A.7: The negative log likelihood curves for the number of background events in the sideband region for both the $P\emptyset D$ water-in and water-out configurations.

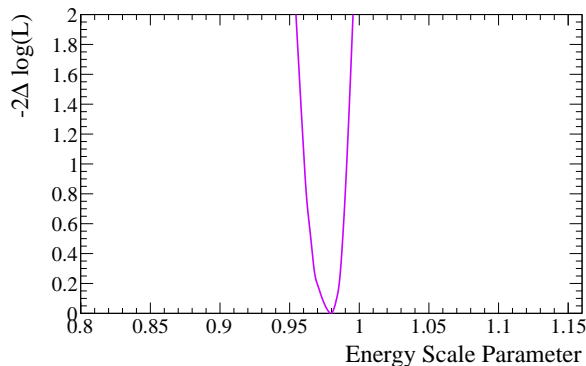
2108 A.1 Unconstrained g Fit

2109 The following series of plots show the negative log likelihood curves for the extended
 2110 maximum likelihood fit without a constraint on g . The one-dimensional negative log like-
 2111 lihood curves are shown as well as the two dimensional comparison between the number
 2112 of signal and the number of background events in the selected and sideband regions. The
 2113 two-dimensional contours give a visual sense of the correlation between the normalization of
 2114 the signal and the background.

A.1. UNCONSTRAINED G FIT

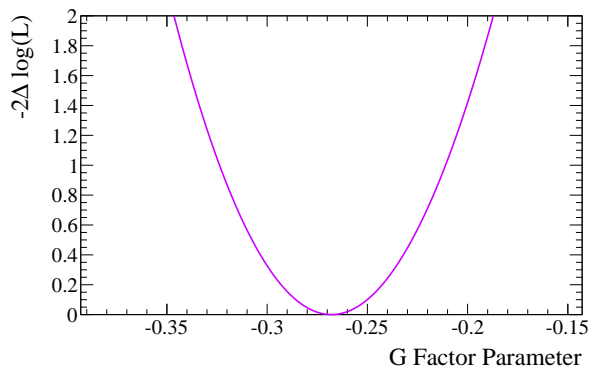


(a) Water-in Configuration

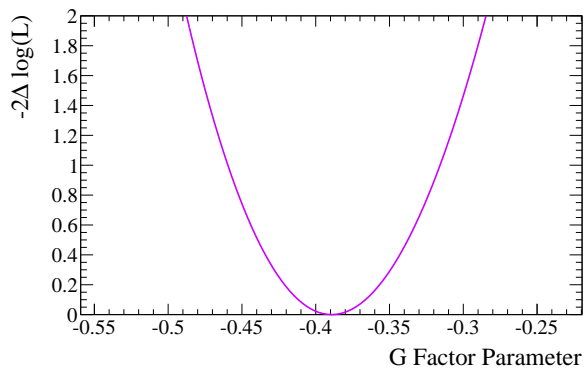


(b) Water-out Configuration

Figure A.8: The negative log likelihood curves for the energy scale parameter for both the P \emptyset D water-in and water-out configurations.

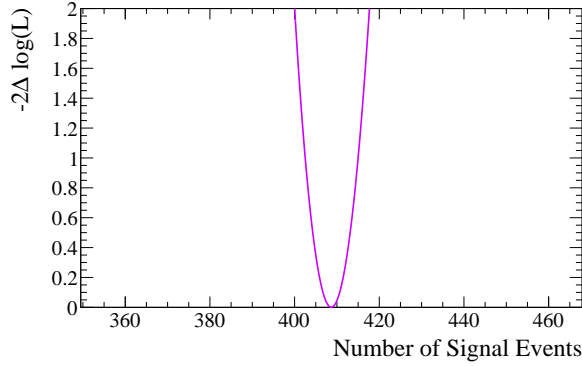


(a) Water-in Configuration

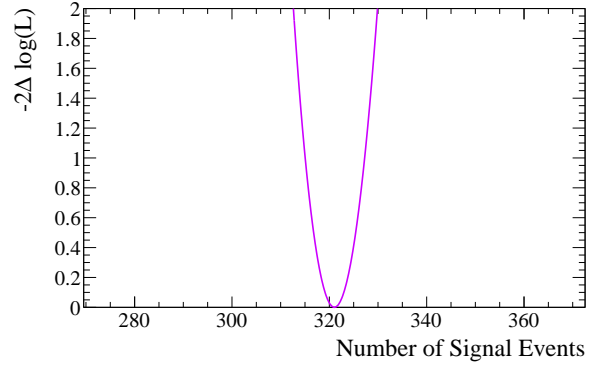


(b) Water-out Configuration

Figure A.9: The negative log likelihood curves for the g factor parameter for both the P \emptyset D water-in and water-out configurations.

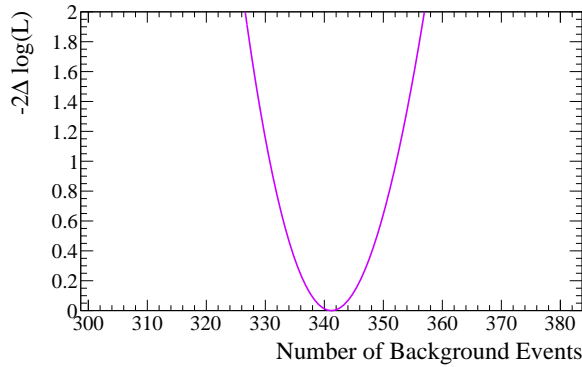


(a) Water-in Configuration

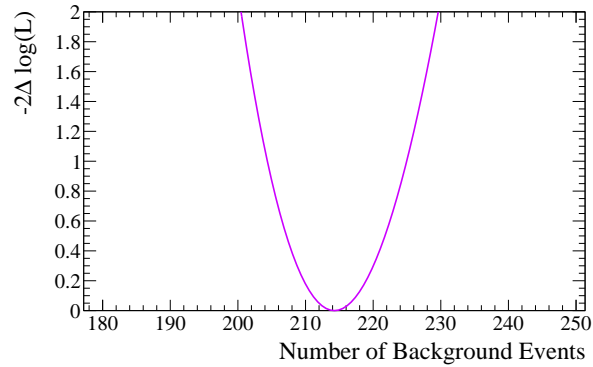


(b) Water-out Configuration

Figure A.10: The negative log likelihood curves for the number of signal events in the selected region for both the $P\emptyset D$ water-in and water-out configurations.



(a) Water-in Configuration



(b) Water-out Configuration

Figure A.11: The negative log likelihood curves for the number of background events in the selected region for both the $P\emptyset D$ water-in and water-out configurations.

A.1. UNCONSTRAINED G FIT

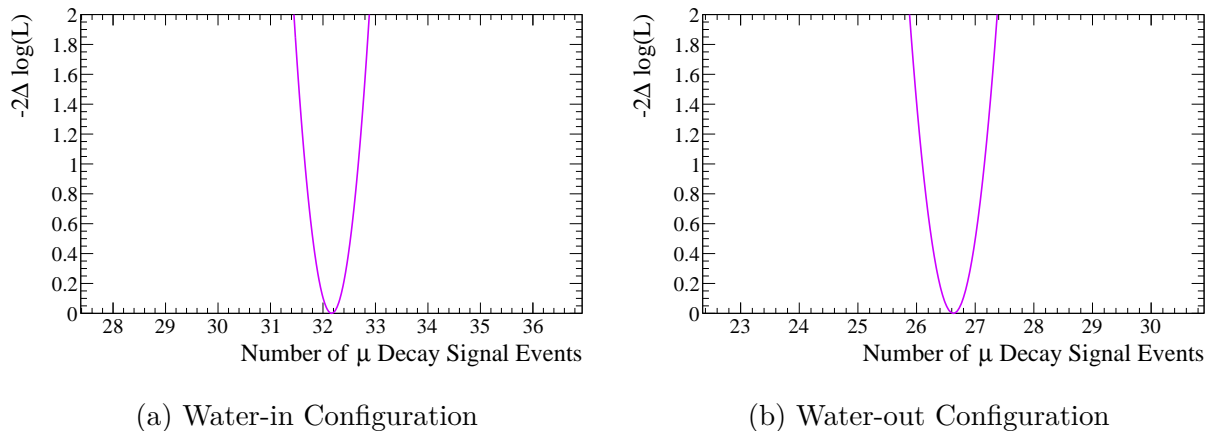


Figure A.12: The negative log likelihood curves for the number of signal events in the sideband region for both the $P\emptyset D$ water-in and water-out configurations.

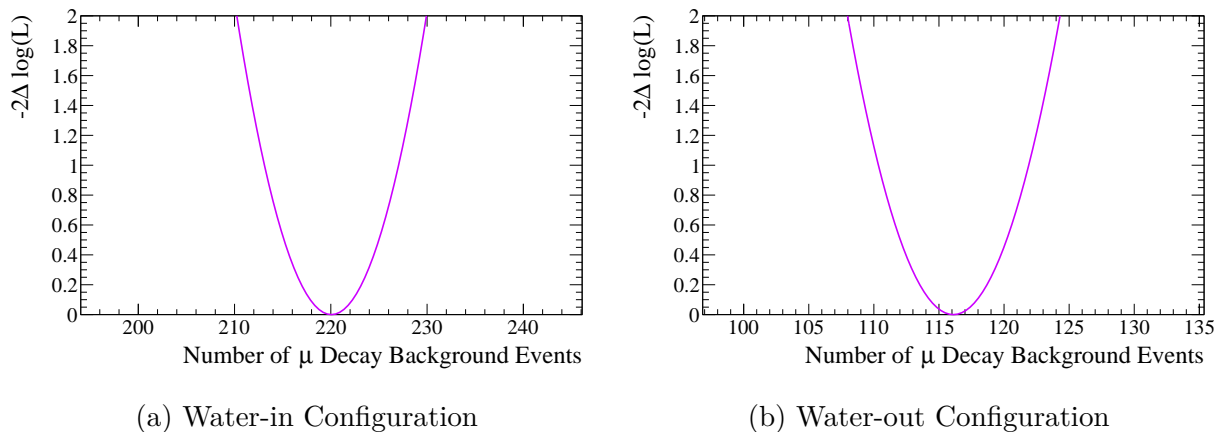
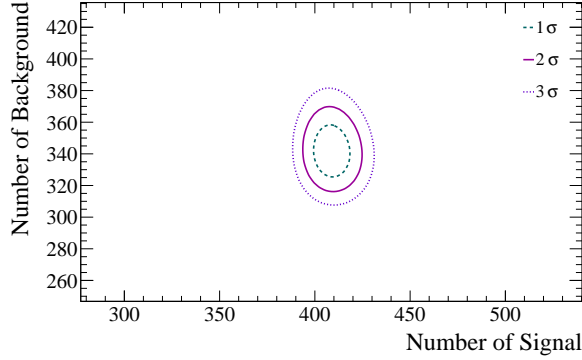
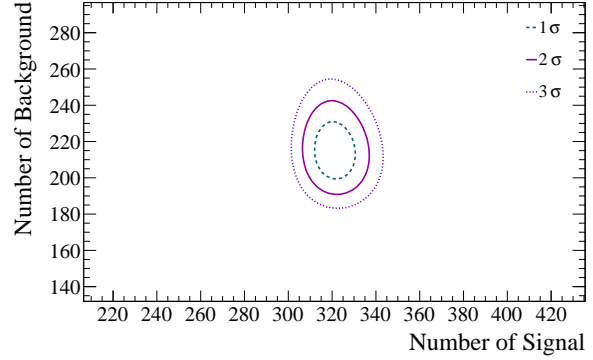


Figure A.13: The negative log likelihood curves for the number of background events in the sideband region for both the $P\emptyset D$ water-in and water-out configurations.

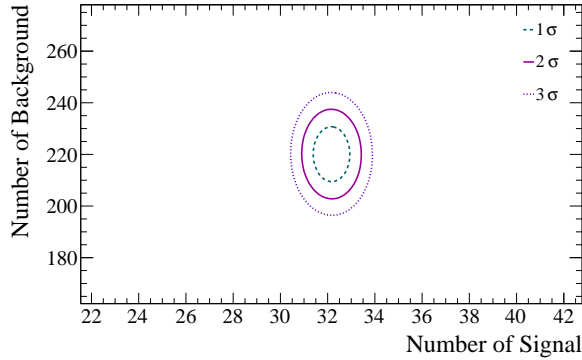


(a) Water-in Configuration

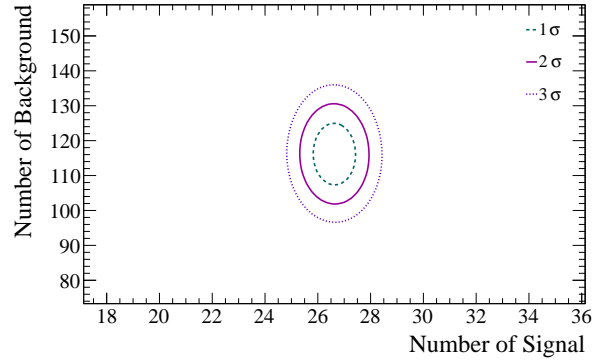


(b) Water-out Configuration

Figure A.14: The negative log likelihood curves for the number of signal events in the sideband region for both the $P\emptyset D$ water-in and water-out configurations.



(a) Water-in Configuration



(b) Water-out Configuration

Figure A.15: The negative log likelihood curves for the number of background events in the sideband region for both the $P\emptyset D$ water-in and water-out configurations.